SPECIAL STUDIES RELATED TO THE IMPERIAL VALLEY EARTHQUAKE OF OCTOBER 15, 1979

FINAL PROJECT REPORT

National Science Foundation

Award PFR-8007418

Award Period: September 1, 1980 to February 28, 1982

John G. Anderson and James N. Brune
Institute of Geophysics and Planetary Physics
Scripps Institution of Oceanography
University of California, San Diego
La Jolla, California 92093

August 30, 1982

50272-101

REPORT DOCUMENTATION PAGE	1. REPORT NO. NSF/CEE-82051	2.	3. Recipient's Accession No. PB82 125202
4. Title and Subtitle: Special Studies Related to the Imperial Valley Earthquake of October 15, 1979, 1982 Final Report			5. Report Date: August 1982 6.
7. Author(s): J.G. Anderson, J.N. Brune			8. Performing Organization Rept. No.
9. Performing Organization Name and Address: University of California at San Diego Institute of Geophysics and Planetary Physics La Jolla, CA 92093			10. Project/Task/Work Unit No. 11. Contract(C) or Grant(G) No. (C) (G) CEE8007418
12. Sponsoring Organization Name and Address: Directorate for Engineering (ENG) National Science Foundation 1800 G Street, N.W. Washington, DC 20550			13. Type of Report & Period Covered: Final 9/1/80 - 2/28/82 14.

15. Supplementary Notes

16. Abstract (Limit: 200 words)

Results are presented of research on the Imperial Valley earthquake of October 15, 1979. A thesis is summarized which presents a formulation for subsurface slip on a known fault as the solution to an inverse problem in which recorded surface ground motion is the data, and which suggests a new method for computing the complete elastic response of a vertically heterogeneous halfspace. Appendices contain a description of strong motion accelerograms recorded in the earthquake from sites south of the border; a preliminary analysis of the accelerograms; an explanation of special problems originating with various accelerograms; an evaluation of the performance of the digital accelerographs in Mexico; and a description of a formal inversion of all the strong ground motion data used to obtain the details of the earthquake source mechanism during the earthquake.

17. Document Analysis a. Descriptors

California
Earthquakes
Accelerometers
Amplitude
Sources
Hazards
Shock waves

b. Identifiers/Open-Ended Terms

Elastic response
Ground motion
Imperial Valley (California)
Mexico

J.N. Brune, /PI

c. COSATI Field/Group

18. Availability Statement	19. Security Class (This Report)	21. No. of Pages
NTIS	20. Security Class (This Page)	22. Price

(See ANSI-Z39.18) See Instructions on Reverse

OPTIONAL FORM 272 (4-77)
(Formerly NTIS-35)
Department of Commerce

TABLE OF CONTENTS

ABSTRACT OF THE DISSERTATION

Forward Simulation and Linear Inversion of Earthquake Ground Motions

by

Allen Hiram Olson

Doctor of Philosophy in Earth Science

University of California, San Diego, 1982

Professor James N. Brune, Co-chairman

Research Geophysicist John A. Orcutt, Co-chairman

In PART I of this dissertation, a new method is presented for computing the complete elastic response of a vertically heterogeneous halfspace. The method utilizes a discrete wavenumber decomposition for the horizontal dependence of the wave motion in terms of a Fourier-Bessel series. The series representation is exact and consequently eliminates the need to numerically integrate a continuous Bessel transform. The vertical and time dependence of the wave motion is obtained as the solution to a system of partial differential equations. These equations are solved numerically by a combination of finite element and finite difference methods which accommodate arbitrary vertical heterogeneities. By using a reciprocity relation, the wave motion is computed simultaneously for all source-observer combinations of interest so that the differential equations need only be solved once. A comparison is made, for layered media, between between the solutions obtained by discrete wavenumber/finite element, wavenumber integration, axisymmetric finite element, and generalized rays.

In PART II of this dissertation, subsurface slip on a known fault is formulated as the solution to an inverse problem in which recorded surface ground motion is the data. Two methods of solution are presented: the least squares method, which minimizes the squared differences between theory and data, and the constrained least squares method which

simultaneously maintains a set of linear inequalities. Instabilities in the solution are effectively eliminated in both methods and the sensitivity of the solution to small changes in the data is quantitatively stated. The inversion methodology is applied to 77 components of near-field ground acceleration recorded during the October 15, 1979 Imperial Valley earthquake. The faulting is constrained to propagate bilaterally away from the epicenter at an average velocity of 90 percent of the shear wave speed on a vertical fault plane extending from the surface to ten kilometers depth. Inequality constraints are used to keep the faulting sequence physically reasonable by maintaining right lateral motion and positive slip velocity. The preferred solution is stable and provides a good fit to the data; it is also realistic and consistent with observed surface offsets and independent estimates of seismic moment.

PUBLICATION CITATIONS

1. Anderson, J.G. and J.E. Luco (1982a). Parametric Study of Near-Field Ground Motion for a Strike-Slip Dislocation Model. Bull. Seism. Soc. Am., in press.

2. Anderson, J.G. and J.E. Luco (1982b). Parametric Study of Near-Field Ground Motions for Oblique Slip and Dip Slip Dislocation Models. Bull. Seism. Soc. Am., in press.

3. Anderson, J.G. and R.S. Simons (1982). Mexicali Valley Accelerogram Date: 1978-1980, Report 82-1, Strong Motion Project, Inst. of Geophysics and Planetary Physics, University of California, San Diego, La Jolla, California.

4. Anderson, J.G., J.N. Brune, J. Prince, and F.L. Vernon III (1982). Preliminary Report on the Use of Digital Strong Motion Recorders in the Mexicali Valley, Baja California, Bull. Seism. Soc. Am., in press.

5. Anderson, J.G. (1982). Preliminary Evaluation of Site Effects at Digital Accelerograph Sites, Mexicali Valley, Mexico, in preparation.

6. Brune, J.N., J. Prince, F.L. Vernon III, E. Mena, and R.S. Simons (1982). Strong Motion Data Recorded in Mexico during the October 15 Main Shock, U.S. Geol. Survey, in press.

7. Luco, J.E. and J.G. Anderson (1982). Steady-State Response of an Elastic Half-Space to a Moving Dislocation of Finite Width, Bull. Seism. Soc. Am., in press.

8. Olson, A.H. (1982). Forward Simulation and Linear Inversion of Earthquake Ground Motions, Ph.D. Thesis, University of California, San Diego.

9. Olson, A.H. and R.J. Apsel (1982). Finite Faults and Inverse Theory with Applications to the 1979 Imperial Valley Earthquake, Bull. Seism. Soc. Am., in press.

10. Singh, S.K., R.J. Apsel, J. Fried, and J.N. Brune (1982). Spectral Attenuation of SH-Waves along the Imperial Fault, Bull. Seism. Soc. Am., in press.

TECHNICAL DESCRIPTION OF PROJECTS AND RESULTS

3.1 Introduction

The Imperial Valley earthquake of October 15, 1979, provided a wealth of strong motion data, both south and north of the U.S.-Mexico international border. This earthquake may be one of the most if not the most important earthquake yet recorded in terms of engineering seismology: (1) it has the highest recorded accelerations and velocities of any earthquake to date, even though it was only moderate in magnitude (6.6) and occurred in relatively highly attenuating sediments; (2) it severely damaged a heavily instrumented building; (3) it was recorded on a special close-spaced digital array and an array of instruments on a bridge almost at the fault trace; (4) it was surrounded by instruments both in the direction of rupture propagation (northwest) and in the direction away from rupture propagation (southeast to our array in Baja California, Mexico), thus allowing for the first time a detailed study of the focusing of energy by rupture propagation; and (5) it was recorded on a large number of digital instruments (7 in our own array) allowing for the first time a detailed comparison of the performance of digital and conventional accelerographs. Because this earthquake is so important and because of the urgency associated with many of these problems (for example, related to siting of nuclear power plants or choices between digital and conventional instrumentation) we considered that it was important to carry out extensive studies related to the data we recorded south of the border and to the aftershock data we recorded on both sides of the border.

We therefore requested support for expenses related to data from

the main shocks recorded south of the border and data from aftershocks on both sides of the border. In particular, we requested funds for (1) preparation and analysis of strong motion data recorded south of the border, most of it on special new digital accelerographs (Terra Technology and Kinemetrics); (2) special instrument checkout and calibration to verify the data recorded; (3) reconnaissance survey of site conditions and shallow site geology at each station; (4) field work, travel expenses and expenses for recording, preparation and analysis of data from numerous aftershocks recorded both on digital seismographs and on digital strong motion instruments; (5) comparison of integration using digital delay recording with integration using conventional records; (6) purchase of a new DCS-300 - DCA-310 combination playback unit; and (7) detailed modeling of the strong motion data to determine the nature of the rupture process during the earthquake

3.2 Preparation and Analysis of Strong Motion Data Recorded South of the U.S.-Mexico Border.

Strong motion accelerograms recorded in this earthquake, together with all other accelerograms from sites south of the U.S. Mexico border for the years 1978-1980 have been catalogued and are now available from the National Geophysical and Solar-Terrestrial Data Center, National Oceanic and Atmospheric Administration, Boulder, Colorado. These data are described in Appendix I. Preliminary analysis of accelerograms from the October 15, 1979 earthquake is given in Appendix II.

3.3 Special Instrument Checkout and Calibration.

Tilt test calibrations were performed, and the results were incor-

porated into the data preparation stage as the accelerograms were prepared for distribution. Special problems originating with individual accelerograms are noted in Appendix I.

3.4 Reconnaissance Survey of Site Conditions and Shallow Site Geology at Each Station.

Appendix III describes an analysis of the coda of the accelerograms to derive the relative site amplifications, as a function of frequency, for digital accelerograph sites.

3.5 Preparation and Analysis of Data from Aftershocks.

All digital aftershock records have been transferred to 9-track computer-compatible magnetic tape, and are available for use by interested scientists.

Spectra and spectral attenuation for selected aftershocks have been studied and are described in Appendix IV, which also shows station locations and locations of some of the more widely recorded aftershocks of the earthquake.

3.6 Comparison of Integration Using Digital Delay Recordings with Integration Using Conventional Photographic Recordings.

Appendix V describes an evaluation of the performance of the digital accelerographs in Mexico, including reliability, noise levels, and integration of the accelerograms.

3.7 Purchase of a new playback unit for digital data.

The playback unit was purchased and is operating satisfactorily.

3.8 Modeling of the strong motion data to determine the nature of the rupture process.

The rupture process of the main shock has been studied with one relatively simple mathematical model and by means of a very sophisticated inverse procedure. Appendix VI describes a parametric study of the phase of strong ground motion caused by passage of the rupture on a nearby fault. We observe that this phase is symmetric with respect to the time when rupture passes the site. Therefore, as described in Appendix VI, this symmetry has been exploited to obtain one estimate of the rupture velocity during this earthquake. Results in Appendix VI, also suggest that layered structure of the earth is more important than asperities or the fault starting and stopping phase in determining the amplitudes of strong ground motion. We also note (Appendix VII) that a dipping fault plane or a dip-slip component of ground motion might lead to some of the asymmetry of ground motion on opposite sides of the fault surface.

Appendix VIII, describes a formal inversion of all the strong ground motion data to obtain the details of the earthquake source mechanism during the earthquake.

APPENDIX I

Mexicali Valley Accelerogram Data: 1978-1980

John G. Anderson, Richard S. Simons

Report 82-1

Strong Motion Project

Institute of Geophysics & Planetary Physics

University of California at San Diego, La Jolla, CA 92093

(Report accompanies data tape of the same title)

(N.B.)

Mexicali Valley Accelerogram Data: 1978-1980

John G. Anderson, Richard S. Simons

Introduction

The Institute of Geophysics and Planetary Physics (IGPP) of the University of California, San Diego and the Instituto de Ingenieria of Universidad Nacional Autónoma de México (UNAM) jointly operate a strong-motion accelerograph network in the Mexicali Valley, Baja California Norte, Mexico. The Mexicali Valley is the southward continuation of the Imperial Valley of California, USA, and as such it sits astride a portion of the strike-slip boundary between the North America plate and the Pacific plate. The Mexicali Valley has a high historical rate of earthquake occurences, with magnitude 6 or larger earthquakes occurring more frequently than once every ten years, on the average. Accelerograph locations are shown in Figure 1 and listed in Table 1.

The network consists of both digital and analog accelerographs. Experiences with the digital recorders are described in Anderson et al. (1982). In the years 1978 to 1980, the IGPP-UNAM accelerograph network recorded accelerograms from two earthquakes with magnitude greater than 6: the October 15, 1979 Imperial Valley earthquake and the June 9, 1980 Mexicali Valley earthquake. In addition, it recorded several smaller events, as listed on Table 2. A tape has been prepared which includes all data from Table 2 for earthquakes with $M_L \geq 4.0$.

Characteristics of the Data

Accelerograms are stored on the tape as one accelerogram per physi-

cal file. Table 3 lists only the accelerograms which are on the tape, and the corresponding file numbers. Each file consists of a 12-line header followed by the acceleration data in a (2X, F8.3,4 (2X, 5I5)) format. Data are equally spaced at 100 or 200 points per second, corrected for the gain of the instrument, but not corrected for dynamic response. Units of acceleration are mm/sec^2, with the data rounded to the nearest integer. Positive integers correspond to positive acceleration of the ground in the component direction identified in the header. The floating point number in the F8.3 format at the start of each line is the time of the first sample of that line relative to the start of the record. Figure 2 contains a listing of the first part of one file.

Table 4, from Mena et al. (1980), lists the instrument characteristics for analog accelerographs which have contributed data in 1979 and 1980. For the DCA-310, and the DSA-1, we do not yet have individual measurements of natural frequency and damping for the force-balance sensors. Nominal natural frequency for the DCA-310 sensors is 30Hz, nominal damping is 70% critical. For the DSA-1 sensors, the nominal natural frequency is 53Hz, and the nominal damping is 64% critical. The digital recorders are designed to record a segment of the background accelerations immediately preceding the motions which caused the recorders to be triggered. The durations of the pre-event data segments varies because the first seismic motions do not necessarily trigger the accelerographs; actual durations are listed in Table 3.

The zero level of acceleration on the data is only approximately removed; i.e. any datum a_i is associated with a true ground acceleration $a_i - a_0$, where a_0 is an unknown for each record. For the digital data

with a leader consisting of pre-event data, a_0 is similar to the values in this leader. However, for reasons explained in Anderson et al. (1982), the leader is not sufficient to accurately define a_0; rather it serves as a check on estimates derived by other means. Because of least-significance-bit errors in the analog-to-digital conversion on some accelerographs, a_0 may differ from the leader by up to several cm/sec^2 in this data. The peak values of acceleration in Table 3 and the file headers are subject to this same uncertainty in a_0.

Analog accelerograms have been digitized by hand at IGPP or at UNAM. Raw accelerations at unequal spacing averaging 30-50 per sec have been converted to equally spaced data points (100/sec) by means of linear interpolation to 600 samples/sec, followed by low-pass filtering (f_c = 40 Hz) and then decimation. For these analog accelerograms, a_0 may be a function of time.

Files 59, 60, and 61, corresponding to the record from station Victoria from the June 9, 1980 earthquake, deserve special mention. Because of difficulty with the playback (discussed by Simons, 1982), there are some gaps in the accelerograms totaling 1 to 2 sec on each channel. These gaps have been flagged by acceleration values of greater than 14000 mm/sec^2 on this tape.

For the users' convenience, preliminary versions of Simons (1982) and Anderson et al. (1982) are attached as appendices.

References

Anderson, J.G., J.N. Brune, J. Prince, F.L. Vernon (1982). Preliminary report on the use of digital strong motion recorders in the Mexicali Valley (in preparation).

Mena, E., I. Mora, J. Prince, J. Brune, L. Alonso, F. Vernon (1980). Sismo del Valle de Mexicali del 9 de Junio de 1980. Primera Parte: Daños observados y analysis preliminar de registros en accelerografos analogicos.

Simons, R.S. (1982). The strong motion record from station Victoria, in J.G. Anderson and R.S. Simons, editors, The Mexicali Valley Earthquake of 9 June 1980, Newsletter, Earthquake Engineering Research Institute (in press).

TABLE 1
ANALOG STRONG MOTION STATIONS IN NORTHERN BAJA CALIFORNIA

Station Name	Location
Aeropuerto Mexicali	32° 39.05'N 115° 19.90'W
Ignacio Zaragoza	32° 11.58'N 116° 29.10'W
Ciencias Marinas	31° 51.85'N 116° 39.70'W
Bufadora	31° 41.22'N 116° 37.40W
Km 62	31° 49.83'N 116° 03.45'W
Sta. Catarina	31° 39.17'N 115° 49.53'W
Valle Trinidad	31° 24.00'N 115° 43.00'W
Mexicali SAHOP	32° 37.05'N 115° 26.25'W
Mexicali Hospital	32° 38.45'N 115° 28.28'W
Mexicali Casa Flores	32° 37.08'N 115° 06.18'W

TABLE 2
CATALOG OF STRONG MOTION DATA FROM MEXICALI VALLEY

Event				Stations That Recorded		
Date	Time	Location	Mag.*	Name	Recorder	Comments
03/11/78	23:57:46.5	32° 15.50'N 115° 07.75'W	4.8	Victoria Delta	SMA-1 SMA-1	Digitized on a Bendix Digitizer
03/12/78	00:30:17.3	32° 19.30'N 115° 05.45'W	4.5	Victoria	SMA-1	Digitized on a Bendix Digitizer
03/12/78	18:42:24.0	32° 15.10'N 115° 05.90'W	4.8	Victoria	SMA-1	Digitized on a Bendix Digitizer
10/10/79	19:48:36.65	32° 17.73'N 115° 19.23'W	4.1	Delta Cerro Prieto	Terra Tech Terra Tech	
10/15/79	23:16:55.09	32° 38.37'N 115° 19.68'W	6.6	Delta Cerro Prieto Chihuahua Compuertas Agrarias Victoria Cucapah Aeropuerto Mexicali (Casa Flores)	Terra Tech Terra Tech Terra Tech Terra Tech Terra Tech Kinemetrics Kinemetrics SMA-1 SMA-1	 No Timing No Timing No Timing; 1 Horiz. Inop. Digitized at UNAM Digitized at UNAM
10/15/79	23:19:29.98	32° 45.94' 115° 26.45'	5.2	Delta	Terra Tech	Triggered on S
10/24/79	06:44:27.15	32° 25.09'N 115° 13.22'W	3.2	Cerro Prieto	Terra Tech	Triggered on S
12/21/79	20:40:23.26	32° 27.03' 115° 11.72'	4.8	Chihuahua Compuertas Cucapah	Terra Tech Terra Tech Kinemetrics	Triggered on S Triggered on S No Timing; 1 Horiz. Inop.
06/09/80	03:28:19.4	32° 11.12' 115° 04.55'	6.1	Chihuahua Victoria Cucapah Cerro Prieto Mexicali (SAHOP) Hospital (3 levels)	Terra Tech Kinemetrics Kinemetrics SMA-1 SMA-1 SMA-1	Triggered on S Severe Dropouts No Timing; 1 Horiz. Inop. Digitized at UNAM Digitized at UNAM Digitized at UNAM
06/09/80	03:29	(Aftershock of above?: Follows by ~40 secs)		Chihuahua Victoria Cucapah Cerro Prieto	Terra Tech Kinemetrics Kinemetrics SMA-1	S-P ~3 secs No Timing; 1 Horiz. Inop., S-P ~4 secs

Event				Stations That Recorded		
Date	Time	Location	Mag.*	Name	Recorder	Comments
06/09/80	03:30:04.7 (P arrival)		4.9	Victoria	Kinemetrics	S-P ~1.7 secs
06/09/80	03:30:28.1 (P arrival)		5.3	Victoria	Kinemetrics	S-P ~2.0 sec
06/09/80	19:47:54.9	32° 23.64'N 115° 11.52'W	3.2	Delta	Terra Tech	Triggered on S
06/09/80	20:17:11.6	32° 16.32'N 115° 09.24'W	2.5	Delta	Terra Tech	Triggered on S
06/09/80	20:31:32.3	32° 13.14'N 115° 05.34'W	3.9	Delta	Terra Tech	Triggered on S
06/09/80	21:05:37.7	32° 23.52'N 115° 10.44'W	2.4	Delta	Terra Tech	Triggered on S
06/09/80	23:26:18.6	32° 16.14'N 115° 09.30'W	3.0	Delta	Terra Tech	Triggered on S
06/09/80	23:33:41.0	32° 21.90'N 115° 12.90'W	4.3	Delta Cerro Prieto	Terra Tech	
06/10/80	00:17:36.9	32° 20.40'N 115° 12.18'W	3.3	Delta	Terra Tech	
06/10/80	00:17:58.8	32° 25.02'N 115° 12.00'W	3.3	Delta	Terra Tech	
06/10/80	00:36:51.0	32° 22.86'N 115° 11.88'W	3.4	Delta	Terra Tech	
06/10/80	01:07:08.6	32° 19.20'N 115° 12.72'W	3.6	Delta	Terra Tech	Triggered on S
06/10/80	01:35:36.6	32° 22.62'N 115° 12.54'W	3.4	Delta	Terra Tech	
06/10/80	01:36:28.1	32° 22.98'N 115° 13.02'W	2.9	Delta	Terra Tech	Triggered on S
06/10/80	01:59:01.9	32° 22.86'N 115° 11:52'W	2.7	Delta	Terra Tech	
06/10/80	05:36:24.0	32° 24.00'N 115° 12.84'W	3.3	Delta	Terra Tech	

* Cal Tech Magnitude (M_L)

Note concerning the interval Oct. 25, 1979 through Mar. 8, 1980 at Station Victoria: The Kinemetrics Digital Recorder at Victoria recorded seven events during this period, with maximum acceleration levels (O-P) ranging from about 15cm/sec^2 to 170cm/sec^2, and S-P's generally less than 4.5 seconds. Lacking timing on the tape it has not yet been possible to correlate these signals positively with the (Cal Tech) catalog of nearby events.

TABLE 3A
1978 DATA (UCSD FILE R.MV78) ON TAPE

Epicenter Date/Time/ Location†	M_L†	Station Inst. Type	UCSD File No.	EDIS Tape File	Component	a_{max} (cm/sec^2)	Duration of PED‡/Record	Comments
Mar 11, 1978	4.8	Victoria	101	1	S45°W	451	0/14.68	MB
23:57:46.5		SMA-1	102	2	up	328	0/ 9.00	M
32°15.50'W			103	3	S45°E	458	0/ 9.67	M
115°07.75'W		Delta	201	4	S45°W	128	0/16.67	MB
		SMA-1	202	5	up	286	0/10.00	M
			203	6	S45°E	299	0/16.68	M
Mar 12, 1978	4.5	Victoria	301	7	S45°W	410	0/11.68	MB
00:30:17.3		SMA-1	302	8	up	88	0/ 7.00	M
32°19.30'N			303	9	S45°E	452	0/11.68	M
115°05.45'W								
Mar 12, 1978	4.8	Victoria	401	10	S45°W	552	0/14.00	MC
18:42:24.0		SMA-1	402	11	up	218	0/10.00	M
32°15.10'N			403	12	S45°E	324	0/13.99	M
115°05.90'W								

† CalTech determinations
‡ PED = Pre-Event Data

TABLE 38
1979 DATA (UCSD FILE R.MV79) ON TAPE

Epicenter Date/Time† Location	M_L†	Station Inst. Type	UCSD File No.	EDIS Tape File	Component	a_{max} (cm/sec^2)	Duration of PED‡/Record	Comments
Oct 10, 1979	4.1	Delta	101	13	N8°W	145	0.30/	AE
19:48:36.65		DCA-310	102	14	down	78	25.81	
32°17.73'N			103	15	S82°W	141		
115°19.23'W		Cerro Prieto	201	16	S57°W	65	1.20/	AE
		DCA-310	202	17	down	57	23.65	
			203	18	S33°E	42		
Oct 15, 1979	6.6	Delta	301	19	N8°W	340	0.64/	AE
23:16:55.09		DCA-310	302	20	down	149	100.15	
32°38.37'N			303	21	S82°W	231		
115°19.68'W		Cerro Prieto	401	22	S57°W	154	0.74/	AE
		DCA-310	402	23	down	196	99.25	
			403	24	S33°E	163		
		Chihuahua	501	25	N12°E	262	0.74/	AE
		DCA-310	502	26	down	211	51.59	
			503	27	N78°W	251		
		Compuertas	601	28	N15°E	184	4.76/	NJ
		DCA-310	602	29	down	72	57.03	
			603	30	N75°W	145		
		Agrarias	701	31	N3°E	351	0.60/	AEI
		DCA-310	702	32	down	889	28.44	
			703	33	N87°W	230		
		Victoria	801	34	N75°E	119	2.58/	BE
		DSA-1	802	35	up	57	86.38	
			803	36	N15°W	165		
		Cucapah	901	37	N85°E	303	9.04/	CEH
		DSA-1	902	38	up	136	92.54	
		Aeropuerto	1001	39	N45°W	256	0/13.60	GC
		SMA-1	1002	40	up	156	0/11.22	G
			1003	41	N45°E	319	0/14.76	G
		Mexicali	1101	42	N00°E	238	0/17.01	GD
		Casa Flores	1102	43	up	328	0/15.77	G
		SMA-1	1103	44	N90°W	435	0/18.97	G
Oct 15, 1979	5.2	Delta	1201	45	N 8°W	108		AF
23:19:29.98		DCA-310	1202	46	down	24	0/18.13	
32°45.94'N			1203	47	S82°W	58		
115°26.45'W								
Dec 21, 1979	4.8	Chihuahua	1401	48	N12°E	114		AF
20:40:23.26		DCA-310	1402	49	down	51	0/14.44	
32°27.03'N			1403	50	N78°W	160		
115°11.72'W		Compuertas	1501	51	N15°E	181		AF
		DCA-310	1502	52	down	54	0/13.74	
			1503	53	N75°W	72		
		Cucapah	1601	54	N85°E	165	1.80/	
		DSA-1	1602	55	up	124	45.89	CEH

† Caltech determinations
‡ PED = Pre-Event Data

TABLE 3C
1980 DATA (UCSD FILE R.MV80) ON TAPE

Epicenter† Date/Time Location	M_L†	Station Inst. Type	UCSD File No.	EDIS Tape File	Component	a_{max} (cm/sec^2)	Duration of PED‡/Record	Comments
Jun 9, 1980	6.1	Chihuahua	101	56	S12°W	182	0.05/	A
03:28:19.4		DCA-310	102	51	down	170	56.41	
32°11.12'N			103	58	S78°E	150		
115°04.55'W		Victoria	201	59	N50°E	959	2.0/	BEKL
		DSA-1	202	60	up	980	99.68	
			203	61	N40°W	858		
		Cucapah	301	62	N85°E	76	1.76/	CEH
		DSA-1	302	63	up	114	87.07	
		Cerro Prieto	401	64	N45°E	613	0/24.49	GB
		SMA-1	402	65	up	288	0/25.55	G
			403	66	N45°W	575	0/24.58	G
		Mexicali SAHOP	501	67	N10°E	110	0/15.72	GD
		SMA-1	502	68	up	56	0/20.24	G
			503	69	N80°W	75	0/15.64	G
		Mexicali Hospital	701	73	N00°E	46	0/18.40	GD
		Basement	702	74	up	25	0/21.95	G
		SMA-1	703	75	N90°W	30	0/25.59	G
		2nd level	601	70	N00°E	139	0/26.10	GD
		SMA-1	602	71	up	52	0/21.14	G
			603	72	N90°W	73	0/25.12	G
		Roof	801	76	N00°E	180	0/37.05	GD
		SMA-1	802	77	up	69	0/20.87	G
			803	78	N90°W	126	0/36.14	G
Jun 9, 1980		Cerro Prieto	1401	82	N45°E	137	0/15.43	GBS
03:29		SMA-1	1402	83	up	77	0/7.97	G
(immediate aftershock)			1403	84	N45°W	104	0/10.23	G
Jun 9, 1980	4.9	Victoria	1201	79	N50°E	272	3.14/	BP
03:30:04		DSA-1	1202	80	up	90	88.32	Q
and			1203	84	N40°W	382		R
Jun 9, 1980 03:30:28	5.3							
Jun 9, 1980	4.3	Delta	2001	85	N8°W	175	0.62/	A
23:33:41.0		DCA-310	2002	86	up	347	15.14	
32°21.90'N			2003	87	S82°W	159		
115°12.90'W								
		Cerro Prieto	2101	88	N45°E	64	0/7.80	GB
		SMA-1	2102	89	vert	32	0/2.92	G
			2103	90	N45°W	31	0/6.31	G

† Caltech determinations
‡ PED = Pre-Event Data

Table 3 Comments

A Accelerogram timed by internal clock

B Accelerogram timed by WWVB radio

C Accelerogram not timed: WWVB not recorded

D Accelerogram not timed

E Digital recording recovered first P-wave motions

F S-wave trigger

G Traces are not simultaneous due to digitization from original film recording

H Third component failed

I Coupling of sensor and pier partially failed: Vertical component unreliable, horizontal components probably less affected.

J Accelerogram triggered in time to record P-wave, but first non-zero motions on all three components coincide with S.

K Difficulty in playback of cassette tape.

L Largest peak accelerations from recovered portions of accelerogram.

M Care was taken during digitization to keep traces simultaneous.

N Accelerogram timed by internal clock, but clock correction was not obtained.

P Continuation of accelerogram from main shock (EDIS Tape File 59).

Q Continuation of accelerogram from main shock (EDIS Tape File 60).

R Continuation of accelerogram from main shock (EDIS Tape File 61).

S Accelerograph at Cerro Prieto recorded continuously between main shock (EDIS Fils 64, 65, 66) and these records. This constitutes only segments which were digitized. Long period motion occurred continuously between main shock and this aftershock.

APPENDIX II

STRONG MOTION DATA RECORDED IN MEXICO DURING THE OCTOBER 15 MAIN SHOCK

James N. Brune[1]

Jorge Prince[2]

Frank L. Vernon III[1]

Enrique Mena[2]

Richard S. Simons[1]

[1]Institute of Geophysics and Planetary Physics
Scripps Institution of Oceanography
University of California, San Diego
La Jolla, California 92093

[2]Instituto de Ingeniería
Universidad Nacional Autónoma de México
México 20, D.F. México

April 28, 1980

STRONG MOTION DATA RECORDED IN MEXICO DURING THE OCTOBER 15 MAIN SHOCK

James N. Brune[1], Jorge Prince[2], Frank L. Vernon III[1], Enrique Mena[2] and Richard S. Simons[1]

ABSTRACT

Seismic signals from the October 15 earthquake were recorded at nine strong motion stations in the Northern Baja California array operated jointly by Mexican and U.S. research interests. Seven of the stations were occupied by three-component digitally-recording accelerographs; the other two contained three-component film-recording accelerographs. This report summarizes the peak accelerations and velocities observed on all components, and the P and S phase arrival times where possible. Four of the stations lacked absolute timing and one station triggered on the S phase rather than the P phase. Near the border, most of the instruments recorded peak horizontal accelerations of about 0.3g, decreasing to 0.17g at the farthest station. The general pattern of strong motion shows considerable complexity.

From each of the digital stations we present playbacks of the three-component accelerograms, as well as integrations of the acceleration records (without instrument correction) to show velocity and displacement. To determine local magnitude, the digital horizontal

strong motion records were converted into equivalent Wood-Anderson seismograms using a deconvolution-convolution technique. The average magnitude from this group is about 6.3, which is somewhat lower than the average magnitude determined to the northwest (6.6), suggesting some focussing of energy to the northwest.

INTRODUCTION

The Imperial Valley earthquake of October 15, 1979 provided a wealth of strong motion data, both south and north of the Mexico - U.S. international border. Most important relative to the data presented here, the earthquake was surrounded by instruments both in the direction of rupture propagation (northwest in the Imperial Valley), and in the direction away from rupture propagation (southeast to our array in Baja California, Mexico). In addition, it was recorded on a large number of digital instruments (seven in our own array) allowing for the first time a detailed comparison of the performance of digital and conventional accelerographs.

PRELIMINARY DESCRIPTION OF DATA RECORDED ON THE NORTHERN BAJA CALIFORNIA STRONG MOTION ARRAY

The Northern Baja California strong motion array was installed as a cooperative Mexico - U.S. project, with U.S. funding by the National Science Foundation (NSF) Research Applied to National Needs (RANN) and Applied Science and Research Applications (ASRA), and Mexican funding by Consejo Nacional de Ciencia y Tecnología (CONACYT) and the Institute of Engineering, Universidad Nacional Autónoma de México.

Initially, 16 SMA-1* film recording instruments were installed (Prince *et al.*, 1977). Prior to the October 15, 1979 Imperial Valley earthquake strong motion records were obtained from the Mesa de Andrade earthquake of December 7, 1976 and the Victoria earthquake swarm of March 1978. We subsequently replaced a number of the SMA-1 instruments with 10 digital accelerographs of the two kinds then available (Terra Technology* and Kinemetrics* instruments), and deployed a cross array of stations to study attenuation of strong motion perpendicular to the fault. At the time of the October 15 earthquake, most of the digital instruments were in operation (two had been temporarily diverted to record possible aftershocks of the March 14, 1979 Petatlán, Mexico earthquake) and most of the piers in the cross array had instruments on them. The part of the array in the Mexicali Valley is shown in Figure 1. Aside from the instruments in the regular array, one instrument operated by the Secretaria de Asentamientos Humanos y Obras Publicas (SAHOP) - UNAM was temporarily at the private residence of Mr. Alfonso Flores in Mexicali.

Most of the instruments performed well. However, no radio time was recorded on any of the Kinemetrics instruments (two digital and two SMA-1, all relying on WWVB radio for time); one of the Terra Technology DCA 310* digital instruments malfunctioned and we have not been able yet to read the cassette tape from it; and another Terra Technology instrument had unexplained erratic low bit behavior. One channel of one of the Kinemetrics digital recorders also failed.

One presumably erroneous recording of a high frequency vertical acceleration occurred at the station Agrarias ($\sim$0.8g at frequencies of $\sim$30 Hz). Inspection of this instrument after the earthquake revealed

*The use of trade names in this publication is intended for descriptive purpose only and does not constitute endorsement by the U.S.G.S.

that one of the mounting bolts was loose on the accelerometer package and this was very likely the cause of the anomalous high frequencies recorded. One corner of the accelerometer package could be oscillated vertically a small amount with one finger. However, the package could not be moved horizontally, and thus we believe that aside from the high frequency cross coupling (which can be filtered out) the horizontal records should be reliable, especially the velocity and displacement. In all, for the main event we obtained 11 records (seven Terra Technology DCA 310, two Kinemetrics digital DSA-1 and two Kinemetrics photographic SMA-1). Table 1 lists the location, orientation and peak accelerations for these records.

Near the border, most of the instruments recorded peak horizontal accelerations of about 0.3g, decreasing to 0.17g at the farthest station. The Cerro Prieto record is of special interest since it is the only record obtained on solid rock south of the border. The stations on solid rock north of the border which recorded this earthquake were at larger distances and recorded considerably lower accelerations (Matthiesen and Porcello, this volume). Cerro Prieto is a massive volcanic cone emplaced through the thick sediments of the Mexicali Valley. Its higher rigidity would normally be expected to reduce the surface accelerations. However, since it is connected to the basement beneath the sediments, one might expect it to transmit high frequency energy to the surface more efficiently than sediments, thus tending to increase the accelerations. Its peak acceleration is somewhat lower than that for nearby stations in sediments. However, its predominant frequency appears to be higher.

Figure 2 shows a plot of peak accelerations as a function of distance from the intersection of the Imperial Fault with the international border, including some of the stations north of the border (Matthiesen and Porcello, this volume). The accelerations to the southeast are quite high to fairly large distances, i.e., they do not show a sharp fall off with distance near the epicenter. The high acceleration observed at Delta at a distance of 33 km is quite surprising.

Figures 3 through 9 show the (unprocessed) three-component acceleration records obtained from the digital accelerographs. Note that the station Compuertas triggered on the S-wave, not the P-wave.

We have done a preliminary integration of the acceleration records to obtain particle velocities and displacements for some of the stations, following Trifunac and Lee (1973). The results are shown in Figures 10 through 29. The records have not been corrected for instrument response at high frequencies. The high pass filter taken for these integrations has a corner frequency of 0.6 Hz. The peak values of velocity for these stations are listed on the figures and tabulated in Table 1.

ARRIVAL TIMES

Since the digital strong motion instruments had delayed recording of 1.6 sec, we can accurately read the onsets of P waves as well as S waves. We have interpreted arrival times as indicated (by dots) on the records shown in Figures 3 through 9. The tabulated values are shown in Table 1.

MAGNITUDES

Since there are no Wood-Anderson recordings to the southeast of the epicenter, the determination of local magnitude, M_L, based primarily on stations to the northwest could be seriously biased, especially if the rupture propagation focussed energy toward the northwest. In order to partly remedy this situation, we have converted the digital strong motion records from the Northern Baja California array into Wood-Anderson equivalent records using the deconvolution-convolution technique suggested by Kanamori and Jennings (1978), and a program to do this written by Alejandro Nava. Magnitudes were then computed from these mock Wood-Anderson records using the standard tables. These magnitudes are listed in Table 1. The average magnitudes from this group of determinations is 6.34. The only solid rock recording, from Cerro Prieto, gives a comparable value of 6.2. These magnitudes are somewhat lower than the average of the magnitudes determined to the northwest, 6.6 (Johnson, this volume) and suggest some focussing of energy to the northwest. Thus, the magnitude which would have been obtained from a uniform sampling of Wood-Anderson records at all azimuths would probably have been about 6.5.

CONCLUSION

The strong motion records of the October 15, 1979 Imperial Valley earthquake recorded in Mexico, combined with the large number of records recorded north of the border provide relatively complete azimuthal coverage with strong motion recordings, i.e., both in the

direction of rupture propagation (northeast) and in the opposite direction. The accelerations (and velocities) are generally higher along the fault to the northwest in the Imperial Valley; however, the pattern of strong motion shows considerable complexity, which is not explained by a simple propagating point source. This may be a result of non-uniform displacement along the rupture and/or structural inhomogeneities. The M_L magnitudes estimated from the strong motion records is about 6.3, somewhat lower than the average magnitude determined from stations to the northwest. Because the data for this earthquake is so extensive, we anticipate that further study will lead to a better understanding of rupture propagation for this earthquake than has been possible for any previous earthquake.

ACKNOWLEDGEMENTS

The installation and operation of the Baja California strong motion array was supported by NSF RANN ENV 75-02939, NSF ASRA PFR77-23829, CONACYT, and the Institute of Engineering, UNAM.

REFERENCES

Kanamori, H. and P. C. Jennings, 1978. Determination of local magnitude, M_L, from strong motion accelerograms, Bull. Seism. Soc. of Amer., 68, 2, pp. 471-485.

Prince, J., J. N. Brune, A. Reyes and A. Nava, 1977. Strong motion instrumentation of Northern Baja California. GSA Abstracts with Programs, 9, 4, p. 484. Meeting of the Seismological Society of America, April 5-7, 1977, Sacramento, California.

Trifunac, M. D. and V. Lee, 1973. Routine computer processing of strong-motion accelerograms, Tech. Rept. EERL 73-03, Earthquake Engineering Dept., Calif. Inst. of Tech., Pasadena.

U.S. Geological Survey, 1977. Western hemisphere strong-motion accelerograph station list - 1976: U.S. Geological Survey Open File Report 77-374, 112 p.

[1] Institute of Geophysics and Planetary Physics
Scripps Institution of Oceanography
University of California, San Diego
La Jolla, California 92093

[2] Instituto de Ingeniería
Universidad Nacional Autónoma
de México
México 20, D. F. México

TABLE 1
(cont'd)

[7] SM = Kinemetrics SMA-1 Film Recorder.
TT = Terra Technology Digital Recorder.
KN = Kinemetrics Digital Recorder.

*This station was temporarily located at the Flores residence in Mexicali, approximately 1 km east of the normal Mexicali SAHOP station (No. 6619). The coordinates given here are those of the Flores residence.

** S - t or S - P is questionable.

*** No absolute timing at station.

**** Film recorders. Acceleration traces could therefore not be readily integrated for velocity or deconvolved/convolved for magnitude.

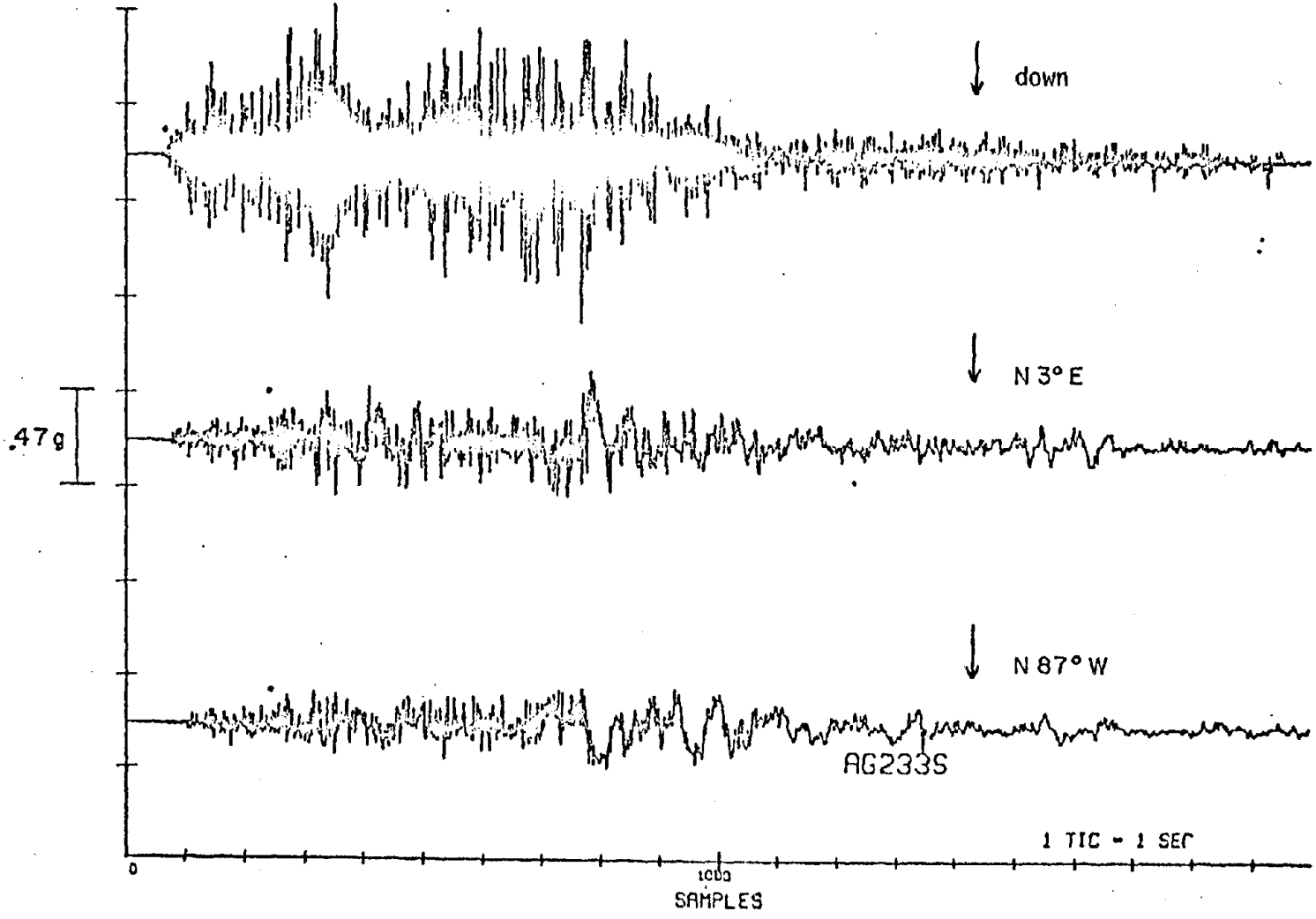

Figure 3. Strong motion record from Agrarias for October 15, 1979 Imperial Valley earthquake (main shock).

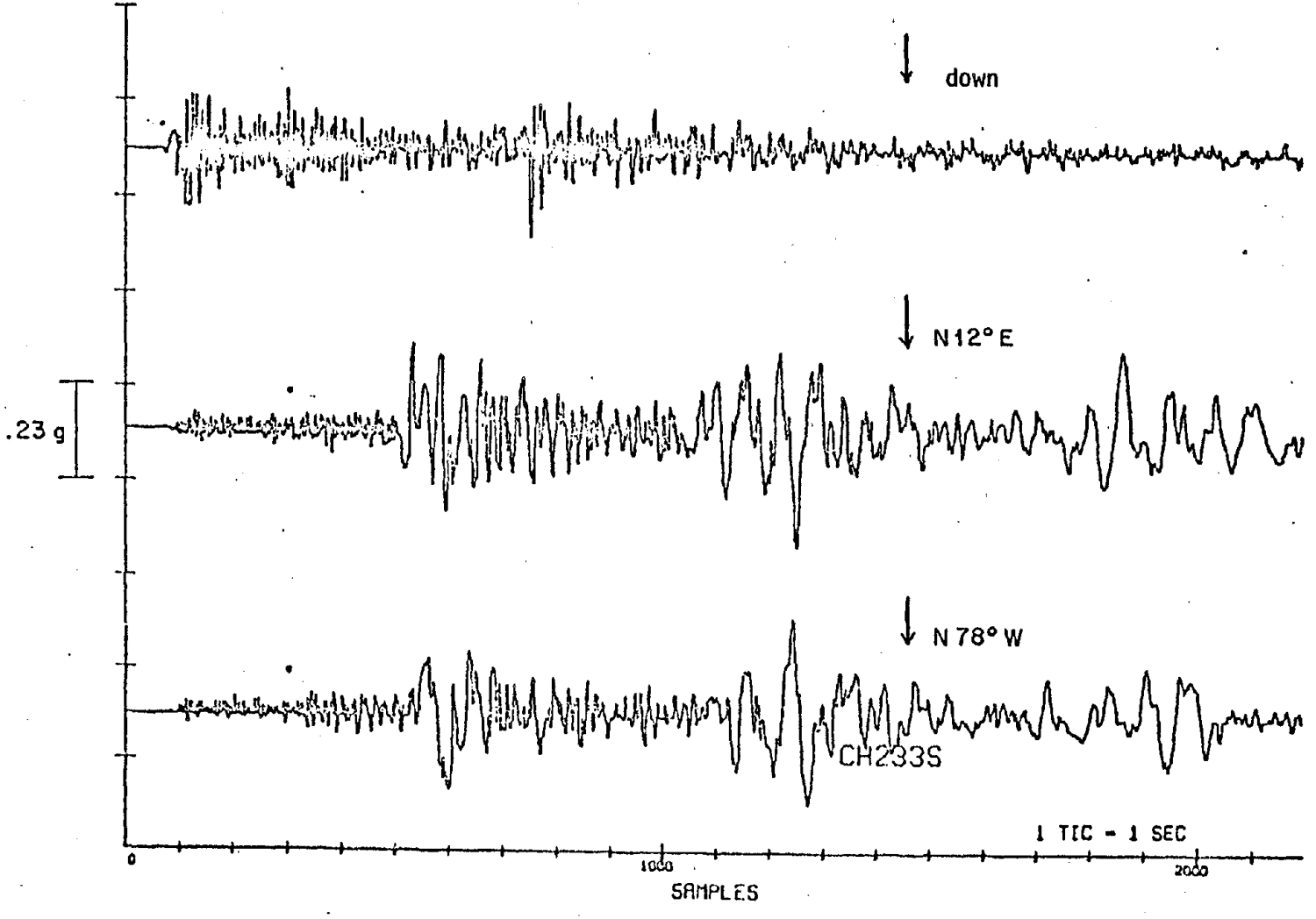

Figure 4. Strong motion record from Chihuahua for October 15, 1979 Imperial Valley earthquake (main shock).

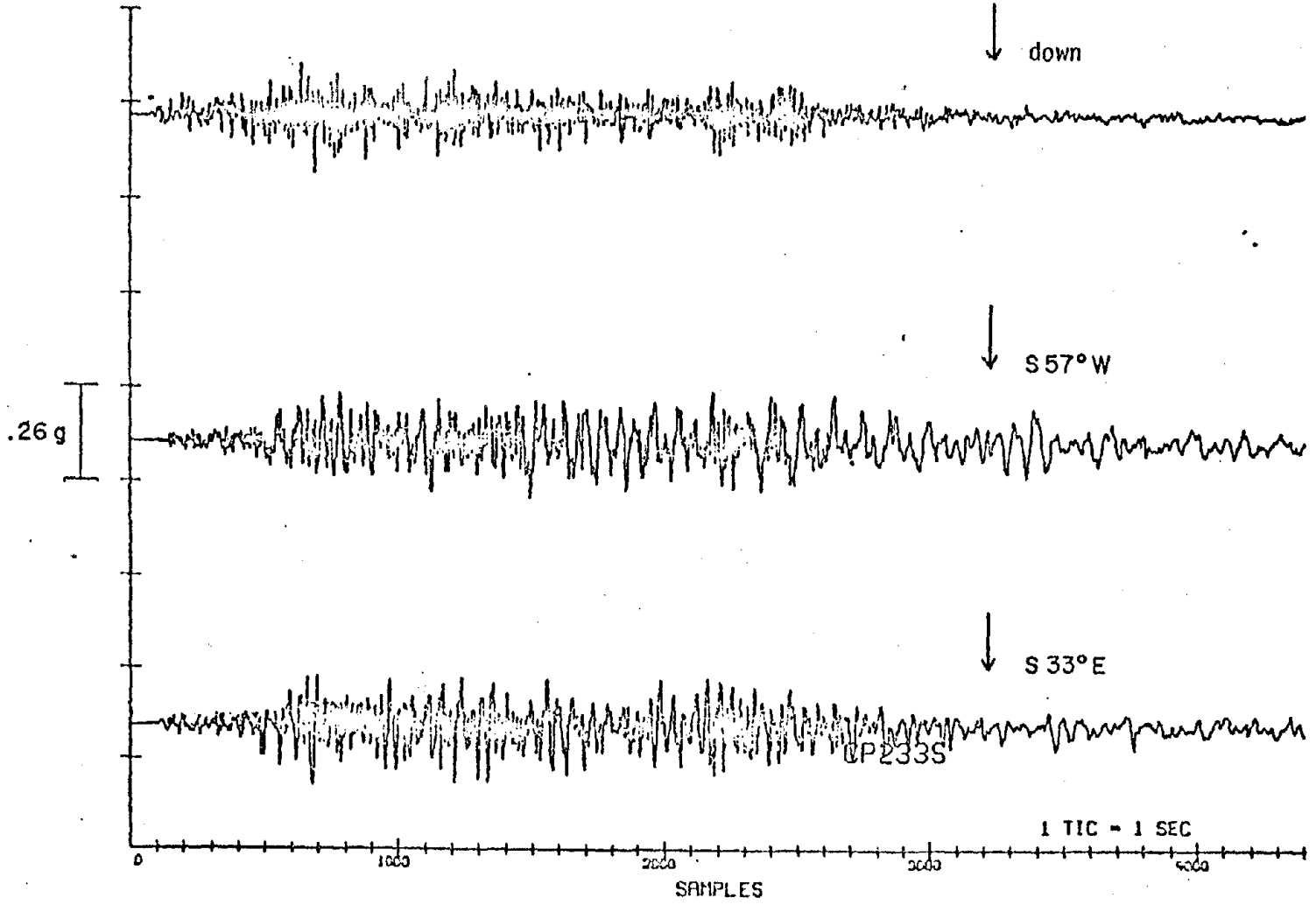

Figure 5. Strong motion record from Cerro Prieto for October 15, 1979 Imperial Valley earthquake (main shock).

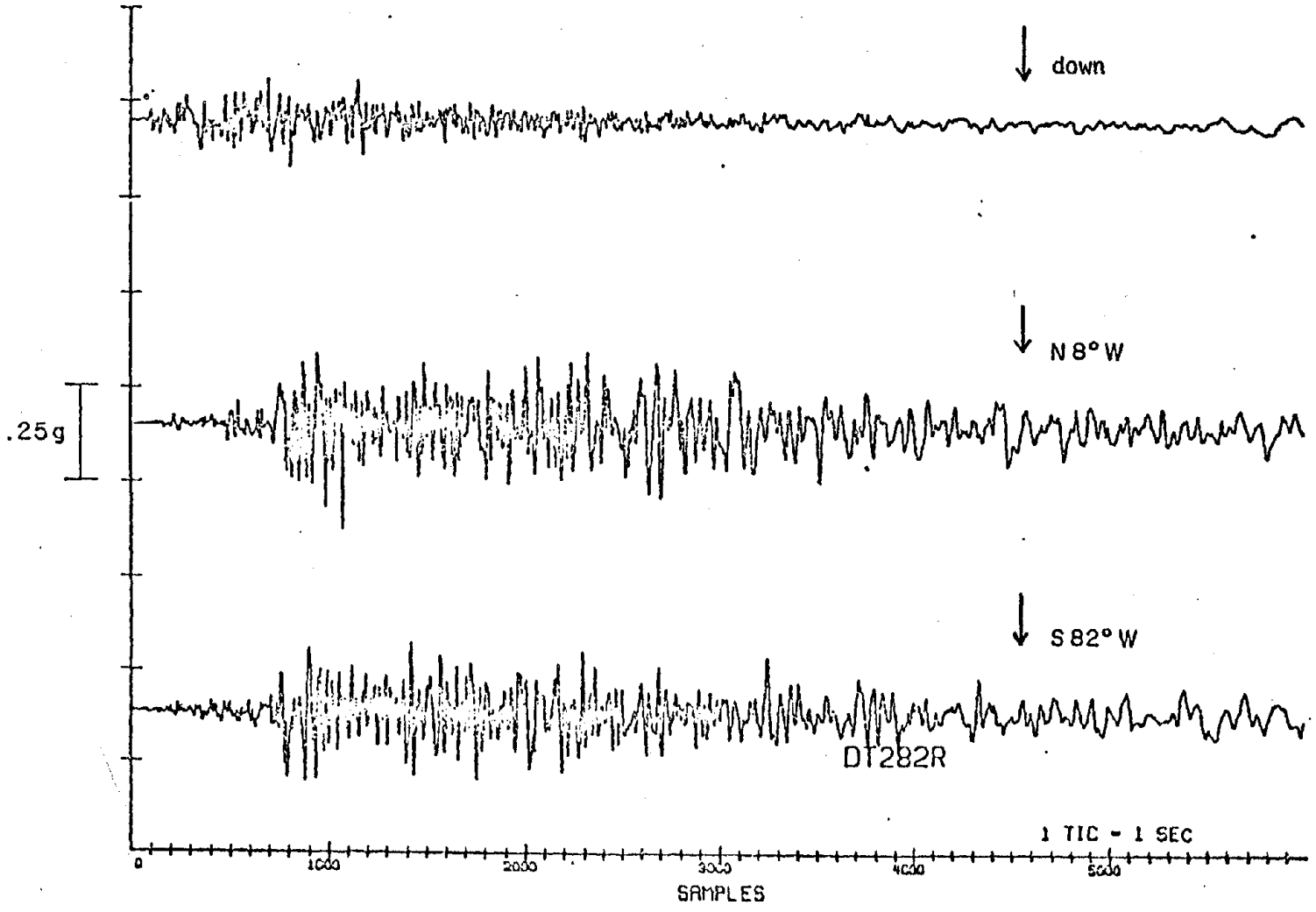

Figure 6. Strong motion record from Delta for October 15, 1979 Imperial Valley earthquake (main shock).

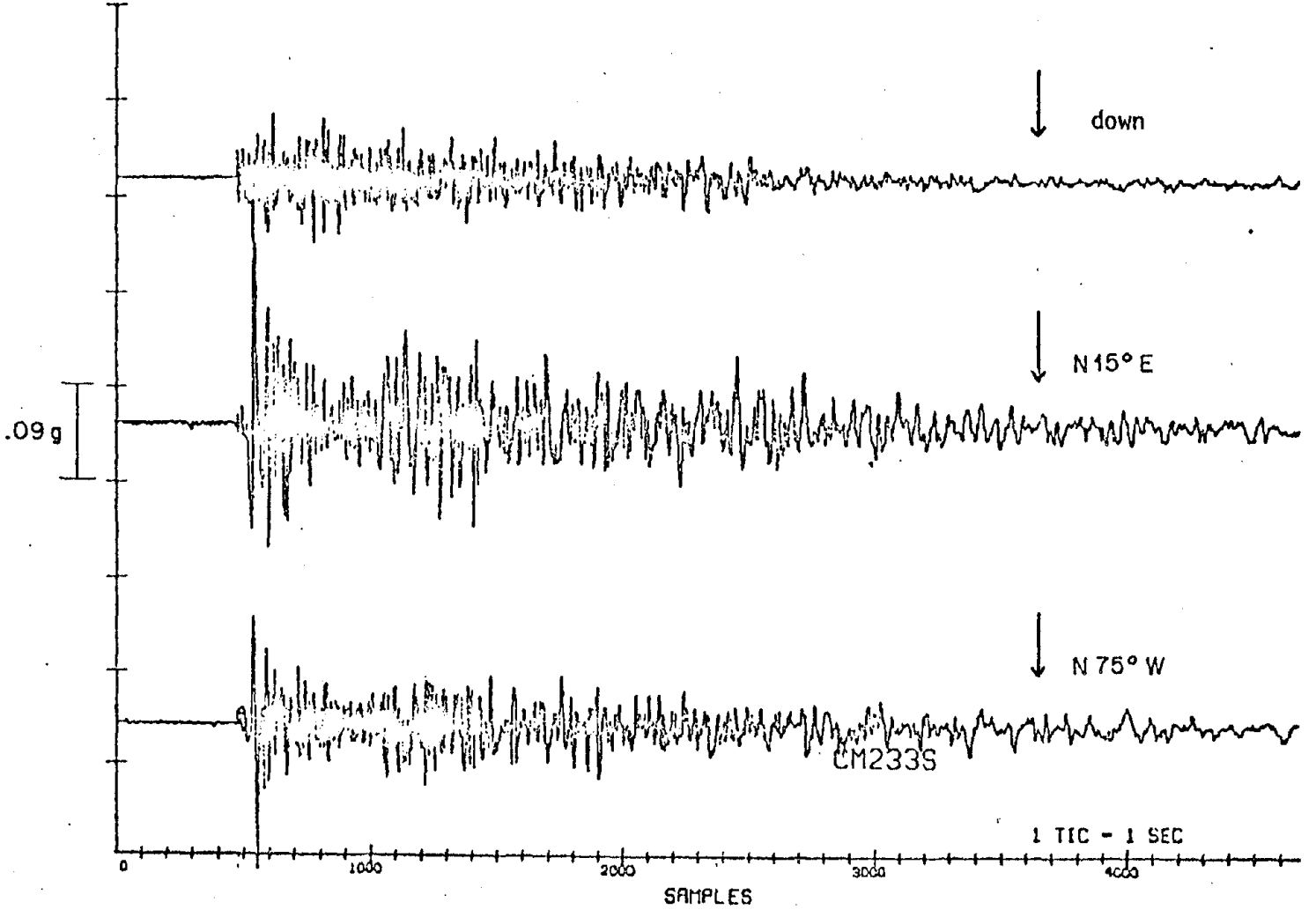

Figure 7. Strong motion record from Compuertas for October 15, 1979 Imperial Valley earthquake (main shock).

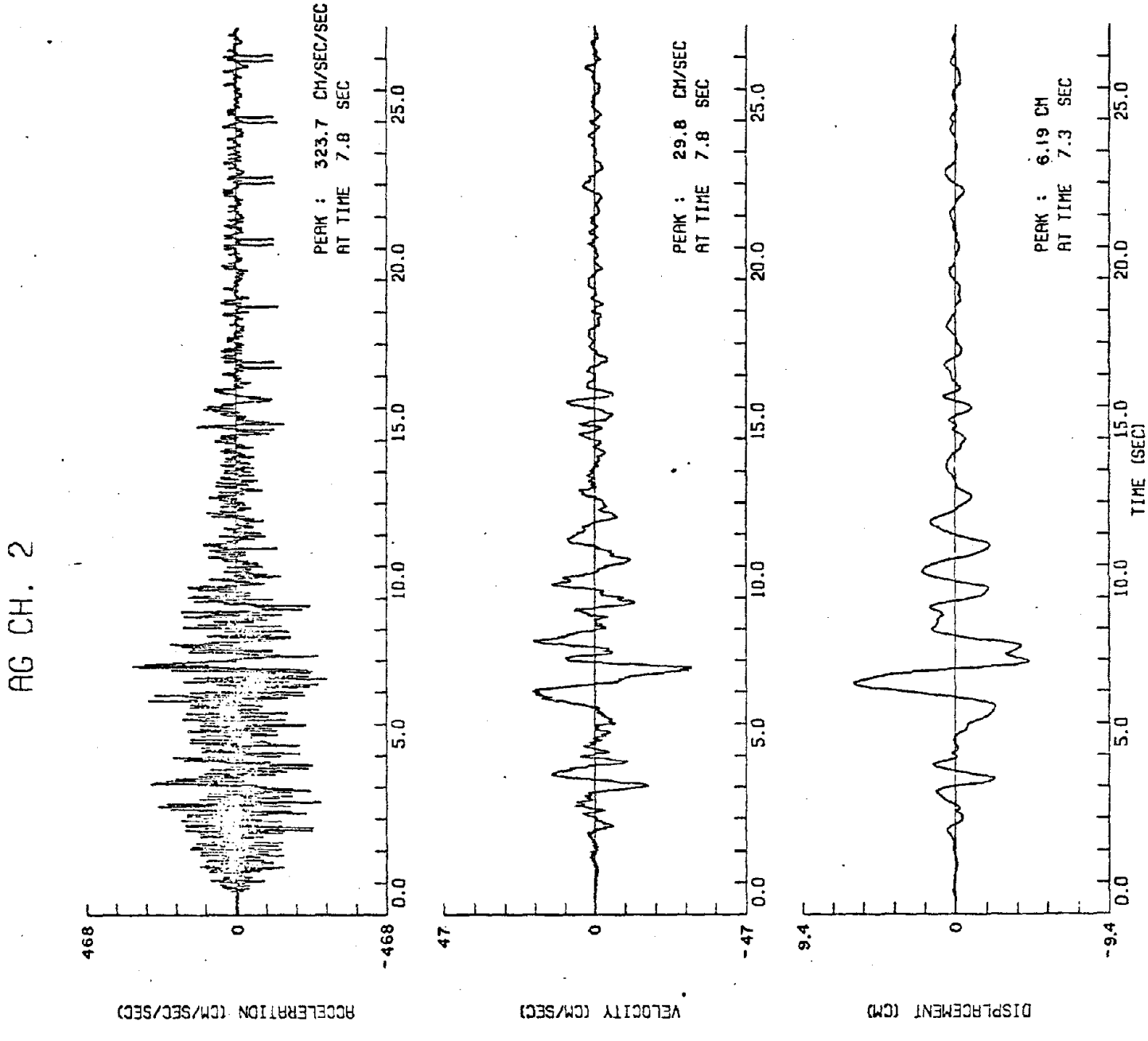

Figure 11. Acceleration, velocity and displacement (not corrected for instrument response) at station Agrarias, N183°E component, from the October 15, 1979 Imperial Valley earthquake.

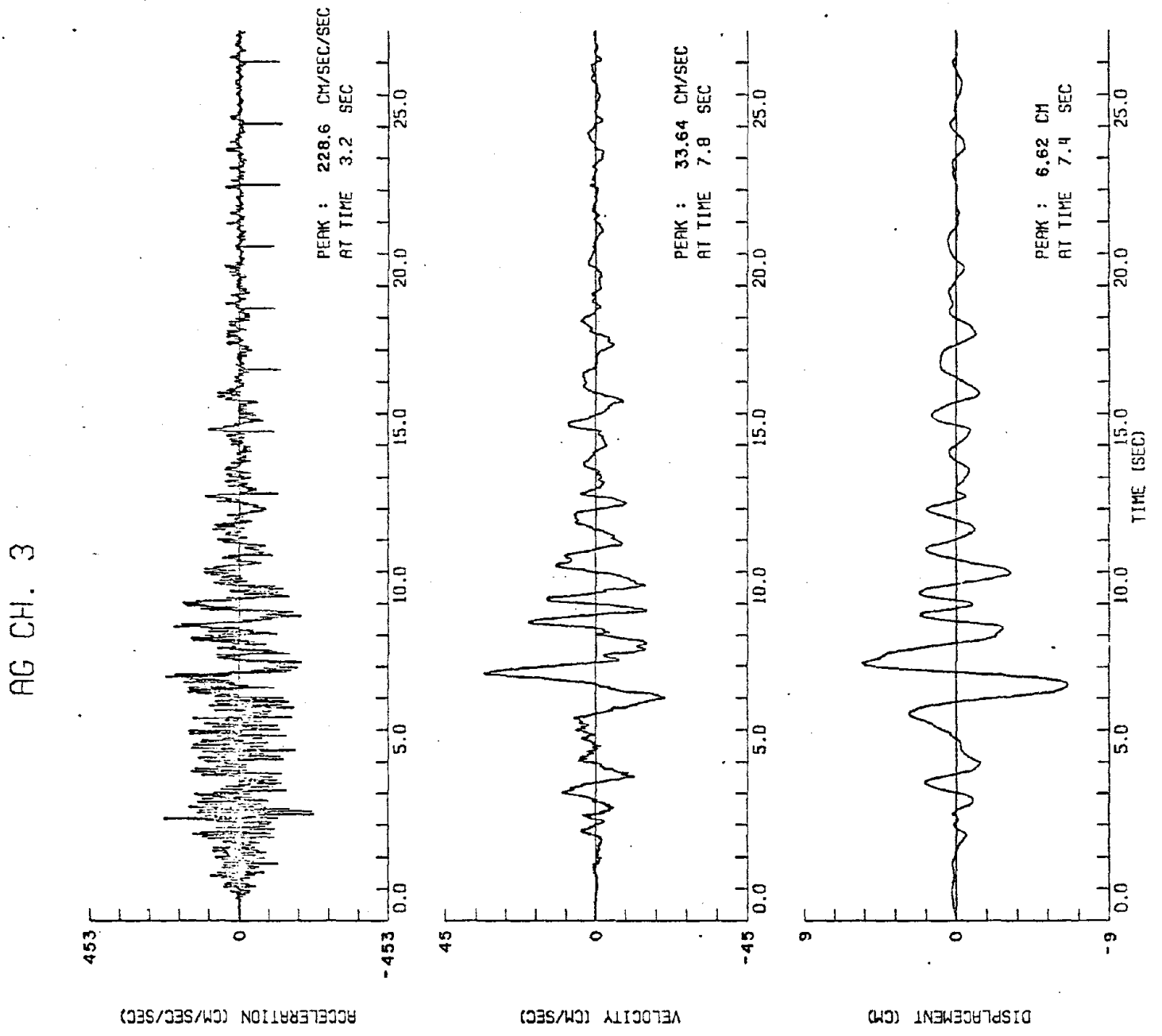

Figure 12. Acceleration, velocity and displacement (not corrected for instrument response) at station Agrarias, N93°E component, from the October 15, 1979 Imperial Valley earthquake.

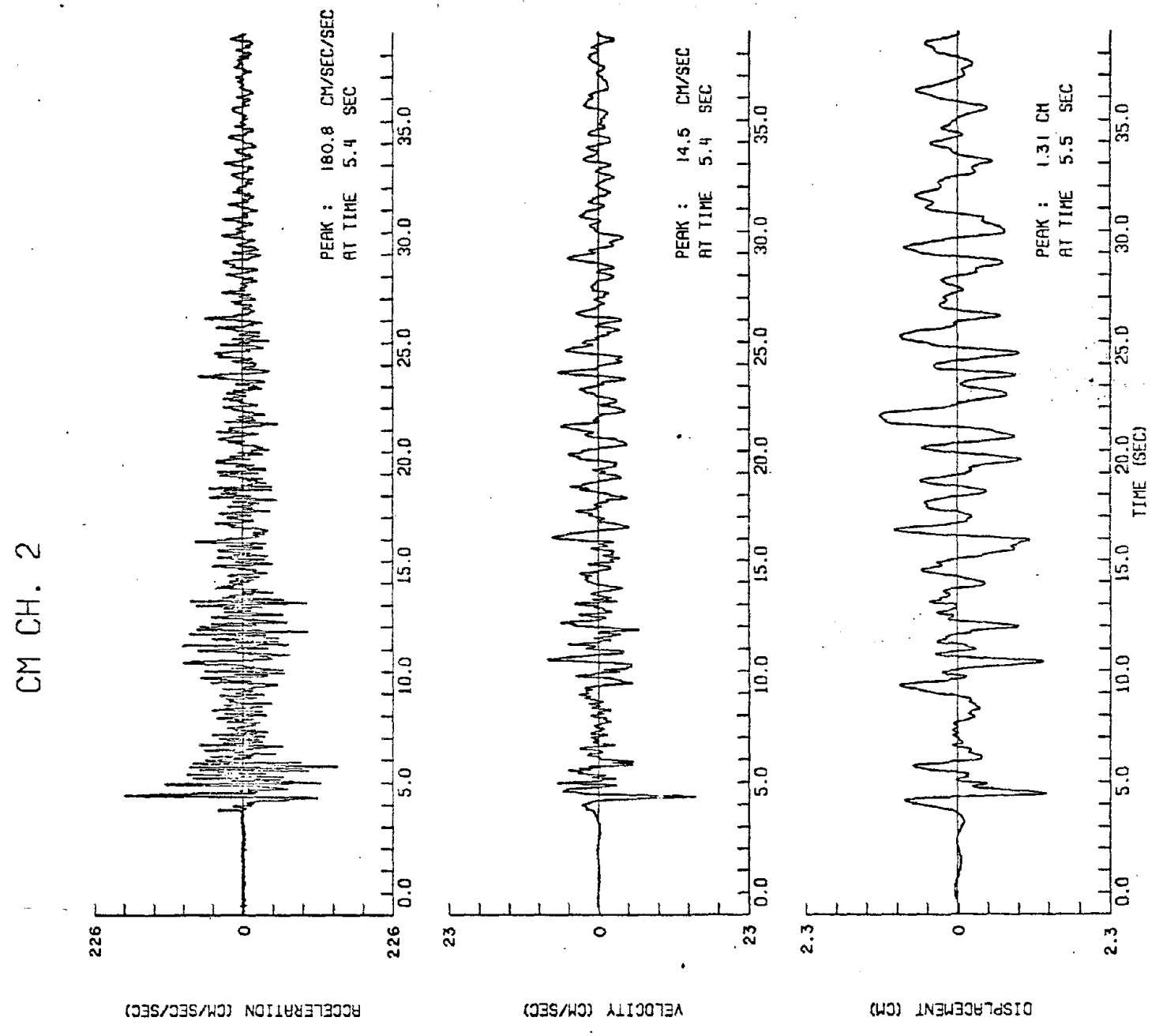

Figure 14. Acceleration, velocity and displacement (not corrected for instrument response) at station Compuertas, N195°E component, from the October 15, 1979 Imperial Valley earthquake.

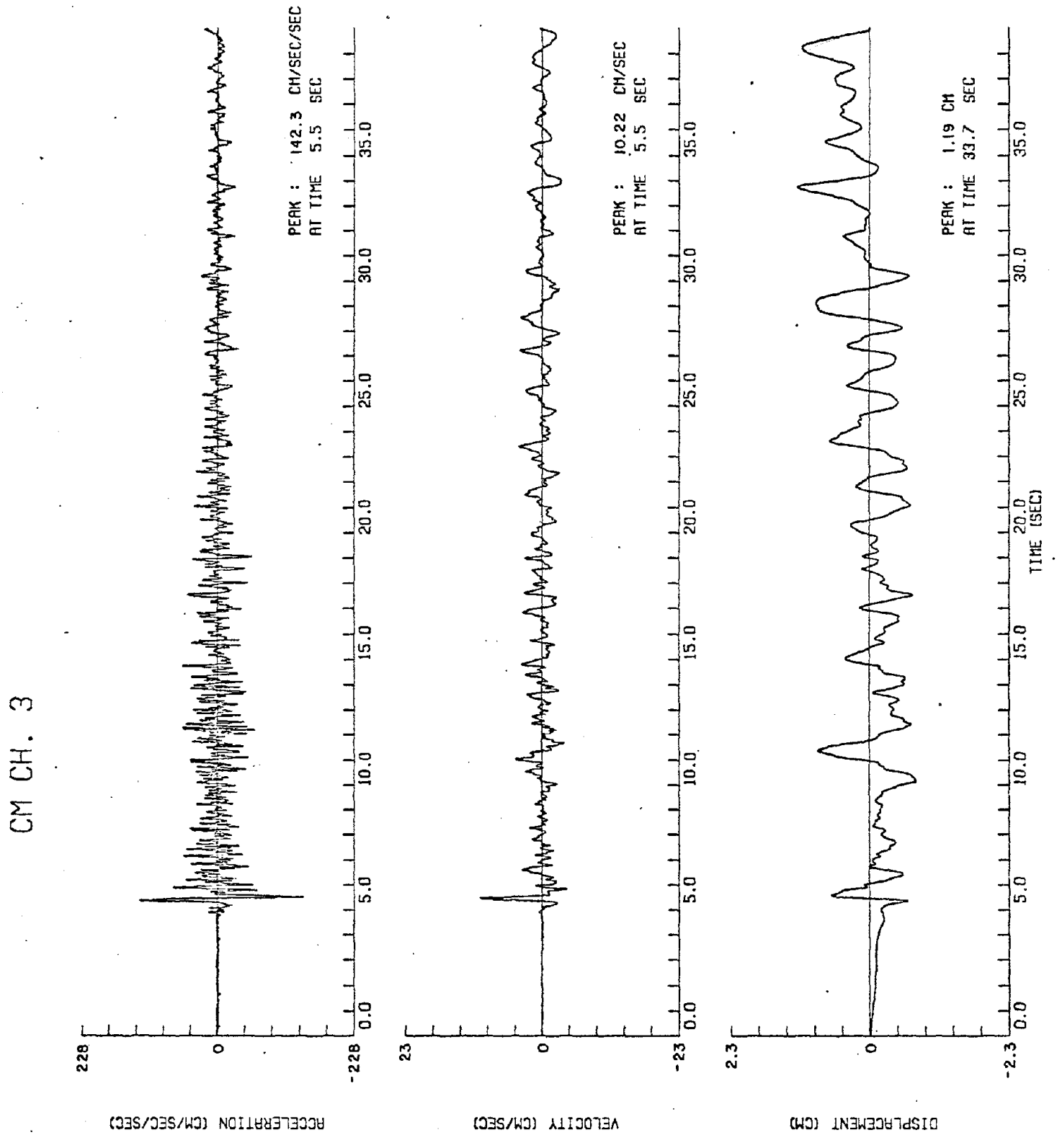

Figure 15. Acceleration, velocity and displacement (not corrected for instrument response) at station Compuertas, N105°E component, from the October 15, 1979 Imperial Valley earthquake.

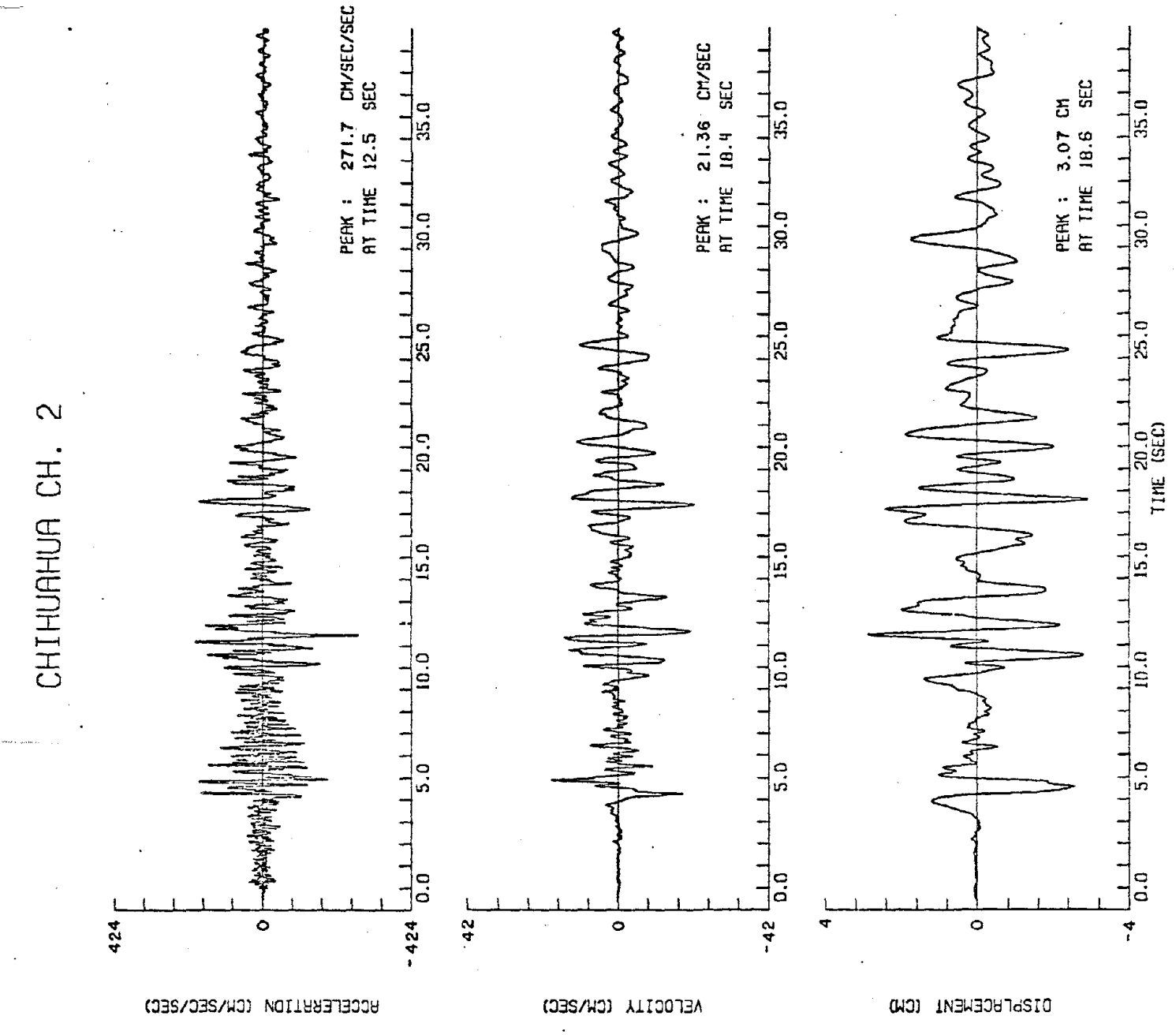

Figure 17. Acceleration, velocity and displacement (not corrected for instrument response) at station Chihuahua, N192°E component, from the October 15, 1979 Imperial Valley earthquake.

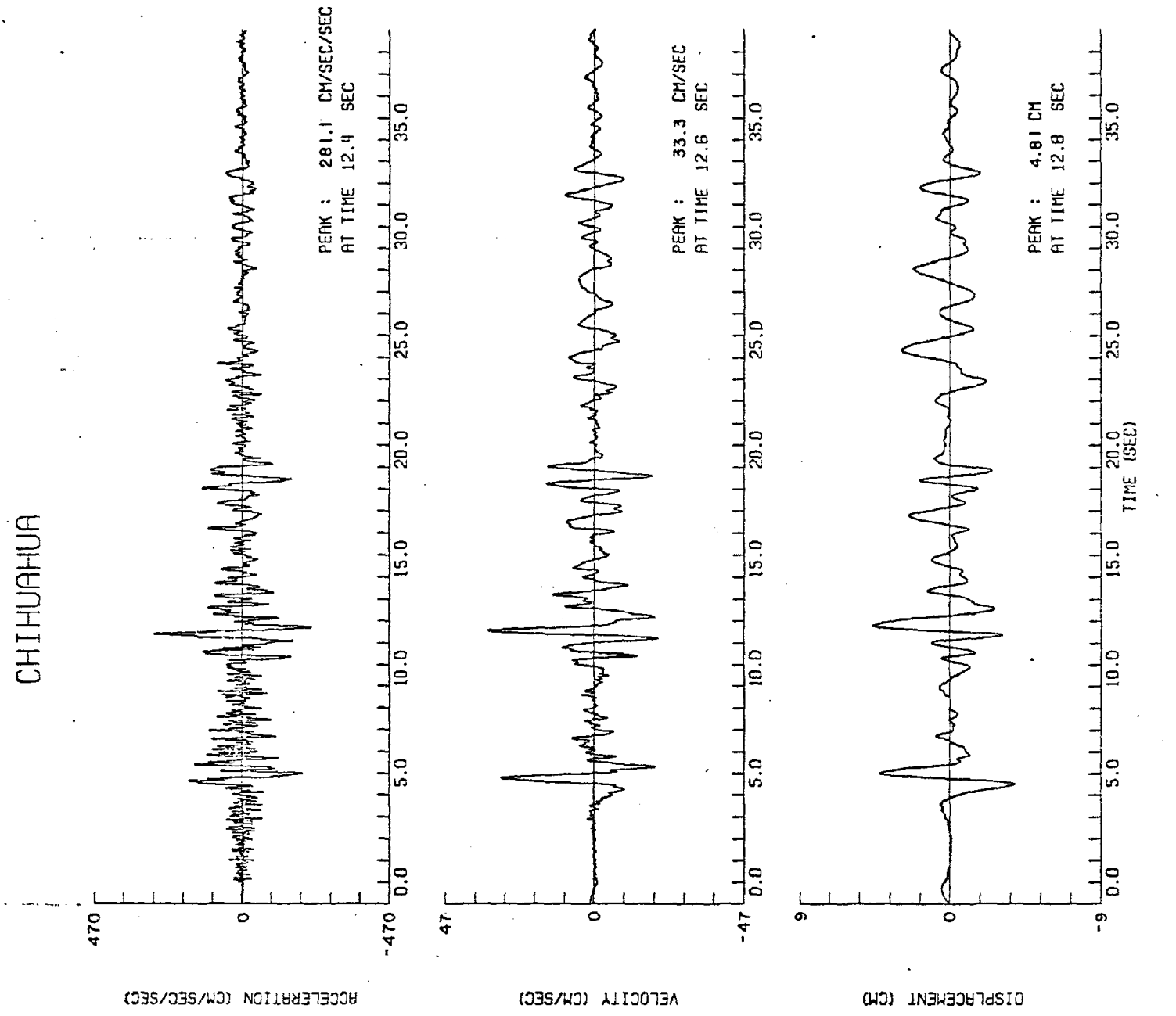

Figure 18. Acceleration, velocity and displacement (not corrected for instrument response) at station Chihuahua, N102°E component, from the October 15, 1979 Imperial Valley earthquake.

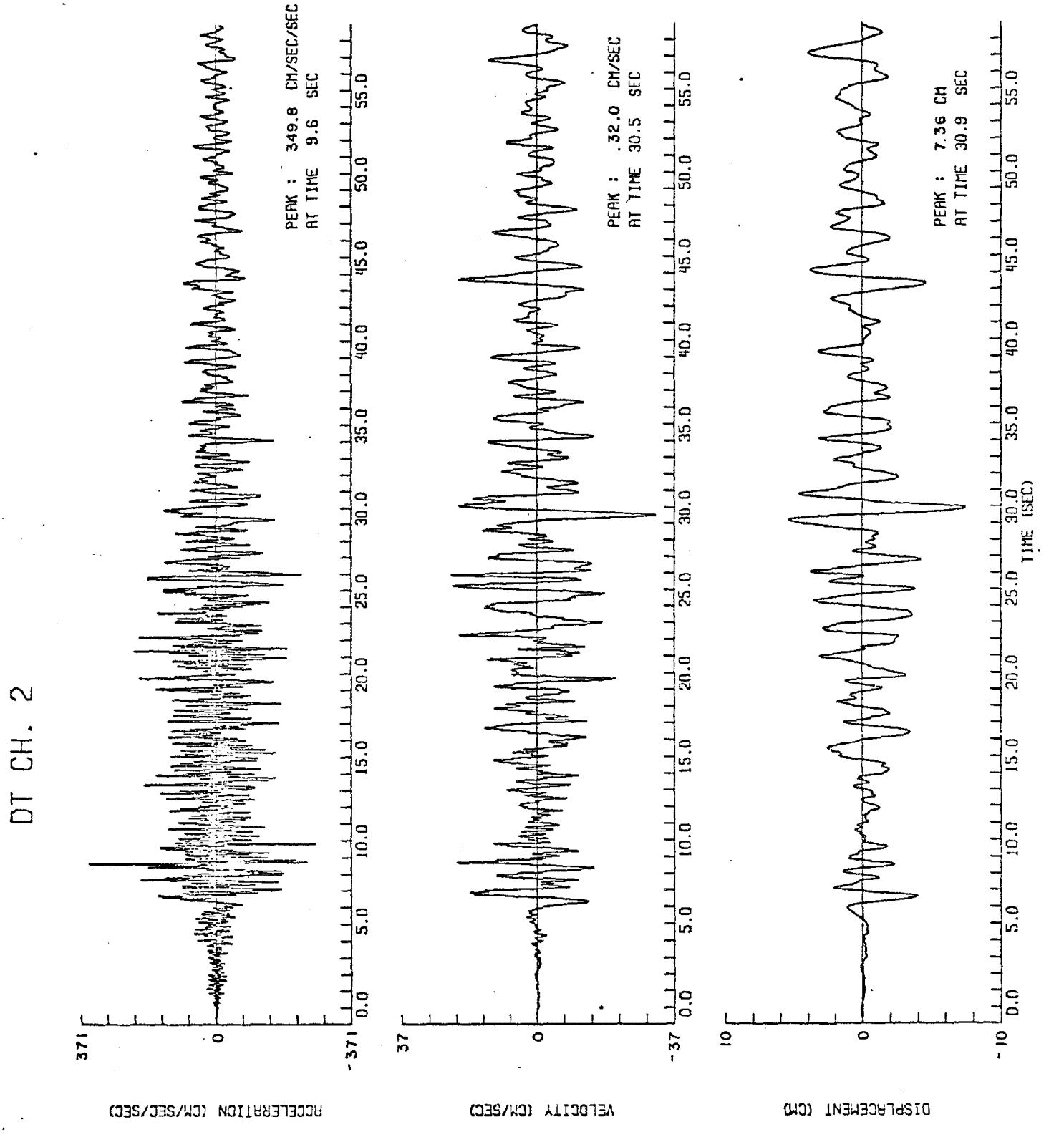

Figure 20. Acceleration, velocity and displacement (not corrected for instrument response) at station Delta, N172°E component, from the October 15, 1979 Imperial Valley earthquake.

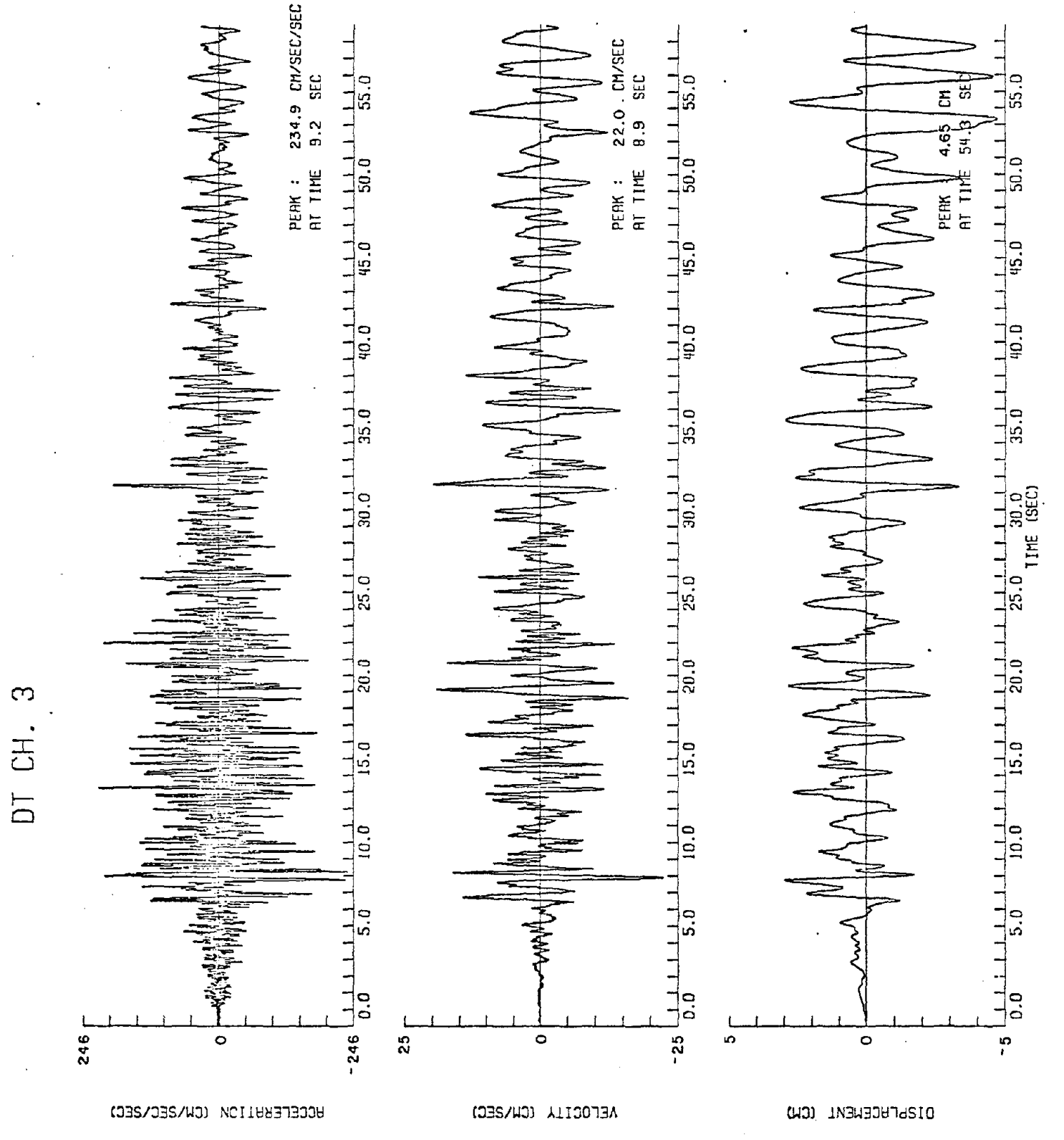

Figure 21. Acceleration, velocity and displacement (not corrected for instrument response) at station Delta, N82°E component, from the October 15, 1979 Imperial Valley earthquake.

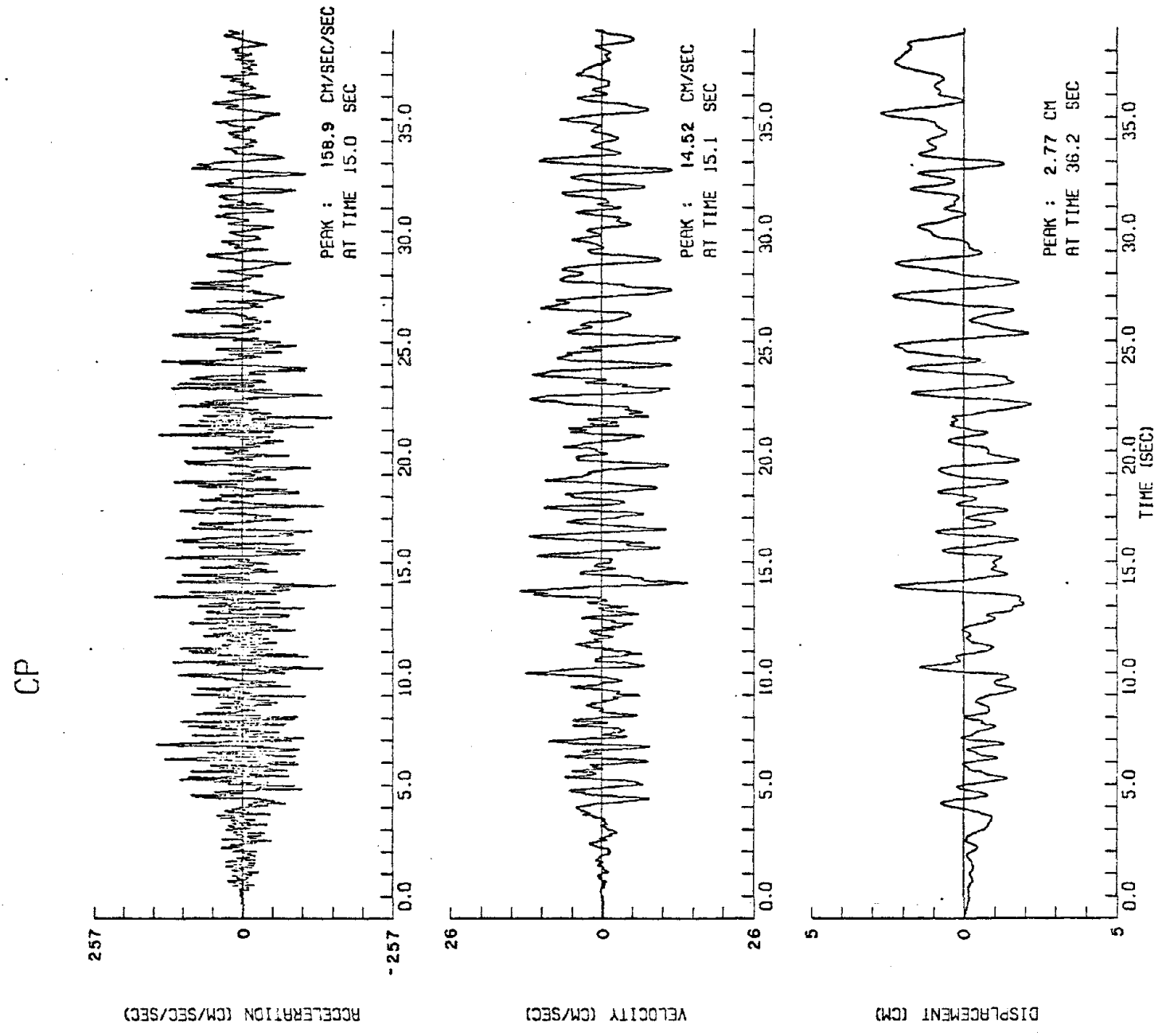

Figure 23. Acceleration, velocity and displacement (not corrected for instrument response) at station Cerro Prieto, N57°E component, from the October 15, 1979 Imperial Valley earthquake.

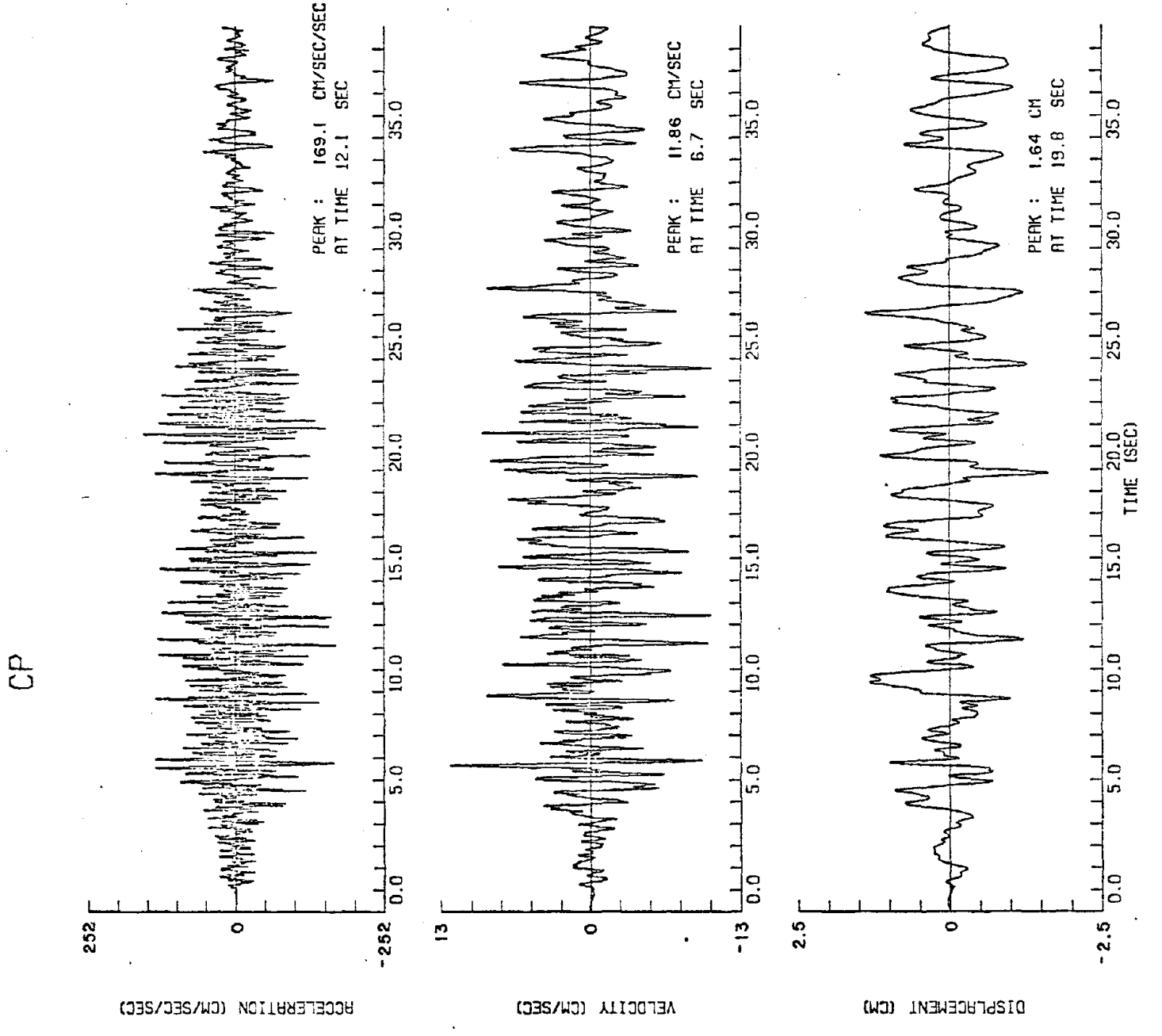

Figure 24. Acceleration, velocity and displacement (not corrected for instrument response) at station Cerro Prieto, N327°E component, from the October 15, 1979 Imperial Valley earthquake.

APPENDIX III

PRELIMINARY EVALUATION OF SITE EFFECTS AT DIGITAL ACCELEROGRAPH SITES, MEXICALI VALLEY, MEXICO

John G. Anderson

Institute of Geophysics and Planetary Physics

Scripps Institution of Oceanography

University of California, San Diego

La Jolla, California 92093

Abstract

An analysis of relative coda amplitudes on six digital accelerograms from the October 15, 1979 earthquake was carried out. Coda amplitudes are greater at Cerro Prieto and at Delta than at other stations. A larger data set needs to be studied before statistically significant conclusions can be reached on the relative site factors at these accelerographs.

Introduction

The coda of local earthquakes, which is the portion of local seismograms of decaying amplitudes after the primary phases have arrived, can be used to evaluate relative site effects on seismic ground motions. This is known from results of Aki (1969), who found relative coda amplitudes for sites near Parkfield, California ranging from 1.0 to 7.8. Tsujiura (1978) also studied relative site excitation, and found that the amplification is frequency dependent. This frequency-dependent relative site amplification can also, in principle, be derived from a sufficiently detailed model for underground structure near each site,

and in the metropolitan Tokyo area, Tsujiura (1973) suggests that the two methods appear to be consistent. The coda method is much simpler.

With the advent of digital recording of strong earthquake ground motion (eg., Anderson et al, 1982) it may become possible to derive the site amplification by means of the coda method using the same instruments which have recorded significant accelerograms. Indeed, there is a possibility that the coda generated by a significant earthquake can be used to derive relative site amplifications. We note that this is not feasible with analog-recording accelerographs because the later portion of the coda of large events, and also the smaller aftershocks, are not usually digitized, primarily because of a low signal-to-noise ratio.

In this paper the coda of six digital strong motion accelerograms from the Imperial Valley earthquake of October 15, 1979 is used to estimate relative site effects at the accelerograph sites. There is a difference between the coda analyzed in this study and the codas which have been analyzed previously. In particular, studies by Aki (1969, 1980, 1981), Aki and Chouet (1975), Tsujiura (1978), and Rautian and Khalturin (1978) all used small earthquakes for the source excitation, in which the coda is excited by a source which is brief in time and localized in space. The theoretical basis for coda analysis implicitly assumes these properties (eg. Aki and Chouet, 1975). The source of the Imperial Valley earthquake, in contrast, probably lasted 10 to 20 seconds, and may have excited immediate aftershocks. The accelerograms provide data on ground motion for times of up to about 100 seconds after the origin time of the earthquake, but to compare several stations one is forced to examine data in the times between 40 to 90 seconds of the

origin of the earthquake. The ground motion in this time window must consist at least partly of coda, as an elapsed time of 40 seconds is sufficient for the coda of small earthquakes to be established. Furthermore, direct body wave arrivals from the primary shock arrive prior to this time interval. However, aftershocks and slow surface waves might be assumed present in this time interval and appear as noise (possibly stronger than the sighal at times) in the coda analysis.

Data Analysis

Figure 1 shows the locations of digital accelerographs in Mexico which recorded the Imperial Valley earthquake. Figure 2 illustrates the times instruments to the south of the U.S.-Mexico border were operating, relative to origin time of the earthquake. The trigger times at Aeropuerto, Casa de Alfonso, Cucapah, and Victoria are inferred from the S-wave arrival times at those stations and the linear approximation to the S-wave arrival times at sites with absolute time control (Agrarias, Chihuahua, Compuertas, Cerro Prieto, Delta). We note that the S-wave arrival time at Cerro Prieto deviates from this linear approximation by about 2.3 seconds; this is not surprising because the Cerro Prieto site is located on a volcano, with a consequent higher velocity path for P- and S-waves to that site. All other sites are on Colorado River delta sediments.

The assumption of the coda method for site analysis is that when coda at different sites are compared for the same time interval, and in the same frequency band, the local site effect is the only source of amplitude differences. Therefore each accelerogram was considered in 10 second time windows from 40-50 sec, 50-60 sec, 60-70 sec, 70-80 sec, and

80-90 sec after the origin time of the earthquake. Accelerograms in each of these time intervals were tapered with a cosine-squared taper to remove end effects of the window, and then filtered into frequency bands: 0.2-0.5 Hz, 0.5-1.0 Hz, 1.0-2.0 Hz, 2.0-5.0 Hz, 5.0-10.0 Hz, and 10.0-20.0 Hz. Filtering was carried out numerically by transforming to the frequency domain, multiplying the Fourier component at frequency f by

$$[\ 1 + (f/f_H)^5\ ]^{-1}\{\ 1 - [\ 1 + (f/f_L)^5\ ]^{-1}\ \} \qquad (1)$$

where f_L and f_H are the lower and higher limits of the frequency band, and then performing the inverse Fourier transform. The RMS acceleration in each frequency band was computed from the filtered accelerogram in the time domain. Figure 3 shows an example of original and filtered accelerations.

Figure 4 shows one horizontal component of acceleration from each of the six stations which were recording in the time interval 40-50 sec. The stations are arranged according to increasing distance from the source (Cucapah, closest, to Victoria, farthest). There are obvious differences in the relative amplitudes at the stations, with Delta and Cerro Prieto the largest, and Cucapah the smallest. Thus if the arrivals in this time interval may validly be regarded as coda, then there are significant relative site amplification factors.

We used the square root of RMS acceleration to characterize the amplitudes in each time band. These factors for the traces in Fig. 4 are: Cucapah, 1.77; Chihuahua, 3.26; Compuertas, 2.77; Cerro Prieto, 6.51; Delta, 13.64; Victoria, 3.06; These factors seem to be a reasonable representation of the relative levels of these accelerograms. By

the use of RMS acceleration, it becomes possible to easily compare relative coda amplitudes as a function of frequency, as was done by Tsujiura (1978). Figure 5 shows values of $(RMS)^{1/2}$ at all stations normalized to the amplitudes which were observed at Victoria. Average values of the RMS acceleration from the two horizontal components at each station were found first, and the square roots of these averages were used to derive the ratios shown in Figure 5.

The decision to use the amplitudes at Victoria to normalize the coda amplitudes at others sites was not arbitrary. As seen in Figure 2, Cucapah, Delta, and Victoria yielded the records of longest duration, so that the choice was among those three. Based on Figure 4, and other comparisons, the site at Delta appears to be anomalous. Furthermore, at Cucapah, one of the two horizontal components failed, and it was judged that the amplitudes from a single component would be less reliable than the average of two horizontal components at Victoria. We note, however, that Victoria is a good choice based on the merits of its records. The noise level on the accelerograph there (a Kinemetrics DSA-1) was lower than the noise at the other sites. Furthermore, as it is farthest from the fault rupture, it is least likely to be affected by small aftershocks. A disadvantage to the Victoria site is that direct waves with a group velocity of 1.0 km/sec to 2.0 km/sec could be arriving from the northern limits of rupture in the time windows considered.

One initial idea was that if the codas were contaminated by direct arrivals, amplitudes would at least be tending toward those of a pure coda, and the ratios in Figure 5 would thus asymptotically approach a final value for later time windows. This hypothesized asymptotic

behavior was not generally obvious, but perusal of Figure 5 shows some cases where it is suggested, such as in the 0.5 Hz to 1.0 Hz frequency band at all stations. In general, however, plots of these ratios with time do not give strong reasons for choosing the ratios in one time interval over that in another interval. Based on data which are plotted by Tsujiura (1978, Figure 5.2), coda amplitude ratios in his study have a scatter of a factor of about 2.5. In Figure 5, scatter of greater than a factor of 3 occurs in only two situations: between 5 Hz and 20 Hz at Cucapah, and between 0.2 Hz and 1.0 Hz at Compuertas. The sudden jump in high frequency amplitudes at Cucapah at 70 sec to 90 sec is apparently caused by an aftershock; the scatter at Compuertas is unexplained at present. Because the scatter of data at the remaining frequencies and stations is more or less consistent with that observed by Tsujiura, it is concluded that this scatter does not contradict the hypothesis that the relative coda amplitudes which are observed here are representative of site effects.

Discussion

Figure 5 gives a reasonable first approximation of relative site effects on coda amplitudes at six of the digital stations which recorded the October 15, 1979 earthquake. Table 1 summarizes these data by giving the median values of relative amplification for each station. The uncertainty associated with entries in Table 1 is estimated to be in the vicinity of a multiplicative factor of 2, on the average, at the 95% confidence level. From Figure 5 and Table 1, using this estimate, it appears that the site factors at Cerro Prieto and at Delta differ significantly from unity across the entire frequency band.

In Figure 6, these factors have been applied to a plot of peak acceleration and distance, to see how the shape of the curve is affected. Figure 6A shows peak acceleration as read from the original accelerograms. In Figure 6B, correction factors for the 5.0 Hz to 10.0 Hz frequency band have been applied, with points for Victoria held fixed. The correction factors control the relative amplitudes, but the absolute level in Figure 6B is not controlled. These corrections have drastically altered the shape of the attenuation curves by implying a much steeper slope for distances less than 25 km. The trend toward increasing acceleration from 25 km to 45 km is unsatisfactory. Relativ coda amplitudes from a more extensive set of records should be analyzed to establish whether or not these relative amplitudes may be used to reduce the scatter in strong motion attenuation data.

Acknowledgements

This research was supported by the National Science Foundation under Grants PFR 80-07418 and CEE 81-200096.

TABLE 1 - Median values of site effects relative to Station Victoria, based on coda amplitudes from the October 15, 1979 accelerograms.

	Frequency band, Hz					
Station	0.2-0.5	0.5-1.0	1.0-2.0	2.0-5.0	5.0-10.0	10.0-20.0
Cucapah	0.66	0.83	1.05	0.67	0.53	0.93
Chihuahua	1.79	1.63	1.40	1.35	1.04	2.00
Compuertas	0.61	0.49	0.52	0.95	1.56	2.38
Cerro Prieto	2.37	2.25	2.67	2.54	1.52	3.83
Delta	5.40	5.40	6.43	4.51	2.55	3.47

REFERENCES

1. Aki, K. (1969). Analysis of the seismic coda of local earthquakes as scattered waves, J. Geophys. Res., 74,, 615-631.

2. Aki, K. and B. Chouet (1975). Origin of coda waves: source, attenuation, and scattering effects, J. Geophys. Res., 80, 3322-3342.

3. Aki, K. (1980). Scattering and attenuation of shear waves in the lithosphere, J. Geophys. Res., 35, 6496-6504.

4. Aki, K. (1981). Source and scattering effects on the spectra of small local earthquakes, Bull. Seism. Soc. Am., 71, 1687-1700.

5. Anderson, J.G., J. N. Brune, J. Pince, and F.L. Vernon III (1982). Preliminary Report on the use of Digital Strong Motion Recorders in the Mexicali Valley, Baja California, Bull. Seism. Soc. Am., in press.

6. Rautian, T.G. and V.I. Khalturin (1978). The use of the coda for determination of the earthquake source spectrum, Bull. Seism. Soc. Am., 63, 923-948.

7. Tsujiura, M. (1978). Spectral analyses of the coda waves from local earthquakes, Bull. Earthquake Res. Inst., 53, 1-48.

FIGURE CAPTIONS

1- Map of Imperial Valley - Mexicali Valley with epicenter of October 15, 1979 earthquake and accelerograph sites in Mexico.

2- Times after origin time of October 15, 1979 earthquake during which accelerographs in Mexico were operating. Vertical lines to represent instrument operation are drawn at the distance between the epicenter of the earthquake at the station.

3- Accelerogram from station Delta (N8°W) in the time interval 40.0 to 50.0 sec after the origin time of the earthquake. Band-pass filtered traces are shown offset from the vertical axis for clarity.

4- Horizontal band-pass filtered accelerograms in the frequency band 2.0 Hz to 5.9 Hz, for the time interval 40 to 50 seconds, from all six digital stations which were operating at the time. All traces except Cucapah are offset from zero acceleration for clarity.

5- Coda amplitude ratios for the horizontal component of acceleration, as a function of frequency. Different symbols indicate different time intervals, as described, in the legend.

6- A. peak accelerations, plotted against epicentral distance, for the six stations subjected to coda analysis.

B. Corrected peak accelerations based on relative coda amplitudes, relative to peak amplitudes at Victoria, which were held fixed. The absolute level in part B is not controlled.

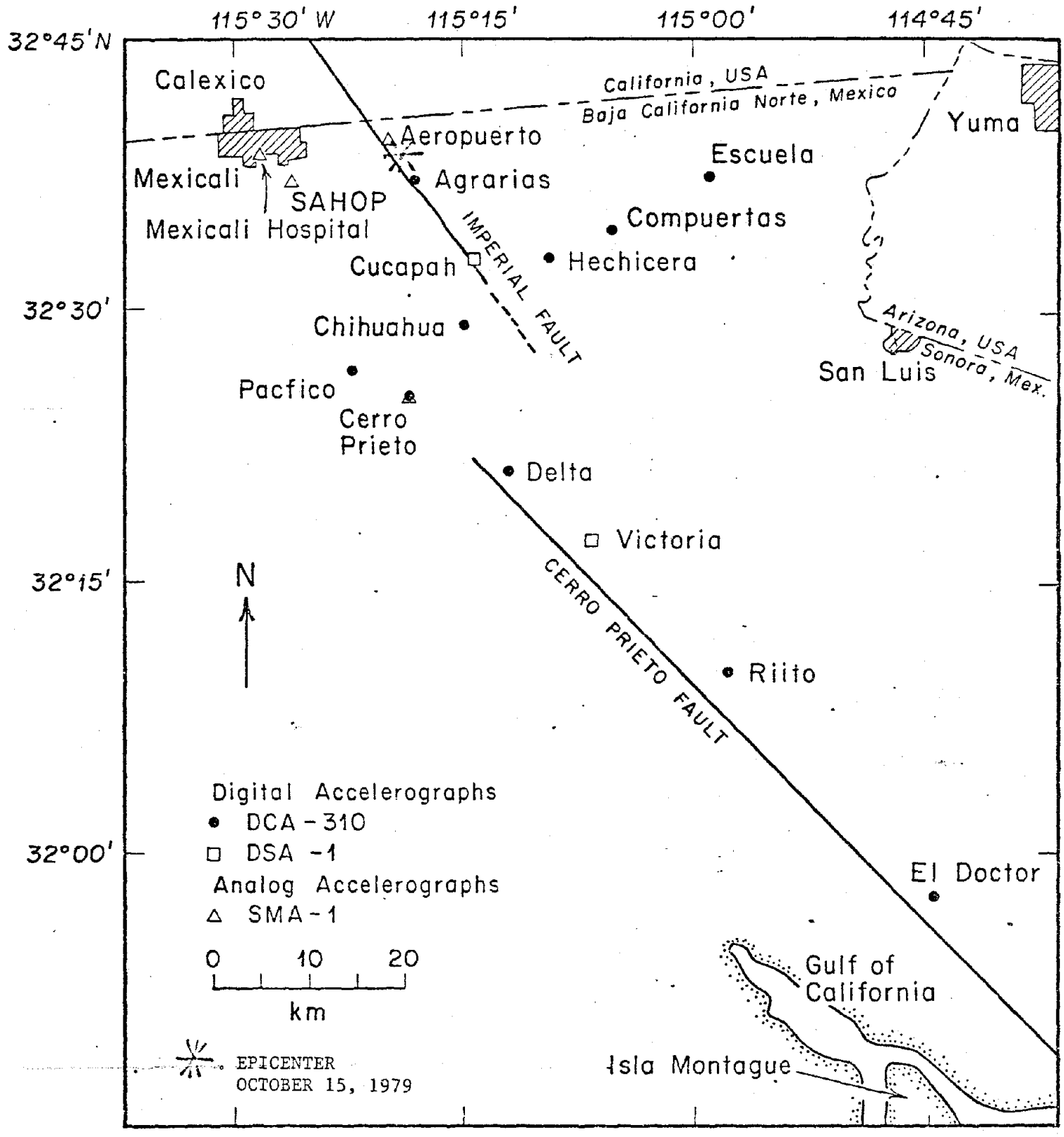
115°30' W
115°15'
115°00'
114°45'
32°45'N
32°30'
32°15'
32°00'
Calexico
California, USA
Baja California Norte, Mexico
Yuma
Aeropuerto
Escuela
Mexicali
SAHOP
Agrarias
Mexicali Hospital
Compuertas
IMPERIAL FAULT
Cucapah
Hechicera
Chihuahua
Arizona, USA
Sonora, Mex.
San Luis
Pacfico
Cerro
Prieto
Delta
Victoria
N
CERRO PRIETO FAULT
Riito
Digital Accelerographs
DCA-310
DSA-1
Analog Accelerographs
SMA-1
0 10 20
km
El Doctor
Gulf of
California
EPICENTER
OCTOBER 15, 1979
Isla Montague

Figure 1

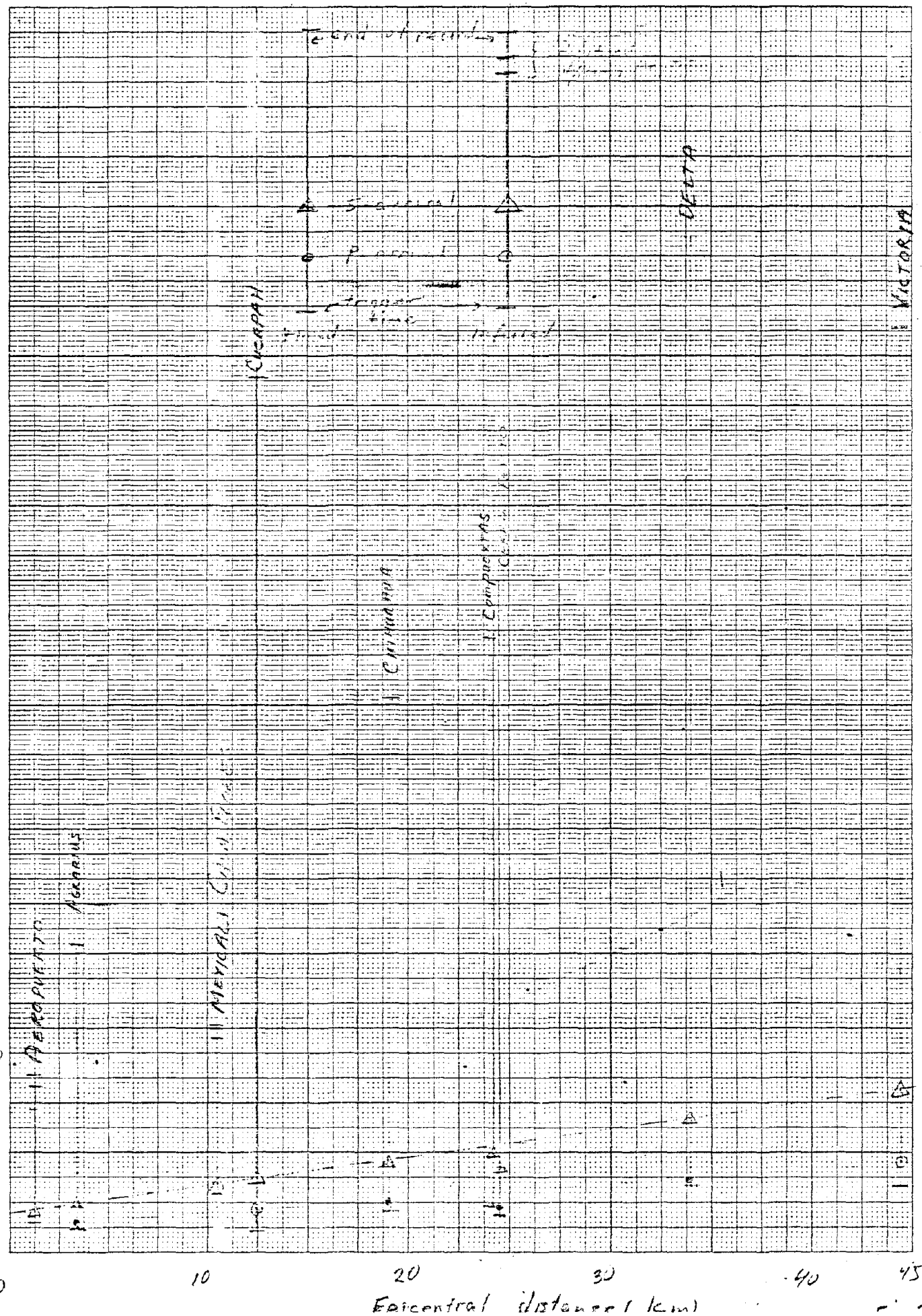

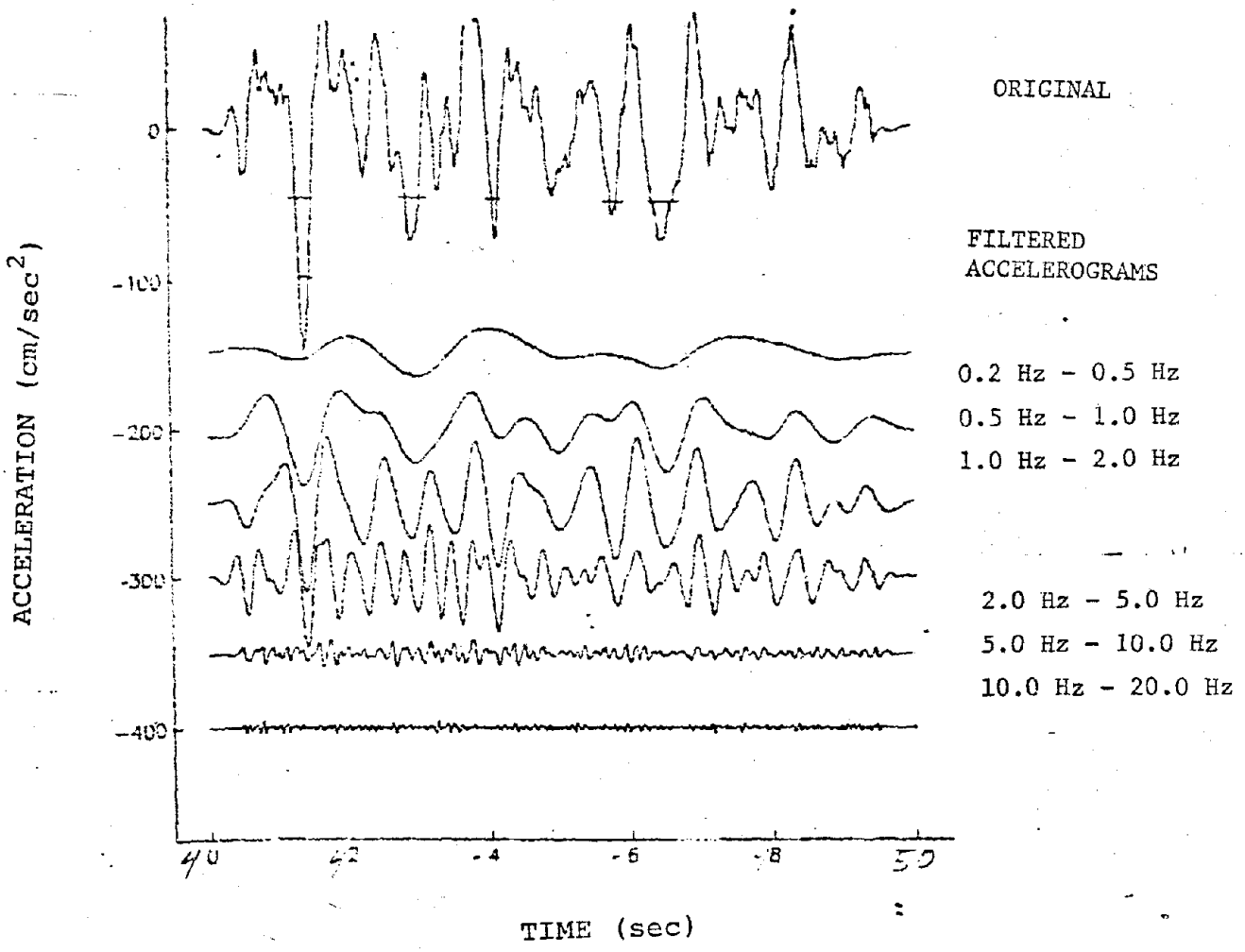
ACCELERATION (cm/sec^2)
0
-100
-200
-300
-400
40
42
44
46
48
50
TIME (sec)
ORIGINAL
FILTERED ACCELEROGRAMS
0.2 Hz - 0.5 Hz
0.5 Hz - 1.0 Hz
1.0 Hz - 2.0 Hz
2.0 Hz - 5.0 Hz
5.0 Hz - 10.0 Hz
10.0 Hz - 20.0 Hz

Figure 3

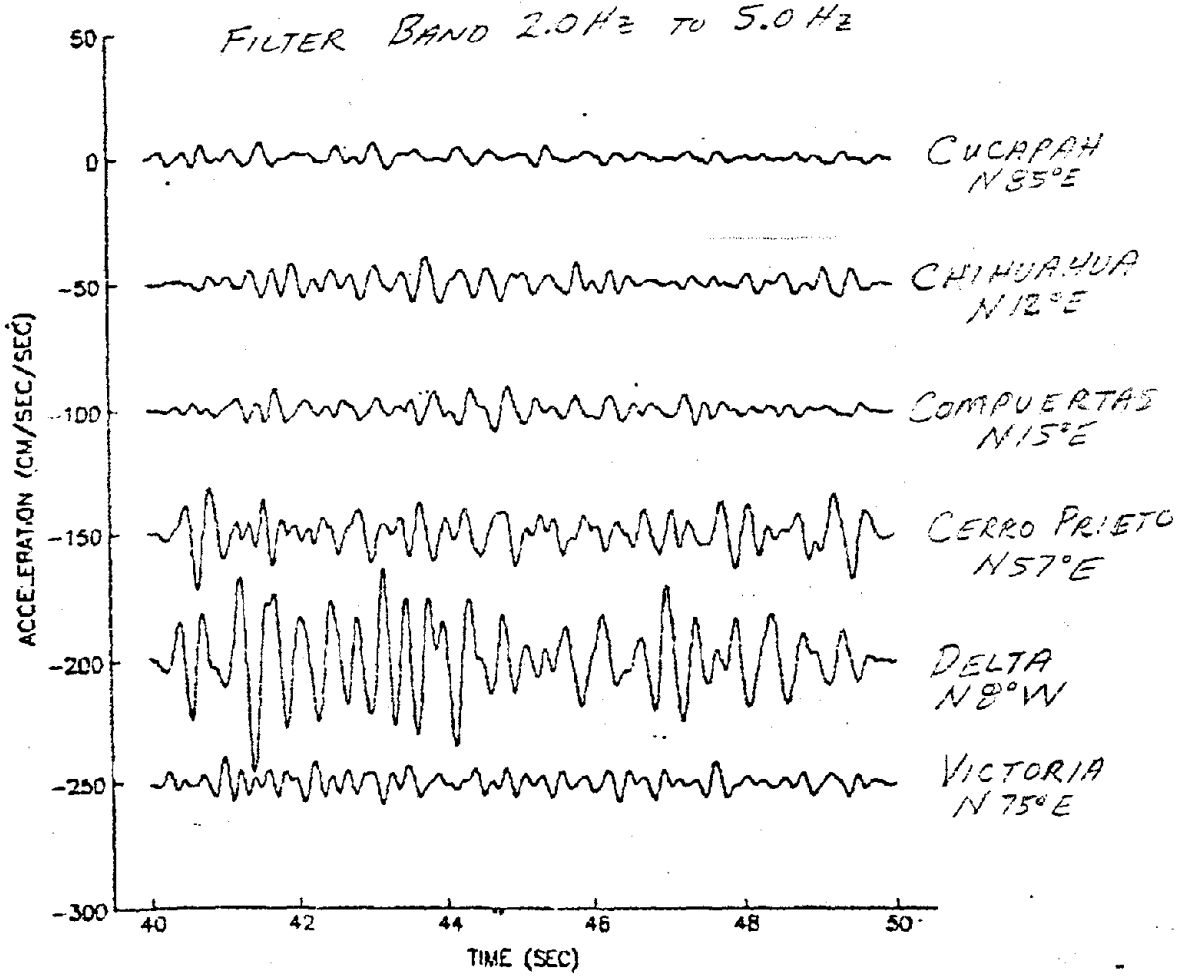
FILTER BAND 2.0 Hz TO 5.0 Hz
50
0
-50
-100
-150
-200
-250
-300
ACCELERATION (CM/SEC/SEC)
40
42
44
46
48
50
TIME (SEC)
CUCAPAH N85°E
CHIHUAHUA N12°E
COMPUERTAS N15°E
CERRO PRIETO N57°E
DELTA N8°W
VICTORIA N75°E

Figure 4

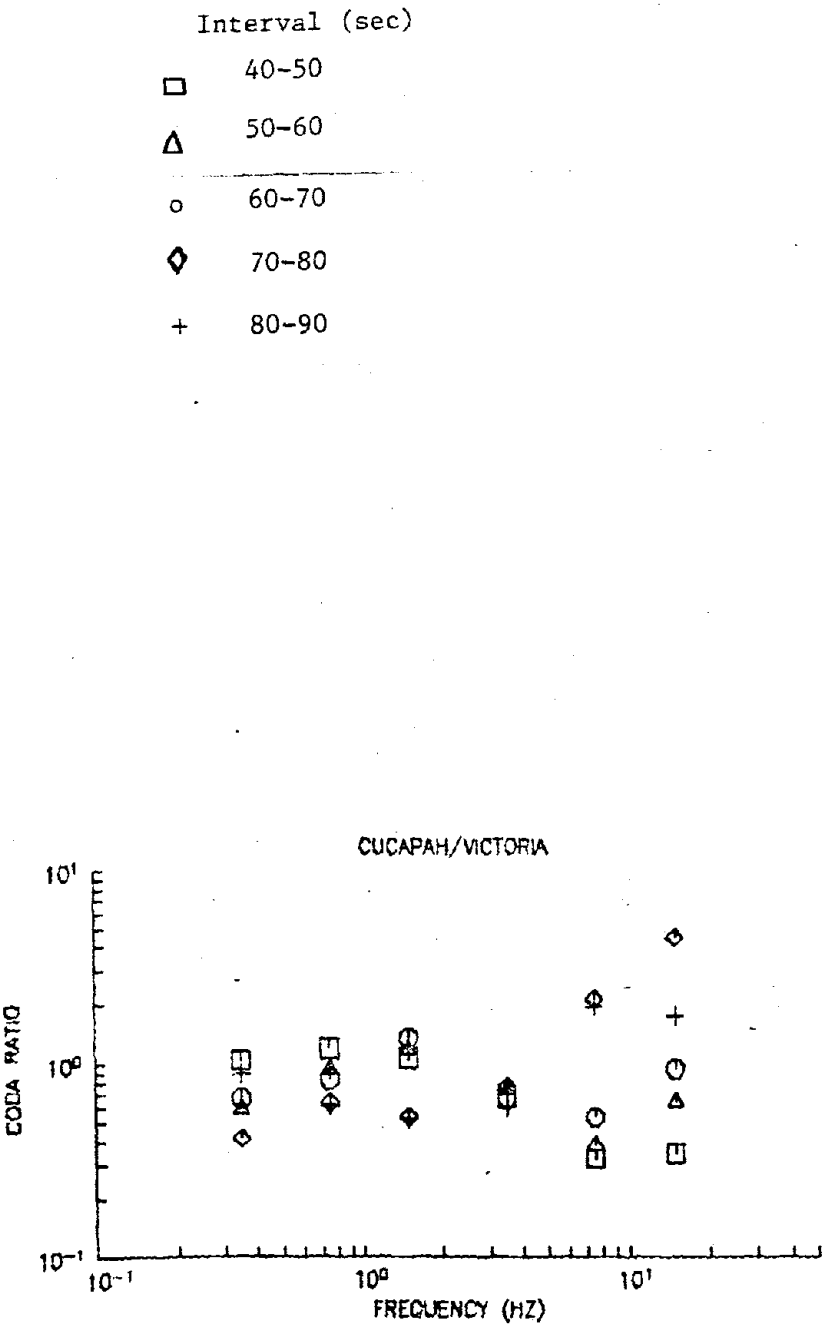
Interval (sec)
40-50
50-60
60-70
70-80
80-90
CUCAPAH/VICTORIA
CODA RATIO
10^1
10^0
10^{-1}
10^{-1}
10^0
10^1
FREQUENCY (HZ)

Figure 5A

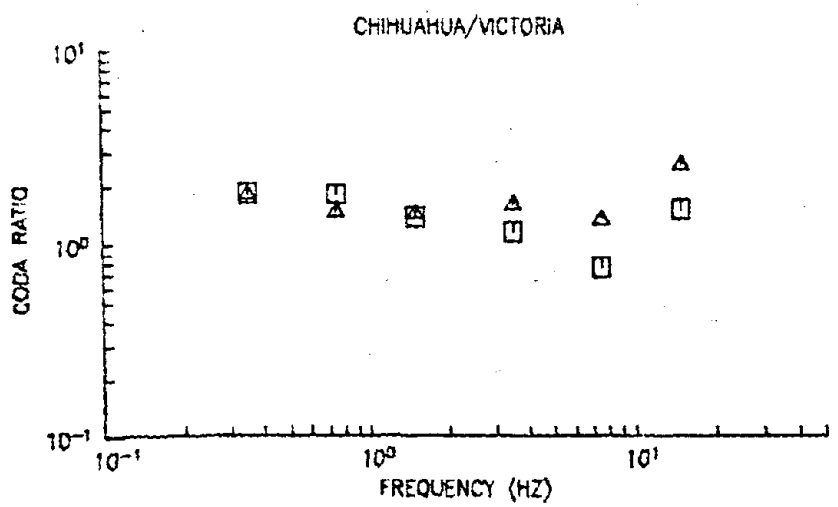
CHIHUAHUA/VICTORIA
CODA RATIO
10^1
10^0
10^{-1}
10^{-1}
10^0
10^1
FREQUENCY (HZ)

Figure 5B

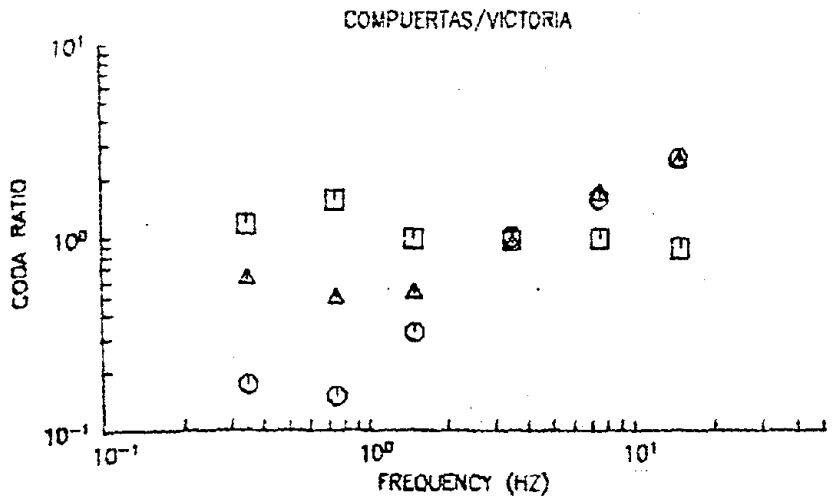
COMPUERTAS/VICTORIA
CODA RATIO
10^1
10^0
10^{-1}
10^{-1}
10^0
10^1
FREQUENCY (HZ)

Figure 5C

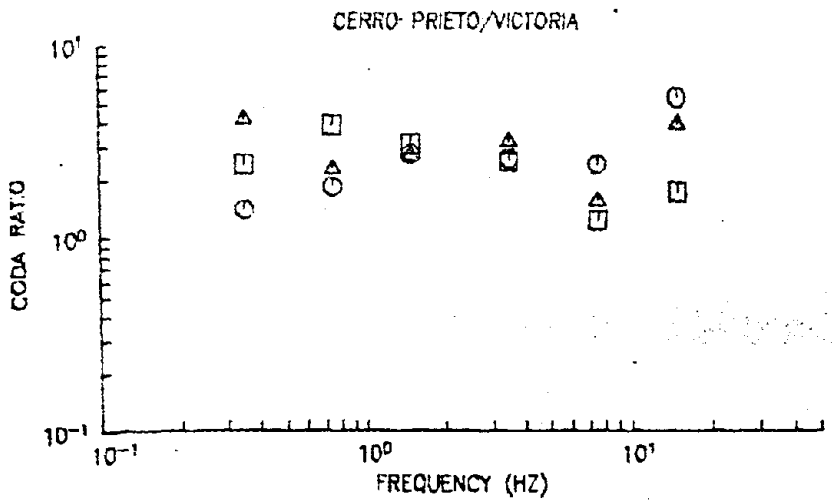
CERRO PRIETO/VICTORIA
CODA RATIO
10^1
10^0
10^{-1}
10^{-1}
10^0
10^1
FREQUENCY (HZ)

Figure 5D

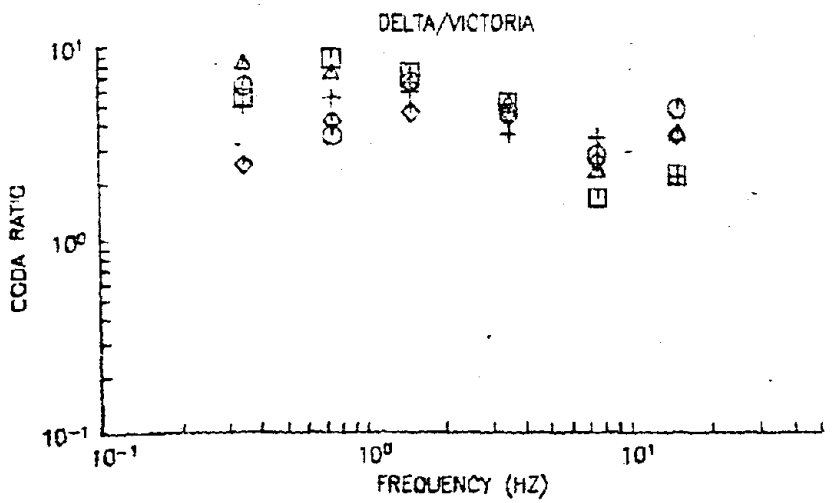
DELTA/VICTORIA
CCDA RATIO
10^1
10^0
10^{-1}
10^{-1}
10^0
10^1
FREQUENCY (HZ)

Figure 5E

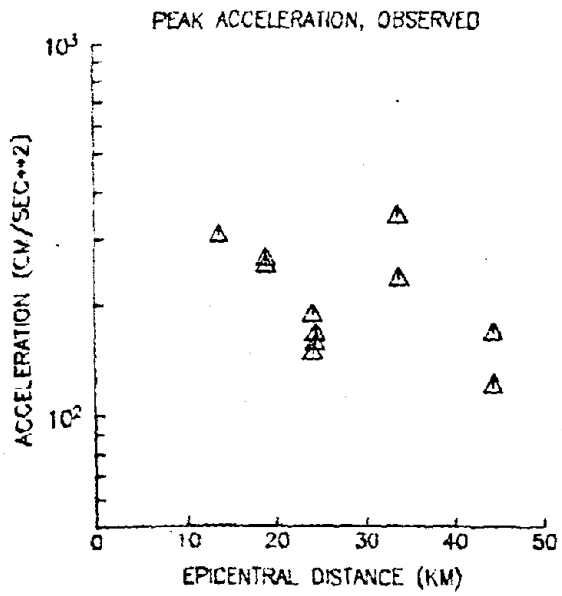
PEAK ACCELERATION, OBSERVED
ACCELERATION (CM/SEC**2)
10^3
10^2
0
10
20
30
40
50
EPICENTRAL DISTANCE (KM)

Figure 6A

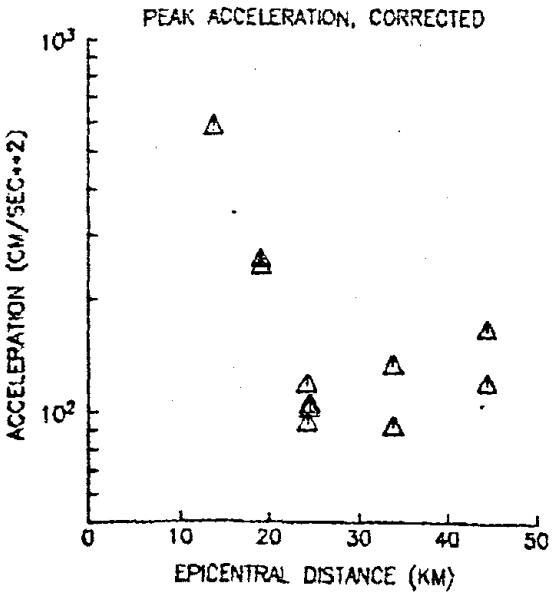
PEAK ACCELERATION, CORRECTED
ACCELERATION (CM/SEC**2)
10^3
10^2
0
10
20
30
40
50
EPICENTRAL DISTANCE (KM)

Figure 6B

FIGURE CAPTIONS

1- Map of Imperial Valley - Mexicali Valley with epicenter of October 15, 1979 earthquake and accelerograph sites in Mexico.

2- Times after origin time of October 15, 1979 earthquake during which accelerographs in Mexico were operating. Vertical lines to represent instrument operation are drawn at the distance between the epicenter of the earthquake at the station.

3- Accelerogram from station Delta (N3°W) in the time interval 40.0 to 50.0 sec after the origin time of the earthquake. Band-pass filtered traces are shown offset from the vertical axis for clarity.

4- Horizontal band-pass filtered accelerograms in the frequency band 2.0 Hz to 5.9 Hz, for the time interval 40 to 50 seconds, from all six digital stations which were operating at the time. All traces except Cucapah are offset from zero acceleration for clarity.

5- Coda amplitude ratios for the horizontal component of acceleration, as a function of frequency. Different symbols indicate different time intervals, as described, in the legend.
   A. Cucapah/Victoria
   B. Chihuahua/Victoria
   C. Compuertas/Victoria
   D. Cerro Prieto/Victoria
   E. Delta/Victoria

6- A. peak accelerations, plotted against epicentral distance, for the six stations subjected to coda analysis.
   B. Corrected peak accelerations based on relative coda amplitudes, relative to peak amplitudes at Victoria, which were held fixed. The absolute level in part B is not controlled.

APPENDIX IV

SPECTRAL ATTENUATION OF SH-WAVES ALONG THE IMPERIAL FAULT

S. K. SINGH

Institutos de Geofísica e Ingeniería
Universidad Nacional Autónoma de Mexico, Mexico 20, D.F. México
(905) 550-5215

R. J. APSEL† AND J. FRIED

Del Mar Technical Associates, P.O. Box 1083, Del Mar, CA 92014
(714) 481-9292

J. N. BRUNE

Institute of Geophysics and Planetary Physics, Scripps Institution of Oceanography
University of California, San Diego, La Jolla, CA 92093
(714) 452-2890

ABSTRACT

Spectral attenuation of SH-waves has been studied to infer Q along the Imperial Fault. The data set consists of six aftershocks of the Imperial Valley earthquake (15 October 1979, M_L = 6.6) digitally recorded up to a distance of 51km. Although there is large variance in Q^{-1} due to scatter in the data, Q below 3.75km appears to be a function of frequency (increasing from about 60 at 3Hz to 500 at 25Hz). High Q values obtained at high frequencies strongly suggest that scattering has not removed a significant amount of energy from the signals and thus, the observed result, Q varying with frequency, is not due to scattering. For sources below 4km the observed average SH-wave spectral amplitudes, A(f,R) along the fault can be fit by

$$A(f,R) = \frac{S(f)}{R} e^{-\pi f t^*} e^{-\pi f t/Q(f)}$$

† Present address: Sierra Geophysics, 15446 Bell-Red Rd., Ste. 400, Redmond, Washington 98052

where f = frequency, R = hypocentral distance, S(f) = source factor, Q(f) = quality factor below about 3.75km, and t = travel time up to 3.75km below the surface. The value of t* for the upper 3.75km is probably between 0.027 and 0.047 (average Q between 100 and 60) depending upon the fall off of S(f) with f (f^{-3} or f^{-2}) beyond the corner frequency.

INTRODUCTION

One of the most critical parameters in simulating earthquake ground motions is the seismic quality factor, Q. Even at short distances, Q is likely to play an important role in the attenuation of seismic shear waves at frequencies above about 1Hz. Present day uncertainty in Q leads to a corresponding uncertainty in the seismic design of buildings and critical structures in earthquake prone areas.

Several regressions on peak ground motion with distance have been made in the past (e.g., Joyner and Boore, 1981; Boore et al., 1980). Attenuation of Fourier amplitude spectra with distance for California earthquakes has been studied by Trifunac [1976], McGuire [1978], and McGuire and Hanks [1980]. Trifunac [1976] reported that the attenution with distance is essentially frequency independent and thus the shape of the spectra does not vary appreciably in the distance range between about 10 and 100km. He found that the attenuation of Fourier amplitudes is adequately described by the empirical amplitude attenuation function of Richter [1958]. McGuire [1978], in a similar study but with somewhat different data set, found the attenuation of Fourier amplitudes with distance as R^{-b} where R is the hypocentral distance and b increases with frequency. The data set for these studies comes from earthquakes with $M > 5$ and from different regions of California. Thus the results from these studies provide an average attenuation relation for California.

It is reasonable to assume that large differences in upper crustal structure will result in large differences in attenuation of seismic waves. Thus, each region should be studied separately. Ideally, for a given region, the data should come from small earthquakes (so that the events could be assumed simple point sources) recorded over large epicentral distances and the crustal structure should be known. If the crust could be approximated by horizontal layers then the theoretical spectra, calculated for different distributions Q, could be matched with data to determine the Q structure of the crust. However, since at wavelengths of interest here (~100m to 3km) the crust is likely to be laterally heterogeneous, the observed attenuation would include the effect of scattering losses as well as the effect of intrinsic Q.

In this study we present results of spectral attenuation of SH-waves along the Imperial fault. The data consists of six aftershocks ($3.0 \leq M_L \leq 3.4$) of the 15 Oct 1979 ($M_L = 6.6$) earthquake which were digitally recorded up to a distance of 51km. The interpretation of the observed average spectra as a function of epicentral distance supports a frequency-dependent Q model.

DATA

Aftershock data used in this study were obtained from portable digital event recorders operated by the Centro de Investigacin Cientfica y de Educacin Superior de Ensenada (CICESE), the Institute of Geophysics and Planetary Physics (IGPP), Scripps Institution of Oceanography, University of California at San Diego, and the U.S. Geological Survey (USGS), Menlo Park. Only those events which triggered three or more stations in an epicentral distance of at least 30km were selected. Six aftershocks ($3.0 \leq M_L \leq 3.4$) fulfilled this criterion. Table 1 gives relevant data on these events. Locations of the

events and the stations are shown in Figure 1. Events 3, 7 and 9 occurred towards the north, events 6 and 8 towards the south, and event 12 was located near the center of the fault segment which broke during the main shock. CICESE stations utilized modified Terra Tech DCA 300 recorders whereas IGPP stations were equipped with Terra Tech DCS 302 recorders. Sensors were Kinemetric 5-sec and Geotech 1-sec seismometers. Specifications of USGS stations (Sprengnether DR100) are given by Fletcher et al. [1981]. Data reduction procedures for IGPP/CICESE and USGS stations are given by Brune et al. [1980] and Fletcher et al. [1981], respectively.

All stations were equipped with three-component sensors. Horizontal sensors were oriented N45°E and N45°W at all CICESE/IGPP stations and in N-S, E-W directions at USGS stations. In theory, the S-wave motion at each station can be resolved in azimuthal (SH) and radial components and, applying a radiation pattern correction, the SH motion can be reduced to the expected SH motion at a station located at the same epicentral distance along the fault. In practice, correcting for the radiation pattern results in an unreliable signal and is very error prone at the frequencies of interest in this study (> 1Hz). We find that stations which are expected to be nearly nodal for P and radial S show significant amount of energy for these phases. The same is true for stations expected to be nearly nodal for SH-wave (see also Boore and Fletcher, 1981, Table 7). To avoid large errors caused by radiation pattern correction, we have chosen only those stations which were located near the fault plane and, in a few cases, near the auxiliary plane. Focal mechanisms of events 7 and 9 are given by Boore and Fletcher [1981] and for event 12 by R. Archuleta (personal communication, 1981). Although these solutions vary slightly, they are consistent with a vertical right lateral strike-slip fault with a strike of about N33°W. We shall assume this mechanism for all six events considered

here. USGS stations were rotated to obtain the SH component. For CICESE/IGPP stations N45°E component was taken as recording SH motion. N45°E is within about 15° from the true azimuthal direction for these stations and events (Figure 1). Tests with USGS data showed that rotation, generally, did not change the spectra in an appreciable manner.

About 2 to 4 seconds of S-wave signal were selected for analysis. Fourier displacement spectra were calculated after applying an instrumental correction. Table 2 gives stations which provided data for each event. Spectra from IVC and HED were found to be anomalous. Signals and spectra from IVC were much lower than expected, perhaps because of instrumental problems or due to its location in a large school building. Spectra from HED appear reasonable at lower frequencies but attenuated much faster at higher frequencies than nearby stations COM and IAA. This is true for events both to the NW (events 3, 7, and 9) and to the SE (events 6 and 8) of HED. The anomalous character of the spectra may be due to local site conditions. HED was located on a sand dune. Whatever the cause of the anomalous behavior of these two stations, the data from these stations were discarded since our interest here is in an investigation of average attenuation along the Imperial fault rather than studying local site effects.

In order to obtain spectral values at the same frequency points for all stations and events, the calculated spectra were globally fit with cubic splines constrained to have continuous first and second order derivatives, and interpolated. The spectra were then smoothed by a low pass filter to remove extreme roughness yet preserving their basic character. For USGS stations only the plots of the signal and the S-wave spectra were available to us at the time of this study. The spectral amplitudes for these stations were smoothed by eye, read, fit by global splines and interpolated.

Spectra of the selected events showed no apparent difference in the corner frequencies at the same epicentral distance range r, although amplitude levels varied. For a given event the spectra at stations in the epicentral distance ranges $2 \leq r \leq 14$km, $22 \leq r \geq 25.5$km, $29.5 \leq r \leq 33.5$km, and $43 \leq r \leq 51$km were similar. For any given event, the recordings were available from only a few stations (Table 2). Rather than analyze individual events separately, it was decided to scale all the events so that the data could be thought of as being obtained from a single aftershock. The scale factors, given in Table 1, were obtained by shifting the spectral plots so that the spectra for stations in groups A ($2 \leq r \leq 14$km), B ($22 \leq r \leq 24.5$km), C ($29.5 \leq r \leq 33.5$km), and D ($43 \leq r \leq 51$km) of different events approximately matched. Scaled station spectra for group A are shown in Figure 2. Spectra in all groups show considerable scatter and oscillation. In order to obtain a representative spectra for each group, the logarithm of spectra in each group was averaged. Figure 3 shows these log averaged spectra along with flanking curves for $\pm$ one standard deviation. (We have also analyzed the data by taking average of the amplitudes rather than the log average. The conclusions reached in this paper are not sensitive to the choice of the averaging process.) The numbers of stations in groups A, B, C, and D are 10, 3, 8, and 5, respectively (Table 3). The average epicentral distance for stations in groups A, B, C, and D are 8, 23, 31.8, and 47.3km, respectively. The average focal depth of the events is 8.5 ± 1.4km. Narrow band filtering at 10-20Hz verified that the high frequency part of the spectra corresponds to primarily S wave energy, even at the greatest distances.

INTERPRETATION

Figure 3 shows our basic data for the average attenuation of SH waves along the Imperial fault. Although the data has been obtained from different

events and instruments the mean curves in these figures should represent the average characteristics of the spectra at epicentral distances of about 8, 23, 32, and 47km.

Our model for interpretation of the data is

$$A(f,R) = \frac{S(f)}{R} e^{-\pi f t/Q} \qquad (1)$$

where $A(f,R)$ is the spectral amplitude at frequency f and hypocentral distance $R = (r^2 + 8.5^2)^{1/2}$, $S(f)$ = source factor, t = total travel time, and Q = quality factor. This is a very simple model valid for a point source in a homogeneous, isotropic, infinite space and a priori might not provide adequate description of attenuation for the complicated Imperial Valley structure [McMechan and Mooney, 1980]. In order to test the validity of Eq. (1) we generated synthetic SH-wave spectra using the Apsel-Luco synthetic seismogram code [Apsel, 1979]. Calculations were made for a point dislocation, with Heaviside slip, buried at 8km and corresponding to a strike-slip faulting on a vertical fault plane. The receivers were located along the fault plane. The crustal model adopted for shear waves, based on the P-wave model of McMechan and Mooney [1980], is given in Table 4. The spectra were calculated at epicentral ranges corresponding to the actual earthquakes and stations (Table 3). These spectra were divided into groups A to D, smoothed and log averaged following the same procedure as used for the observed data. Two test cases were considered. In the first case the Q of each layer was effectively infinite. It was found that the smoothed spectra decreased very nearly as 1/R, independent of frequency, in epicentral range of interest. $S(f)$, as expected, was constant with frequency. This means that 1/R the geometrical spreading assumption in Eq. (1) does not introduce an important error.

In the second test case we assigned Q to each layer according to the following relation:

$$Q = 2\pi + 10\beta^{3.5} \qquad (2)$$

where β = shear wave velocity of the layer (km/sec). Calculated spectra were smoothed, log averaged, and grouped. From these average spectra at the four average epicentral distances of 8.0, 23.0, 31.8, and 47.3km, we attempted to recover the source factor S(f) and Q. Taking logarithm (base 10) of both sides. Eq. (1) can be rewritten as

$$\log A(f,R) + \log R = \log S(f) - \left|\frac{1.364\ f}{Q}\right| t \ . \qquad (3)$$

For each frequency we have four data points and two unknowns. Solving EQ (3) at each frequency we obtained $Q \simeq 250$, independent of frequency, but the inferred source factor, S(f), instead of being constant with frequency, as was actually the case, decayed rapidly with f. The reason turned out to be simple. The upper crustal layers have very low velocities (Table 4) with β increasing from about 0.5km/sec at the surface to about 2.5km/sec at 4km. For sources below 4km the waves travel nearly vertically through these layers and the travel time is essentially independent of distance. Thus the attenuation in the upper shallow layers is essentially independent of distance and the method cannot distinguish this from a variation in source spectrum. Let $t^* = \int_{path} dt/Q = t_s/Q_s$ where t_s is the vertical travel time in the upper 4km of crust and Q_s is the equivalent Q. t^* is nearly independent of R for these nearly vertically incident rays. For the Imperial Valley crustal structure, Eq. (1) can then be rewritten as

$$A(f,R) = \frac{S(f)e^{-\pi f t^*}}{R}\, e^{-\pi f t/Q} \qquad (4)$$

where t now is total travel time minus t_s and Q is the quality factor of the layered half-space below the stack with t^* = constant. Equation (4) can be written as

$$\log A(f,R) + \log R = \log G(f) - \left|\frac{1.364\ f}{Q}\right| t \qquad (5)$$

where

$$G(f) = S(f)\ e^{-\pi f t^*} \ . \qquad (6)$$

We reinterpreted the theoretical spectra for case two by including the effect of constant t^* in the upper 3.75km. For the model (Table 4) t_s is about 2.7 sec and $t^* = 0.113$. The resulting Q was about 280 with both Q and S(f) independent of frequency. Predicted spectra with $t^* = 0.113$ and $Q = 280$ in Eq. (4) are in excellent agreement with the calculated average spectra of case two (Figure 4).

From the test cases we conclude the following:

(1) 1/R is reasonable for a geometrical spreading factor for the Imperial Valley crustal structure in the epicentral range of interest in this study.

(2) For the Imperial Valley crustal structure it is reasonable to assume that the shear waves would propagate vertically in the upper 4km or so of the crust. For this reason, it is not possible to determine Q of these upper layers from sources located below 4km without making assumptions regarding the source factor S(f). We can only solve for G(f) in Eq. (6) and the average Q of the assumed half-space model below 4km.

(3) Considering the vertical distribution of Q due to the layering, it is remarkable that the simple relation given in Eq. (4) (with constant Q) predicts the average synthetic spectra of case two so well. This gives us confidence that the observed data can also be interpreted with Eq. (4).

For the interpretation of the actual observed spectra we followed the same procedure as for case two. At each frequency point, the observed aver-

aged spectral values, A(f,R), at the four epicentral ranges were used to solve for G and Q^{-1} in Eq. (5). Figures 5 and 6 show plots of G(f) and Q^{-1}. Q clearly appears to be a function of frequency, increasing from about 60 at 3Hz to about 500 at 25Hz. The variance in log A(f,R) can be roughly assigned as 0.123 (s.d. = $\pm$ 0.35) independent of f and R (see Figure 3). Variance in Q^{-1} corresponding to this variance in log A(f,R) was calculated. Figure 6 shows $\pm$ one s.d. curves for Q^{-1}. Large s.d. in the value of Q^{-1} implies that Q^{-1} is not well constrained.

In order to see if a constant Q below 3.75km would fit the data equally well, we solved Eq. (5) at all frequencies and ranges simultaneously constraining Q to be a constant. This resulted in a Q of about 240. Predicted spectra at the four ranges with Q as a function of frequency and Q = 240 are shown in Figure 3 along with observed spectra. It is not surprising that Q(f) model predicts the observed average spectra better than Q = constant model, since Q(f) was obtained by fitting the data at each frequency. At close distances the constant Q model underestimates the average spectra at lower frequencies, and overestimates it at higher frequencies (Group A, Figure 3a). The converse is true at far distances (Group D, Figure 3d). This can be seen more clearly in Figure 7. Neither of the two models fit the observed data well for group B (Figures 3b and 7b). This is probably because only three spectra were available in this distance range (Table 3) and two of these were from the same station (IAA). Local site conditions may have resulted in the anomalous nature of the observed average spectra. Although the constant Q model predicts the spectra roughly within the error of the data (except for group B where the Q(f) model also does not fit well at low frequencies) the misfit to observed average data at close and far distances suggests that Q(f) is a more acceptable model. Observed similar average spectral shapes at dif-

ferent distance ranges is best explained by frequency dependent Q below about 4km. Our experience with depth dependent Q in the second model, as discussed earlier, shows that Q(z) can be approximated by an average constant Q independent of frequency. Thus variation of Q with depth is not a likely explanation for the frequency dependence of the observed Q. It is possible that the standard error in observed average data (Figure 3) would decrease if each individual spectra were heavily smoothed before averaging. This would result in smaller variance of Q^{-1}. This, however, has not been attempted here.

Further support for the Q(f) model comes from plots of G(f) shown in Figure 5. Recall that $G(f) = S(f)\, e^{-\pi f t^*}$. If we take the constant Q assumption, G(f) in Figure 5 decays as $\sim f^{-1}$ between 2 to 10Hz, and $\sim f^{-3}$ above 10Hz. Various studies on source theory suggest that S(f) should fall off as $f^{-\gamma}$ ($2 \leq \gamma \leq 3$) at high frequencies (e.g., Brune, 1970; Madariaga, 1976; Brune et al., 1979). This implies that the second term in G(f) (involving t*) is essentially constant, i.e. that t* is very small (Q > 200). However, intuitively one would expect the upper 4km of Imperial Valley to have rather low Q. The G(f) curve assuming Q a function of frequency in Figure 5 does not lead to this difficulty. Let us take the corner frequency of the events studied as 7Hz which corresponds to a source radius of about 200m according to Brune's model [Brune, 1970]. Assuming f^{-2} decay beyond 7Hz for S(f), a $t^* \simeq 0.0477$ is obtained from G(f) for the Q(f) model. This gives an average Q of about 60 in the upper 3.75km. If S(f) is assumed to decay as f^{-3} we obtain a $t^* \simeq 0.027$, the corresponding average value of Q being about 100. Thus, only a rough bound on the value of t* between 0.027 and 0.047 is possible since it is dependent on the source function. Although t* may also be frequency dependent we cannot resolve it from our data set.

CONCLUSIONS

Analysis of spectral attenuation of SH waves along the Imperial fault suggests a frequency-dependent Q below about 4km. The estimated Q^{-1} values shown in Figure 6 indicate that: (1) Q is very high at high frequencies ~400-500 at 20-25Hz, (2) Q values are probably lower at 5-10Hz, ~70-140, and may decrease to values lower than 30 at lower frequencies, although the standard deviations at lower frequencies (~1Hz) are too large to establish this for certain. Because of the longer wavelengths compared to path lengths at lower frequencies, the reliability of the Q determination is lower.

Although taking the extreme curve within the standard deviation bounds would allow a Q almost independent of frequency, we consider this unlikely. Even if this extreme interpretation were accepted, the conclusion that Q is very high at high frequencies would remain, and it would have to be concluded that Q is also quite high (>100) at lower frequencies.

The fact that such high values of Q were obtained at high frequencies strongly suggests that scattering has not removed a significant amount of energy from the signals, and that the apparent variation of Q with frequency is not a result of scattering.

Frequency dependent Q for the lithosphere from coda as well as shear waves have been reported by several authors [Aki and Chouet, 1975; Rautian and Khalturin, 1978; Tsujiura, 1978; Aki, 1980a,b]. Q(f) for Imperial fault is lower than for the regions considered by these authors. It is quite reasonable to expect a lower Q along an active fault zone. Bakun and Bufe [1975] report Q for SH waves between 75 and 100 (1 to 12Hz) along the San Andreas fault in central California.

The attenuation in the upper 4km is essentially independent of epicentral distance since for sources below 4km the waves travel nearly vertically

regardless of distance. This attenuation can be described by $e^{-\pi ft^*}$. The value of t^*, based on f^{-2} or f^{-3} model for the source radiation beyond corner frequency, lies between 0.047 (average $Q \simeq 57$) and 0.027 (average $Q \simeq 100$). Any frequency dependence of the Q in the upper 4km cannot be resolved by the present data set.

Taking $Q(f) \simeq 20f$ ($25 > f > 3$Hz) as suggested by our data, the attenuation with distance, $[e^{-\pi ft/Q(f)}]/R$, can be written as $-e^{-0.05R}/R$. This decay of spectral amplitudes (valid for sources below 4km) is greater than those reported by Trifunac [1976] and McGuire [1978]. It is also greater than the attenuation of peak acceleration and velocity with distance, $e^{-0.006R}/R$, as reported by Joyner and Boore [1981]. The difference may be due to anomalous attenuation along the fault. Source characteristics of larger events which constitute the data set used by these other authors may also be a factor in the difference of the attenuation, although the situation may be more complex for larger events, since at high strain amplitudes nonlinear attenuation may come into effect.

Greater resolution of Q would have been possible if we had more stations recording the same event over larger range. Obviously, an understanding of high frequency seismic wave attenuation would benefit greatly by improving both the quality and the quantity of digital data from events located at different focal depths.

Acknowledgments. We are grateful to D. Chavez and J. Fletcher for providing us with data; M. Reichle, A. Olson, J. Anderson, R. Archuleta, and M. Caputo for helpful discussions; L. Munguía and R. Simons for help in computation, and A. Reyes for a preprint prior to publication. Computational facilities provided by USGS, Menlo Park, and Del Mar Technical Associates is gratefully acknowledged. During the course of this study one of us (SKS) was on sabbatical leave at IGPP. This research was supported in part by NSF grants PFR-79-26539, PFR-80-07418, and USGS 14-08-0001-19852.

REFERENCES

Aki, K., 1980a. Attenuation of shear-waves in the lithosphere for frequencies from 0105 to 25 Hz. Phys. Earth Planet. Int. 21, 50-60.

Aki, K., 1980b. Scattering and attenuation of shear waves in the lithosphere. J. Geophys. Res. 85, 6496-6504.

Aki, K. and B. Chouet, 1975. Origin of coda waves: Source, attenuation and scattering effects. J. Geophys. Res. 80, 3322-3342.

Apsel, R., 1979. Dynamic Green's functions for layered media and applications to boundary-value problems, Ph.D. thesis, University of California at San Diego, La Jolla, CA.

Bakun, W.H. and C.G. Bufe, 1975. Shear-wave attenuation along the San Andreas fault zone in central California. Bull. Seism. Soc. Am. 65, 439-459.

Boore, D.M., W.B. Joyner, A.A. Oliver III, and R.A. Page, 1980. Peak acceleration, velocity, and displacement from strong-motion records. Bull. Seism. Soc. Am. 70, 305-321.

Boore, D.M. and J.B. Fletcher, 1981. A preliminary study of selected aftershocks of the 1979 Imperial Valley earthquake from digital acceleration and velocity recordings, U.S.G.S. Professional Paper (in press).

Brune, J.N., 1970. Tectonic stress and the spectra of seismic shear waves from earthquakes. J. Geophys. Res. 75, 4997-5009.

Brune, J.N., R.J. Archuleta, and S.H. Hartzell, 1979. Far-field S-wave spectra, corner frequencies and pulse shapes. J. Geophys. Res. 84, 2262-2272.

Brune, J.N., R.S. Simons, F. Vernon, L. Canales, and A. Reyes, 1980. Digital seismic event recorders: Description and examples from the San Jacinto fault, the Imperial fault, the Cerro Prieto fault and the Oaxaca, Mexico subduction fault. Bull. Seism. Soc. Am. 70, 1395-1408.

Fletcher, J.B., R.L. Zepedda, and D.M. Boore, 1981. Digital seismograms of aftershocks of the Imperial Valley, California earthquake of October 15, 1979. U.S.G.S. Open File Report 81-655.

Joyner, W.B. and D.M. Boore, 1981. Peak horizontal acceleration and velocity from strong-motion records including records from the 1979 Imperial Valley, California earthquake. Bull. Seism. Soc. Am. 71, 2011-2038.

Madariaga, R., 1976. Dynamics of an expanding circular fault. Bull. Seism. Soc. Am. 68, 803-822.

McGuire, R.K., 1978. A simple model for estimating Fourier amplitude spectra of horizontal ground acceleration. Bull. Seism. Soc. Am. 68, 803-822.

McGuire, R.K. and T.C. Hanks, 1980. RMS accelerations and spectral amplitudes of strong ground motion during the San Fernando, California earthquake. Bull. Seism. Soc. Am. 70, 1907-1919.

McMechan, G.D. and W.M. Mooney, 1980. Asymptotic ray theory and synthetic seismograms for laterally varying structures: Theory and application to the Imperial Valley, California. Bull. Seism. Soc. Am. 70, 2021-2035.

Rautian, T.G. and V.I. Khalturin, 1978. The use of coda for determination of the earthquake source spectrum. Bull. Seism. Soc. Am. 68, 923-948.

Richter, C.F., 1958. Elementary Seismology, Freeman, San Francisco.

Trifunac, M.D., 1976. Preliminary empirical model for scaling Fourier amplitude spectra of strong ground acceleration in terms of earthquake magnitude, source-to-station distance and recording site conditions. Bull. Seism. Soc. Am. 66, 1343-1373.

Tsujiura, M., 1978. Spectral analysis of the coda waves of local earthquakes. Bull. Earthquake Res. Inst. 53, 1-48.

FIGURE CAPTIONS

Figure 1. Location map. Epicenters and stations used in this study are shown by heavy dots and triangles, respectively.

Figure 2. Fourier displacement-spectra of various events at stations in an epicentral range of 2 to 14km (Group A). Spectra of different events have been scaled (see Table 1 and text) and smoothed to remove extreme roughness. Spectra for other groups show similar scatter.

Figure 3. Log averaged spectra (thick curve) along with flanking curves (thin) for $\pm$ 1 s.d. for different groups. Also shown are predicted spectra for $Q(f)$ (model), dotted curve, and Q (const) model, dashed curve (see text). (a) Group A (2—14km). (b) Group B (22—24.5km). (c) Group C (29.5—36.5km). (d) Group D (43—51km).

Figure 4. Synthetic log average spectra for the second test model for different groups. Predicted spectra obtained from the interpretation of the synthetic spectra, based on Eq. (5), is shown. The fit is excellent. (a) Group A. (b) Group B. (c) Group C. (d) Group D.

Figure 5. $G(f) = S(f)e^{-\pi f t^*}$ (Eq. 6) obtained from interpreting observed spectra using Eq. (5). Dotted curve $Q(f)$ model, dashed curve Q (const.) model.

Figure 6. Q^{-1} as a function of frequency (thick curve) along with $\pm$ 1 s.d. curves (thin dashed curve).

Figure 7. Ratio of predicted to observed average spectra for $Q(f)$ model (dotted curve) and Q (const.) mode (dashed curve). (a) Group A. (b) Group B. (c) Group C. (d) Group D.

TABLE 1

Aftershocks used in this study. Scaling factor refers to the factor by which S-Wave spectra of the event has been multiplied so that the events could be grouped together as one event (see text).

Event No.	Date	Time (H:M:S)	Lat. °N	Lat. °W	Depth (km)	M_L [4]	Scaling Factor
3[1]	Oct. 18, 1979	13:20:26.61	32.872	115.513	8.8	3.2	1/2
6[2]	Oct. 19, 1979	19:42:36.69	32.480	115.219	9.4	3.3	1
7[1]	Oct. 20, 1979	05:04:07.43	32.912	115.540	9.0	3.0	1
8[2]	Oct. 20, 1979	07:25:23.43	32.484	115.212	9.7	3.1	5/2
9[2]	Oct. 20, 1979	14:52:54.93	32.884	115.499	5.9	3.3	1
12[3]	Oct. 31, 1979	11:43:46.45	32.738	115.413	8.0	3.4	1/3

[1]Origin, location, and depth from Fletcher, et al. (1981).

[2]Origin, location, and depth from D. Chavez (personal communication, 1981).

[3]Origin, location, and depth from R. Archuleta (personal communication, 1981).

[4]M_L from C. Johnson (personal communication, 1981).

TABLE 2

Stations providing data for each event. Data from IVC and HED were not used in analysis because of instrument problem and/or abnormal character.

Event No.	Stations* Used in Analysis
3	TAM, IAA, COM, HED, IVC
6	TAM, IAA, COM, HED, IVC, MEQ
7	TAM, IAA, COM, HED, IVC, MEQ, FBR, SLD
8	TAM, IAA, HED, IVC, MEQ
9	TAM, IAA, COM, HED, IVC, MEQ, FBR, JMS
12	AFB, BCS, FBR, GPN, HUS, SLD

*CICESE stations: TAM, IAA, COM; IGPP stations: MEQ, IVC, HED; USGS stations: AFB, BCS, FBR, GPN, GRS, HUS, JMS, SLD. JMS: forced balanced accelerometer, all others velocity sensors.

TABLE 3

Epicentral distance ranges defining groups A to D and stations contributing to data in each group

Group	Epicentral Distance Range, km	Stations (epicentral distance, km)	Average Epicentral Distance, km
A	$2 \leq r \leq 14$	TAM(10.5), TAM(10.5), FBR(4.0) SLD(8.5), FBR(2.0), JMS(6.0) MEQ(3.0), BCS(8.0), HUS(13.5) GPN(14.0)	8.0 ± 4.2
B	$22 \leq r \leq 24.5$	IAA(22.0), IAA(24.5), COM(22.5)	23.0
C	$29.5 \leq r \leq 33.5$	COM(29.5), IAA(31.5), COM(33.0) IAA(35.5), AFB(29.5), SLD(31.5), COM(29.5), IAA(31.5)	31.8 ± 2.3
D	$43 \leq r \leq 51$	TAM(43.0), MEQ(51.0), MEQ(51.0), TAM(47.5), TAM(44.0)	47.3 ± 3.8

TABLE 4

Crustal model of Imperial Valley, based on McMechan and Mooney (1980), used in the generation of synthetic spectra.

Layer	Thickness, km	P-Wave Velocity, km/sec	S-Wave Velocity, km/sec	Density gm/cm^3
1	0.10	1.690	0.500	2.04
2	0.15	1.790	0.818	2.06
3	0.50	2.167	1.010	2.13
4	0.50	2.533	1.200	2.21
5	0.50	2.900	1.410	2.28
6	0.50	3.267	1.620	2.35
7	0.50	3.633	1.850	2.43
8	0.50	4.000	2.080	2.50
9	0.50	4.367	2.330	2.57
10	0.50	4.733	2.590	2.65
11	0.50	5.100	2.870	2.72
12	0.50	5.375	3.060	2.77
13	0.50	5.650	3.260	2.83
14	5.25	5.750	3.320	2.85
15	0.30	6.700	3.870	3.04
16	0.30	6.900	3.980	3.08
17	0.30	7.100	4.100	3.12
18	1.31	7.300	4.210	3.16
19	2.50	7.800	4.500	3.26
20	∞	8.100	4.670	3.32

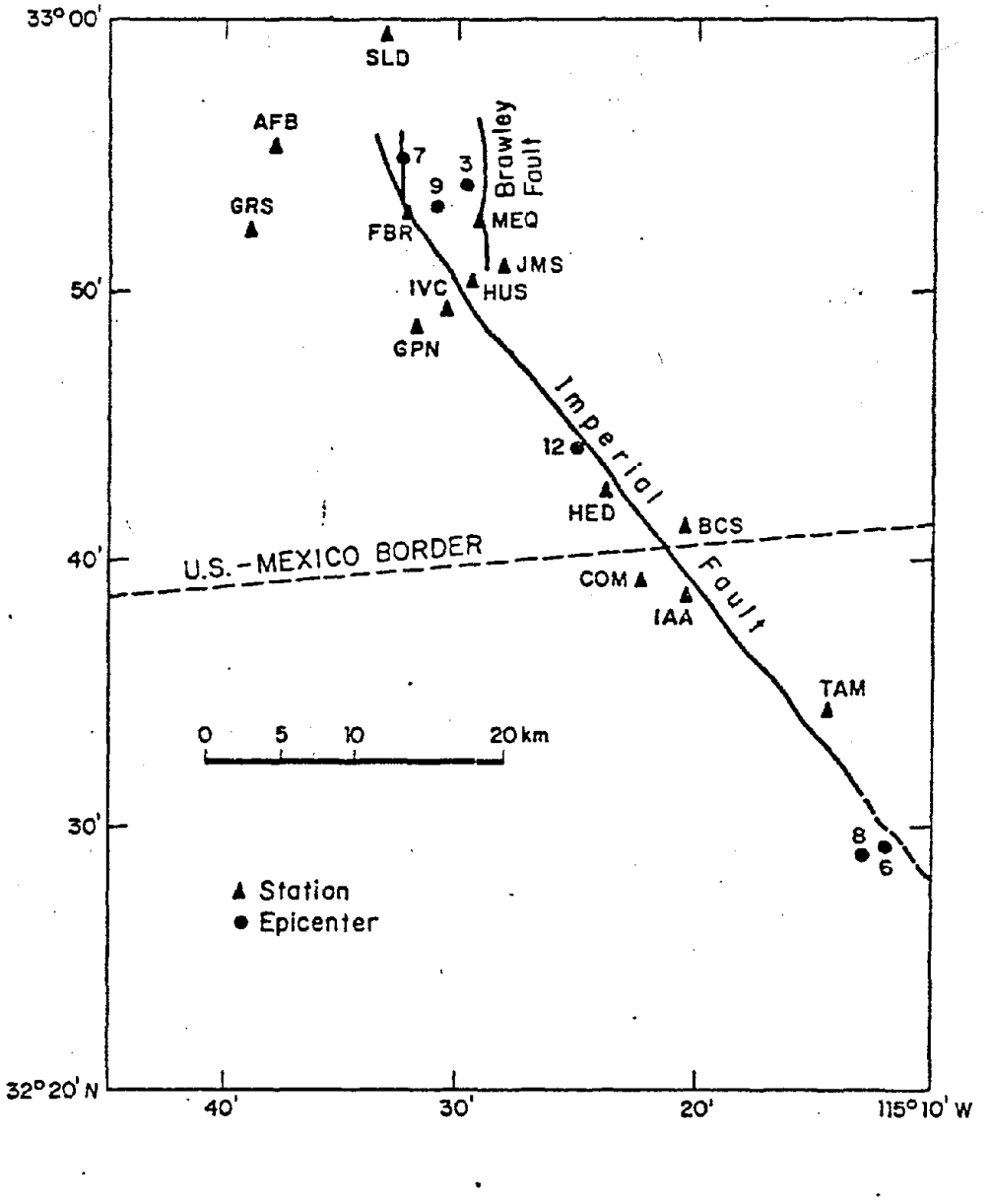

Figure 1. Location map. Epicenters and stations used in this study are shown by heavy dots and triangles, respectively.

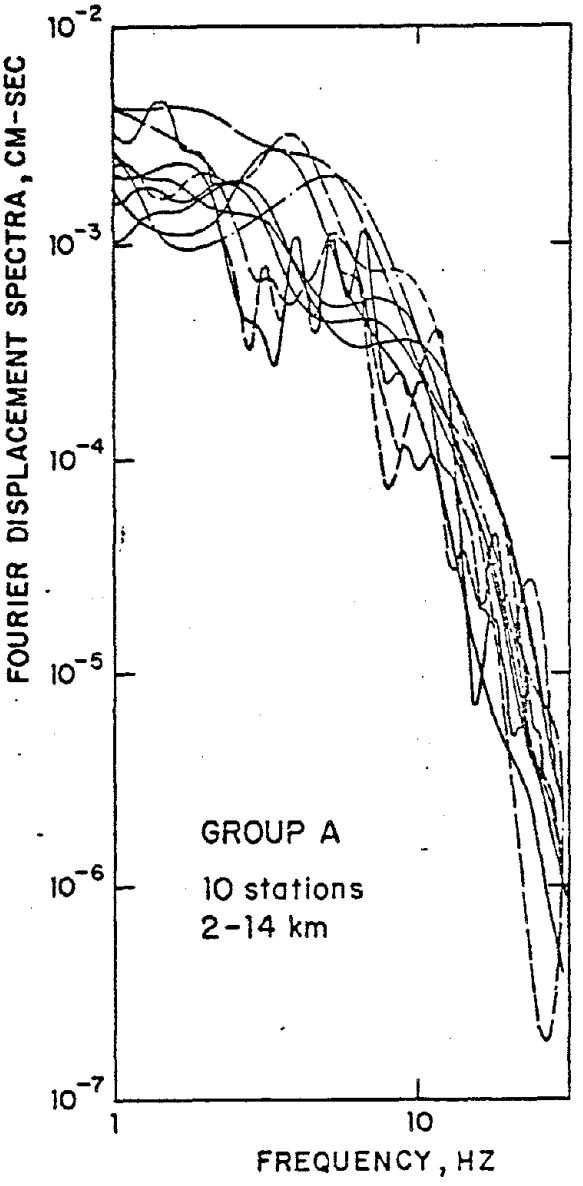

Figure 2. Fourier displacement-spectra of various events at stations in an epicentral range of 2 to 14km (Group A). Spectra of different events have been scaled (see Table 1 and text) and smoothed to remove extreme roughness. Spectra for other groups show similar scatter.

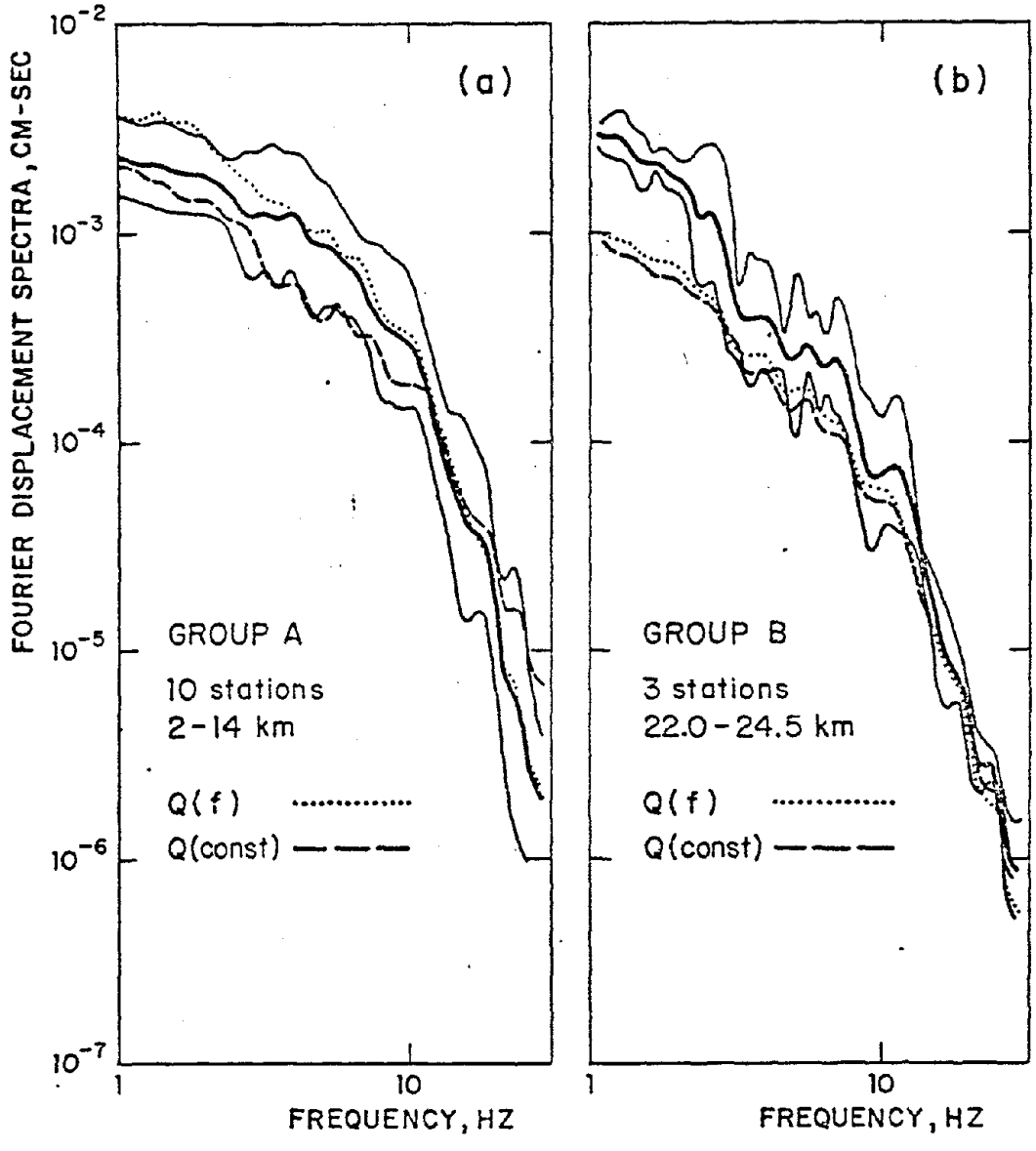

Figure 3a

Figure 3b

Figure 3. Log averaged spectra (thick curve) along with flanking curves (thin) for ± 1 s.d. for different groups. Also shown are predicted spectra for $Q(f)$ (model), dotted curve, and Q (const) model, dashed curve (see text). (a) Group A (2—14km). (b) Group B (22—24.5km). (c) Group C (29.5—36.5km). (d) Group D (43—51km).

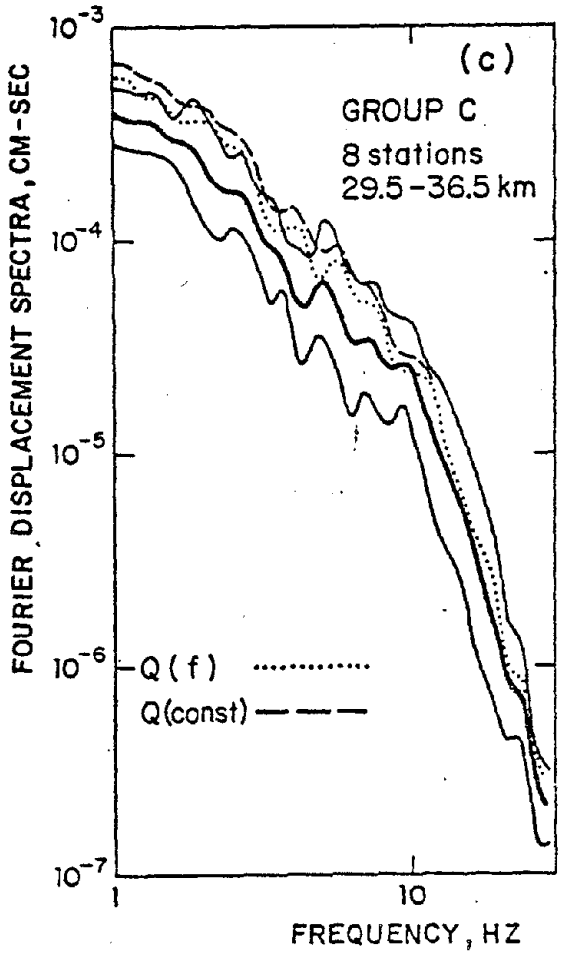

Figure 3c

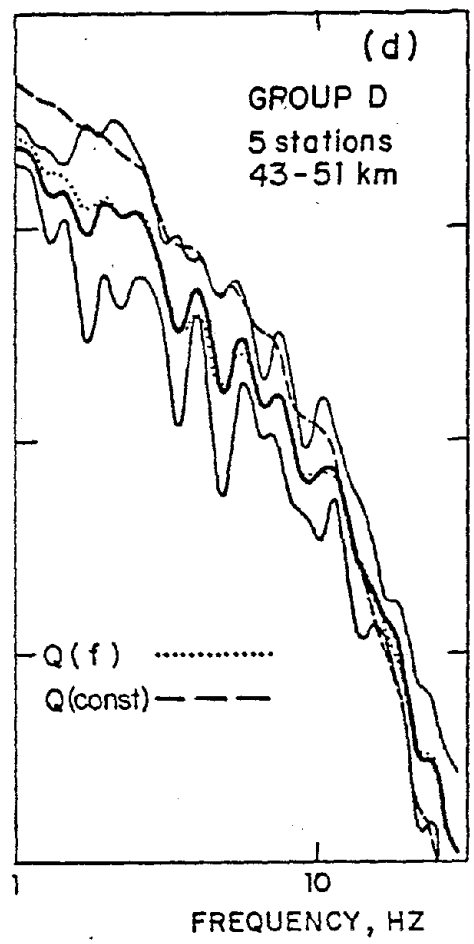

Figure 3d

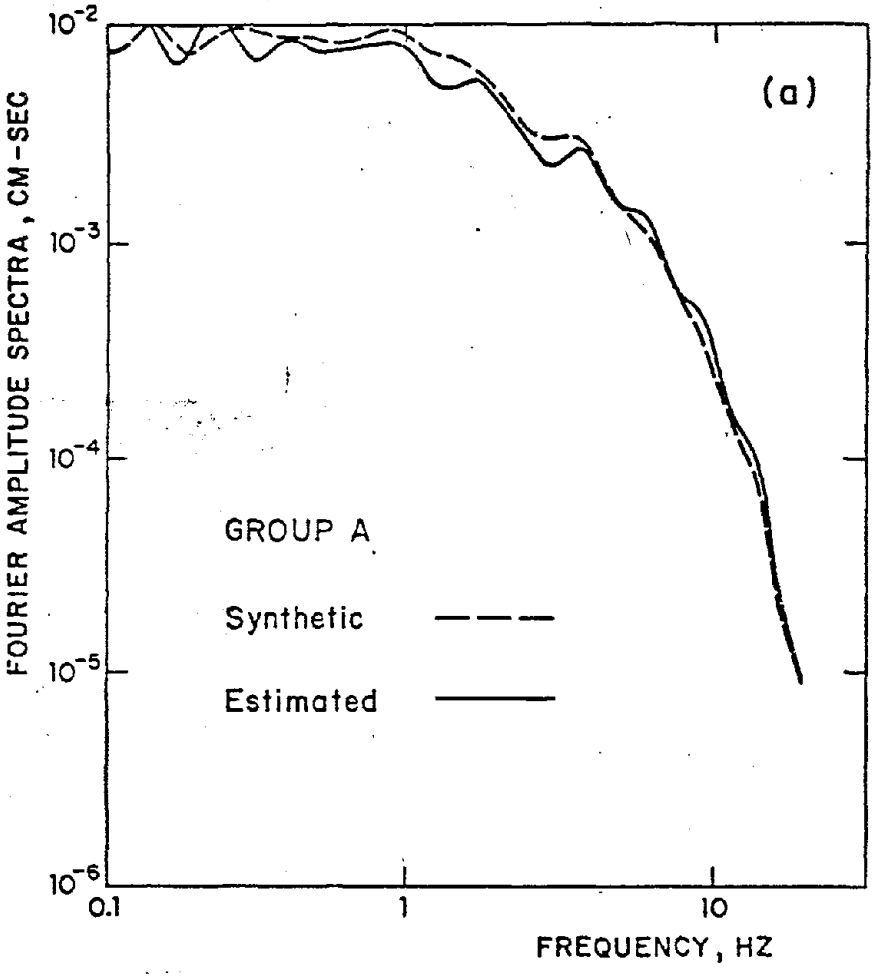

Figure 4a

Figure 4. Synthetic log average spectra for the second test model for different groups. Predicted spectra obtained from the interpretation of the synthetic spectra, based on Eq. (5), is shown. The fit is excellent. (a) Group A. (b) Group B. (c) Group C. (d) Group D.

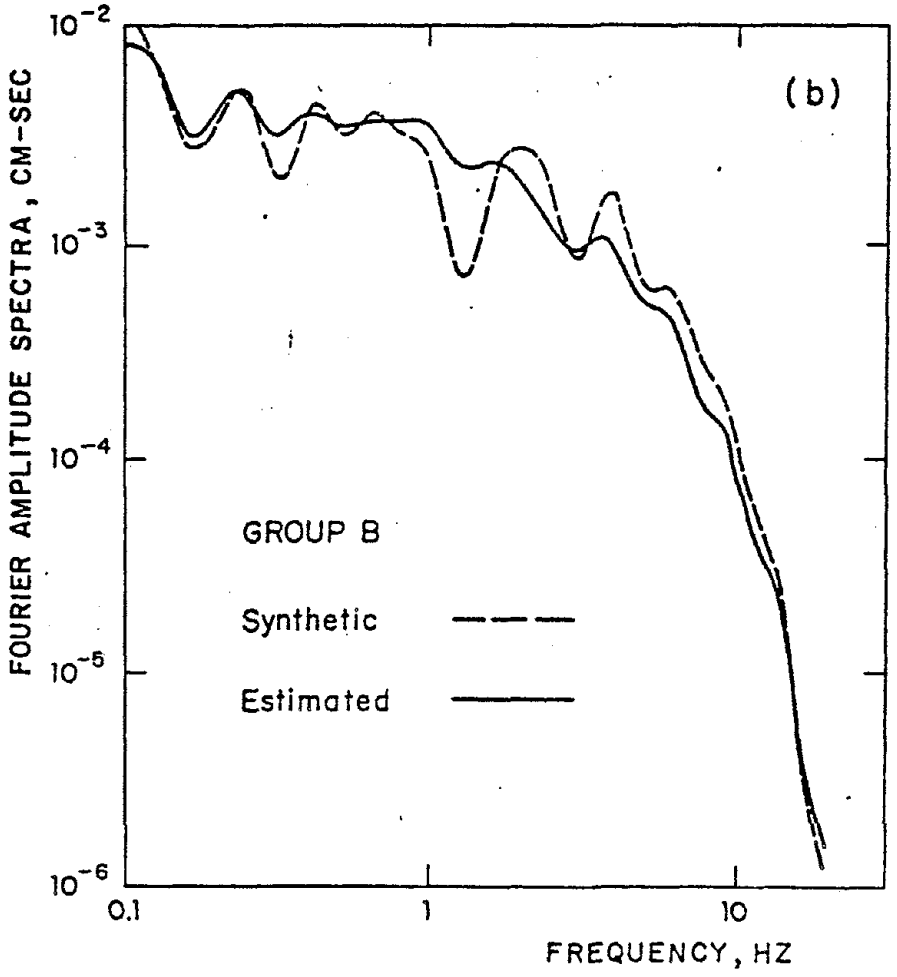
FOURIER AMPLITUDE SPECTRA, CM-SEC
10^{-2}
10^{-3}
10^{-4}
10^{-5}
10^{-6}
(b)
GROUP B
Synthetic
Estimated
0.1
1
10
FREQUENCY, HZ

Figure 4b

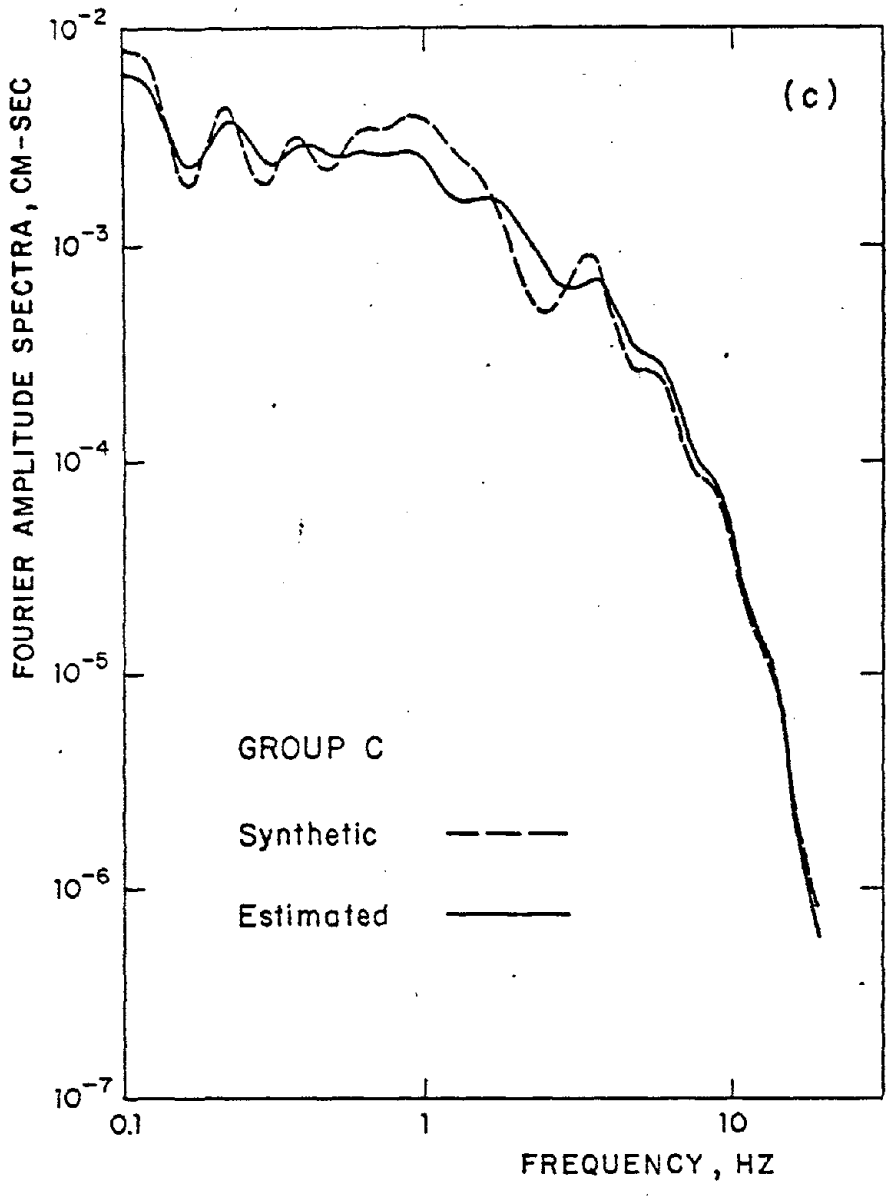
(c)
FOURIER AMPLITUDE SPECTRA, CM-SEC
10^{-2}
10^{-3}
10^{-4}
10^{-5}
10^{-6}
10^{-7}
GROUP C
Synthetic
Estimated
0.1
1
10
FREQUENCY, HZ

Figure 4c

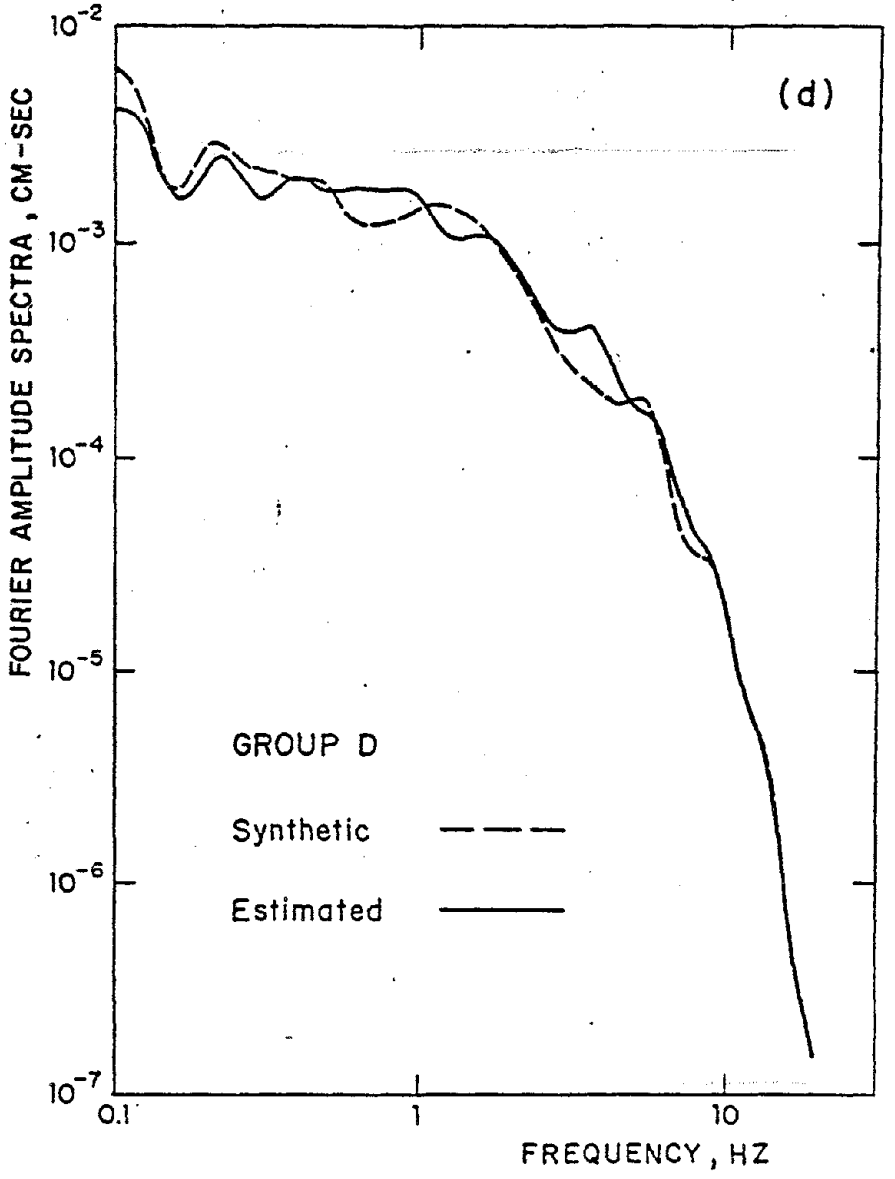
(d)
FOURIER AMPLITUDE SPECTRA, CM-SEC
10^{-2}
10^{-3}
10^{-4}
10^{-5}
10^{-6}
10^{-7}
GROUP D
Synthetic
Estimated
0.1
1
10
FREQUENCY, HZ

Figure 4d

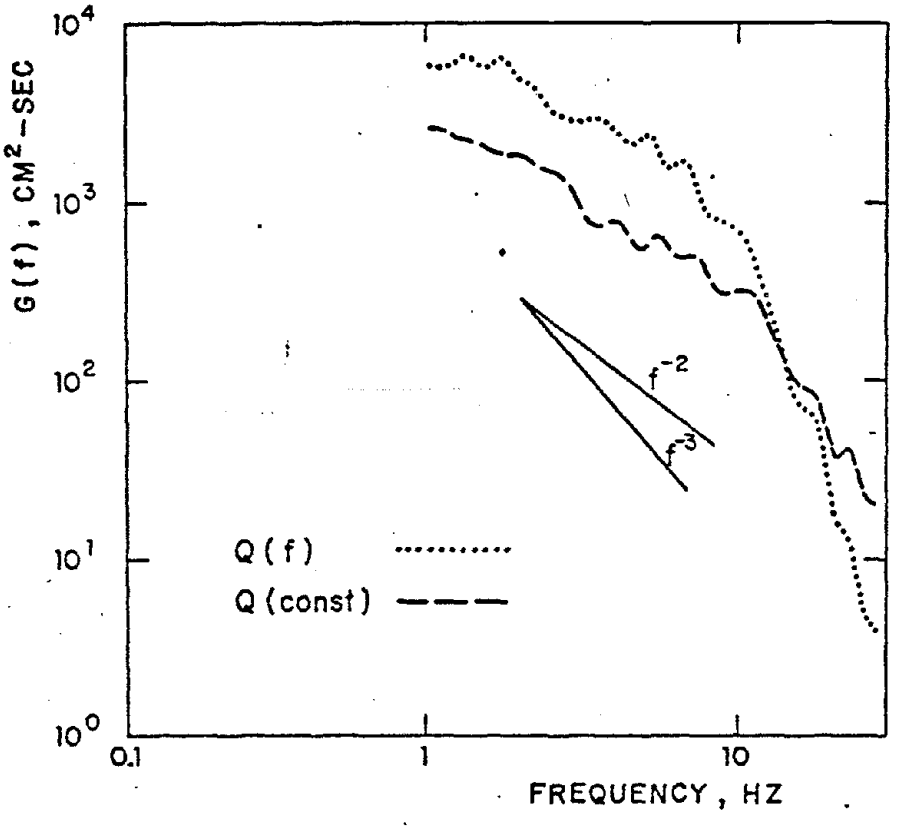

Figure 5. $G(f) = S(f)e^{-\pi ft^*}$ (Eq. 6) obtained from interpreting observed spectra using Eq. (5). Dotted curve $Q(f)$ model, dashed curve Q (const.) model.

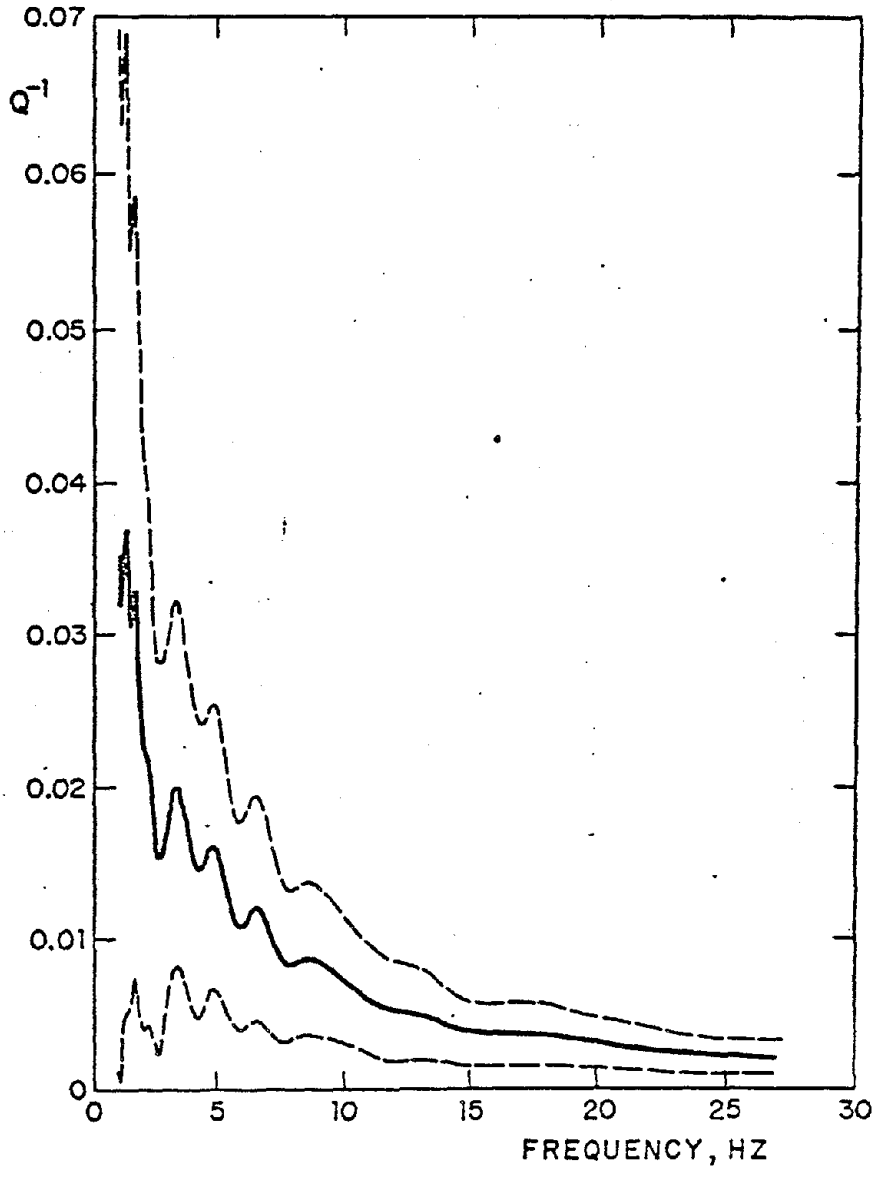

Figure 6. Q^{-1} as a function of frequency (thick curve) along with ± 1 s.d. curves (thin dashed curve).

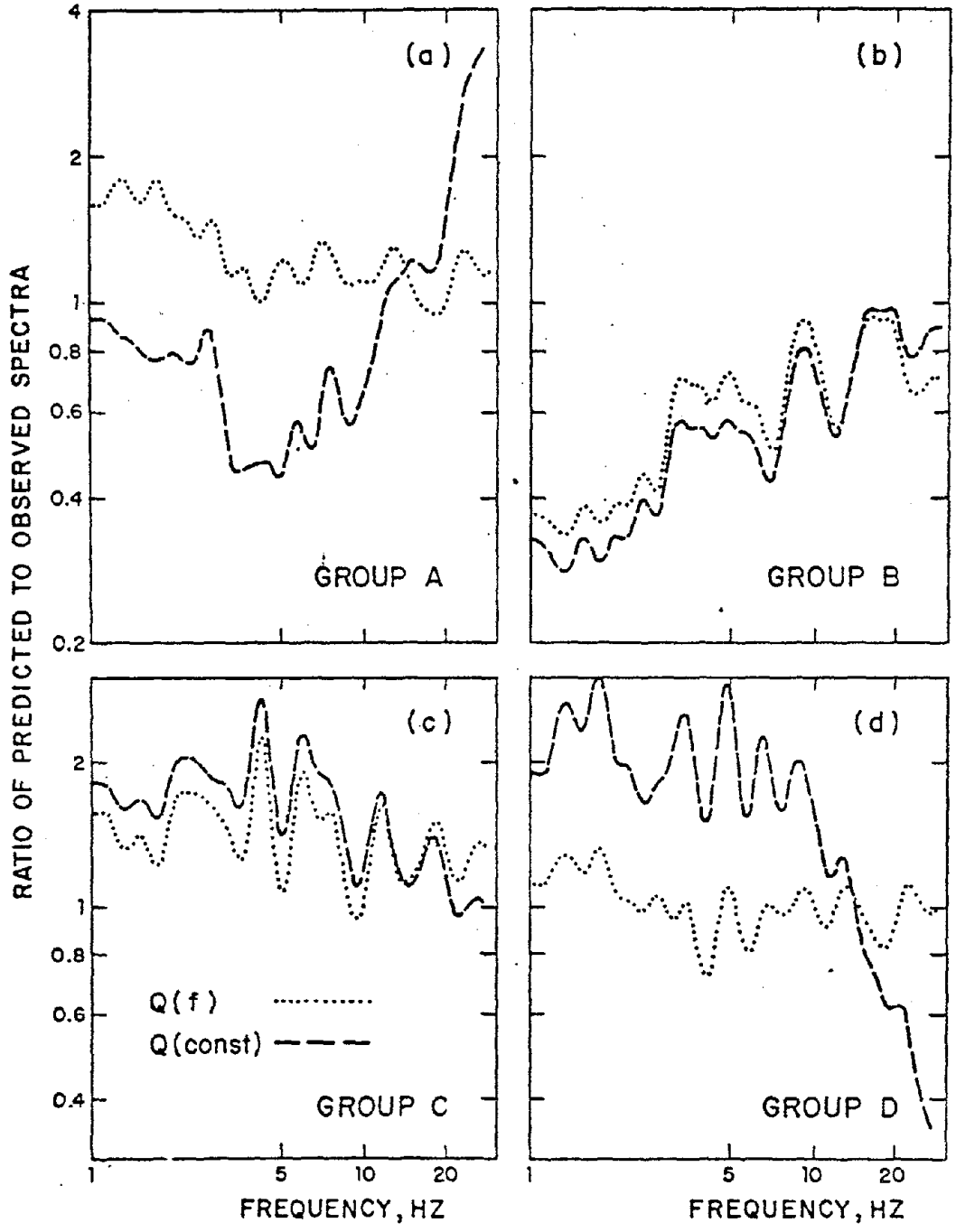

Figure 7. Ratio of predicted to observed average spectra for $Q(f)$ model (dotted curve) and Q (const.) mode (dashed curve). (a) Group A. (b) Group B. (c) Group C. (d) Group D.

APPENDIX V

PRELIMINARY REPORT ON THE USE OF DIGITAL STRONG MOTION RECORDERS IN THE MEXICALI VALLEY, BAJA CALIFORNIA

John G. Anderson, James N. Brune, Jorge Prince, Frank L. Vernon III

ABSTRACT

A network of 12 digital strong-motion accelerographs has been operating in the Mexicali Valley, Baja California, Mexico since 1978. The instruments have operated reliably, except for external problems, such as power failures and site harassment. Data from two important earthquakes and several smaller shocks have been recovered. The data recovered to date have a noise level which appears to be no worse than that on digitized records from analog strong motion accelerographs, in spite of design errors which resulted in increased instrumental noise levels in several of the accelerographs (these design errors have recently been corrected). Digital recording of strong motion promises great advantages over analog recording through recovery of the initial motions, rapid playback, greater dynamic range, and lower equivalent instrumental noise level because digitization is not required.

Institute of Geophysics and Planetary Physics (JGA,JNB,FLV)
Scripps Institution of Oceanography
University of California at San Diego
La Jolla, California 92093

Instituto de Ingenieria (JP)
Universidad Nacional Autonoma de Mexico
Apartado Postal 70-472
Mexico 20, D.F., Mexico

INTRODUCTION

Brune et al. (1980) have previously described the advantage of digital recording of seismic motions. Since 1978, the Institute de Ingenieria, Universidad Nacional Autonoma de Mexico and the Institute of Geophysics and Planetary Physics, University of California, San Diego have operated a network of digital strong motion accelerographs in the Mexicali Valley, Baja California, Mexico. Through December 1980, these instruments had recorded, in the near field, the Imperial Valley earthquake (October 15, 1979, M_L = 6.4), the Victoria earthquake (June 9, 1980, M_L = 6.1) and a number of smaller earthquakes. This represents a unique data set of digital strong motion recordings from large earthquakes. This paper describes the array and evaluates the performance of the instruments to date.

DESCRIPTION OF THE NETWORK

Figure 1 is a map showing the locations of the Mexican accelerograph stations and the Imperial and Cerro Prieto faults. A description of the digital stations is included in Table 1. The digital accelerographs consist of two types of commercial available instruments: Terra Technology DCA 310 digital recorders coupled to external force balance sensors, and Kinemetrics DSA-1 digital models with force balance sensors mounted inside the case. Both types of unit record on magnetic tape within interchangeable, and reusable, cassettes. Figure 1 also shows locations of analog accelerographs maintained by Universidad Nacional Autonoma de Mexico.

The DCA-310 is a three-channel digital recorder specified to have

12-bit accuracy. There is not any filtering on the data signals in the recorder. However the accelerometer has a three-pole low-pass response at 30Hz. The DCA-310 samples each channel 100 times per second and has a 1.92 second pre-event memory.

The DSA-1 also is a three-channel digital recorder with 12-bit accuracy specified. It has a two-pole low-pass filter at 50Hz. The DSA-1 samples each channel 200 times a second and we have 2.56 seconds of pre-event memory.

The accelerographs are, except at the Cerro Prieto site, mounted on concrete piers which have been built on the sediments of the Imperial Valley. Figure 2 shows photographs of two sites. The piers have a cross section (map view) of about 0.8m x 1.2m, and are between 0.05m and 0.50m high, with most about 0.25m high. Designs differ by the extent to which the pier extends below the sediment surface: some are very shallow, some about 0.8m, and some have two concrete piles at alternate corners. The instruments are mounted inside an iron housing on the top of the concrete pier with dimensions about 0.66m x 0.53m x 0.33m high. A somewhat larger heat shield is mounted above this housing with about 3cm clearance. A 3m high post has been installed on each pier, and is used for mounting solar panels, overhead electrical connections, and WWVB antennas. This post is guyed to the ground with three wires. Some of the stations are described in Oñate et al. (1981).

The Cerro Prieto accelerograph is mounted on the concrete floor of a communications building on the Cerro Prieto volcanic cone. This slab is poured directly on the basaltic rocks of the north-east slope of the volcano, at an elevation of about 140m above the valley floor.

Digital cassettes from the DCA-310 accelerographs are returned to the lab at the Institute of Geophysics and Planetary Physics (IGPP), University of California at San Diego (UCSD), where the data is transferred to computer tape as described by Brune et al. (1980). The Instituto de Ingenieria at UNAM is presently developing a capability to carry out this processing step. At present, tapes from the Kinemetrics accelerographs must be returned to the factory to transfer the data to computer tape.

In the Terra Technology instruments, timing is accomplished by a crystal-controlled internal clock. During instrument inspection trips, radio station WWVB is recorded on the magnetic tape, so that in the lab the clock correction for the internal clock is determined to ±5ms. Our experience with these internal clocks is that while they may drift rapidly, this drift is usually a fairly linear function of time. For example, between June 1980 and December 1980, drift rates varied between 0.15 and 0.75 sec/day, depending on the instruments, probably because the clock oscillator frequencies are not set exactly to the correct value.

Errors in the clock correction are a result of deviations from this average drift rate. For any sequence of three or more clock corrections, the intermediate corrections can be compared with the correction one would have inferred on the basis of the end points in the sequence only. The clock correction errors derived in this manner are shown in Figure 3, for four stations, for the later half of the year 1980. At Agrarias and El Doctor, Figure 3 shows that the largest errors were less than 1 sec. At Riito, the largest error was about 1.7 sec. The

greatest deviation from a linear trend occurs at the Chihuahua site. Curiously, in the first half of 1980, the drift rate at this site was only about 0.18 sec/day, with deviations comparable to the other three stations. This is our only example of a clock where the drift rate changed suddenly and by a large factor (from 0.18 to probably greater than 0.7) in a few weeks or less. If the clock at Chihuahua exemplifies the greatest sudden change in drift rate, if that drift rate changes at the time of an earthquake, and if clock corrections are determined within 24 hours after an earthquake, the consequent errors in interpolating to the trigger time of an accelerograph will never exceed 0.5 sec. Based on the other stations however, one would not expect clock correction errors to exceed 0.1 sec.

Our Kinemetrics accelerographs do not have internal clocks; they depend on a direct recording of WWVB radio time. In our experience, this system has not worked well, and this timing has been achieved on fewer than 50% of the accelerograms recorded to date, probably because of irregular reception of the radio signal.

RELIABILITY

The harsh environment of the Mexicali Valley provides a severe reliability test for the digital accelerographs. Summer temperatures are regularly above 100°F (38°C), there is no shade for the accelerograph piers, and the air is filled with dust every day as a consequence of farming activities. However, this environment has not been a direct cause of instrument failures. The most frequent (and most frustrating) cause of instrument failures has been failure of the power supply to maintain the internal batteries in a charged condition. We have used

two battery charging systems: solar panels, which are prone to become coated with dust in parts of the valley, and AC power, and which is not always reliable. Sites with reliable power supplies, and which have been free of harassment, such as Aeropuerto (solar panel), Cerro Prieto (AC), Chihuahua (AC), and El Doctor (solar panel), have operated reliably.

DATA RECOVERED TO DATE

Table 2 lists the more important data which the combined analog and digital network recorded through December 1980. Analog station locations are given by Switzer et al. (1981) and Anderson and Simons (1982). The two largest earthquakes in Table 2 are the October 15, 1979 Imperial Valley earthquake and the June 9, 1980 Victoria earthquake. Data from the October 1979 main shock have been described by Brune et al. (1981). Data from the June, 1980 earthquake is described by Anderson et al. (1982). Data from all of the events with magnitude greater than 4.0 has been submitted to EDIS for distribution, in an uncorrected format resembling Volume I (Trifunac and Lee, 1973) but at equally spaced time points (Anderson and Simons, 1982).

QUALITY OF THE DATA

The digital data to date appears to be of as good quality as analog accelerograms, but with the advantages of digital recording. A primary difference between these accelerograms and the analog records is the recording of a pre-event leader. This made the data useful for two seismological purposes:

(1) Determination of the arrival times of first P-wave for location of the earthquake, and

(2) Determination of the direction of first motions, for further study of the earthquake source.

We found some problems on the accelerograms, which we discuss here to illuminate some of the areas where special attention must be paid to digital recording. Occasional large spikes (isolated samples with amplitude nearly full scale) appeared on several traces from the Terra Technology instruments; these were easily recognized, and replaced by reasonable values determined from adjacent data. The DCA-310 accelerographs had a faulty analog-to-digital converter design (since corrected) which caused a problem we describe as low-bit dropout: the least significant bits had preferred values, and thus were not recorded accurately. This did not affect the most significant bits corresponding to levels greater than ~.03g. Figure 4 shows an extreme example of this type of failure. Some DCA-310 records show non-zero noise levels prior to the start of strong motion, as recorded by the digital pre-event memory of the instruments. This noise is from the power supply lines coupled through the accelerometers. An example of this is shown on the record from Delta (Figure 5).

The above problems have been solved by Roberto Quaas and Frank Vernon. The problems are in no way intrinsic to digital strong motion recording in general.

The DSA-1 records showed nearly quiet traces prior to the start of strong motion, as they should (Figure 6). One component of DSA-1

records from Cucapah was lost during part of our experiment because of dirt around the force balance sensor; the sensor is not separately sealed as it is on the DCA-310. We had trouble playing back the accelerogram from the June 10, 1980 earthquake as recorded on the DSA-1 at Victoria, also apparently as a result of dirt on the recording heads inside the instruments, as documented by Simons (1982).

Figures 7 and 8 show a comparison of quiet traces from three of the digital recorders with a quiet trace from a Kinemetrics SMA-1 accelerograph, as digitized by the University of Southern California (USC) (Lee and Trifunac, 1979). Figure 7 shows between 25 and 40 sec of quiet traces, and on Figure 8 the time scale is expanded by a factor of 5 to show greater detail.

The SMA-1 trace shows large, long-period deviations from the zero level, while the three digital records do not. In current processing methods (Lee and Trifunac, 1979), these long periods are partially removed by subtracting a fixed trace from the acceleration trace. The digital record from Delta shows approximately periodic negative spikes, the source of which has not yet been identified. Isolated spikes like these, can easily be recognized and replaced with reasonable values during analysis of digital records. The Cucapah record, in Figures 7 and 8, recorded on a Kinemetrics DSA-1, shows a significantly lower noise level than the two digital records from DCA-310 accelerographs. A surprising feature of this record is that the small earthquake at the start of the record (peak acceleration 17cm/sec^2 at ~35Hz, $M_L \simeq 3$) is associated with a shift of the zero level by one least count. The above problems all introduce long-period noise into the data.

The high-frequency errors on the SMA-1 trace, as seen in Figure 8, show a sawtooth-shaped curve. The source of this is the digitization process, in which the line on the film, as it is digitized, crosses the grid of digitization points at a small angle. Hence periodically the digitizer reports the center of the trace shifted upward by one grid unit resulting in a staircase-shaped approximation to the line. The digitizing system subsequently rotates this line to a horizontal orientation, to cause the sawtooth shape. At a typical SMA-1 sensitivity of 1.8cm = 1g, the digitizer resolution of 50 microns corresponds to an acceleration of 2.7cm/sec^2, consistent with the sawtooth heights in Figure 7. The sawtooth in Figure 7 has a frequency of about 3Hz. The average digitization noise from the USC system exceeds the noise level associated with hand digitization for these and lower frequencies. This type of noise is apparently absent from accelerograms digitized on the laser system used by the United States Geological Survey (Raugh, 1981).

DIRECT INTEGRATION AND LONG PERIOD NOISE

In the data stream which is recorded on the digital cassette, the position of zero counts does not necessarily represent the equilibrium position of the sensor. Thus to determine absolute acceleration values, and to integrate to velocity and displacement, one needs to know what digital count data value (a_0) does represent zero acceleration. We note that when an analog accelerogram is digitized, the zero position must be estimated at each time point of the record. In digital recording, the zero level is represented by the same digital count level throughout the record; thus the baseline problem is simplified significantly. Furthermore, for an instrument which is operating correctly, the digital leader

allows the definition of a_0 to within one count, corresponding to about 1cm/sec^2 on the DCA-310, or about 0.5cm/sec^2 on the DSA-1. It is readily seen that an error in a_0 (Δa_0) of this size is unacceptable for direct integration, however, as this allows an uncertainty in velocity (ΔV) of $\Delta V = \Delta a_0 t$ and an uncertainty in the displacement (ΔU) of $\Delta U = 1/2 \Delta a_0 t^2$. For a record with duration 50 sec, the velocity estimates at the end can be in error by 50cm/sec, and displacement in error by 1250cm for $\Delta a_0 = 1.0$cm/sec^2.

For a properly operating accelerograph, the earth and/or system noise will sometimes cause the pre-event count level to oscillate more or less randomly between two levels; the proportion of counts at each level may then provide a better estimate of a_0 from the leader. Alternatively, one might consider the superposition of a sinusoidal signal with known amplitude onto the leader (dithering) to assure that roundoff errors in both directions will be present in approximately the correct proportion. The standard deviation S_n in the estimate of a_0 from a leader of duration n counts is then $S_1 n^{-1/2}$. If we take $S_1 = 1/12$, corresponding to a uniform distribution of round-off errors, and a leader of 100 points, one obtains $S_{100} = 1/120$ count. When 1 count = 1 cm/sec^2, an error Δa_0 of this magnitude would lead to $\Delta V = 0.42$ cm/sec and $\Delta u = 10$ cm at the end of a 50 sec record. To obtain an uncertainty of less than 1cm in displacement at the end of a 50 sec accelerogram, one would need about 10^4 points in the leader to determine a_0 with sufficient accuracy by this technique. We note that for small earthquakes with shorter duration of shaking, a larger value of Δa_0 can be tolerated. For example, to integrate a 10-second accelerogram directly, 100 samples of pre-event data are sufficient to obtain a_0.

Alternatively, one can use assumed properties of the integrated accelerogram to define a_0. This allows several possibilities, which may be evaluated on the basis of their physical consequences. The simplest is to require the velocity to be zero at the end of the record; this method fails when shaking continues beyond the end of the recording. The requirement that displacement return to zero fails under this condition and also if a static offset occurred. Because static offsets are possible, it is also not reasonable to minimize any average measurements of the distance of the displacement trace from zero offset. Therefore, the most reasonable constraint may be that the velocity vary about zero in some minimum sense. In particular, we investigated the requirement that $\int_{t_0}^{t_1} v^2(t)dt$ is a minimum, where t_0 and t_1 represent timepoints near the beginning and the end of the shaking. To prevent the leader from causing a biased initial velocity, we needed to remove it from the integration. The displacement traces from three stations, derived for this definition of a_0, are shown in Figure 9. We note that the long-period deviations and the apparent offsets at the ends of the traces in Figure 9 are inconsistent with the mechanism for this earthquake (e.g. Hartzell and Helmberger, 1982; Olson, 1982). Other stations showed deviations from zero of up to about five times larger than these shown on Figure 9. From these traces, one might find a value for a_0 which would lead to displacement ranging more nearly about zero, but long period deviations from zero would remain. We infer that the long period components in Figure 9 are at least partially caused by noise, and that for these records some filtering is necessary to accompany integration.

We have attempted to estimate the long-period noise level of analog

and digital accelerograms from the Imperial Valley, October 15, 1979 earthquake. This was done by a filtering scheme in which the amplitudes of long-period ground displacements were measured as they were removed. By this determination, the average amplitude of long-period noise on the digital DCA-310 accelerographs was about the same as the amplitude on Kinemetrics SMA-1 analog accelerographs as digitized by the U.S. Geological Survey. The noise level on the digital DSA-1 accelerographs appeared to be smaller by a factor of about 3 or 4. Some component of the long-period motions, treated as noise, may in fact have been actual ground motion. Based on the unreasonable appearance of the displacement traces prior to the noise removal, however, we conclude that our estimates of noise levels are dominated by instrumental or digitization noise, and not by ground motions. Significantly lower noise levels are anticipated for future records from the DCA-310 instruments because, as mentioned earlier, the noise estimates were made on DCA-310 records which were recorded under a condition of faulty analog-to-digital conversion, since corrected.

For a properly operating accelerograph and analog-to-digital converter, the resolution is ultimately limited by round-off to the least significant bit. At high amplitude or high frequencies one approximation for this noise source is a random round-off error of ± 0.5 or less of one significant bit at each point in time. Figure 10 shows the second integral of three randomly generated accelerograms using this noise model, with the integration constant estimated in the same manner as for the data in Figure 9.

The long period displacements generated from these random signals

have amplitudes about 1/20 the amplitudes of the long periods which look like noise on Figure 9. This suggests that for records derived from properly operating accelerograms, and the procedure we have used to estimate a_0, errors in displacements over 50-second time intervals due to roundoff will be of the order of 1-2cm or less.

At long period and/or low amplitude recordings <0.1g, <1Hz successive round-off errors will be correlated in the sense that near the peaks, and for still lower frequencies or amplitudes near the axis crossings, successive roundoff errors will be in the same direction. Depending on amplitude and frequency these errors may or may not cause a major influence on the integrations. We have not investigated this topic further at this time.

SUMMARY

We are successfully recording strong ground motion on digital accelerographs in the Mexicali Valley of Mexico. Due to electronic design and quality control deficiencies, the amplitude of noise on the digital accelerograms which have been recorded to date is much larger than that expected from random round-off errors. In that sense, these initial results from digital strong motion recorders have been somewhat discouraging in that a true test of the ultimate capabilities and advantages of digital recordings was not possible. We are encouraged, however, by our experience to date, that direct digital recording of strong motion will eventually yield great advantages over analog recording, since the difficulties encountered have not been of a fundamental nature.

Acknowledgments

This research was supported by the United States National Science Foundation under Grants PFR 79-26539 and PFR 80-07418, and by (Mexican sources).

Anderson, J.G., J. Prince, J.N. Brune and R.S. Simons (1982). Strong motion accelerograms, in J.G. Anderson and R.S. Simons, ed., The Mexicali Valley earthquake of 9 June, 1980, EERI, in press.

Anderson, J.G. and R.S. Simons (1982). Mexicali Valley accelerogram data: 1978-1980. Report 82-1, Strong Motion Project, Institute of Geophysics and Planetary Physics, University of California at San Diego, La Jolla, California.

Brune, J.N., R.S. Simons, F. Vernon, L. Canales and A. Reyes (1980). Digital seismic event recorders: description and examples from the San Jacinto fault, the Imperial fault, the Cerro Prieto fault and the Oaxaca, Mexico subduction fault, Bull. Seism. Soc. Am. 70, 1395-1408.

Brune, J.N., J. Prince, F.L. Vernon III, E. Mena, and R.S. Simons (1981). Strong motion data recorded in Mexico during the October 15 main shock, in USGS Professional Paper on the Imperial Valley earthquake (in press).

Hartzell, S. and D.V. Helmberger (1982). Strong-motion modeling of the Imperial Valley earthquake of 1979, Bull. Seism. Soc. Am. 72, 571-596.

Lee, V.W. and M.D. Trifunac (1979). Automatic digitization and processing of strong motion accelerograms, Report No. 79-15, Department of Civil Engineering, University of Southern California, Los Angeles.

Olson, A.H. (1982). Finite faults and inverse theory with applications to the 1979 Imperial Valley earthquake, submitted for publication.

Oñate, M., G. Beriones, J. Jiménez, E. Mena and F. Vernon (1981). Reconstrucción y acondicionamiento de algunas estaciones en Baja

California y Sonora (Proyecto Conjunto UNAM - Universidad de California, San Diego), Instituto de Ingenieria, Universidad Nacional Autonoma de Mexico.

Raugh, M. (1981). Procedures for analysis of strong-motion records, abstract, Earthquake Notes 52, No. 1, 17.

Simons, R.S. (1982). The strong motion record from station Victoria, in J.G. Anderson and R.S. Simons, eds., The Mexicali Valley earthquake of 9 June 1980, EERI, in press.

Switzer, J., D. Johnson, R. Maley and R. Mattiesen (1981). Western hemisphere strong-motion accelerograph station list - 1980, Open File Report 81-664, United States Department of the Interior Geological Survey, Menlo Park, California.

FIGURE CAPTIONS

Figure 1. Map showing locations of digital accelerographs in the Mexicali Valley. Analog accelerograph sites maintained by UNAM are also shown. The location of the Cerro Prieto fault may be in error by a few kilometers at any given point.

Figure 2A. Accelerograph pier at the Agrarias site.

Figure 2B. Accelerograph pier at Chihuahua site.

Figure 3. Deviation of clock corrections from a linear trend at four of the DCS-310 accelerographs during the latter half of 1980. The dashed lines were drafted on the figure to guide the eye between adjacent data points, shown by solid symbols. The average drift rate, over the entire time interval, is shown with the station name.

Figure 4. Initial section of accelerogram from the Chihuahua station for the earthquake of October 15, 1979. The frequent clipping of peaks at preferred levels illustrates a problem which we describe as low bit dropout, which has subsequently been corrected (discussed in text).

Figure 5. Initial section of accelerogram from Delta station for the earthquake of October 15, 1979. The initial section shows a non-zero noise level caused by a power supply problem.

Figure 6. Initial section of accelerograms from Cucapah, recorded on a Kinemetrics DSA-1 accelerograph. The third component was not recovered from the digital data cassette as a result of some unknown instrumental malfunction.

Figure 7. Acceleration traces at times when there is no input from ground motion.

Figure 8. Like Figure 7, except with an expanded time scale.

Figure 9. Direct integration of five accelerogram traces from the October 15, 1979 Imperial Valley earthquake. These are integrated by 1) assuming $v_0 = 0$, 2) deleting the leader to avoid a biased velocity at the start of the data, and 3) minimizing the integral of V^2 from times 0.05 to 50.0 sec by the choice of zero level acceleration.

Figure 10. Direct integration of three synthetic accelerogram traces. The traces were generated by a pseudo-random number generator with amplitudes at each point in the range -0.5cm/sec^2 to 0.5cm/sec^2, to simulate the effect of random round-off in the analog-to-digital converter. Traces were integrated as in Figure 9.

TABLE 1

DIGITAL STRONG MOTION STATIONS IN NORTHERN BAJA CALIFORNIA

Name	Location and Elevation	Instrument	Surface Geology and Water Table Elevation
Islas Agrarias	32° 37.25'N 115° 18.07'W 15m	Terra-Technology DCA 310	alluvium ?
Cucapah	32° 32.72'N 115° 14.08'W 17m	Kinemetrics DSA-1	alluvium ?
Cerro Prieto	32° 25.23'N 115° 18.07'W 140m	DCA 310	basaltic tephra ?
Delta	32° 21.37'N 115° 11.70'W 13m	DCA 310	alluvium ?
Victoria	32° 17.32'N 115° 06.18'W 13m	Kinemetrics DSA-1	alluvium 5m
Riito	32° 09.84'N 114° 57.66'W 11m	DCA 310	alluvium ?
El Doctor	31° 57.8'N 114° 44.5'W ~10m	DCA 310	alluvium ?
Pacifico	32° 26.55'N 115° 22.35'W 9m	DCA 310	alluvium ?
Chihuahua	32° 29.05'N 115° 14.40'W 15m	DCA 310	alluvium ?
Compuertas	32° 34.35'N 115° 05.00'W 23m	DCA 310	alluvium 7m
Hechicera	32° 32.80'N 115° 08.75'W 20m	DCA 310	alluvium ?
Escuela	32° 37.35'N 115° 59.13'N 25m	DCA 310	alluvium 7m

TABLE 2
CATALOG OF STRONG MOTION DATA FROM MEXICALI VALLEY

Event				Stations That Recorded		
Date	Time	Location	Mag.*	Name	Recorder	Comments
03/11/78	23:57:46.5	32° 15.50'N 115° 07.75'W	4.8	Victoria Delta	SMA-1 SMA-1	Digitized on a Bendix Digitizer
03/12/78	00:30:17.3	32° 19.30'N 115° 05.45'W	4.5	Victoria	SMA-1	Digitized on a Bendix Digitizer
03/12/78	18:42:24.0	32° 15.10'N 115° 05.90'W	4.8	Victoria	SMA-1	Digitized on a Bendix Digitizer
10/10/79	19:48:36.65	32° 17.73'N 115° 19.23'W	4.1	Delta Cerro Prieto	Terra Tech Terra Tech	
10/15/79	23:16:55.09	32° 38.37'N 115° 19.68'W	6.6	Delta Cerro Prieto Chihuahua Compuertas Agrarias Victoria Cucapah Aeropuerto Mexicali (Casa Flores)	Terra Tech Terra Tech Terra Tech Terra Tech Terra Tech Kinemetrics Kinemetrics SMA-1 SMA-1	 No Timing No Timing No Timing; 1 Horiz. Inop. Digitized at UNAM Digitized at UNAM
10/15/79	23:19:29.98	32° 45.94' 115° 26.45'	5.2	Delta	Terra Tech	Triggered on S
10/24/79	06:44:27.15	32° 25.09'N 115° 13.22'W	3.2	Cerro Prieto	Terra Tech	Triggered on S
12/21/79	20:40:23.26	32° 27.03' 115° 11.72'	4.8	Chihuahua Compuertas Cucapah	Terra Tech Terra Tech Kinemetrics	Triggered on S Triggered on S No Timing; 1 Horiz. Inop.
06/09/80	03:28:19.4	32° 11.12' 115° 04.55'	6.1	Chihuahua Victoria Cucapah Cerro Prieto Mexicali (SAHOP) Hospital (3 levels)	Terra Tech Kinemetrics Kinemetrics SMA-1 SMA-1 SMA-1	Triggered on S Severe Dropouts No Timing; 1 Horiz. Inop. Digitized at UNAM Digitized at UNAM Digitized at UNAM
06/09/80	03:29	(Aftershock of above?: Follows by ~40 secs)		Chihuahua Victoria Cucapah Cerro Prieto	Terra Tech Kinemetrics Kinemetrics SMA-1	S-P ~3 secs No Timing; 1 Horiz. Inop., S-P ~4 secs

Event				Stations That Recorded		
Date	Time	Location	Mag.*	Name	Recorder	Comments
06/09/80	03:30:04.7 (P arrival)		4.9	Victoria	Kinemetrics	S-P ~1.7 secs
06/09/80	03:30:28.1 (P arrival)		5.3	Victoria	Kinemetrics	S-P ~2.0 sec
06/09/80	19:47:54.9	32° 23.64'N 115° 11.52'W	3.2	Delta	Terra Tech	Triggered on S
06/09/80	20:17:11.6	32° 16.32'N 115° 09.24'W	2.5	Delta	Terra Tech	Triggered on S
06/09/80	20:31:32.3	32° 13.14'N 115° 05.34'W	3.9	Delta	Terra Tech	Triggered on S
06/09/80	21:05:37.7	32° 23.52'N 115° 10.44'W	2.4	Delta	Terra Tech	Triggered on S
06/09/80	23:26:18.6	32° 16.14'N 115° 09.30'W	3.0	Delta	Terra Tech	Triggered on S
06/09/80	23:33:41.0	32° 21.90'N 115° 12.90'W	4.3	Delta Cerro Prieto	Terra Tech	
06/10/80	00:17:36.9	32° 20.40'N 115° 12.18'W	3.3	Delta	Terra Tech	
06/10/80	00:17:58.8	32° 25.02'N 115° 12.00'W	3.3	Delta	Terra Tech	
06/10/80	00:36:51.0	32° 22.86'N 115° 11.88'W	3.4	Delta	Terra Tech	
06/10/80	01:07:08.6	32° 19.20'N 115° 12.72'W	3.6	Delta	Terra Tech	Triggered on S
06/10/80	01:35:36.6	32° 22.62'N 115° 12.54'W	3.4	Delta	Terra Tech	
06/10/80	01:36:28.1	32° 22.98'N 115° 13.02'W	2.9	Delta	Terra Tech	Triggered on S
06/10/80	01:59:01.9	32° 22.86'N 115° 11.52'W	2.7	Delta	Terra Tech	
06/10/80	05:36:24.0	32° 24.00'N 115° 12.84'W	3.3	Delta	Terra Tech	

* Cal Tech Magnitude (M_L)

Note concerning the interval Oct. 25, 1979 through Mar. 8, 1980 at Station Victoria: The Kinemetrics Digital Recorder at Victoria recorded seven events during this period, with maximum acceleration levels (O-P) ranging from about 15cm/sec^2 to 170cm/sec^2, and S-P's generally less than 4.5 seconds. Lacking timing on the tape it has not yet been possible to correlate these signals positively with the (Cal Tech) catalog of nearby events.

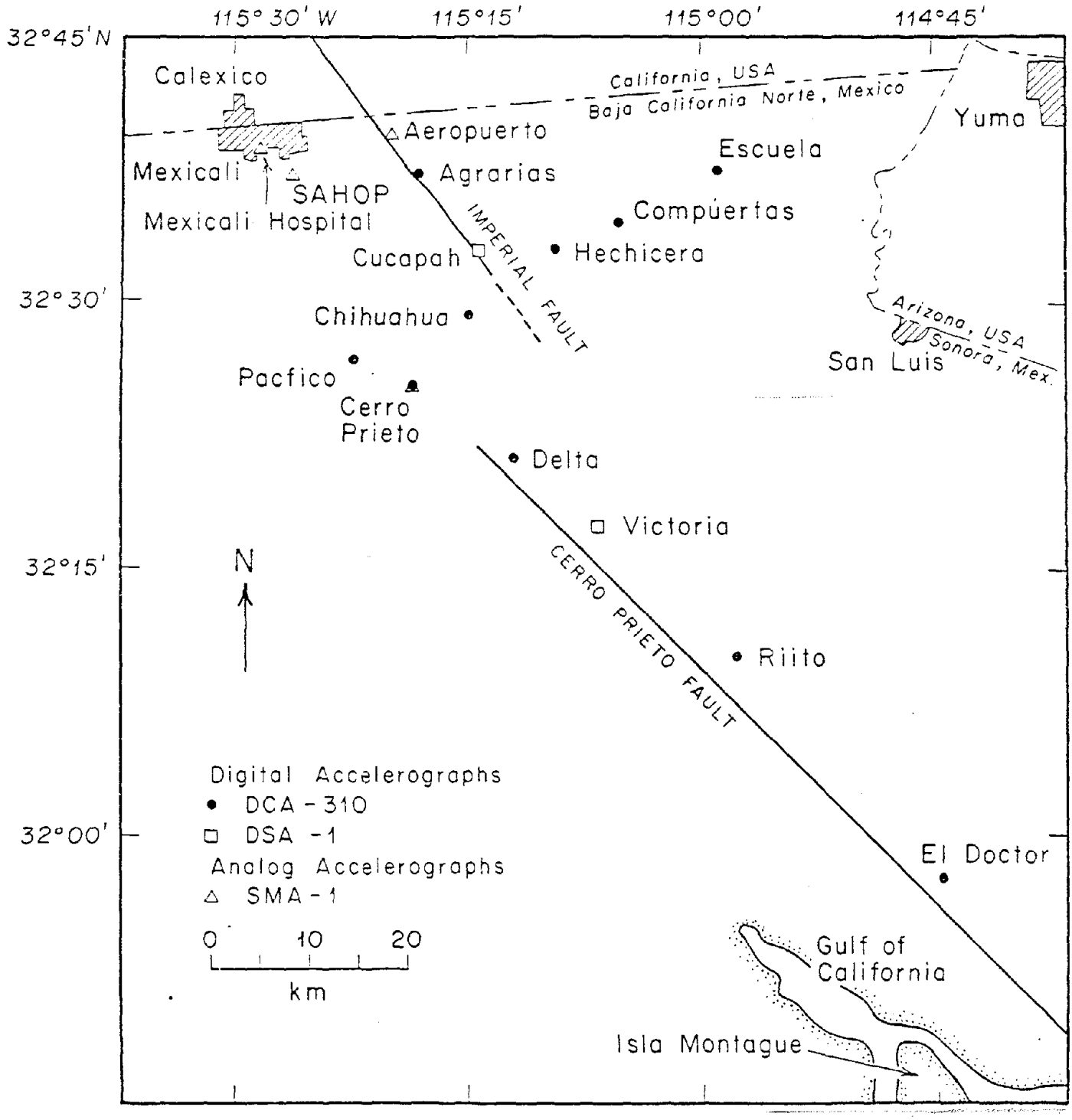
115° 30' W
115°15'
115°00'
114°45'
32°45'N
32°30'
32°15'
32°00'
Calexico
California, USA
Baja California Norte, Mexico
Yuma
Aeropuerto
Escuela
Mexicali
Agrarias
SAHOP
Mexicali Hospital
Compuertas
IMPERIAL FAULT
Cucapah
Hechicera
Chihuahua
Arizona, USA
Sonora, Mex.
San Luis
Pacfico
Cerro Prieto
Delta
Victoria
N
CERRO PRIETO FAULT
Riito
Digital Accelerographs
DCA - 310
DSA - 1
Analog Accelerographs
SMA - 1
0 10 20
km
El Doctor
Gulf of California
Isla Montague

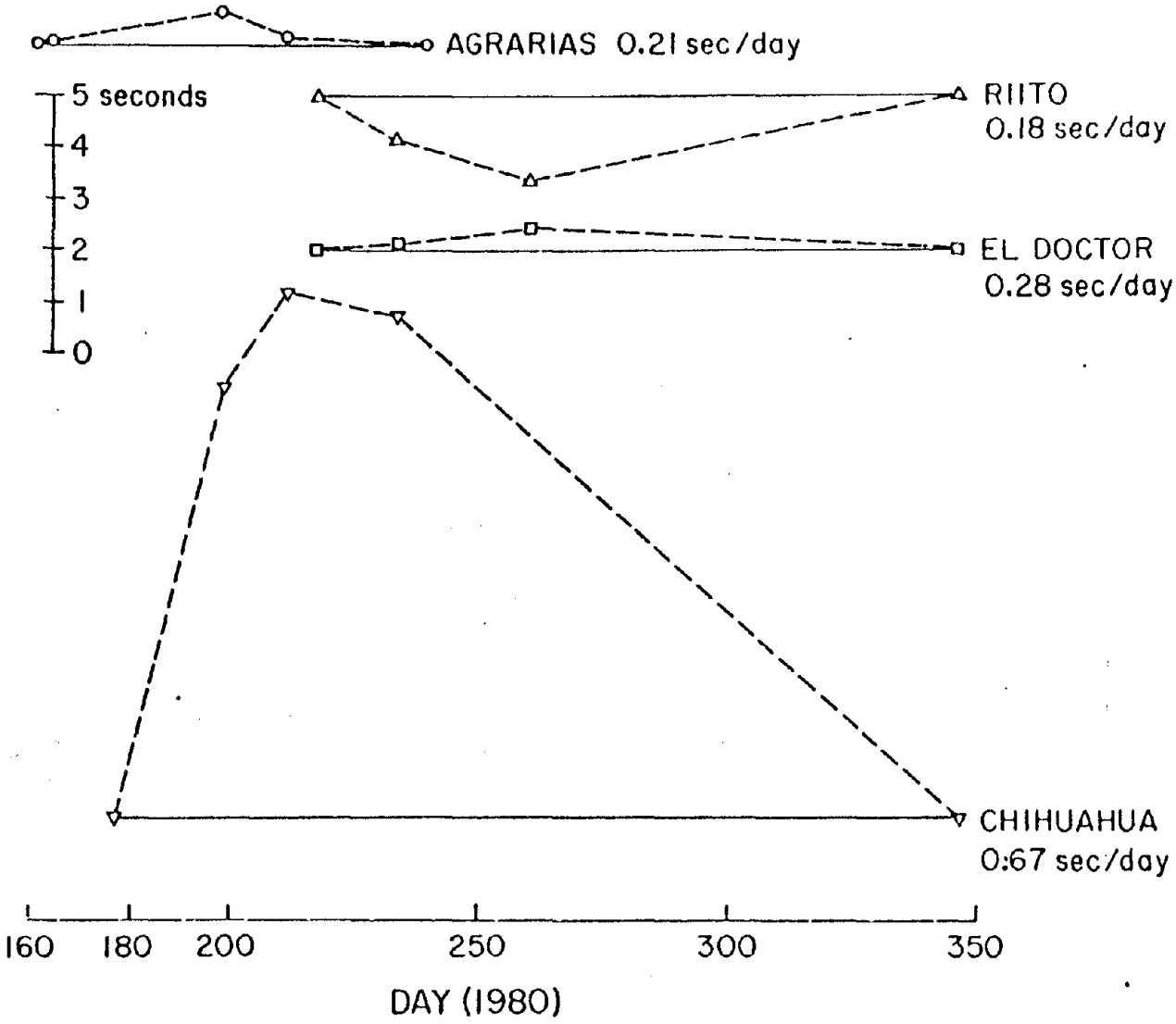
AGRARIAS 0.21 sec/day
5 seconds
4
3
2
1
0
RIITO
0.18 sec/day
EL DOCTOR
0.28 sec/day
CHIHUAHUA
0:67 sec/day
160
180
200
250
300
350
DAY (1980)

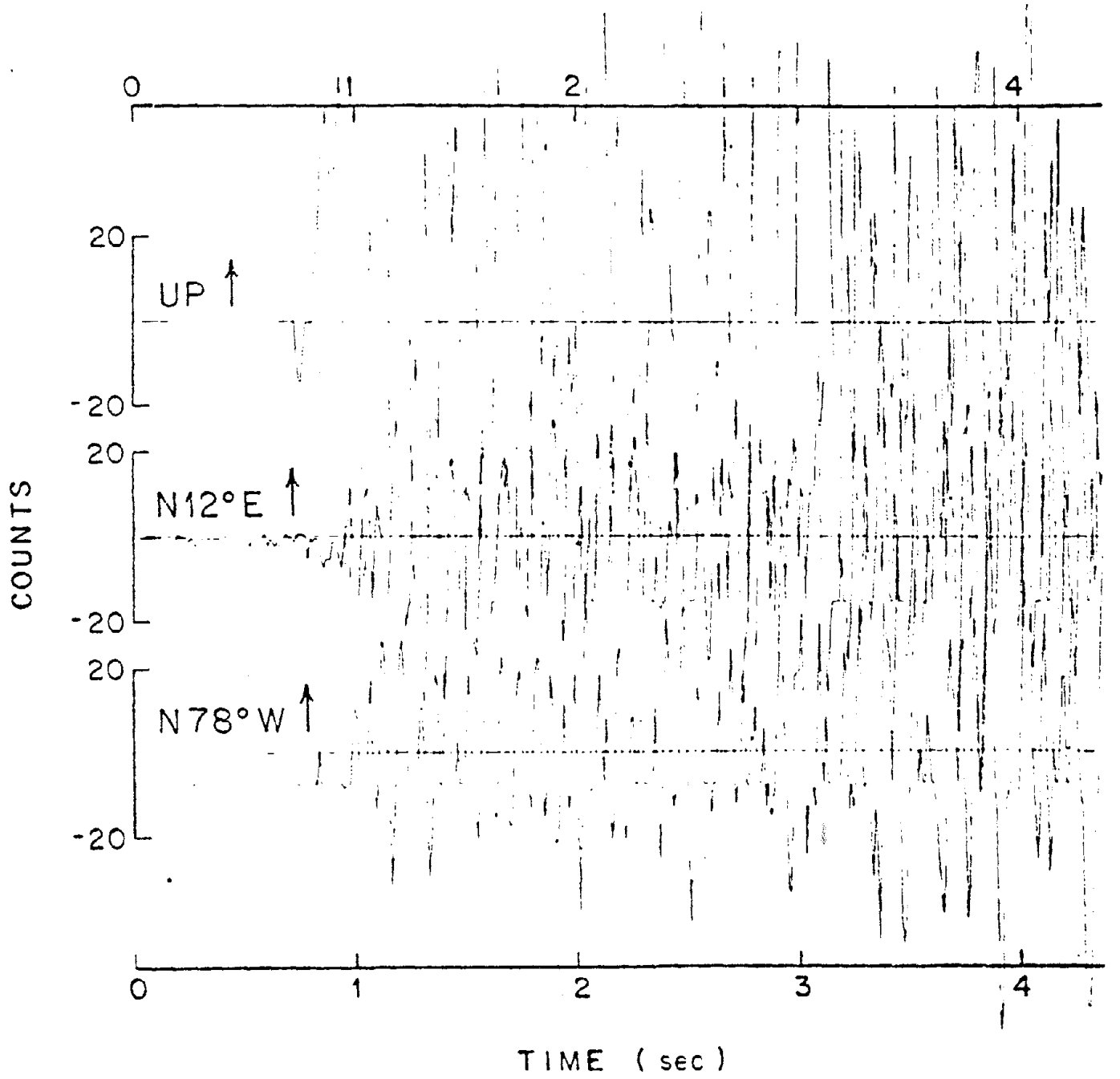
CHIHUAHUA
OCT 15, 1979 2316 GMT
IMPERIAL VALLEY, CALIF.
0
1
2
4
20
UP
-20
20
N12°E
-20
20
N78°W
-20
COUNTS
0
1
2
3
4
TIME (sec)

DELTA
OCT 15, 1979 2316 GMT
IMPERIAL VALLEY, CALIF.

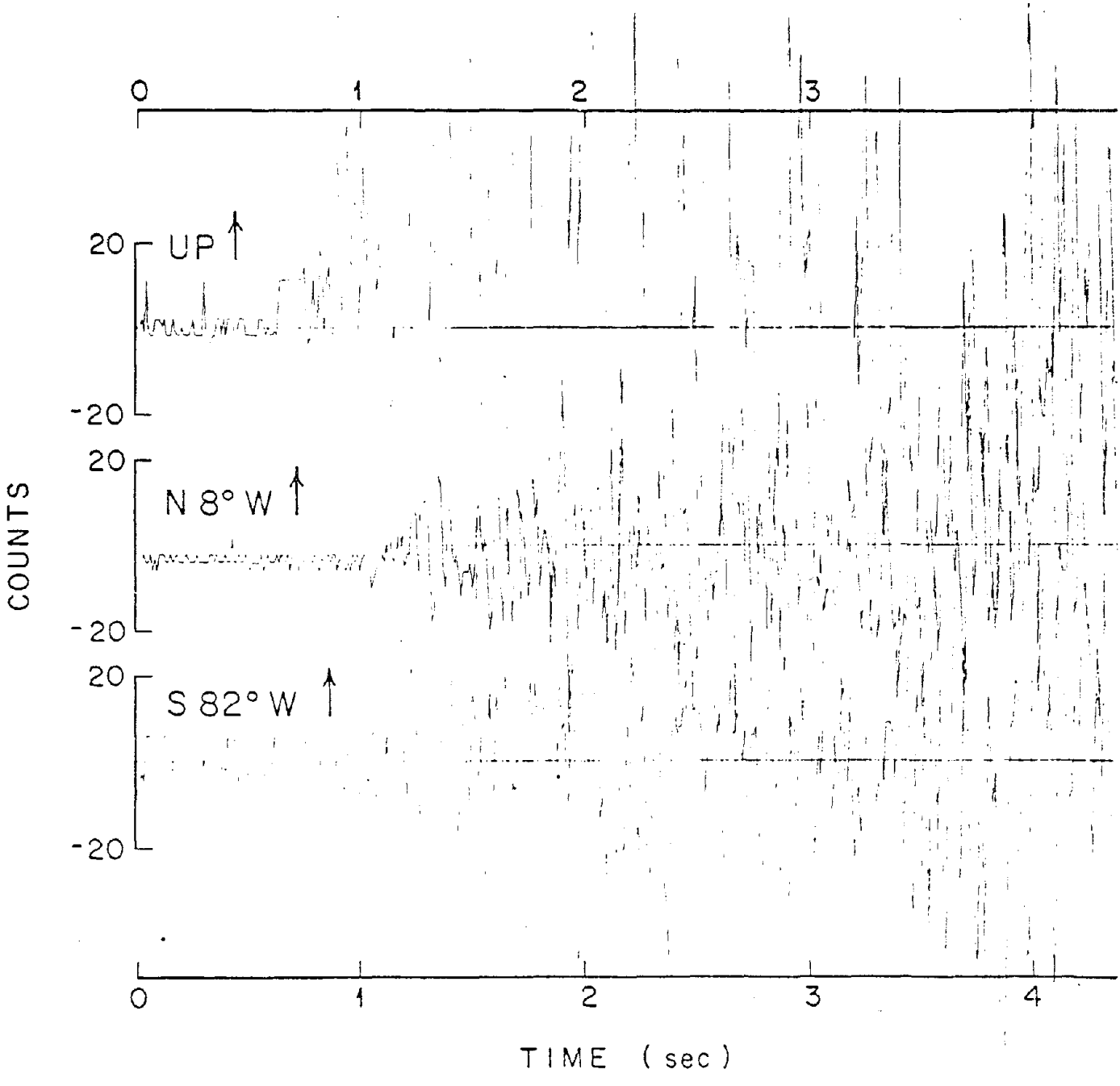

CUCAPAH
OCT 15, 1979 2316 GMT
IMPERIAL VALLEY, CALIF.

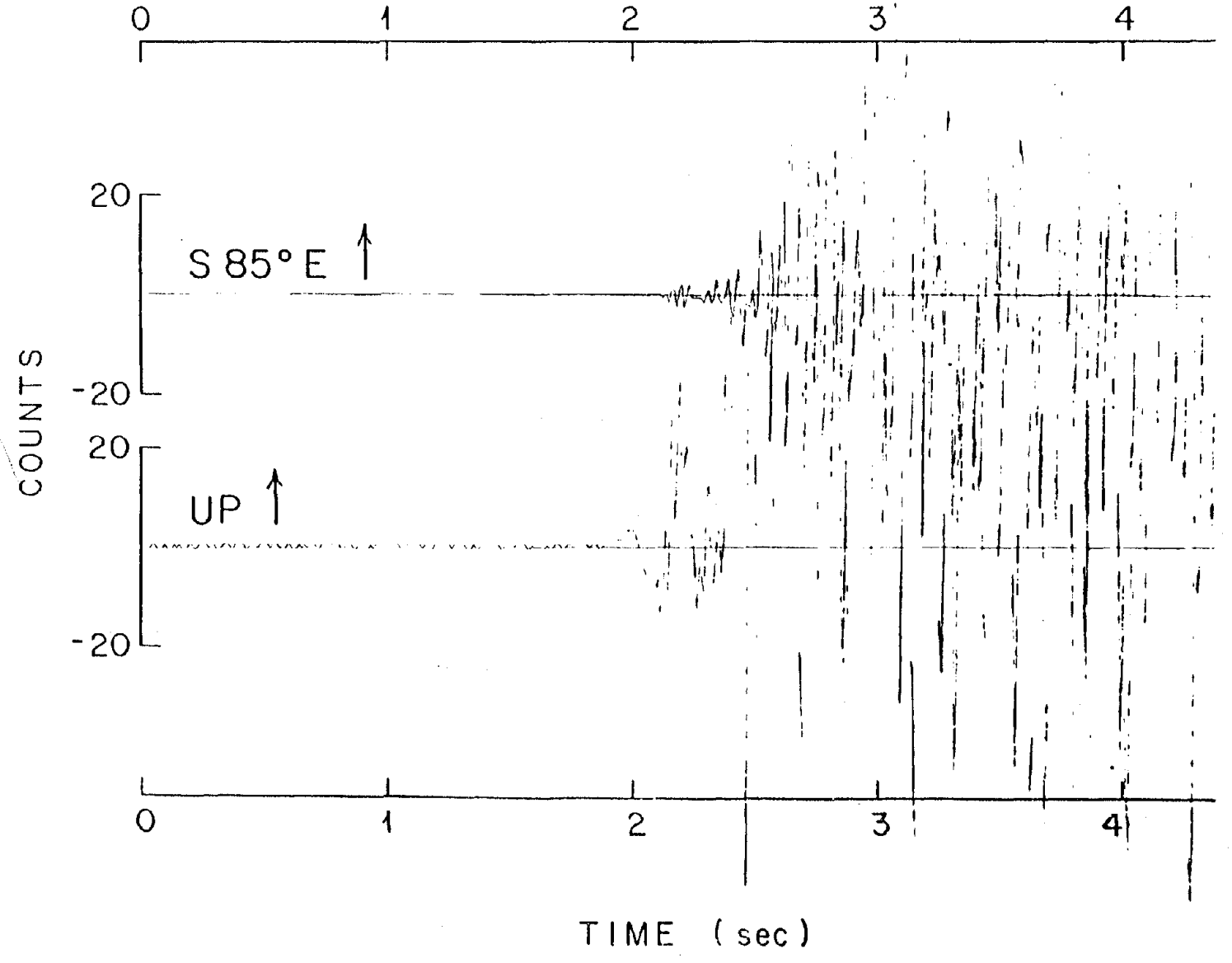

QUIET TRACE ACCELEROGRAMS

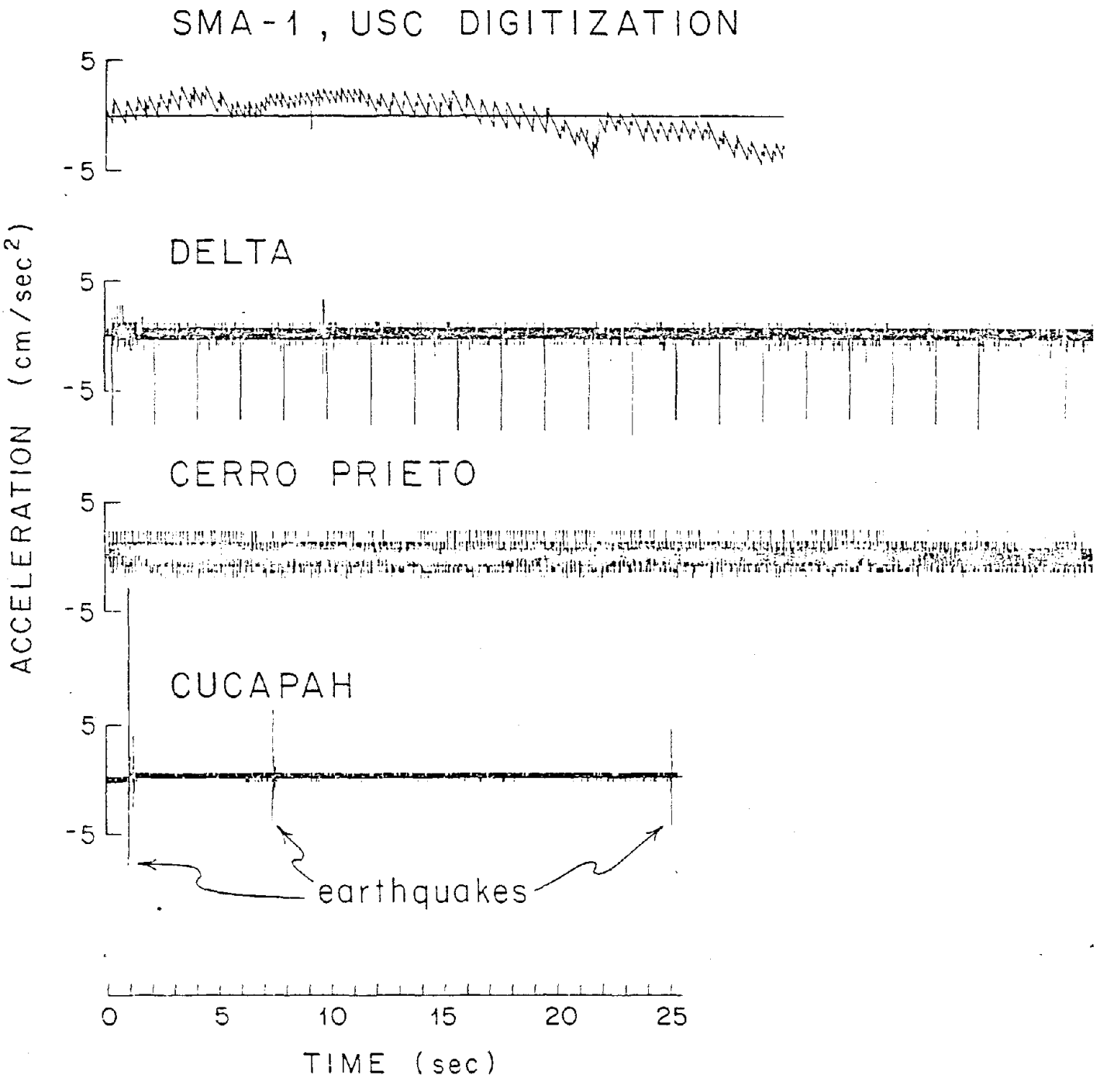

QUIET TRACE ACCELEROGRAMS

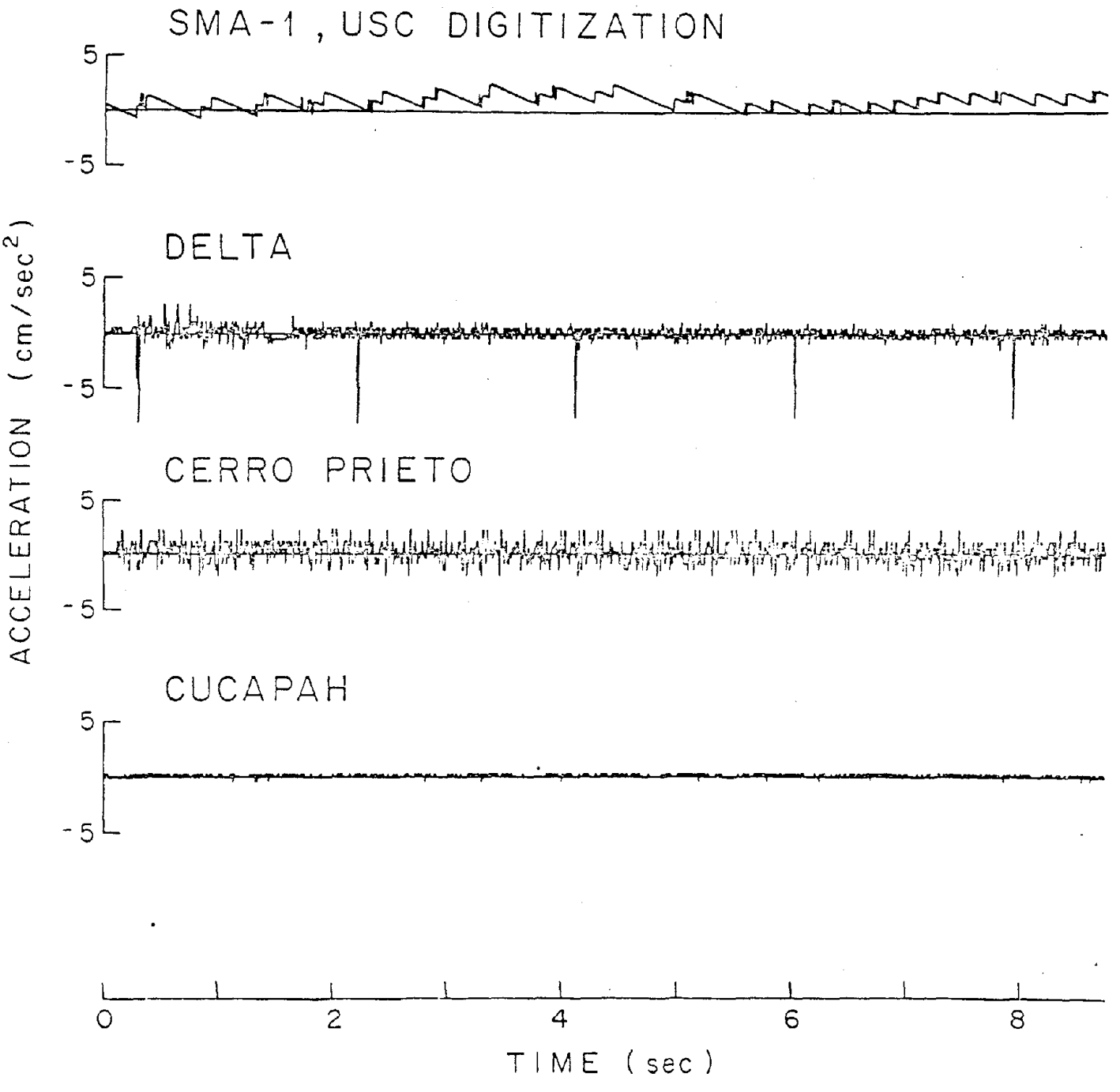

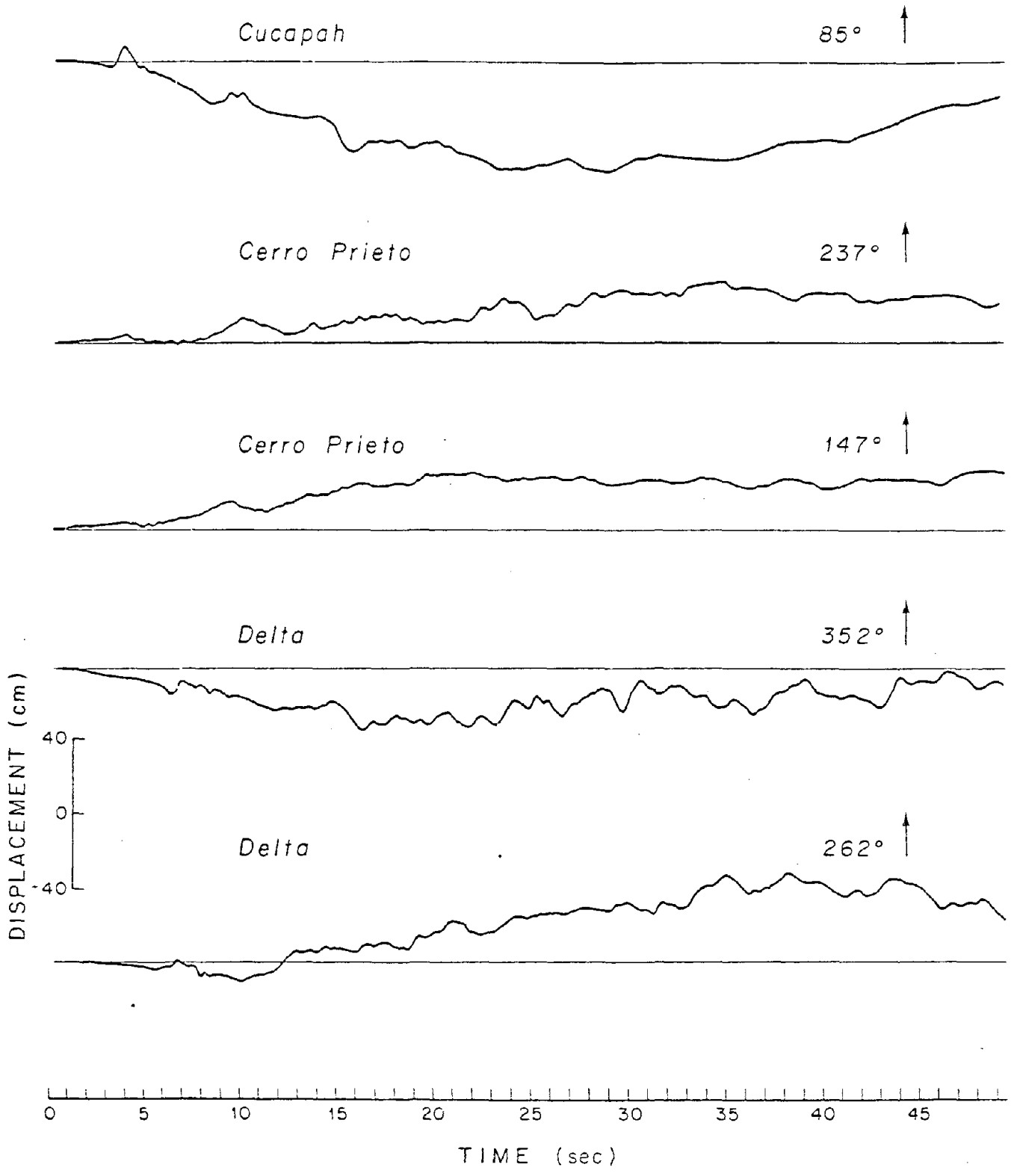
Cucapah
85°
Cerro Prieto
237°
Cerro Prieto
147°
Delta
352°
Delta
262°
DISPLACEMENT (cm)
40
0
-40
0
5
10
15
20
25
30
35
40
45
TIME (sec)

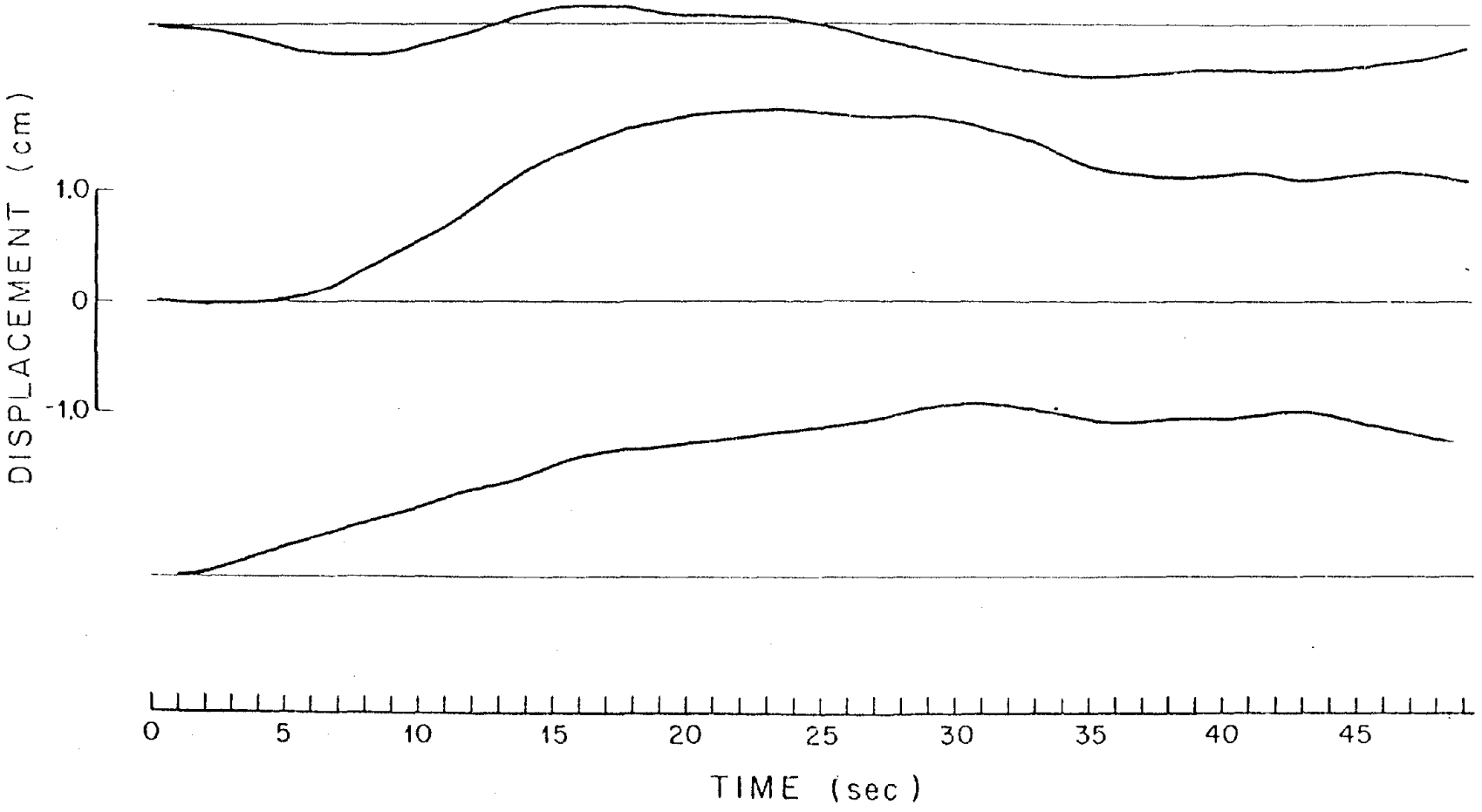
DISPLACEMENT (cm)
1.0
0
-1.0
0
5
10
15
20
25
30
35
40
45
TIME (sec)

APPENDIX VI

PARAMETRIC STUDY OF NEAR-FIELD GROUND MOTION FOR A STRIKE-SLIP DISLOCATION MODEL

By John G. Anderson and J. Enrique Luco

ABSTRACT

The near-field motion on the surface of a uniform half-space caused by the passage of the rupture on a vertical, strike-slip fault has been studied by the use of a dislocation model. The fault is modeled by an infinitely long buried dislocation of finite width; rupture propagates horizontally along this fault and past the observation points with a constant rupture velocity lower than the Rayleigh wave velocity. Peak amplitudes caused by the passing rupture front are primarily controlled by the depth of the top of the fault and the rupture velocity, when the slip on the fault and the rise time are held constant. A non-vertical rupture front distorts the pulse shape, but does not have an important effect on peak amplitudes.

One may interpret the motion caused by a finite fault, with constant rupture velocity and slip, rupturing past a site as consisting of a starting phase, a phase associated with the passage of the rupture event, and a stopping phase. The motions caused by the infinite-length fault dislocation model, considered in this paper, correspond to the rupture passage phase.

Institute of Geophysics and Planetary Physics, Scripps Institute of Oceanography, University of California, San Diego, La Jolla, California 92093 (J.G.A.).

Department of Applied Mechanics and Engineering Sciences, University of California, San Diego, La Jolla, California 92093 (J.G.A. and J.E.L.).

Compared with empirical correlations and observations in Imperial Valley, California, the model yields peak amplitudes of acceleration which are typically a factor of 6 too small. Effects caused by layered structure in the earth, which are absent from the dislocation model, are the most likely source of this discrepancy.

INTRODUCTION

Several kinematic models of extended faults are now available to generate synthetic strong ground motion near the fault. These models, which were reviewed by Luco and Anderson (1982), have yielded insight about the characteristics of strong ground motions and the faulting processes which generate these motions. The kinematic models have not yet, however, been fully applied to the study of some of the outstanding questions about the nature of strong motions in close proximity to the fault. Important questions which kinematic models might help to solve include the way in which amplitudes of strong motion behave near the fault, the sensitivity of strong ground motions to various dynamic parameters, and the estimation of strong motions in the near field of major earthquakes, for which observational data is scarce. Accomplishment of this latter goal must await future observational and earthquake modeling advances to determine correct values for the dynamic parameters which describe motion on the fault itself. However, the shapes of attenuation curves and the effects of dynamic parameters can be studied, at least at long periods, systematically and inexpensively with existing models.

Recently, the authors (Luco and Anderson, 1982) have presented a dislocation model which yields velocity on the surface of an elastic half space for an infinite-length, finite width fault. The fault is buried and does not intersect the surface. Rupture propagates with an inclined, rectilinear rupture front along the length of the fault, from $-\infty$ to ∞, at a velocity less than the Rayleigh wave velocity. Such dislocations may be a reasonable approximation to the fault displacements which generate the strong ground

motions near a long fault, except at its ends. Thus the model might apply to sites adjacent to the ruptured section of a strike-slip fault, but removed from the epicenter, in earthquakes with rupture lengths of tens to hundreds of kilometers (such as California or Turkey), sites above subduction zones which are prone to long rupture lengths (such as in Alaska or Chile), or any other site likely to be near a causative fault in which the ratio of the rupture length to width is large.

In more general terms and for the intermediate frequency range in which spatial variations of slip and rupture velocity can be ignored it is possible to think of the total motion in the vicinity of a finite fault as resulting from a starting phase, a phase associated with passage of the rupture front and a stopping phase. To a first approximation, the contribution of the passage of the rupture front to the total motion is independent of the length of the fault and corresponds to the steady-state solution for an infinitely long fault as in the model previously considered by the authors (1982). We note that the radiation patterns of the starting and stopping phases are such that some components of the motion associated with these phases nearly vanish in the vicinity of the fault and, consequently, in these components the contribution of the phase associated with passage of the rupture front is dominant. In particular, this situation occurs in the vicinity of a vertical strike-slip fault in which the parallel and vertical components of motion associated with the starting and stopping phases are practically zero close to the fault (refer to Fig. 13 and its discussion in the text). Independently of whether the pulse associated with passage of the rupture front represents a dominant contribution or not, a detailed study of this pulse seems warranted. In addition to providing information about one of the com-

ponents of the total strong ground motion in the near source region, such a study may create the basis for isolating this pulse from available near-source records with the possibility of obtaining additional source information such as rupture velocity, average slip and fault thickness.

The steady-state dislocation model of the authors (1982) provides a good opportunity for a systematic parametric study of the pulse associated with passage of the rupture front. Studies based on previous dislocation models have considered the effects of source type and site location (e.g. Haskell, 1969; Haskell and Thomson, 1972; Thomson and Haskell, 1972) as well as rupture velocity (e.g. Boore et al, 1971; Boore and Zoback, 1974; Levy and Mal, 1977) on ground motion. Numerous other studies, oriented toward matching observed ground motions in specific earthquakes, have illustrated the effects of variations of some of the faulting parameters. The Luco and Anderson (1982) model is sufficiently complex to include some faulting phenomena typically not covered by some of the earlier models while retaining enough simplicitiy that its full range of parameters can be both grasped and explored with a limited computer budget.

The synthetic motions generated by the Luco and Anderson model for a number of particular choices of faulting parameters are studied in this paper. These particular models all correspond to strike-slip motion on a vertical fault; within this constraint the other parameters are varied extensively. The extension to oblique-slip and dip-slip motion and to faults with an arbitrary dip will be presented in a subsequent paper (Anderson and Luco, 1982). One of the limitations of the model with respect

to actual long faults in the earth is the absence of layering. Because of the effects introduced by layering we do not expect that the amplitudes calculated will be realistic. However, the trends obtained in the study should be of value in assessing the importance of the various parameters. In addition to the detailed parametric study and with the objective of estimating the effects of layering and other source characteristics not included in the model, we have compared the peak amplitudes of synthetic motion with average peak accelerations and velocities predicted by regression of strong motion data (Joyner et al, 1981). Finally, some of the synthetic accelerations and velocities are compared with observations from the October 15, 1979 Imperial Valley earthquake.

DESCRIPTION OF THE DISLOCATION MODEL

The fault model considered in the parametric study is illustrated in Fig. 1. It corresponds to an infinitely long fault of finite width buried in an elastic half-space. The rupture is modelled by a uniform shear dislocation which propagates from $-\infty$ to ∞ with a uniform horizontal rupture velocity c_1. The rupture front is assumed to be rectilinear and, in general, it may be inclined. The inclination of the rupture front is controlled by the ratio of the horizontal rupture velocity c_1 to the rupture velocity in the dip direction c_2. The parametric study described herein is limited to the case of vertical strike-slip faults, as shown in Fig. 1, and to ruptures in which the velocity c_1 is lower than the Rayleigh wave velocity in the medium. Except where indicated, the slip function considered corresponds to a step dislocation of amplitude Δ_o.

The numerical results presented below have been obtained using the analytical solution derived by the authors (Luco and Anderson, 1982) in which the velocity on the surface of the half-space for a step dislocation is given in terms of a simple finite integral. The solution corresponds to a steady state in which the response is invariant for an observer moving parallel to the fault with a speed equal to the rupture velocity c_1. For an observer at $x = 0$, the time $t = 0$ corresponds to the time of passage of the rupture in front of the observation point.

Velocities on the surface of the half-space were calculated at a step of 0.1 sec for 20 sec long synthetics and 0.2 sec for longer synthetics. Acceleration and displacement pulses were obtained by numerical differentia-

tion and integration of the velocity pulses, respectively. In some cases, smaller time steps had to be used to obtain stable acceleration values. With one exception, we have used $\alpha = \sqrt{3}\ \beta = 6.0$ km/sec for the calculations in this paper. In this case, corresponding to a Poisson's ratio of 0.25, the Rayleigh wave velocity is $c_R = \beta\left[2 - 2/\sqrt{3}\right]^{1/2}$ (Ewing et al, 1957, p. 33). Thus $\beta \cong 3.4641$ km/sec and $c_R \cong 3.1849$ km/sec.

179

PROPERTIES OF THE SOLUTION FOR VERTICAL STRIKE-SLIP FAULTING

Characteristics of the acceleration, velocity and displacement pulses as a function of distance to the fault. Figures 2, 3 and 4 show, respectively, synthetic acceleration, velocity and displacement pulses at various distances y from a vertical, strike-slip fault characterized by z_u = 2 km and z_d = 10 km. The slip on the fault corresponds to a step dislocation of amplitude Δ_o = 100 cm propagating with rupture velocities c_1 = 3.184 km/sec and $c_2 = \infty$. For y = 0, the x- and z- components are nodal, and, consequently, the y-component is dominant for small values of y. The peak amplitudes occur at a horizontal distance of about 2 km which corresponds to the depth of the top of the fault. Figs. 2 and 3 indicate that the duration of the acceleration and velocity pulses increases with distance, the effect being most prominent for the y-component of motion. As noted by Luco and Anderson (1982) the synthetic velocity and acceleration pulses are symmetric or anti-symmetric with respect to t = 0 for this case in which the rupture front is vertical ($c_2 = \infty$).

As shown in Fig. 4, the static values of the y- and z-components of displacement are zero, while the x-component shows a significant permanent offset. The calculated static offsets obtained by integration over a 20 sec time window have been compared with those resulting from exact static two-dimensional solutions with excellent agreement for stations at distances shorter than 20 km (Luco and Anderson, 1982). As observed by other authors, the perpendicular component of displacement u_y is the most prominent in the near-field. Finally, we note that, in this case ($c_2 = \infty$), the y and z displacement components are symmetric with respect to t = 0.

Niazi (1973) has previously noted near-symmetry in numerical results for a finite-length, two-dimensional fault model with rupture velocity much lower than the shear-wave velocity, and Aki and Richards (1980, p. 859) have observed that the displacement is symmetric when an anti-plane, two-dimensional dislocation propagates past the observer.

Variation of peak amplitudes with distance to the fault and position of the fault. The distributions of peak acceleration, velocity and displacement versus distance to the fault are shown in Fig. 5 for three fault models. The upper (solid) curves correspond to a vertical, strike-slip fault of width W = 8 km located between the depths z_u = 1 km and z_d = 9 km. The intermediate (dash) curves correspond to a fault of width W = 8 km located between the depths z_u = 2 km and z_d = 10 km. Both of these models are characterized by a slip Δ_o = 100 cm. The lower (dash-dot) curves are for a fault of width W = 16 km located between the depths z_u = 2 km and z_d = 18 km with a slip of amplitude Δ_o = 50 cm. All three models are characterized by the same seismic moment per unit length of fault and by rupture velocities c_1 = 3.0 km/sec (c_1 = 0.94 c_R) and c_2 = ∞.

Inspection of Fig. 5 reveals that the largest peak amplitudes occur at a distance comparable to the depth of the top of the fault, z_u. Furthermore, as z_u increases, the peak amplitudes decrease. For $y < z_u$ the peak values of $\ddot{u}_y$ are approximately proportional to z_u^{-2}, while the peak values of $\dot{u}_y$ are approximately proportional to z_u^{-1}. The additional factor of z_u^{-1} in $\ddot{u}_y$ arises because the velocity pulse width decreases as z_u. For $y < z_u$, the location of the bottom of the fault has little effect on peak amplitudes as

evidenced by the uniform factor of 2 difference between the results for z_u = 2 km, z_d = 10 km, Δ_o = 100 cm and z_u = 2 km, z_d = 18 km and Δ_o = 50 cm. For larger values of y (y > 10 km) all three fault models lead to similar peak amplitudes.

Effects of rupture velocities on pulse shapes and peak amplitudes. The amplitudes of synthetic ground motion are sensitive to the value of the rupture velocity as emphasized by Boore et al (1971) and Boore and Zoback (1974). Fig. 6 illustrates the effect of the horizontal rupture velocity c_1 on the amplitude and shape of the synthetic velocity for an observer at a distance of 10 km from a vertical, strike-slip fault characterized by z_u = 2 km, z_d = 10 km and $c_2 = \infty$. The variation of the peak acceleration, velocity and displacement with c_1/c_R is shown in Fig. 7 for the same fault model and observer position. Peak accelerations and peak velocities exhibit large amplifications as the horizontal rupture velocity, c_1, approaches the Rayleigh wave velocity in the medium, c_R. The effects are stronger on the x- and z-components which for $c_1 \approx c_R$ are dominated by P, SV and Rayleigh waves while the y-component is controlled by SH waves. Peak displacements are the least sensitive to rupture velocity. In particular, the peak displacement in the x-component corresponds to the static displacement and, consequently, is independent of the rupture velocity in the dislocation model.

The effects of horizontal rupture velocity c_1 on the distribution of peak velocity versus distance to the fault are illustrated in Fig. 8. In addition to the increase in amplitude as c_1 approaches c_R the results shown in Fig. 8 indicate a marked change in the rate of attenuation of the x- and z-components with distance while

the rate of attenuation of the y-component remains essentially unchanged. As c_1 approaches c_R the x- and z-components show a significantly lower attenuation with distance than for lower values of the rupture velocity c_1. This observation combined with the increase in amplitude in the x- and z-components as c_1 tends to c_R suggests the presence of a Rayleigh wave contribution to u_x and u_z for $c_1 \approx c_R$. We have not investigated the effect of changes in Poisson's ratio on the amplitudes of ground motion obtained by use of our model. Boore et al (1971) found that for their two-dimensional model and for a fixed value of c_1/β, amplitudes increased as β/α increased.

The numerical results presented this far have been based on the assumption that $c_2 = \infty$, implying that the rupture fronts are vertical. Next, we examine the effects of non-vertical rupture fronts on pulse shapes and peak amplitudes. Fig. 9 shows synthetic velocity pulses at a distance from the fault of 2 km for two rupture models : the results on the left corresponds to a rupture which initiates at the bottom (z_d = 10 km) of the fault and then propagates upward and to the right with velocities of 2.5 and 3.0 km/sec, respectively; the results on the right correspond to a rupture which initiates at the top (z_u = 2 km) of the fault and then propagates downward and to the right with velocities of 2.5 and 3.0 km/sec, respectively. For finite values of c_2, i.e. for inclined rupture fronts, the pulse shapes are no longer symmetric or anti-symmetric with respect to t = 0. However, there is a surprising time-reversal symmetry between the two sets of results shown in Fig. 9. Except for the sign of motion, the synthetics for one case can be obtained from those of the other case by reversing time.

The effects of the vertical rupture velocity c_2 on the synthetic velocities for an observer at a distance of 10 km from the fault are illustrated in Fig. 10. The fault model is characterized by z_u = 2 km, z_d = 10 km, c_1 = 3.0 km/sec and Δ_0 = 100 cm. In this figure it is possible to see the evolution from the case $c_2 = \infty$, where the synthetics are symmetric or anti-

symmetric about t = 0, to cases where the asymmetry is more pronounced. The results shown in Fig. 10 indicate that the peak velocities at a distance of 10 km are not strongly affected by the value of c_2. The variation of peak velocities with vertical rupture velocity c_2 is shown in Fig. 11 for observers at distances of 2 and 10 km. The effects of c_2 on peak velocities appear to be somewhat stronger at shorter distances to the fault but are considerably less pronounced than the effects of the horizontal rupture velocity c_1.

Effect of rise time on acceleration pulses. All of the models considered so far assume a slip function in the form of a step. To study the effects of a finite rise time on pulse shapes and peak amplitudes we consider slip functions corresponding to ramps of finite duration, τ. The response for any prescribed slip function can be obtained by appropriate convolution with the synthetics already described for a step slip function. We note, however, that the acceleration response for an infinite ramp characterized by slip velocity $\dot{\Delta}_o$ corresponds to the velocity response for a step function of amplitude Δ_o after substitution of Δ_o by $\dot{\Delta}_o$. Thus, the velocities (in cm/sec) shown in Fig. 3 for a step dislocation of amplitude Δ_o = 100 cm can be interpreted as accelerations (in cm/sec^2) for an infinite ramp dislocation with slip velocity $\dot{\Delta}_o$ = 100 cm/sec.

Synthetic accelerograms at a station located at a distance y = 2 km from the fault for slip functions corresponding to a suite of finite ramps with various rise times, τ, are shown in Fig. 12. In these calculations, the slip velocity $\dot{\Delta}_o$ has been assumed to be constant and equal to 100 cm/sec. The rupture is characterized by z_u = 2 km, z_d = 10 km, c_1 = 3.0 km/sec and $c_2 = \infty$. The results presented in Fig. 12 indicate that for short rise times

(τ < 0.4 sec) the acceleration pulse shapes are essentially the same as those obtained for a step dislocation as shown in Fig. 2. In this case, the amplitudes scale with the final slip $\Delta_o = \dot{\Delta}_o \tau$. For rise times longer than 2 sec the peak amplitudes become essentially independent of the value of the rise time and depend only on the slip velocity. For long rise times, the synthetic accelerations separate into two pulses corresponding to the initiation and termination of rupture at a point. As discussed above, each one of these pulses has the same form as the velocity pulses shown in Fig. 3 for a step dislocation. In general, the peak accelerations for any finite rise time and for a given slip velocity are lower than twice the peak acceleration for the separated rupture initiation pulse. For intermediate values of the rise time (0.5 sec < τ < 2.0 sec) the peak accelerations are almost twice the limiting value corresponding to the separated rupture initiation pulse for long rise times but are considerably lower than the corresponding peak accelerations for a step dislocation with the same final slip. Comparison of the results in Fig. 12, for τ = 1 sec, with those shown in Fig. 5 reveals that the peak accelerations for the finite ramp are between 0.43 and 0.50 of the values for a step dislocation of equal final slip (100 cm). The corresponding ratios for peak velocities are 0.59 to 0.78, and, for displacement 0.75 to 1.0. As expected, the reductions with respect to the results for a step dislocation are the greatest for peak accelerations which are more sensitive to the high frequency differences between the finite ramp and the step slip functions.

COMPARISON WITH FINITE-LENGTH FAULT MODELS

To illustrate the relationship between the ground motion generated by faults of finite length and the motion calculated on the basis of our infinite length model we have made some comparisons with results obtained by the use of Haskell's model for faults of various length. The results, shown in Fig. 13, were calculated as in Anderson and Richards (1975) and verified by a program based on the formulation given by Boatwright and Boore (1975). In Fig. 13, velocities at a station located at mid-length of a finite fault in a unbounded medium are compared with velocities from our model for an infinite length fault in a half-space. The Haskell model was used because comparable calculations for velocities from a long finite fault in a half space are much more expensive. These calculations are for a site at a distance of $y = 2$ km perpendicular to a fault extending from $z = 2$ km to $z = 10$ km.

Figure 13 shows velocity from finite faults of half-length equal to 6 km, 18 km, 42 km, and 78 km. As an example on the finite fault with half-length of 18 km, rupture initiates at $x = -18$ km, propagates past the observation point at $x = 0$, and then continues on, finally stopping at $x = 18$ km. We note, however, that the contribution to the synthetics from those parts of the fault with x beyond 11.9 km would fall outside the time window shown in fig. 13. Furthermore, because of directivity, the velocities caused by motion on the fault at $x > 0$ are small compared to the velocities caused by motion at $x < 0$.

Based on Fig. 13, we interpret the ground motion caused by a finite fault propagating past a site as consisting of three phases: a starting phase, a rupture passage phase, and a stopping phase. The rupture passage phase is what is considered by the steady-state dislocation model which we have studied in this paper; the starting and stopping phases are contributed by fault finiteness.

The parallel(x) and vertical (z) components of velocity may be considered together on Fig. 13. For these components, the starting phase is nodal on the plane of the fault; therefore motions close to even a short fault are similar to the assymptotic limits for an infinite-length fault. The synthetic $\dot{u}_z$ for a fault with an 18 km half-length is very similar to the synthetic $\dot{u}_z$ for a fault with a 78 km half-length. On the $\dot{u}_x$ component, the synthetic velocity pulse essentially achieves its final form for half-lengths of between 18 km and 42 km. We note also that the peak x- and z- components of velocity from the finite fault change by less than a factor of 2 as the fault length approaches infinity. Differences between the 78 km fault in the infinite space and the infinite-length fault in the half space arise because the interaction of P and SV waves with the free surface is neglected in the Haskell model.

On the y- component, the starting phase is not nodal, and the finite fault must be much longer before the velocity approaches the shape associated with the assymptotic limit of an infinite -length fault. For faults with half-length of 6 km and 18 km, the starting phase and the rupture passage phase are unseparated. For a half-length of between 18 km and 42 km, the

starting phase and rupture passage phase begin to separate, and for a half-length of 78 km, these phases are well separated in time. The rupture passage phase for the finite fault in a full-space closely resembles the pulse on the infinite fault in a half-space because the pulse is composed largely of SH-waves. The largest peak velocities on $\dot{u}_y$ develop for faults with half lengths of 15 to 24 km, and are about 3.5 times as large as the isolated rupture passage phase.

Calculations for a lower rupture velocity of 2.5 km/sec (0.72β) revealed that the separation of the starting and rupture passage phases began to occur for faults of half-length between 10 km and 20 km. The relative importance of the starting phase and the rupture passage phase was not significantly altered from that shown in Fig. 13. However, for the $\dot{u}_y$ pulse generated by a Haskel model with rupture velocity of 2.5 km/sec, half length of 40 km and width of 8 km, the ratio of the amplitude of the rupture passage phase to the starting phase increases from 0.4 to 1.3 as the depth of the top of the fault with respect to the observer decreases from 2 km to 0 km.
We note that the starting phase associated with a finite Haskell-type fault may be stronger than starting phases in the earth. In the earth, the starting phase originates from a point, rather than a line. Furthermore, the rupture velocity may not instantaneously achieve the final value.

In summary, the rupture passage phase which we have studied may be the dominant part of the x- and z- components of velocity, and also an important part of the y- component of velocity close to finite faults of moderate length.

COMPARISON WITH STRONG GROUND MOTION DATA

To assess the importance of the source and propagation medium characteristics not included in our steady-state disclocation model (starting and stopping phases, spatial variation of slip and rupture velocity, and layering) we have compared the results of the model with actual ground motion data. The comparative study included: calculation of synthetic values of M_L and comparison with the appropriate value of M_L for the assigned seismic moment per unit length of the model, comparison of synthetic peak amplitudes with average peak amplitudes from correlations, and comparison of filtered synthetic accelerograms with filtered data from the Imperial Valley earthquake of October, 1979.

Evaluation of M_L from synthetic accelerograms . The moment per unit length of (M_o/L) for all of the calculations in this paper except those in Fig. 12 is 2.6×10^{24} dyne-cm/km: this value is roughly consistent with values of M_o/L for California strike slip earthquakes in the 6-3/4 to 7 magnitude range. For example, M = 6-3/4 can be associated with $M_o \approx 1.3 \times 10^{26}$ dyne-cm and $L \approx 60$ km which gives moment per unit length of 2.2×10^{24} dyne-cm/km. For these large fault lengths, our model, for distances to the fault in the range from 0 to 20 km may be relevant to prediction of long period components of strong ground motion near the fault, but away from the ends.

We calculated M_L from the synthetics, after the procedure of Kanamori and Jennings (1978), to determine if our simple model gives the proper amplitude and attenuation of synthetic Wood-Anderson seismograph response

with distance. We found that M_L has very different values when estimated from the parallel and perpendicular components of the synthetic accelerograms. Furthermore, M_L depends strongly on the propagation velocity. For c_1 = 3.0 km/sec, M_L peaks at a value of 5.8 at a distance comparable to the top of the fault (z_u = 2km); for c_1 = 3.184 km/sec, M_L from the largest component is approximately constant out to 20 km and ranges between 6.0 to 6.2. These values of M_L are considerably smaller than the values of 6-3/4 to 7 which would be expected for an actual California earthquake of comparable slip, and imply synthetic Wood-Anderson instrument responses 3 to 10 times smaller than expected.

Comparison with regresssion results. Fig. 14(a) shows a comparison of peak accelerations obtained by Joyner, Boore, and Porcella (1981) by regression from existing strong motion accelerograms. Fig. 14(b) compares our calculated peak velocities with regression results. Peak values from our model are too small. Based on the results which have been shown earlier, one could manipulate the faulting parameters somewhat to improve the agreement. For example, by choosing the depth to the top of the fault equal to 1.0 km and using a rupture velocity c_1 = 3.184 km/sec, one could achieve peak accelerations of about 800 cm/sec^2 at $y \lesssim 1$ km, and peak velocities of about 50 cm/sec.

Comparisons with acceleration recordings from the 1979 Imperial Valley Earthquake. The October 15, 1979 Imperial Valley earthquake (M_W = 6.5) was recorded on over 30 strong motion accelerographs, including a linear array of stations (stations 1 to 13) which is perpendicular to the causative Imperial Fault. For a map showing the station locations, as well as the digitized accelerograms, the reader is referred to Brady

et al (1980). The epicenter was located about 24 km southeast of where this array crosses the fault, and surface displacements appeared between stations 6 and 7, implying that rupture propagated toward the northeast, and toward these stations. Observed surface rupture terminates about 10 km northwest of the array, but intense aftershock activity north of the array could be responsible for part of the northern-most surface expression. Because several of the stations in the transverse array are close to the surface expression of the faulting, we infer that the geometry is favorable for comparison with our model.

Fig. 15 illustrates the transverse component of velocity obtained at accelerograph stations 6 and 7, and a synthetic pulse generated by our model for a site at y = 1.0 km. Stations 6 and 7 are each about 1 km from the fault trace, on opposite sides of the fault. The observed motions at stations 6 and 7 differ at high frequencies as shown in Fig. 15. The rise time (τ = 1.5 sec) on the synthetic fault was selected to duplicate the time interval between the positive and negative peak of the observations. We note that this value of rise time is consistent with the conclusion reached by Day (1982) that estimates for the rise time in long faults are given by $\tau = W/2c_1$ or $\tau = W/2\beta$. For the model used, the first estimate is τ = 0.5 x 9 km/2.0 km/sec = 2.25 sec and the second is τ = 0.5 x 9/2.89 = 1.6 sec. Also, Hartzell and Helmberger (1982) used a rise time of 1.0 sec in their modelling study of the Imperial Valley earthquake. The synthetic velocity is about a factor of 15 too small in amplitude, and also lacks the high-frequency energy which is evident in the observations. A greater rupture velocity would significantly decrease, but not eliminate, the amplitude discrepancy.

Fig. 16 shows a comparison of the attenuation with distance from the fault of the peak acceluations from low-pass filtered accelerograms and low-pass filtered synthetics. Record sections which include the direct S-wave pulse were selected and filtered for this purpose. The filter is symmetric, has a corner frequency of 0.5 Hz and the Fourier amplitude spectrum decreases at a rate of f^{-5} at frequencies above this corner. The filtered accelerograms are shown in Fig. 17.

On Fig. 16 the value of y assigned to each station was measured from a linear approximation of the fault trace. Stations beyond either end of the ruptured fault section were not included. We note that the synthetic accelerograms, whose peak values after filtering appear on Fig. 16, are derived for 100 cm fault slip with a step time function. This value of slip appears to be reasonable. The teleseismic moment of 6×10^{25} dyne-cm (Kanamori and Regan, 1981) implies an average offset of about 60 cm on a fault plane 35 km long by 9 km wide. Olson (1982) obtains a moment of 9×10^{25} dyne-cm from inversion of accelerograph data; this would imply an average slip of about 95 cm on the same fault plane. The comparison in Fig. 16 also reveals that the synthetics underestimate the peak amplitudes of the filtered recording, in this case by a factor of 5 to 8.

We have noted the symmetry of the synthetic accelerograms about the time rupture propagates past the observation point. Since several of the accelerograms in Fig. 17 are timed, we used the timing of the peak of the filtered pulses ($\ddot{u}_y$) to estimate the average rupture velocity. The results are given in Table 1. The stations which are closest to the fault ($y \leq 6$km) all give a rupture velocity of 1.80 to 1.95 km/sec based

on this analysis. This value is smaller than estimates of about 2.5 km/sec obtained by Harzell and Helmberger (1982) and much smaller than the estimate 3.3 to 5.0 km/sec of Olson (1982). We observe that if one considers a finite rise time τ, the rupture front arrives at a time $\tau/2$ before the peak, so that Δt in Table 1 would be decreased. Furthermore, if the rupture front is not vertical, the peak corresponds to the time the top of the fault passes the stations (e.g. Figs. 9 and 10). Thus differences between results in Table 1 and the inversion study of Hartzel and Helmberger (1980) may be reconcilable.

Discussion of amplitude comparisons. The previous comparisons indicate that the steady-state dislocation model in a uniform half-space underpredicts observed peak velocities and accelerations. On Fig. 14a, model estimates of peak accelerations are a factor of 2 to 8 too small at distances less than 2 km. The model with c_1 = 3.184 km/sec = 0.9997 C_R is a factor of 3 too small. On Fig. 14b, model estimates for peak velocities are a factor of 4 to 6 too small to distances of 20 km; in this case the model with c_1 = 3.184 km/sec has an attenuation rate which is too slow. On Fig. 16 model predictions for filtered peak perpendicular accelerations are a factor of 5 to 8 too small. The corresponding ratio on the parallel component depends on distance. However, an intermediate rupture velocity (say $c_1 \approx 3.1$ km/sec) would possibly match the observed attenuation with distance at a level which is also a factor of 5 or 6 too small. We conclude that overall, this model underestimates peak velocities and accelerations by a factor which depends on rupture velocity, and that for rupture velocities which yield shapes of attenuation curves comparable to observations, that factor is about 6.

We can identify a number of phenomena in the earthquake which are absent from our model, and which might help account for this overall difference of a factor of 6. Perhaps the most significant are: (i) finiteness of the fault and associated starting and stopping phases; (ii) asperities on the fault and associated possible spatial variations of slip and rupture velocity, and (iii) layering and the possibility of transonic or supersonic rupture in the shallower earth layers.

The comparisons shown in Fig. 13 of the results for an infinite length

model with those for a finite rectangular fault indicate that the amplitudes of the starting and stopping phases are not sufficiently different from the amplitudes of the rupture passage pulse to explain the difference observed. It must be considered also that the starting phase in a Haskell model may be larger than on an actual fault in which the rupture may have to accelerate to the final rupture velocity (Kiusalaas and Mura, 1964).

Small scale asperities also would tend to increase the amplitudes of acceleration and velocity by introducing a greater amount of high frequency energy. This is accomplished essentially by introducing starting and stopping phases from small sources distributed throughout the fault plane. We note, however that when the Imperial Valley accelerograms were filtered, this did not decrease the discrepancy between these data and the synthetic calculations. We conclude that asperities are not the major source of the differences between the results of the dislocation model and the observations.

Finally, we turn our attention to the effects of layering. Bouchon (1979) examined sythetic displacements for the case of a single layer over a half space, as a simulation of ground motion at station 2 for the Parkfield, Ca., June 1966 earthquake. He found that the upper layer, with thickness of 1.5 km and P- and S- velocities at about 45% of the velocities in the underlying half space, caused the perpendicular (u_y) component of displacement to be amplified by a factor of 8, while the parallel and vertical components were amplified by a factor of 2 compared to results for a uniform half-space. Alternative layered models could cause amplifications greater than 2 relative to the half space. The large amplification of the perpendicualr component was caused by a shock wave generated by a rupture velocity which exceeded the shear velocity in the layer. A

transonic rupture velocity is also suggested in the solution of Olson (1982) for the Imperial Valley earthquake mechanism. The results of Bouchon suggest that the major cause of the amplitude discrepancy between the results of our model and the observations can be ascribed to the effects of layering. As noted by Bouchon (1979) we observe that previous uniform full-space or half-space models for the Parkfield 1966 earthquake [Aki (1968), Haskell (1969), Trifunac and Udwadia (1974), Anderson (1974), Kawazaki (1975) and Levy and Mal (1976)] have significantly overstimated the slip required to match the perpendicular displacement pulse observed at station 2. The uniform medium models which lead to reasonable estimates for the slip require the assumption that the fault intersects the free-surface.

Based on the previous discussion we conclude that the steady-state dislocation model studied after modification to include the effects of layering could provide a useful tool in estimating near source ground-motion. Although the extension to layered media will increase the computational cost, the model would be significantly more economical than models for finite faults in layered media.

SUMMARY

The effects of several parameters on surface motions at sites adjacent to an infinitely long, finite-width, strike-slip fault in a uniform half space have been examined thoroughly. The study verifies the importance of the horizontal rupture velocity in determining amplitudes of ground motion. In the model, a non-vertical rupture front is not an important factor in determining the peak amplitudes of ground motion, but it can considerably modify the synthetic pulse shapes. At close distances, the depth of the top of the fault, and the slip on the fault, are more important than the fault width, but at large distances from the fault the moment per unit length appears to control the peak amplitudes.

Synthetic motions adjacent to Haskell models of finite-length faults in an infinite medium can be regarded as composed of a starting phase, a rupture passage phase, and a stopping phase. The rupture passage phase is a prominent component of the total ground motion when it is separated from the starting phase. The pulse generated by the infinite-length dislocation model considered in this paper is the equivalent, for a half space, of the rupture passage phase generated by the Haskell models.

When compared with observations, the model underestimates peak accelerations and peak velocities in the near field. This underestimate occurs both at high frequencies and in the intermediate frequency range in which asperities are supposed to be of little importance. Furthermore, the amplitudes of starting and stopping phases do not appear to be sufficient to explain the differences. We conclude that the effects introduced by layering are therefore the most probable cause of the larger amplitudes in observational data.

ACKNOWLEDGEMENTS

D. M. Boore generously supplied a computer program based on Boatwright and Boore formulation of the Haskell dislocation. This research was supported by NSF Grants PFR-79-26539 and PFR-80-07418.

REFERENCES

Aki, K. (1968). Seismic displacements near a fault, J. Geophys. Res. 73, 5359-5376.

Aki, K. and P.G. Richards (1980). Quantitative Seismology, W. H. Freeman and Company, San Francisco.

Anderson, J.G. (1974). A dislocation model for the Parkfield earthquake, Bull. Seism. Soc. Am., 64, 671-686.

Anderson, J.G. and J.E. Luco (1982). Parametric study of near-field ground motions for oblique-slip and dip-slip dislocation models, submitted to Bull Seism. Soc. Am. for publication.

Anderson, J.G. and P.G. Richards (1975). Comparison of strong ground motion from several dislocation models, Geophys. J. 42, 347-373.

Boatwright, J. and D.M. Boore (1975). A simplification in the calculation of motions near a propagating dislocation, Bull. Seism. Soc. Am. 65, 133-138.

Boore, D.M., K. Aki and T. Todd (1971). A two-dimensional moving dislocation model for a strike slip fault, Bull. Seism. Soc. Am. 61, 177-194.

Boore, D.M. and M.D. Zoback (1974). Near-field motions from kinematic models of propagating faults, Bull. Seism. Soc. Am. 64, 321-342.

Bouchon, M. (1979). Predictability of ground displacement and velocity near an earthquake fault: An example: The Parkfield earthquake of 1966, J. Geophys. Res. 84, 6149-6156.

Brady, A.G., V. Perez, and P.N. Mork (1980). The Imperial Valley earthquake, October 15, 1979. Digitization and processing of accelerograph records. Open file report 80-703, United States Department of the Interior Geological Survey, Menlo Park, CA.

Day, S.M. (1982). Three-dimensional finite difference simulation of fault dynamics: rectangular faults with fixed rupture velocity, Bull. Seism. Soc. Am. 72, 705-727.

Ewing, W.M., W.S. Jardetzky, and F. Press (1957). Elastic waves in layered media, McGraw Hill Book Company, New York, 380 pages.

Hartzell, S. and D. Helmberger (1982). Strong-motion modeling of the Imperial Valley earthquake of 1979, Bull. Seism. Soc. Am. 72, 571-596.

Haskell, N.A. (1969). Elastic displacements in the near-field of a propagating fault, Bull. Seism. Soc. Am. 59, 865-908.

Haskell, N.A. and K.C. Thomson (1972). Elastodynamic near-field of a finite propagating tensile fault, Bull. Seism. Soc. Am. 62, 657-697.

Joyner, W.B., D.M. Boore and R.L. Porcella (1981). Peak horizontal acceleration and velocity from strong-motion records including records from the 1979 Imperial Valley, California, earthquake, Open File Report 81-365, U.S. Department of the Interior Geological Survey, Menlo Park, California.

Kanamori, H. and P.C. Jennings (1978). Determination of local magnitude, M_L, from strong-motion accelerograms, Bull. Seism. Soc. Am. 68, 471-485.

Kanamori, H. and J. Regan (1981). Long-period surface waves generated by the Imperial Valley earthquake of 1979, U.S.G.S. Professional Paper on the Imperial Valley earthquake (in press).

Kawasaki, I. (1975). On the dynamical process of the Parkfield earthquake of June 28, 1966, J. Phys. Earth, 23, 127-144.

Kiusalaas, J. and T. Mura (1964). On the motion of a screw dislocation, in Recent Advances in Engineering Science (edited by A.C. Eringen) Gordon Beach, New York, pp. 543-564.

Levy, N.A. and A.K. Mal (1976). Calculation of ground motion in a three-dimensional model of the 1966 Parkfield earthquake; Bull. Seism. Soc. Am., 66, 405-423.

Levy. N.A. and A.K. Mal (1977). The influence of source parameters on strong ground motion, Proc. 6th World Conference on Earthquake Engineering, New Delhi.

Luco, J.E. and J.G. Anderson (1982). Steady-state response of an elastic half-space to a moving dislocation of finite width, Bull. Seism. Soc. Am. (submitted).

Niazi, A. (1973). Elastic displacements caused by a propagating crack in an infinite medium: an exact solution, Bull. Seism. Soc. Am. 63, 357-379.

Olson, A. (1982). Finite faults and inverse theory with applications to the 1979 Imperial Valley earthquake, Bull. Seism. Soc. Am. (in press).

Thomson, K.C. and N.A. Haskell (1972). Elastodynamic near-field of a finite transverse shear fault, J. Geophys. Res. 77, 2574-2582.

Trifunac, M.D. and F.E. Udwadia (1974). Parkfield, California earthquake of June 27, 1966: A three-dimensional moving dislocation, Bull. Seism. Soc. Am., 64, 511-533.

TABLE 1

Estimate of Rupture Velocity for the
Imperial Valley, Oct. 15, 1979 Earthquake

Station	Δx (km)[1]	Peak time[2]	$\left(\begin{matrix}\text{Peak time} - \\ \text{Origin time}\end{matrix}\right)^3 = \Delta t$(sec)	Rupture velocity = $\Delta x/\Delta t$(km/sec)
Array #2	23.6	23:17:09.1	14.6	1.62
#4	23.2	23:17:07.3	12.8	1.81
#5	24.6	23:17:07.7	13.2	1.86
#6	24.6	23:17:67.3-68.2	12.8-13.7	1.92-1.80
#8	23.6	23:17:66.7	12.2	1.93
#11	22.4	23:17:08.3	13.8	1.62

1. Distance along the fault from epicenter to projection of observation point onto the fault, measured from Fig. 1 of Brady, et. al. (1980) ±0.3 km.

2. GMT, October 15, 1979, ±0.1 sec. These are based on start times of accelerograms given by Porcella and Matthiesen (1979) and Porcella (personal communication).

3. Based on origin time 23:16:54.5 (Brady, et. al., 1980).

FIGURE CAPTIONS

Figure 1. Description of fault model and coordinate systems.

A. Three dimensional view. The plane z = 0 is the free surface. The plane shaded area represents a vertical fault; rupture occurs only between z_u and z_d, but extends to $\pm \infty$ in the x-direction.

B. Plan view of the plane which contains the fault. The shaded portion represents the area which has ruptured at time t. Slip on the fault is independent of location within the shaded area and is constrained to be horizontal.

Figure 2. Synthetic acceleration pulses at various distances from a vertical, strike-slip fault characterized by z_u = 2 km and z_d = 10 km. The slip on the fault corresponds to a step dislocation of amplitude Δ_0 = 100 cm propagating with velocities c_1 = 3.184 km/sec and $c_2 = \infty$.

Figure 3. Synthetic velocities corresponding to the accelerations shown in Figure 2.

Figure 4. Synthetic displacements corresponding to the accelerations shown in Figure 2.

Figure 5. Peak values of synthetic acceleration, velocity, and displacement, as a function of distance y for three vertical, strike-slip faulting models.

All three models have the same moment per unit length. All three models have c_1 = 3.0 km/sec and $c_2 = \infty$. The solid line (—) corresponds to a model with z_u = 1 km, z_d = 9 km, and Δ_o = 100 cm. The dash line (---) corresponds to a fault with z_u = 2 km, z_d = 10 km, and Δ_o = 100 cm. The dash-dot line (-·-·) corresponds to a fault with z_u = 2 km, z_d = 18 km, and Δ_o = 50 cm.

Figure 6. Synthetic velocity pulses from a vertical, strike slip fault with z_u = 2 km, z_d = 10 km, $c_2 = \infty$, Δ_o = 100 cm, at a distance y = 10 km. The horizontal rupture velocity c_1 is given four values approaching the Rayleigh wave velocity in the half space, $c_R \cong 3.1849$ km/sec.

Figure 7. Effects of horizontal rupture velocity c_1 on peak amplitudes of acceleration, velocity, and displacement for a vertical, strike-slip fault with z_u = 2 km, z_d = 10 km, Δ_o = 100 cm, and other parameters as shown in the figure.

Figure 8. Effect of horizontal rupture velocity c_1 on the distribution of peak velocities as a function of distance y for a vertical strike slip fault with z_u = 2 km, z_d = 10 km, $c_2 = \infty$, and Δ_o = 100 cm.

Figure 9. Effects of vertical rupture velocity c_2 on synthetic velocities for two models of a vertical, strike slip fault with z_u = 2 km, z_d = 10 km, c_1 = 3.0 km/sec, y = 2 km and Δ_o = 100 cm. For the case on the left, with c_2 negative, rupture occurs first at the lower edge of the fault for any

selected location x, and proceeds upward; for the case on the right, with c_2 positive, rupture reaches a location x at the top edge of the fault first and proceeds downward.

Figure 10. Effects of vertical rupture velocity c_2 on synthetic velocities from a vertical, strike-slip fault with z_u = 2 km, z_d = 10 km, c_1 = 3 km/sec, Δ_o = 100 cm, and at y = 10 km.

Figure 11. Effect of c_2 on the peak velocity at y = 2 and 10 km for a vertical strike-slip fault with z_u = 2 km, z_d = 10 km, c_1 = 3 km/sec and Δ_o = 100 cm.

Figure 12. Synthetic acceleration pulses caused by a vertical, strike-slip fault which has a slip function described by a ramp with finite duration, τ, and slip velocity Δ_o = 100 cm/sec. The rupture is characterized by z_u = 2.0 km, z_d = 10.0 km, c_1 = 3.0 km/sec and c_2 = ∞. The observation point is at y = 2 km.

Figure 13. Comparison of synthetic velocity from an infinite-length fault in half-space and several related, finite-length models in an infinite space. Velocity from the infinite-length fault (solid line) results from a vertical, right-lateral strike-slip fault with z_u= 2 km, z_d = 10 km, c_1 = 3.0 km/sec, and c_2 = ∞. The time history of dislocation at each point is a finite ramp with slip velocity 200 cm/sec and rise time 0.5 sec, giving a total offset of 100 cm. At time = 0, the rupture front is at x = 0; the station location is x = 0 km, y = 2 km. The finite fault rupture models are sections of this infinite fault centered

at x = 0, with half-length as given. The kinematic fault-dislocation and fault-receiver geometry are the same as for the infinite fault. Velocities from these finite faults, shown as broken lines, are calculated as in Anderson and Richards (1975), and are multiplied by a factor of 2. Note that the vertical scale for $\dot{u}_y$ is twice the vertical scale for $\dot{u}_x$ and $\dot{u}_z$.

Figure 14. Peak accelerations (a) and velocities (b) from our calculations, (Δ_0 = 100 cm, $c_2 = \infty$), compared with values predicted by the regression of Joyner, Boore, and Porcella (1981).

Figure 15. Comparison of 10.0 second section of observed velocity at stations 6 and 7 during the October 15, 1979 Imperial Valley earthquake with a synthetic record. Components are oriented perpendicular to the fault (230^o). Peak to peak amplitudes of each trace are given on the right. Synthetic is calculated with α = 5.0 km/sec, $\beta = \alpha/\sqrt{3}$, z_u = 1.0 km, z_d = 10.0 km, c_1 = 2.0 km/sec, Δ_0 = 100 cm, $\dot{\Delta}_0$ = 67 cm/sec (giving a rise time of 1.5 sec), and y = 1.0 km.

Figure 16. Peak accelerations from low-pass filtered synthetics, compared with peaks from low-pass filtered body-wave pulses of the Imperial Valley earthquake of October 15, 1979. The filter has a corner frequency of 0.5 Hz. Each accelerograph location is indicated by a code : B = Bonds Corner, C = Calexico, H = Holtville, numbers 1 to 13 correspond to stations of the transverse array. Circles represent stations southwest of the fault, and triangles represent stations northeast of the fault. Data from the El Centro Differential Array is referred to as station 9. Models use a fault displacement of 100 cm, which may differ from average during the Imperial Valley earthquake.

Figure 17. Low-pass filtered S-wave accelerations from transverse array recordings of the Imperial Valley earthquake of October 15, 1979. Data from the El Centro Differential Array is referred to as station 9. Frequencies greater than 0.5 Hz are removed. The relative timing of the records is based on visual alignment of the peak of the pulse on the perpendicular (230°) component. The surface expression of the Imperial fault passes between stations 6 and 7, and the surface expression of the Brawley fault passes between stations 5 and 6. Distance from a linear approximation to the surface expression of the fault, equivalent to y (Fig. 1), is shown in parentheses next to each station number. Dashed lines (S) show filtered synthetic accelerograms for z_u = 1 km, z_d = 9 km, c_1 = 3.0 km/sec, c_2 = ∞, and Δ_o = 225 cm at y = 2 and y = -2.

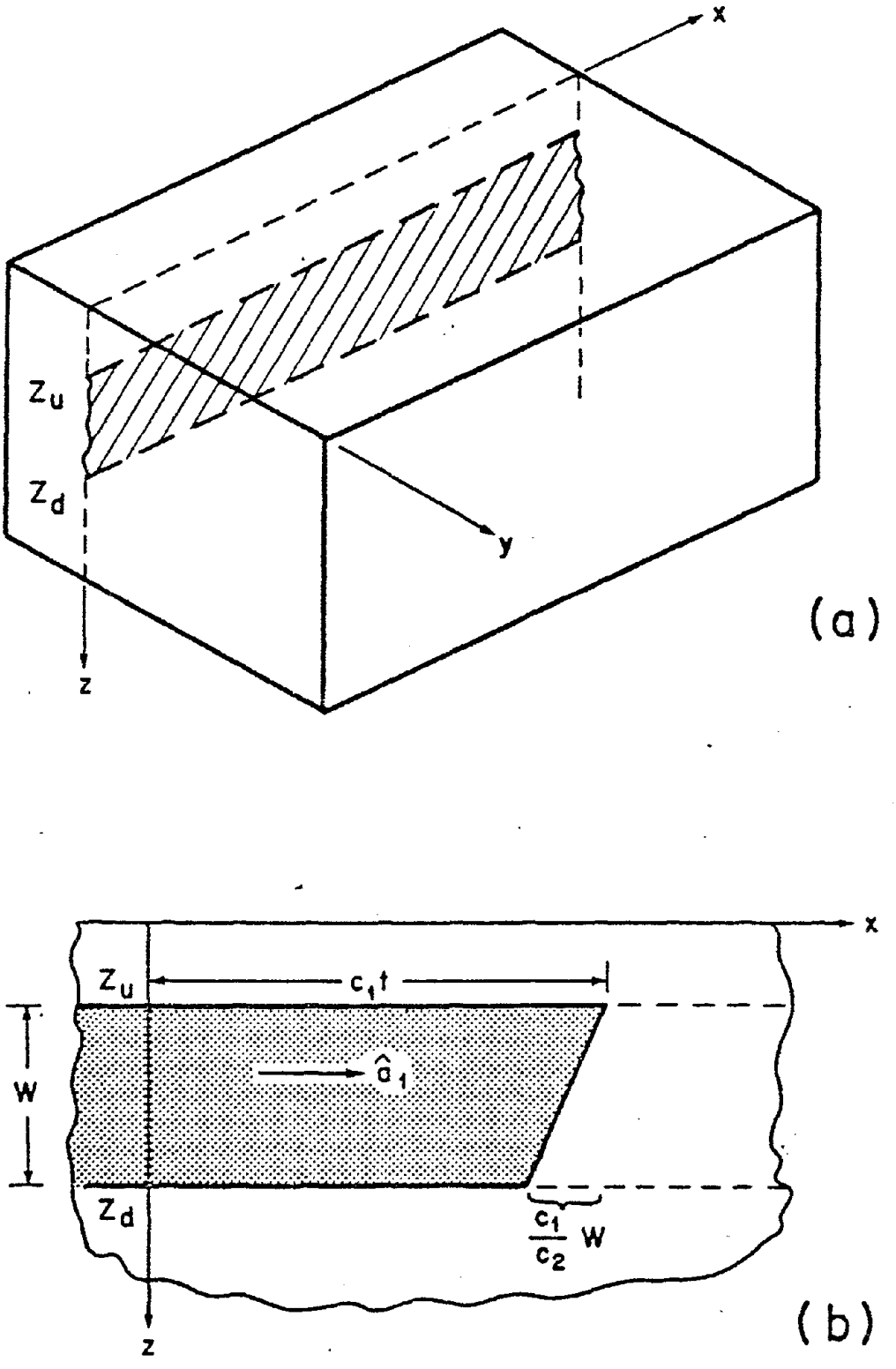

Figure 1

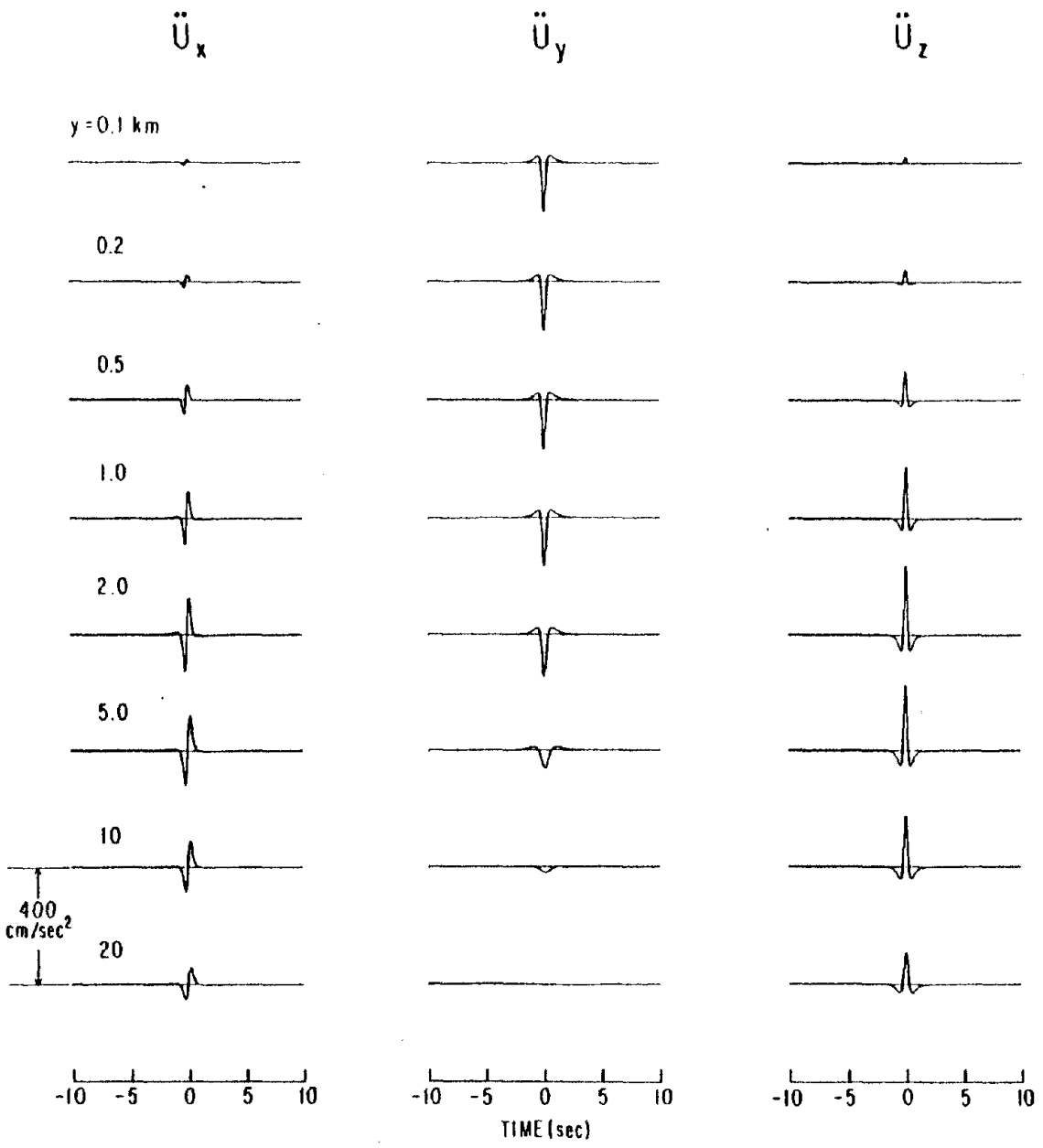
$\ddot{U}_x$
$\ddot{U}_y$
$\ddot{U}_z$
y = 0.1 km
0.2
0.5
1.0
2.0
5.0
10
20
400 cm/sec²
-10 -5 0 5 10
TIME (sec)

Figure 2

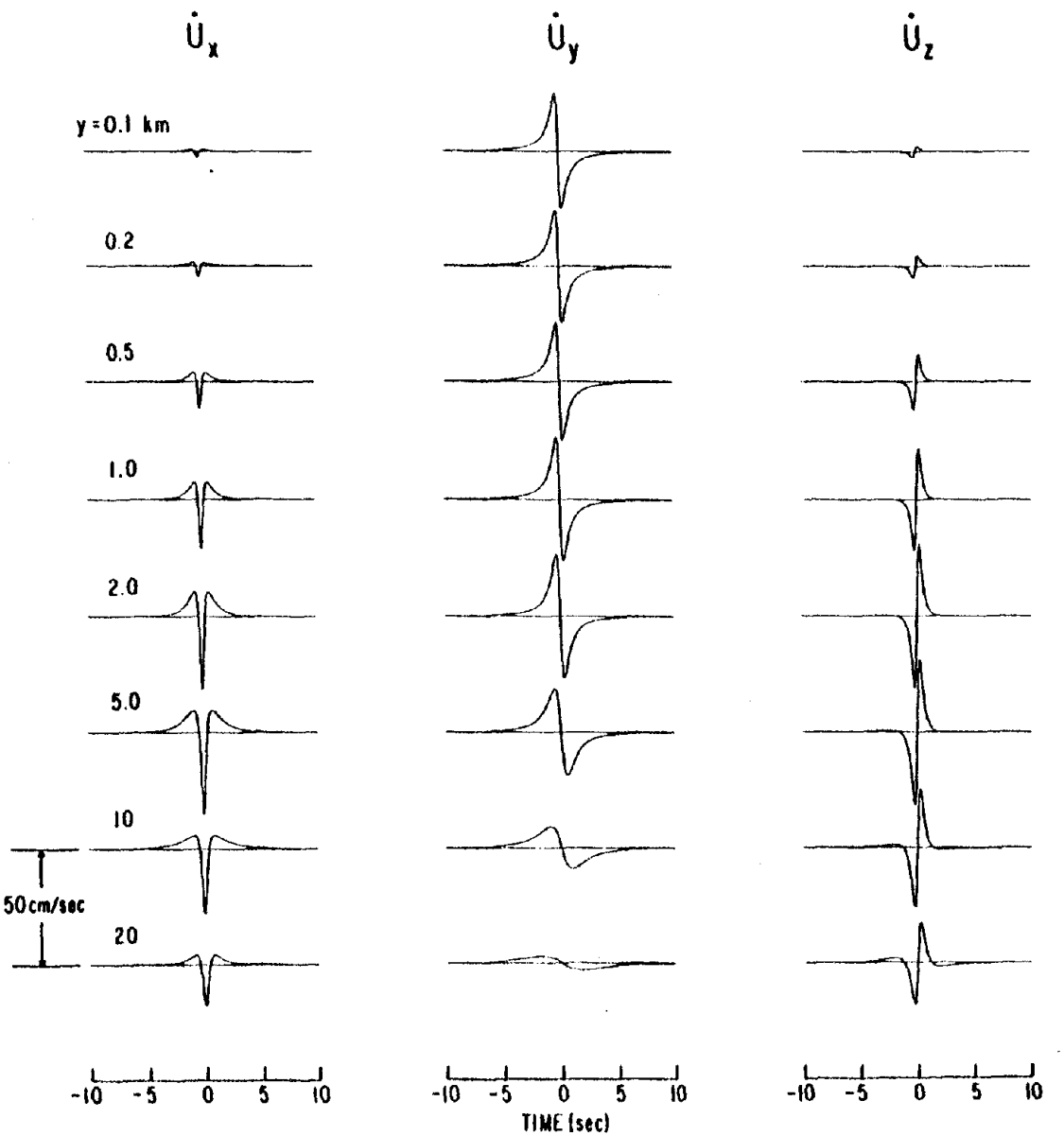
$\dot{U}_x$
$\dot{U}_y$
$\dot{U}_z$
y = 0.1 km
0.2
0.5
1.0
2.0
5.0
10
20
50 cm/sec
-10 -5 0 5 10
-10 -5 0 5 10
TIME (sec)
-10 -5 0 5 10

Figure 3

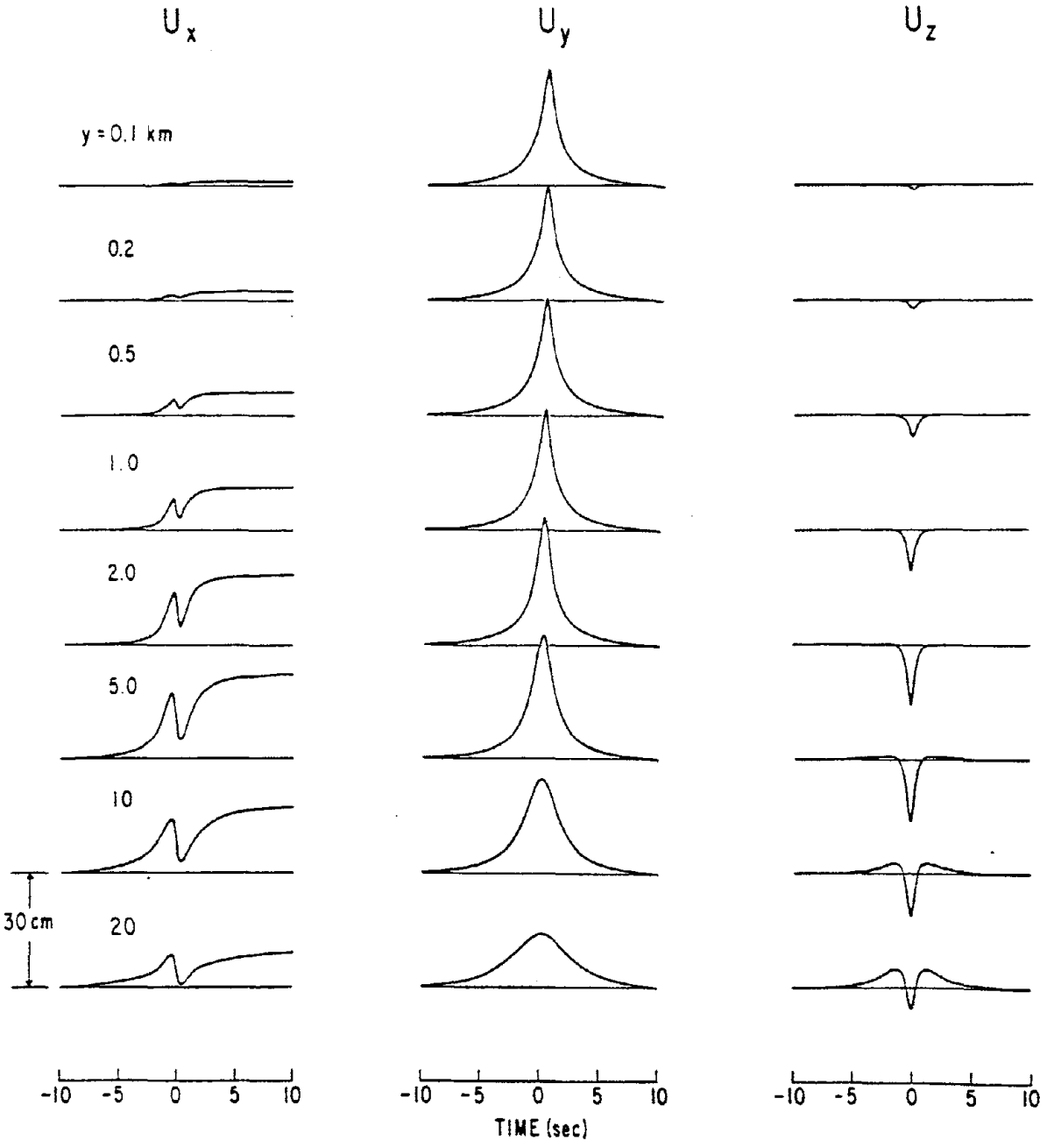
U_x
U_y
U_z
y = 0.1 km
0.2
0.5
1.0
2.0
5.0
10
20
30 cm
-10 -5 0 5 10
-10 -5 0 5 10
-10 -5 0 5 10
TIME (sec)

Figure 4

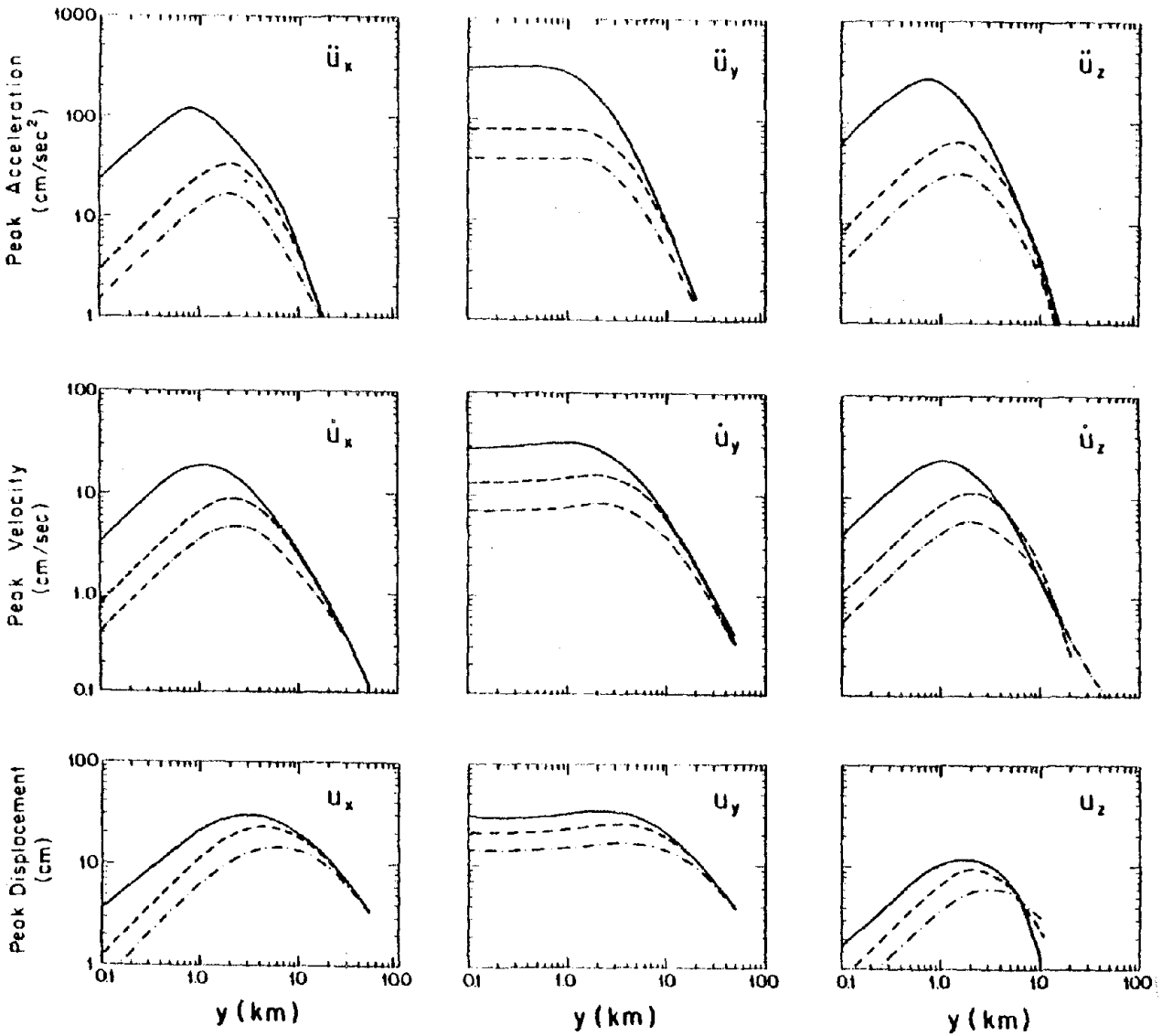
Peak Acceleration (cm/sec²)
Peak Velocity (cm/sec)
Peak Displacement (cm)
ü_x
ü_y
ü_z
u̇_x
u̇_y
u̇_z
u_x
u_y
u_z
1000
100
10
1
0.1
0.01
1.0
10
100
y (km)

Figure 5

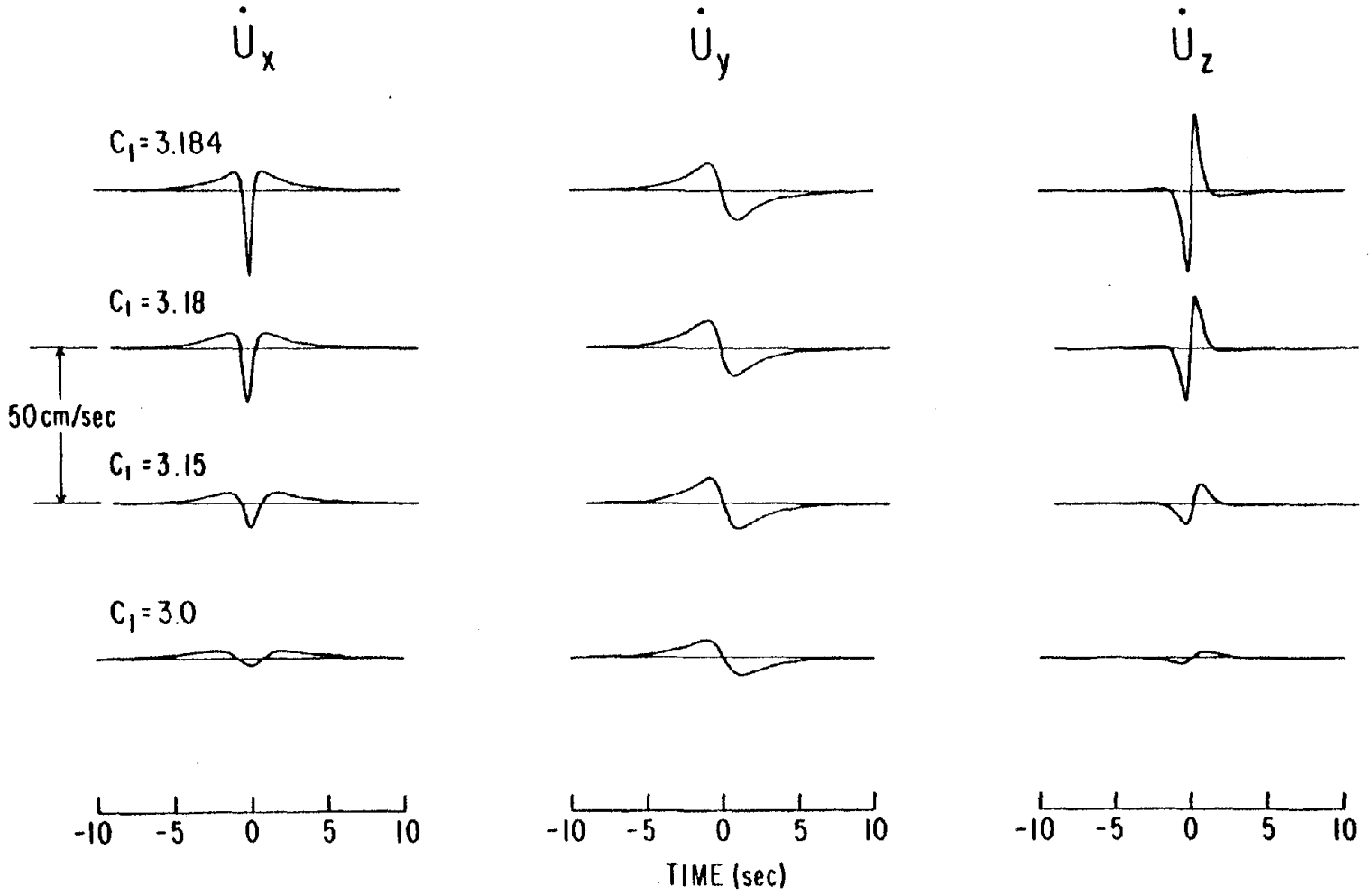
$\dot{U}_x$
$\dot{U}_y$
$\dot{U}_z$
$C_1 = 3.184$
$C_1 = 3.18$
50 cm/sec
$C_1 = 3.15$
$C_1 = 3.0$
-10 -5 0 5 10
-10 -5 0 5 10
-10 -5 0 5 10
TIME (sec)

Figure 6

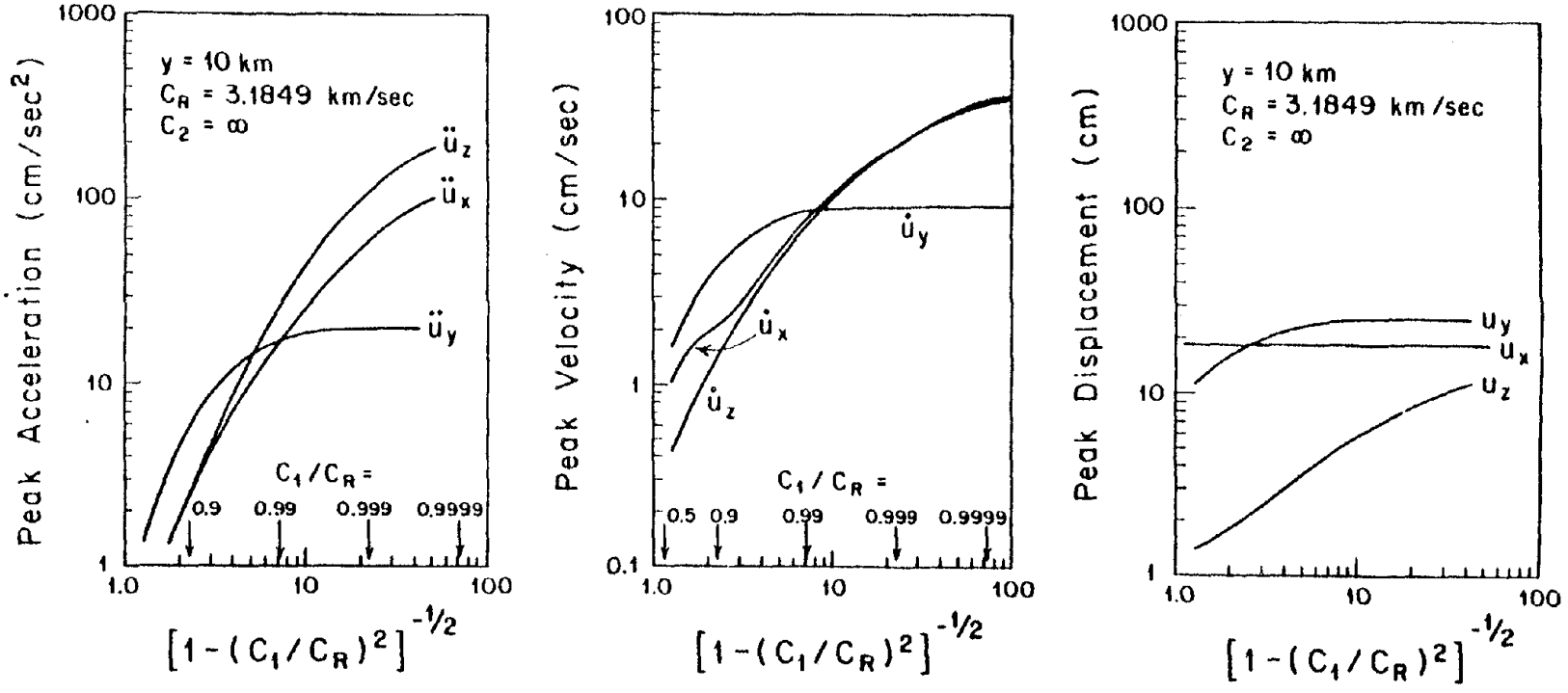
Peak Acceleration (cm/sec²)
y = 10 km
C_R = 3.1849 km/sec
C_2 = ∞
ü_z
ü_x
ü_y
C_1 / C_R =
0.9
0.99
0.999
0.9999
1000
100
10
1
1.0
10
100
[1 - (C_1 / C_R)²]^-1/2
Peak Velocity (cm/sec)
u̇_y
u̇_x
u̇_z
C_1 / C_R =
0.5
0.9
0.99
0.999
0.9999
100
10
1
0.1
Peak Displacement (cm)
u_y
u_x
u_z

Figure 7

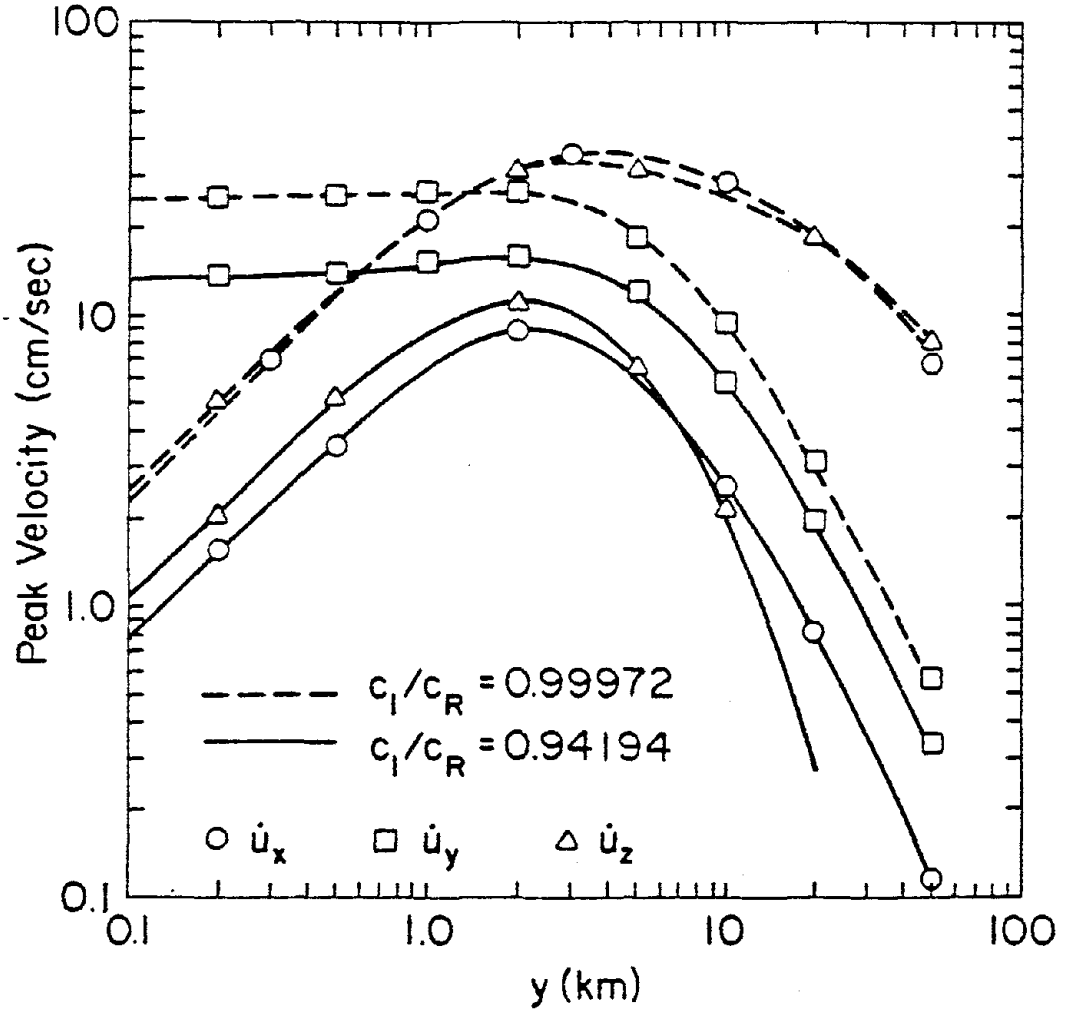
100
10
1.0
0.1
Peak Velocity (cm/sec)
0.1
1.0
10
100
y (km)
$c_l/c_R = 0.99972$
$c_l/c_R = 0.94194$
$\dot{u}_x$
$\dot{u}_y$
$\dot{u}_z$

Figure 8

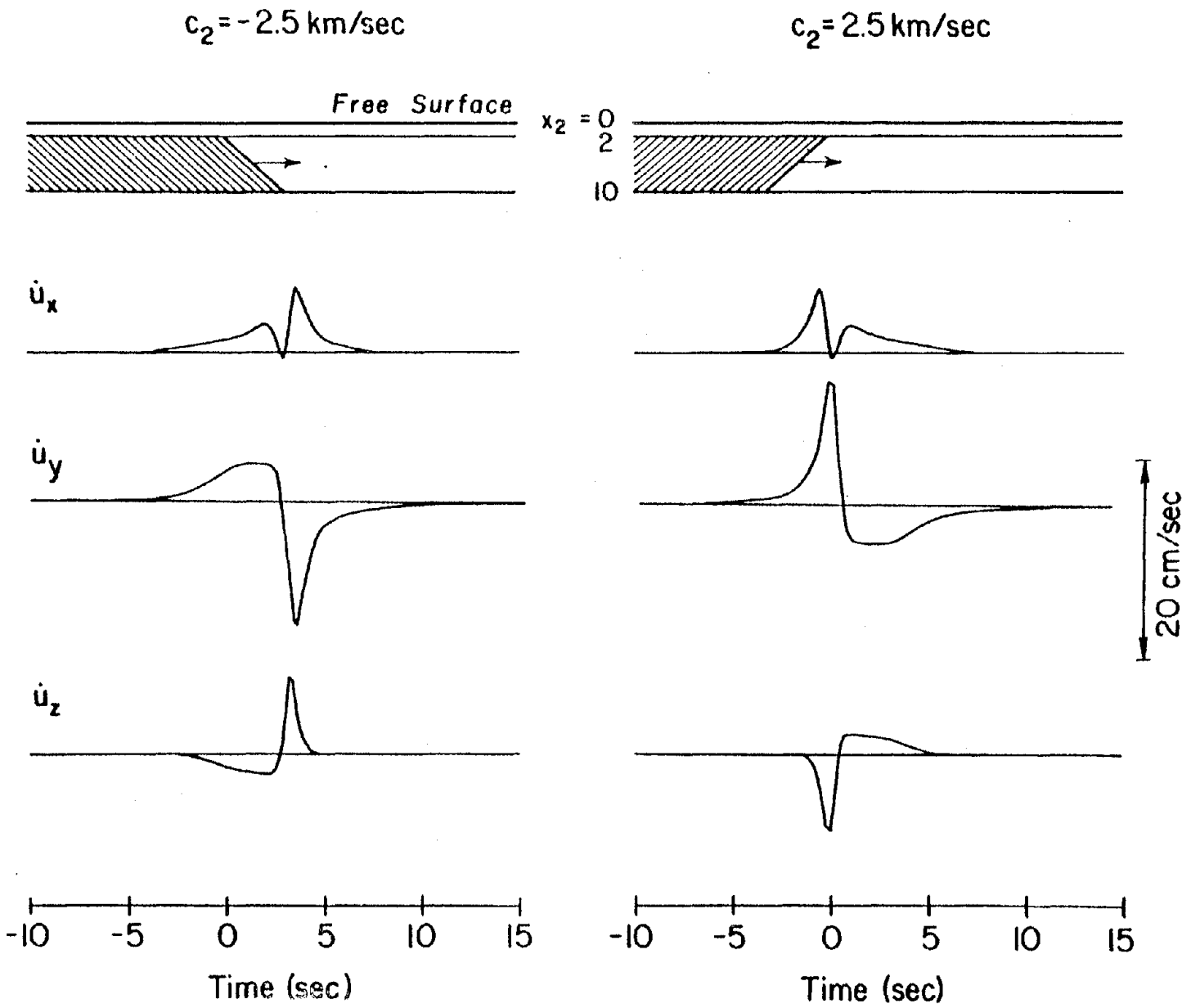
$c_2 = -2.5$ km/sec
$c_2 = 2.5$ km/sec
Free Surface
$x_2 = 0$
2
10
$\dot{u}_x$
$\dot{u}_y$
$\dot{u}_z$
20 cm/sec
-10
-5
0
5
10
15
Time (sec)
-10
-5
0
5
10
15
Time (sec)

Figure 9

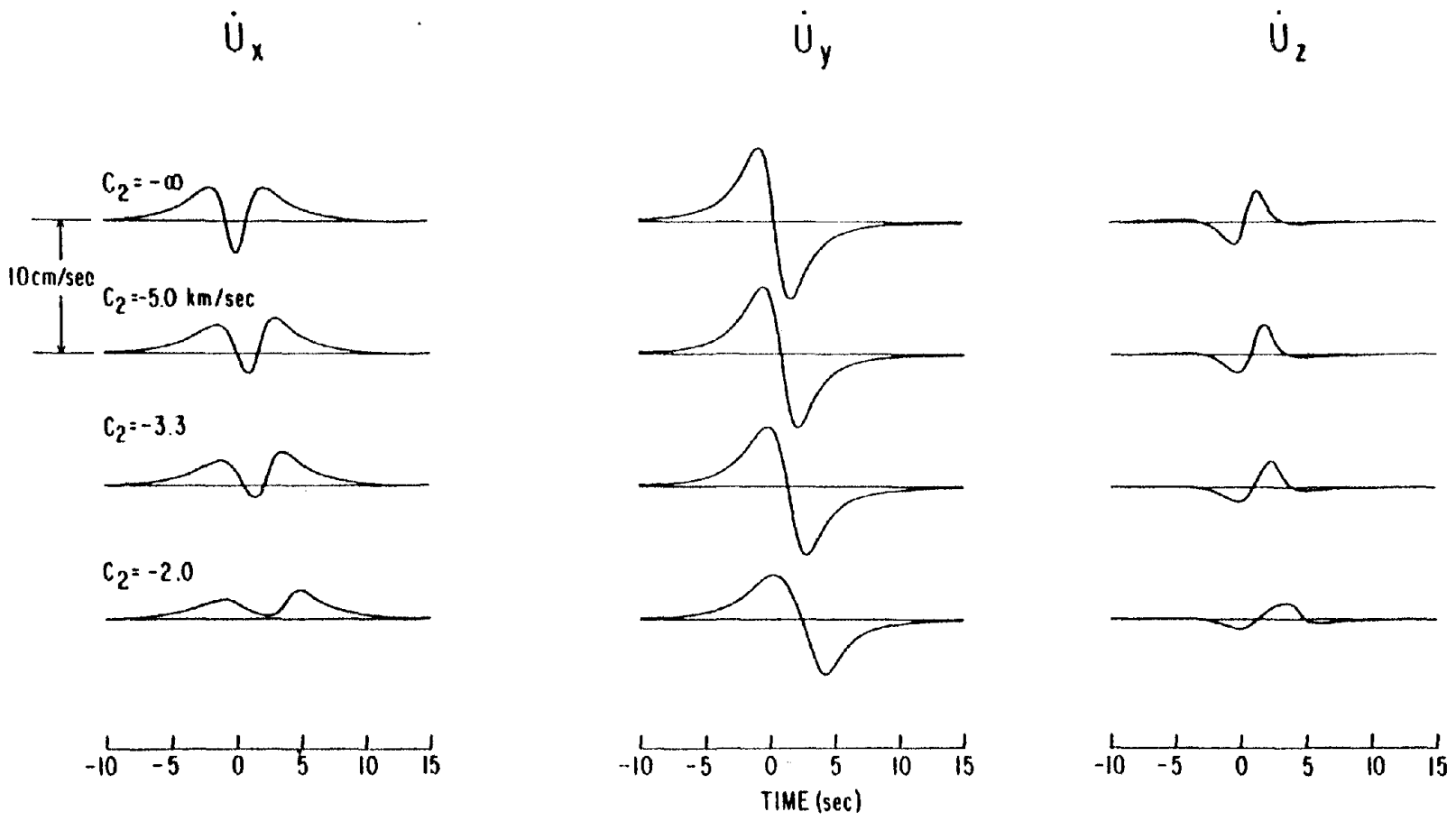
$\dot{U}_x$
$\dot{U}_y$
$\dot{U}_z$
$C_2 = -\infty$
10cm/sec
$C_2 = -5.0$ km/sec
$C_2 = -3.3$
$C_2 = -2.0$
-10 -5 0 5 10 15
-10 -5 0 5 10 15
-10 -5 0 5 10 15
TIME (sec)

Figure 10

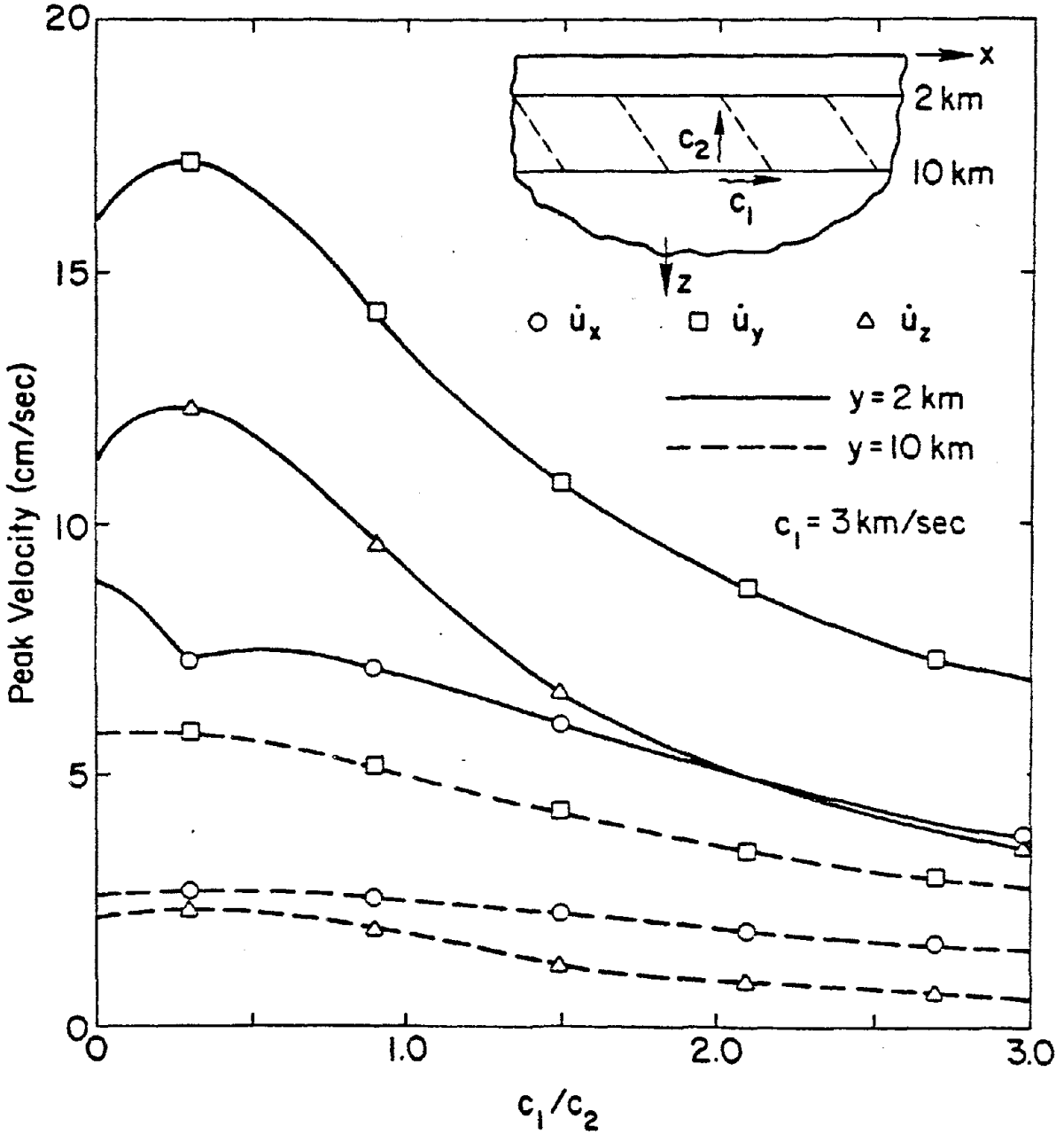
20
15
10
5
0
0
1.0
2.0
3.0
Peak Velocity (cm/sec)
c_1/c_2
x
2 km
10 km
c_2
c_1
z
$\dot{u}_x$
$\dot{u}_y$
$\dot{u}_z$
y = 2 km
y = 10 km
c_1 = 3 km/sec

Figure 11

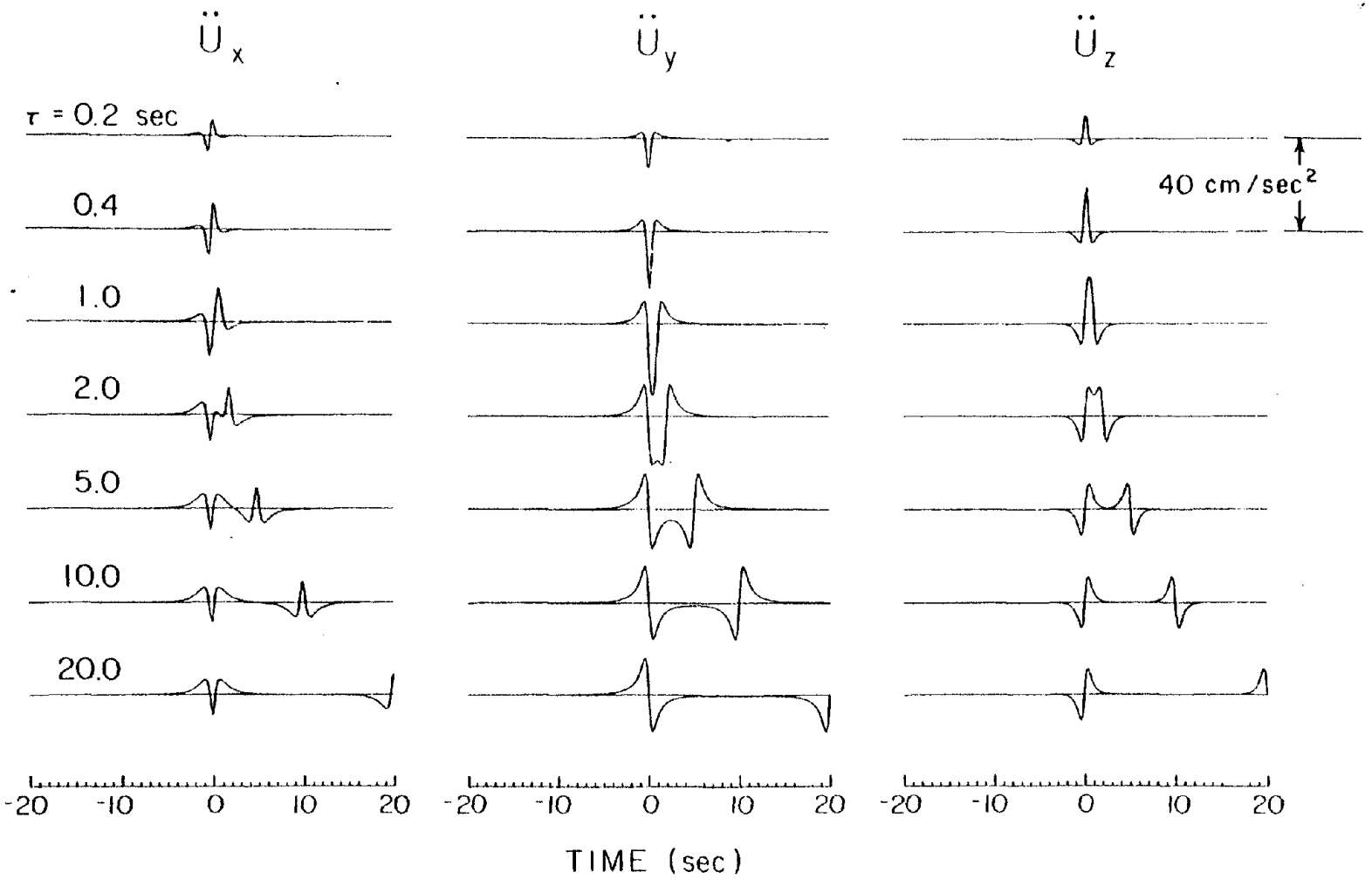
$\ddot{U}_x$
$\ddot{U}_y$
$\ddot{U}_z$
τ = 0.2 sec
0.4
1.0
2.0
5.0
10.0
20.0
40 cm/sec²
-20 -10 0 10 20
-20 -10 0 10 20
-20 -10 0 10 20
TIME (sec)

Figure 12

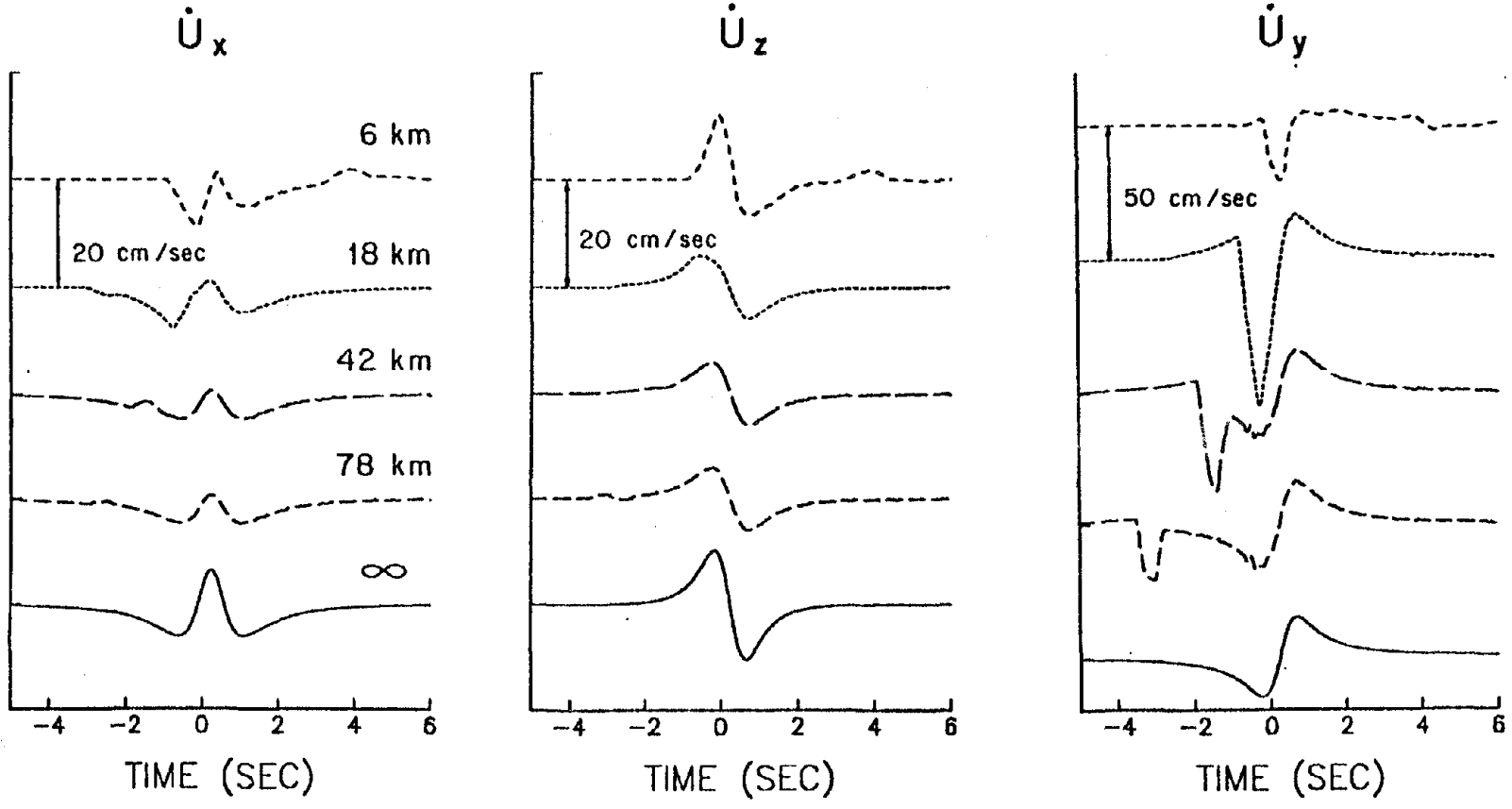
$\dot{U}_x$
6 km
20 cm/sec
18 km
42 km
78 km
∞
−4 −2 0 2 4 6
TIME (SEC)
$\dot{U}_z$
20 cm/sec
−4 −2 0 2 4 6
TIME (SEC)
$\dot{U}_y$
50 cm/sec
−4 −2 0 2 4 6
TIME (SEC)

Figure 13

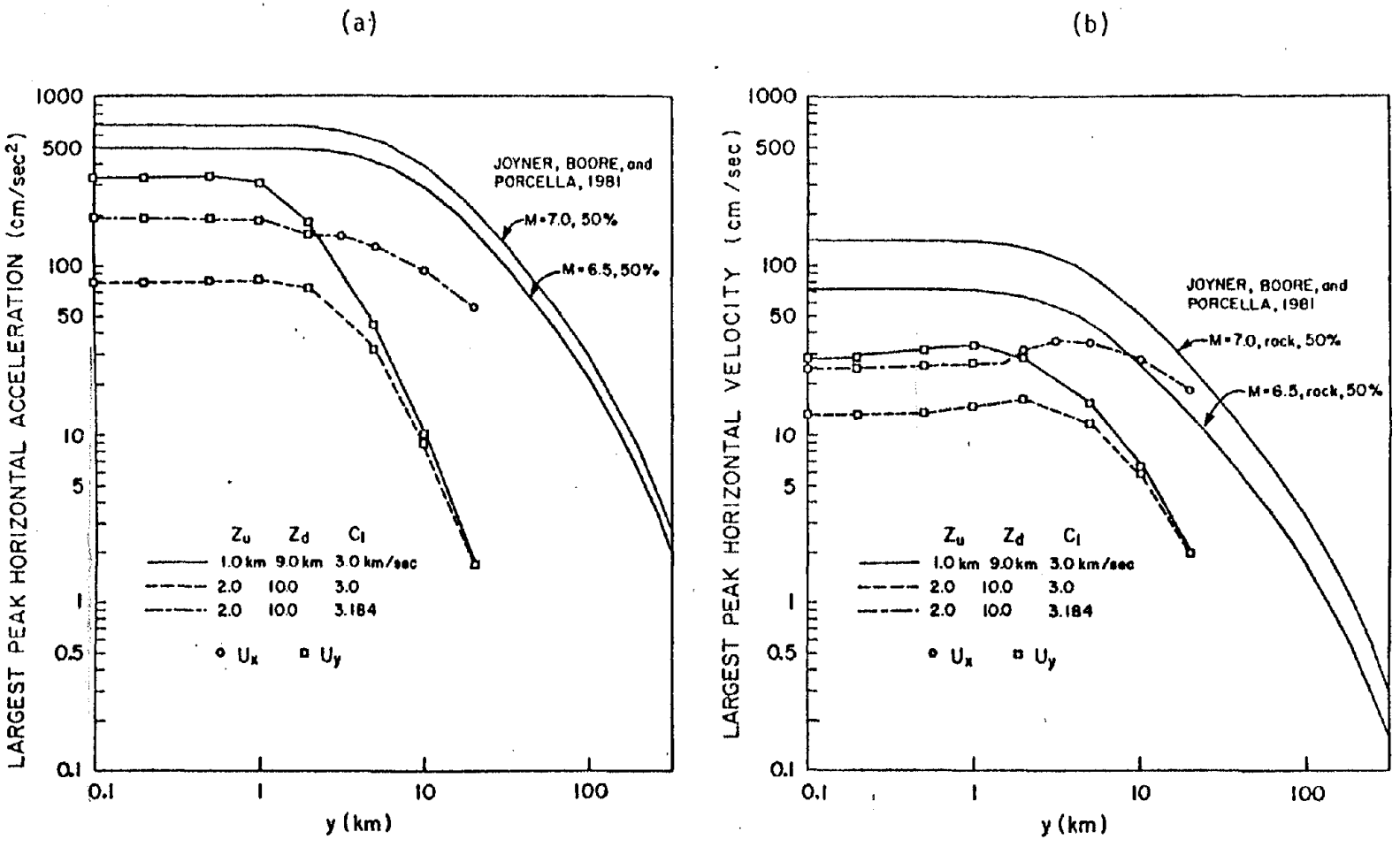
(a)
(b)
LARGEST PEAK HORIZONTAL ACCELERATION (cm/sec²)
LARGEST PEAK HORIZONTAL VELOCITY (cm/sec)
y (km)
JOYNER, BOORE, and PORCELLA, 1981
M=7.0, 50%
M=6.5, 50%
M=7.0, rock, 50%
M=6.5, rock, 50%
Zu Zd Cl
1.0 km 9.0 km 3.0 km/sec
2.0 10.0 3.0
2.0 10.0 3.184
Ux Uy

Figure 14

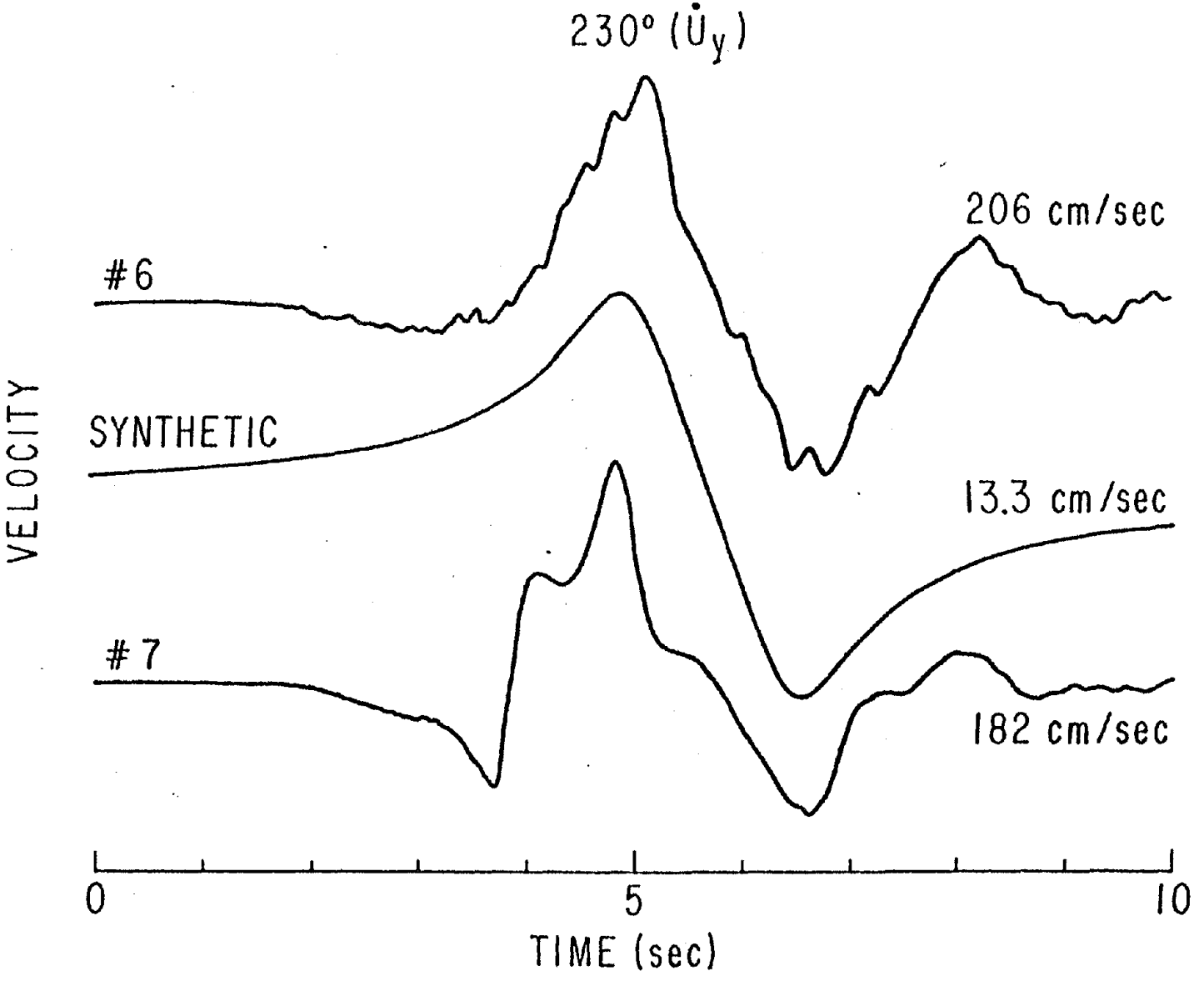
230° ($\dot{U}_y$)
206 cm/sec
#6
SYNTHETIC
13.3 cm/sec
#7
182 cm/sec
VELOCITY
0
5
10
TIME (sec)

Figure 15

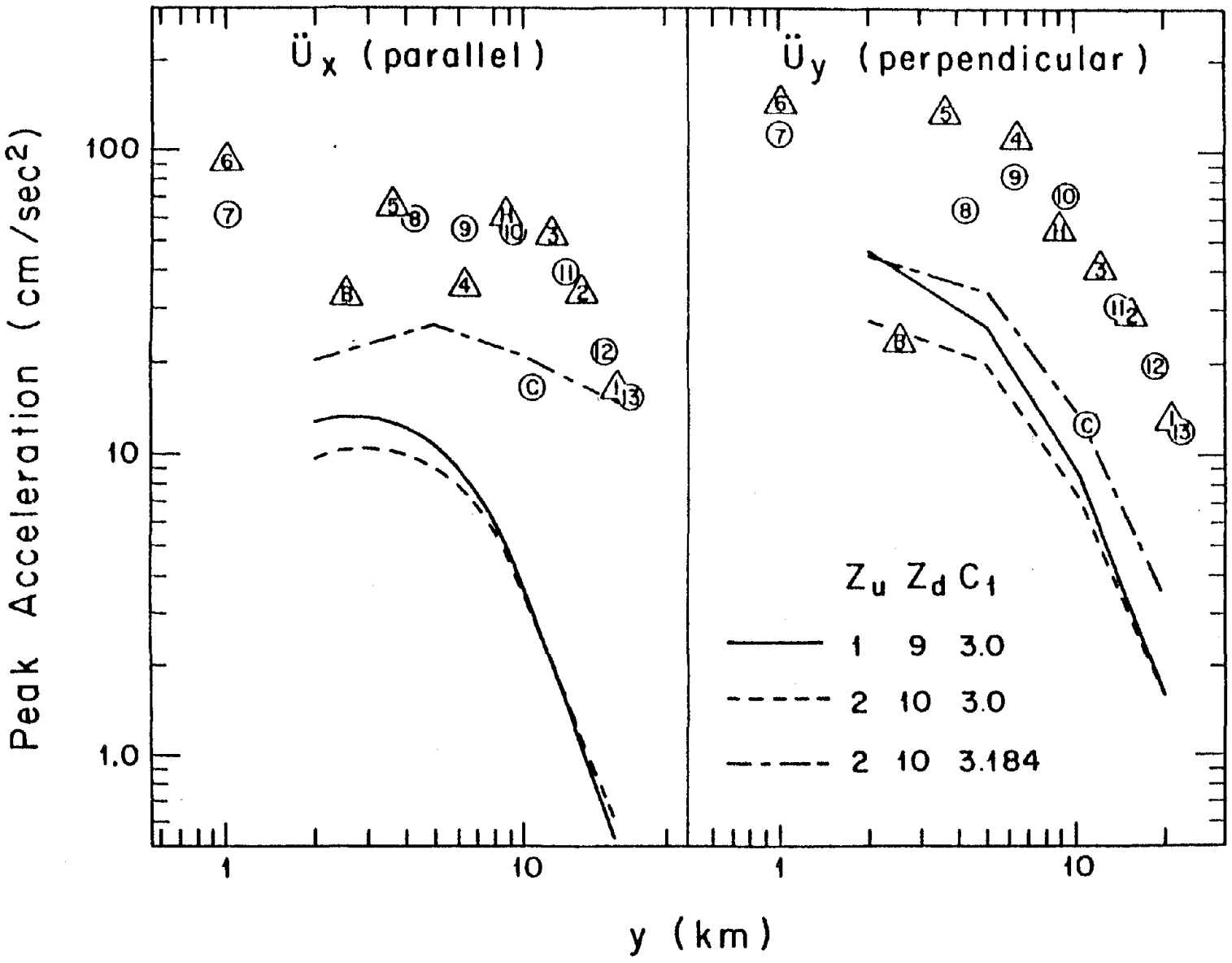
Ü x (parallel)
Ü y (perpendicular)
Peak Acceleration (cm/sec2)
100
10
1.0
1
10
y (km)
Zu Zd C1
1 9 3.0
2 10 3.0
2 10 3.184

Figure 16

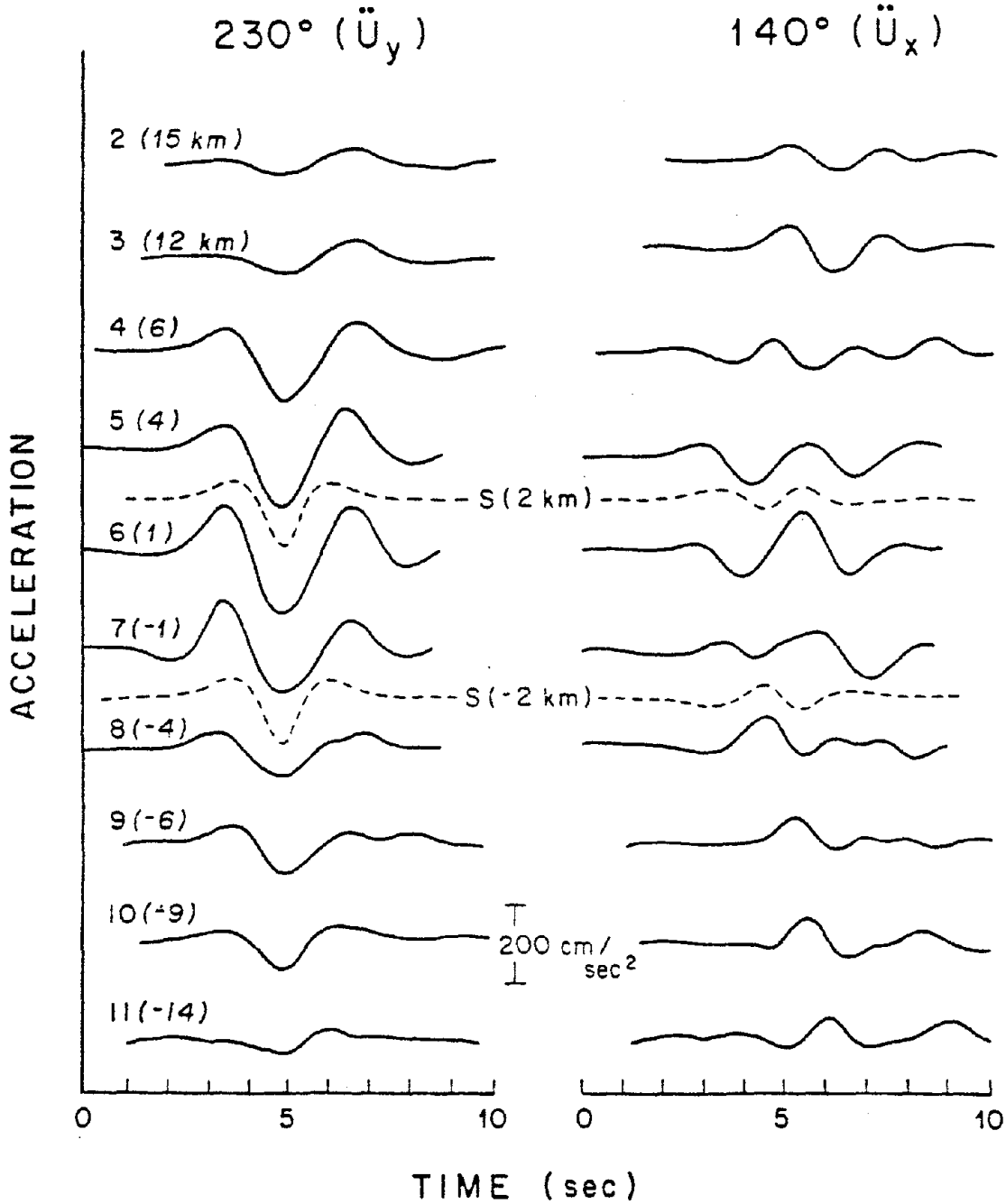
230° ($\ddot{U}_y$)
140° ($\ddot{U}_x$)
2 (15 km)
3 (12 km)
4 (6)
5 (4)
S (2 km)
6 (1)
7 (-1)
S (-2 km)
8 (-4)
9 (-6)
10 (-9)
11 (-14)
200 cm/sec²
ACCELERATION
0
5
10
0
5
10
TIME (sec)

Figure 17

PARAMETRIC STUDY OF NEAR-FIELD GROUND MOTIONS FOR OBLIQUE-SLIP AND DIP-SLIP DISLOCATION MODELS

by

John G. Anderson and J. Enrique Luco

ABSTRACT

The near-field motion on the surface of a uniform half-space for oblique-slip and dip-slip faults has been studied by the use of a dislocation model. The fault is modeled by an infinitely long buried dislocation of finite width; rupture propagates horizontally along the fault and past the observation points with a constant rupture velocity lower than the Rayleigh wave velocity. In addition to those parameters which control peak amplitudes near a vertical, strike-slip fault (depth of the top of the fault, horizontal rupture velocity), the dip of the fault plays an important role. The slip direction and the angle between the rupture front and the down-dip direction of the fault also become increasingly important in determining amplitudes of peak ground motions as the dip of the fault decreases from vertical to shallow angles. In some regions near a thrust fault, peak amplitudes are significantly greater than the largest values near a vertical, strike-slip fault.

Institute of Geophysics and Planetary Physics, Scripps Institute of Oceanography, University of California, San Diego, La Jolla, California 92093 (J.G.A.).

Department of Applied Mechanics and Engineering Sciences, University of California, San Diego, La Jolla, California 92093 (J.E.L and J.G.A).

DRAFT, submitted to the Bulletin of the Seismological Society of America for publication, August, 1982.

INTRODUCTION

This article is a continuation of the parametric study on strong ground motion which was initiated by Anderson and Luco (1982). The previous paper studied the effect of several parameters on the strong ground motion in the near field of a vertical strike-slip fault in a uniform half-space. The fault is modeled by an infinitely long buried dislocation of finite width; rupture propagates horizontally along the fault and past the observation points with a constant rupture velocity lower than the Rayleigh velocity. We now extend the previous results to dipping faults and to faults which include a dip-slip component of ground motion. Since Anderson and Luco (1982) thoroughly studied the strike-slip fault, our approach will be to begin with that case, and see what happens as we deviate from the pure strike slip. We will study the evolution of ground motion for cases which are intermediate between pure strike-slip and pure thrust, and then study the pure thrust case in more detail.

Previous parametric studies of three dimensional oblique-faulting or thrust-faulting in a half-space on a model of comparable complexity have apparently not been carried out. A number of two-dimensional models have been presented (Mal, 1972; Schafer, 1973; Brock, 1975; Niazi, 1975; Litehiser, 1976; Bouchon and Aki, 1977; Bouchon, 1978; Madariaga, 1980). These models assume that the rupture velocity along the horizontal dimension of the fault is infinite, in contrast to the model considered here which assumes a finite horizontal rupture velocity.

DESCRIPTION OF THE MODEL

The model derived by Luco and Anderson (1982) gives the ground motion near a fault of finite width and infinite length, which is embedded in a uniform half-space. Figure 1 illustrates the geometry of the fault model and the coordinate systems employed. The fault has a strike parallel to the x axis (Fig. 1A) and may have an arbitrary dip, γ , which is measured from the horizontal y axis. Faulting

occurs as a uniform shear dislocation between the depths $z_u \leqslant z \leqslant z_d$. For the general case of a fault with dip different from 90°, the vertical projection of the fault to the free surface extends over the range $y_u \leqslant y \leqslant y_d$. The width of the fault is $W = \sqrt{(z_d - z_u)^2 + (y_d - y_u)^2} = (z_d - z_u)/\sin\gamma$.

Figure 1B illustrates the rupture model in the fault plane. The rupture front travels from $x = -\infty$ to $x = \infty$ at a constant longitudinal rupture velocity c_1, where c_1 must be less than the Rayleigh wave speed. For an observer at $x = 0$, the time $t = 0$ corresponds to the time of passage of the rupture in front of the observation point. As shown in Figure 1B, the rupture front need not be parallel to the dip direction of the fault. Luco and Anderson introduced a "transverse rupture velocity," c_2, which describes the rate at which the rupture front crosses the width of the fault at fixed x. The slip direction on this fault may be arbitrary and it is described by the rake angle ϕ, measured in the fault plane from the horizontal axis. The shape of the time function for slip is the same throughout the fault, and, in this paper, we use a step offset.

The numerical results presented below have been obtained using the analytical solution derived by the authors (Luco and Anderson, 1982) in which the velocity on the surface of the half space is given in terms of a single, finite integral. Accelerations are obtained by numerical differentiation of the synthetic velocity; displacements by numerical integration. Velocities were calculated at a time increment of 0.02 sec and for a total duration of 20 seconds.

EVOLUTION FROM STRIKE-SLIP TO DIP-SLIP DISPLACEMENTS ON THE FAULT

Anderson and Luco (1982) thoroughly examined the case of a vertical ($\gamma = 90°$) strike-slip ($\phi = 0°$) fault. Some review of the results of Anderson and Luco (1982) would seem to be appropriate. For the vertical strike slip fault, they examined characteristics of the acceleration, velocity, and displacement pulses resulting from this model as a function of distance to the fault, as a function of

horizontal and transverse rupture velocities, and as a function of rise time. The components u_x and u_z are nodal at the fault plane, and achieved peak values at distances y comparable to the depth of the top of the fault. A geometrical factor which controls these peak values is the depth of the top of the fault; the width of the fault is not important (unless it approaches zero). The horizontal rupture velocity c_1 has an important role in controlling peak values, with u_x and u_z being more sensitive than u_y to c_1 when c_1 is near the Rayleigh velocity. The vertical rupture velocity c_2 did not play an important role in modifying peak amplitudes, unless it became much smaller than c_1, but it did significantly modify the pulse shapes. An intriguing aspect of the solution is that for infinite c_2, $\dot{u}_x$ is symmetric about $t = 0$, while $\dot{u}_y$ and $\dot{u}_z$ are anti-symmetric. Finally, the effect of increasing rise time is to reduce the amplitudes of acceleration and velocity to values which are less, and sometimes considerably less, than those seen for the step offset.

This study introduces the effect of changes in two more parameters: the fault dip (γ) and the rake (ϕ). To examine the evolution from vertical strike slip ($\phi = 0°, \gamma = 90°$) to dip slip ($\phi = \pm 90°, \gamma \leqslant 90°$), we will first look at the effect of the rake for a vertical fault, second look at the effect of dip on waves generated by a strike slip fault, and third look at the effect of the rake on waves generated by a dipping fault. We begin by examining how a change in the rake affects synthetic motions near a vertical fault. Thus Fig. 2 illustrates the change in synthetic displacement, velocity, and acceleration for a site at $y = 5.0\ km$ as the rake changes from $0°$ to $-90°$ on a vertical fault. Other parameters for the synthetics in Fig. 2 are $\alpha = \sqrt{3}\beta = 6.0$ km/sec, $c_1 = 3.0$ km/sec, $c_2 = \infty$, the slip on the fault, $\Delta_o = 100$ cm, $z_u = 2.0\ km$, and $z_d = 10.0\ km$. The parameters α, β, c_1, Δ_o, z_u, and z_d are held at those values for all calculations in this paper. Figure 2 illustrates that the symmetry of $\dot{u}_x$ and the anti-symmetry of $\dot{u}_y$ and $\dot{u}_z$ of strike-slip faulting is absent for arbitrary rake, but a complementary symmetry exists for pure dip-slip faulting. In particular, a component which was symmetric for strike-slip becomes anti-symmetric for dip-slip, and a component with anti-symmetric motions for strike-slip faulting becomes symmetric for dip slip faulting. A second characteristic of the results shown in Fig. 2 is that the peak amplitudes are relatively insensitive to the rake. The components most affected by variation of the rake are $\dot{u}_z$ and u_z, which are increased by a factor of the order of 2 to 3, and $\ddot{u}_y$ which

suffers a reduction also by a factor of the order of 2 to 3 as the rake varies from 0° to −90°. These observations are further illustrated in Fig. 3, which shows the peak values from Fig. 2 and from additional calculations as a function of the rake.

Next we consider the effect of the dip angle on a fault with pure strike slip motion. The observer is at a point 5 km from the vertical projection of the top of the fault to the free surface ($y - y_u = 5$ km) as shown in Fig. 4. The calculations use a constant offset on the fault, and consequently the moment per unit length increases in these calculations as the dip decreases. In particular, $M_o/L \; \alpha \, W\alpha \; \frac{1}{\sin\gamma}$. In shifting the dip from 90° to 15°, this causes an increase of M_o/L by a factor of 3.86. We have not normalized to constant M_o/L because Anderson and Luco (1982) found that close to the fault, the actual slip was a more important factor in determination of peak amplitudes than the width of the fault.

Figure 5 illustrates the synthetic motions generated for three different dip angles. These synthetics give the motions at the site $y - y_u = 5$ *km* for strike slip on faults with dips of 90°, 60°, and 30°. As in Fig. 2, these synthetics are generated for c_2 infinite. In Figure 5, one sees that while the general features of the pulse shapes are not changed as the dip decreases, the amplitudes increase considerably. Peak amplitudes from Fig. 5 are transferred to Fig. 6, where they are shown as a function of the dip. Peak accelerations $\ddot{u}_x$ and $\ddot{u}_z$ increase by factors of 26 and 37, respectively, as the dip decreases from 90° to 15°. These increases are much larger than the increase in the moment, which as mentioned is only a factor of 3.86. Thus for strike-slip motion on the fault, the dip of the fault plays an important role in the determination of peak amplitudes of ground motion. We note that as the dip decreases, the closest distance from the observer to the fault also decreases.

Next, we investigate the effect of a variable rake on the synthetic pulses generated by a dipping fault. Figure 7 shows the evolution of synthetic acceleration, velocity, and displacement for a site at $y - y_u = 5$ *km*, and for infinite c_2, caused by a fault with a dip of 30° as the rake changes from 0° (pure strike-slip faulting) to −90° (pure thrust faulting). Qualitatively the results shown in Figure 7 resemble those on Figure 2 for a vertical fault: arbitrary rake disrupts the symmetry, and the amplitudes of some components are modified by a factor of the order of 2 to 3. The peak acceleration in the y - component experiences a reduction by a factor of the order of 6 as the rake varies from 0° to −90°. Peak

amplitudes corresponding to this case are shown on Figure 8. It is interesting that strike slip on the dipping fault causes stronger shaking than pure dip-slip motions.

To summarize this section, we have studied the evolution from strike-slip to dip slip faulting. These calculations indicate that the peak amplitudes are quite sensitive to the dip, and less sensitive to the rake.

FURTHER PARAMETRIC STUDIES ON DIP-SLIP FAULTING

The effects of dip angle on the synthetic motions and peak amplitudes for a site near a thrust fault are illustrated in Figures 9-11. We have used the same geometry as in Figure 4 for these calculations. Figure 9 shows synthetic motions generated when $c_2 = \infty$, as it has been in the previous figures. Figure 10 departs from this, and shows the effect of a finite value for the transverse rupture velocity, $c_2 = -2.5$ km/sec. For this case, at any location x along the fault, the rupture occurs first at the bottom of the fault, and propagates across the width of the fault at 2.5 *km/sec*. The symmetry properties which appear on Figure 9 are absent from Figure 10. The differing delays in the time of occurrence of peak accelerations and velocities is caused because these peaks occur when rupture at the top of the fault passes in front of the observation point; with the successively greater width of faults of smaller dip, it takes longer for rupture to pass from the bottom edge to the top edge of the fault. With the exception of the u_y - component, the peak amplitudes shown in Figures 9 and 10 and summarized in Fig. 11 do not appear to be strongly affected by the dip of the fault. The largest effects occur for peak accelerations which show an increase by a factor of the order of 3 as the dip decreases from 90° to 15°. The peak amplitudes for the transverse component u_y show a strong dependence on the dip angle and exhibit a minimum at a dip = 45°. Figures 9 and 10 indicate that the sense of motion of the u_y - component is reversed between dips of 30° and 60°.

The amplitudes of the acceleration and velocity pulses which are shown in Fig. 10 for finite c_2 are much smaller than those shown in Figure 9 for infinite c_2. Peak amplitudes for the two values of the transverse rupture velocity c_2 are shown on Figure 11. Differences of a factor of 2 to 3 seem to prevail for velocity, and factors of 3 to 10 for acceleration. The exception to this pattern is the u_y - component which for dip angles near 45° and for $c_2 = -2.5$ km/sec exhibits larger peak values for $\ddot{u}_y$ and $\dot{u}_y$ and equal peak values for u_y than the results for $c_2 = \infty$.

In Figure 12, we plot profiles of peak values of acceleration, velocity, and displacement along the free surface for a thrust fault with a dip of 30° and c_2 infinite. The upper edge of the fault lies beneath $y = 3.46$ km. Peak values in the x and z components of motion occur in the vicinity of this point ($y = 3.46$ km), while the peaks of the y-components are shifted slightly toward smaller values of y. Figure 12 shows considerable asymmetry in y, with a less rapid decrease in peak values at $y > 0$, above the fault plane, and illustrates the extreme dependence of peak amplitude on position. We attempted, unsuccessfully, to correlate details of the shapes of the curves in Fig. 12 (such as the minimum of u_y at $y \approx 0$) with the radiation patterns for a point dislocation (Aki and Richards, 1980, p. 80-81) at the top edge of the fault. As pointed out by Archuletta and Hartzell (1981), motion at any one time results from contributions from different parts of the fault, and different wave types. Our failure to isolate a simple radiation pattern effect which correlates with details in Fig. 12 emphasizes that even though the position of the top edge of the fault is among the dominant parameters in determining the peak values, the entire extent of the fault contributes to the motion.

ON MEASURE OF DISTANCE TO FAULTS

The available data with respect to peak accelerations, velocities and displacements are typically organized on the basis of different measures of distance to the fault. In recent correlations, for instance, Campbell (1981) uses as measure of distance the closest distance to the fault while Joyner et al (1981) and Joyner and Boore (1981) use horizontal distance to the closest point on the vertical

projection of the fault area on the free surface. For vertical faults which intersect the free surface these two measures of distance coincide. For dipping faults the differences may be significant. This is shown in Fig. 13, where the peak amplitude results presented in Fig. 12 for a dipping thrust fault (dip $= 30°$ are plotted versus three different measures of distance. These measures correspond to : distance from the site to the closest point on the fault surface (R-Closest), distance to the top edge of the fault (R-Top), and horizontal distance to closest point on the vertical projection of the rupture area on the free surface (R-Projection). The distance R-Top was motivated by our observation that the depth of the top of the fault is more important than the width of the fault in determining near-field peak amplitudes.

Inspection of Fig. 13 reveals that the definition R-Closest tends to reduce the differences between components and between points at the same value of R-Closest but on different blocks. Even with this definition of distance differences of about one order of magnitude can be observed in the distribution of peak accelerations. The distance R-Projection causes a large scatter at $R \approx 0$ (for the purpose of plotting, the peak amplitudes at R-Projection $= 0$ are shown to the left of a broken scale since all points on the upper block above the fault are assigned the same distance $R = 0$. We note that our steady-state dislocation model over an infinitely long fault introduces a lower number of characteristic distances than a finite fault for which the use of a single measure of distance may introduce additional scatter.

Joyner and Boore (1981) used the larger of the two horizontal components of acceleration in their regression; Campbell (1981) selected the average of the two horizontal components. For the long period ground motions given by our calculations, Fig. 13 shows that one of the two components is systematically smaller than the other. This would seem to violate Campbell's implicit assumption, in taking average values, that both horizontal components obey the same distribution. As pointed out by Hadjian (1978), in actual accelerograph data, the instrumental axes may be oriented randomly with respect to the fault and, often, with respect to other accelerographs. However, if one vector component in fault based coordinates is systematically larger, such an effect will persist, with scatter, on randomly oriented axes. Incidentally, axes in our synthetic calculation are not necessarily oriented such that the largest peak acceleration will appear on one of the two components. The high frequencies which are

present in observations but absent from our calculations might be distributed identically in all vector orientations, but that is not known a-priori.

SUMMARY

Within the context of the steady-state, infinite length dislocation model described by Luco and Anderson (1982) we have investigated the importance of several parameters on the pulse shapes and amplitudes of ground motion near a fault. In a separate paper (Anderson and Luco, 1982) we have studied in detail the case of vertical, strike-slip faults. In the present paper we have analyzed the cases of oblique-slip and dip-slip fault models. In this section, we attempt to summarize the results obtained in both studies.

First, we have found that the location of the observation point relative to the fault, and especially the top of the fault, plays an important, and expected role, in determining peak amplitudes of ground motion. Distance from the fault is the most easily recognized effect of location. A radiation pattern effect is also present, but is not always simply related to the radiation pattern from a point source. Near a dipping fault, peak amplitudes are different at equal distances but in opposite blocks.

Static faulting parameters which we studied included the depths of the top and bottom of the fault, the offset and the moment per unit length. Near the fault, the depth of the top of the fault and the offset (for short rise time) have a profound effect on the peak amplitudes; the depth of the bottom of the fault, and thus the moment per unit length, do not appear to play a dominant role at distances less than about twice the depth of the bottom.

For a strike-slip type earthquake, the dip of the fault had an order-of-magnitude effect on the peak amplitudes. On a dip-slip fault, the dip is less important, but still plays a prominent role in determining peak amplitudes. Shallow dipping faults cause larger peak amplitudes than near-vertical faults. The rake, or slip direction on the fault plane is relatively unimportant (within a factor of 2) in

determining peak amplitudes for a vertical fault, and slightly more important as the fault becomes more shallow-dipping.

The dynamic parameters considered included the rupture velocities c_1 and c_2, and the rise time. The horizontal rupture velocity c_1 was found in Anderson and Luco (1982) to play a crucial role in determining peak accelerations, and a successively lesser role in peak velocities and peak displacements. When the rupture velocity c_1 is close to the Rayleigh wave velocity of the medium, the effect is most impressive. For the strike-slip fault, on which this effect was studied, peak accelerations change by a factor of about 4 for a less than one percent change in c_1 as c_1 approaches the Rayleigh wave velocity. The transverse rupture velocity, c_2, was not very important on the vertical, strike-slip fault, but on the dipping fault it may reduce peak accelerations and velocities considerably. In all cases, it plays an important role in modifying pulse shapes.

The role of the rise time is also important, especially as one extrapolates this model to larger magnitude earthquakes in which the rise time is still unknown. Scholz (1981) has pointed out that if the larger slip in a large magnitude earthquake is accomplished within the same rise time as for a smaller earthquake, the peaks of ground motion would be considerably greater than they would be if the rise time is proportional to the slip.

In a study of vertical strike-slip faults (Anderson and Luco, 1982) we found that the results from the steady-state dislocation model in a uniform half-space underestimate the observed amplitudes of motion. Inclusion of the effects of layering are expected to eliminate this discrepancy (Bouchon, 1979). It is possible that similar effects would affect the results presented here for oblique-slip and dip-slip fault models.

ACKNOWLEDGEMENTS

We thank D. Boore for helpful comments on a preliminary version of this paper. This research was supported by the National Sciences Foundation under Grants PFR-79-26539 and PFR-80-07418.

REFERENCES

Aki, K. and P.G. Richards (1980). Quantitative Seismology, Theory and Methods, WH Freeman and Company, San Francisco.

Anderson, J. G. and J. E. Luco (1982). Parametric study of near-field motions for a strike-slip fault model, (submitted for publication).

Archuletta, R.J. and S.H. Hartzell (1981). Effects of fault finiteness on near-source ground motion, Bull. Seism. Soc. Am. 71, 939-957.

Boore, D.M. and M.D. Zoback (1974). Two-dimensional kinematic fault modeling of the Pacoima Dam strong-motion recordings of the February 9, 1971 San Fernando earthquake, Bull. Seism. Soc. Am. 64, 555-570.

Bouchon, M. (1978). A dynamic crack model for the San Fernando earthquake, Bull. Seism. Soc. Am. 68, 1555-1576.

Bouchon, M. and K. Aki (1977). Discrete wave-number representation of seismic-source wave fields, Bull. Seism. Soc. Am. 67, 259-277.

Brock, L.M. (1975). Surface motions due to fault slip in the vertical mode with friction, Bull. Seism. Soc. Am. 65, 1653-1666.

Campbell, K.W. (1981). Near-source attenuation of peak horizontal acceleration, Bull. Seism. Soc. Am., 71, (in press).

Hadjian, A.H. (1978). On the correlation of the components of strong ground motion, Proceedings of the Second International Conference on Microzonation for safer construction - research and application Vol. III, San Francisco, California, 1199-1210.

Joyner, W.B., and D.M. Boore (1981). Peak horizontal acceleration and velocity from strong-motion records including records from the 1979 Imperial Valley, California, earthquake, Bull. Seism. Soc. Am. (in press).

Joyner, W.B., D.M. Boore and R.L. Porcella (1981). Peak horizontal acceleration and velocity from strong-motion records including records from the 1979 Imperial Valley, California, earthquake, Open File Report 81-365, U.S. Department of the Interior Geological Survey, Menlo Park, California.

Litehiser, J.J. (1976). Near-field seismograms from a two-dimensional propagating dislocation, Ph.D. Thesis, University of California, Berkeley.

Luco, J. E. and J. G. Anderson (1982). Steady-state response of an elastic half-space to a moving dislocation of finite width, (submitted for publication).

Madariaga, R. (1980). A finite two-dimensional kinematic fault in a half-space, Publ. Inst. Geophys. Pol.Acad. Sc., A-10 (142), 33-47.

Mal, A.K. (1972). Rayleigh waves from a moving thrust fault, Bull. Seism. Soc. Am. 62, 751-762.

Niazi, A. (1975). An exact solution for a finite, two-dimensional moving dislocation in an elastic half-space with application to the San Fernando earthquake of 1971, Bull. Seism. Soc. Am. 65, 1797-1826.

Schafer, J. (1973). Strong ground motion from dip-slip faulting, M.S. Thesis, Dept. of Mechanics and Structures, University of California, Los Angeles.

Scholz, C.H. (1981). Scaling laws for large earthquakes consequences for physical models, preprint.

FIGURE CAPTIONS

Figure 1. Coordinate systems and fault model used in these calculations.

Figure 2. Evolution of synthetic waveforms on a vertical fault as the slip direction (rake) changes from pure strike slip (Rake $= 0°$) to pure thrust (Rake $= -90°$). This plot shows synthetic displacement (top), velocity (center) and acceleration (bottom). Other parameters are dip $= 90°$, $y = 5.0$ km, $y_u = 0.0$ km, $c_1 = 3.0$ km/sec, $c_2 = \infty$, $\Delta_o = 100$ cm, $z_u = 2.0$ km, $z_d = 10.0$ km. Synthetics are calculated at 50 points per second.

Figure 3. Peak amplitudes as a function of rake near a vertical fault. Faulting parameters are the same as those for Figure 2. Symbols are: circle $- U_x$, square $- U_y$, triangle $- U_z$. Symbols are plotted at all values of the rake where calculations were carried out; curved lines are cubic spline interpolations.

Figure 4. Observer-fault geometry for results shown in Figures 5 and 6.

Figure 5. Evolution of synthetic waveforms above a strike slip fault of variable dip. The observation point is on the upper block, 5.0 km from the vertical projection of the top of the fault. Dip of $90°$ corresponds to a vertical fault. Synthetic displacement is at the top, velocity in the center, and acceleration at the bottom. Parameters are rake $= 0°$, $y - y_u = 5.0$ km, $c_1 = 3.0$ km/sec, $c_2 = \infty$, $\Delta_o = 100$ cm, $z_u = 2.0$ km, $z_d = 10.0$ km. Synthetics are calculated at 50 pts/sec.

Figure 6. Peak amplitudes above a strike-slip fault of variable dip at a site on the upper fault block, 5.0 km from the vertical projection of the top edge of the fault. Model parameters are the same as in Figure 5. Symbols are circle $-U_x$, square $-U_y$, triangle $-U_z$. Symbols are plotted at each point where calculations are carried out, curves are cubic spline interpolations between these points.

Figure 7. Evolution of synthetic waveforms on a dipping fault (dip $=30°$) as the slip direction changes from pure strike slip (rake $=0°$) to pure thrust (rake $=-90°$). The observation point ($y-y_u=5$ km) is above the fault on the upthrust block. Synthetic displacement is at the top, velocity in the center, and acceleration at the bottom. Parameters are dip $=30°$, $y-y_u=5.0$ km, $c_1=3.0$ km/sec, $c_2=\infty$, $\Delta_o=100$ cm, $z_u=2$ km, $z_d=10.0$ km. Synthetics are calculated at 50 points/second.

Figure 8. Peak amplitudes as a function of rake on the upper block of a dipping fault. Model parameters are the same as those of Figure 7. Symbols are circle $-U_x$, square $-U_y$, triangle $-U_z$. Symbols are plotted at each value of the rake where calculations were carried out; curved lines are cubic spline interpolations.

Figure 9. Evolution of synthetic waveforms above a thrust fault of variable dip. The observation point is on the upper block, 5.0 km from the vertical projection of the top of the fault. Dip of $90°$ corresponds to a vertical fault. Synthetic displacement is at the top, velocity at center, acceleration at the bottom. Parameters are rake $=-90°$, $y-y_u=5.0$ km, $c_1=3.0$ km/sec, $c_2=\infty$, $\Delta_o=100$ cm, $z_u=2.0$ km, $z_d=10.0$ km. Synthetics are calculated at 50 points/sec.

Figure 10. Equivalent of Figure 9, except that $c_2 = -2.5$ km/sec.

Figure 11. Peak amplitudes above a thrust fault of variable dip at a site on the upper fault block, 5.0 km from the vertical projection of the top edge of the fault. Model parameters are the same as in Fig. 9 and 10. Solid lines correspond to $c_2 = \infty$, dashed lines to $c_2 = -2.5$ km/sec. Symbols are circle $-U_x$, square $-U_y$, triangle $-U_z$. Symbols are plotted at each point where calculations are carried out; curves are cubic spline interpolations between these points.

Figure 12. Peaks in acceleration, velocity, and displacement along a profile of sites perpendicular to a thrust fault with dip 30°. The upper edge of the fault occurs at $y_u = 3.464$ km. Model parameters are dip 30°, $c_1 = 3.0$ km/sec, $c_2 = \infty$, $\Delta_o = 100$ cm, $z_u = 2.0$ km, $z_d = 10.0$ km. Symbols are circle $-U_x$, square $-U_y$, triangle $-U_z$. Symbols are plotted at each point where calculations were performed, curves are cubic spline interpolations between these points.

Figure 13. Peak amplitudes from Fig. 12 plotted against three measures of distance to the fault : R-Closest is the distance between the closest point on the fault rupture and the site, R-Top is the distance between the top edge of the fault rupture and the site, and R-Projection is the distance between the site and the nearest surface location of a vertical projection of the fault. Dashed lines connect points with $y - u_u > 0$ (on the upthrust block) and solid lines connect points with $y - y_u < 0$. Circles indicate peak values of the u_x component, and squares indicate peak values of the u_y component; the vertical component is not plotted. The vertical line of points on the attenuation curves plotted against R-Projection are all from sites above the fault plane (R-Projection = 0), and have been plotted to the left of a broken scale.

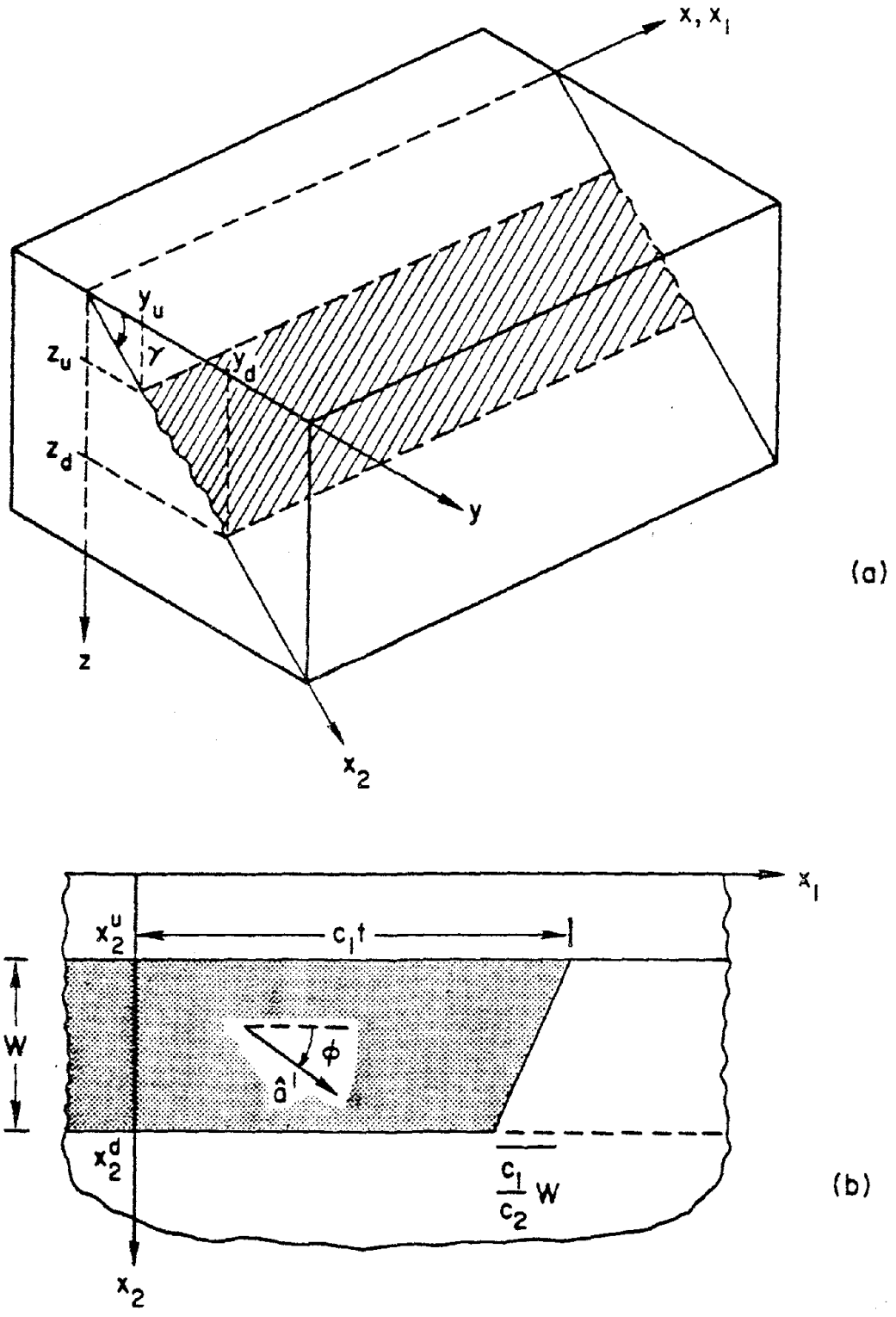

Figure 1. Coordinate system and fault model used in these calculations.

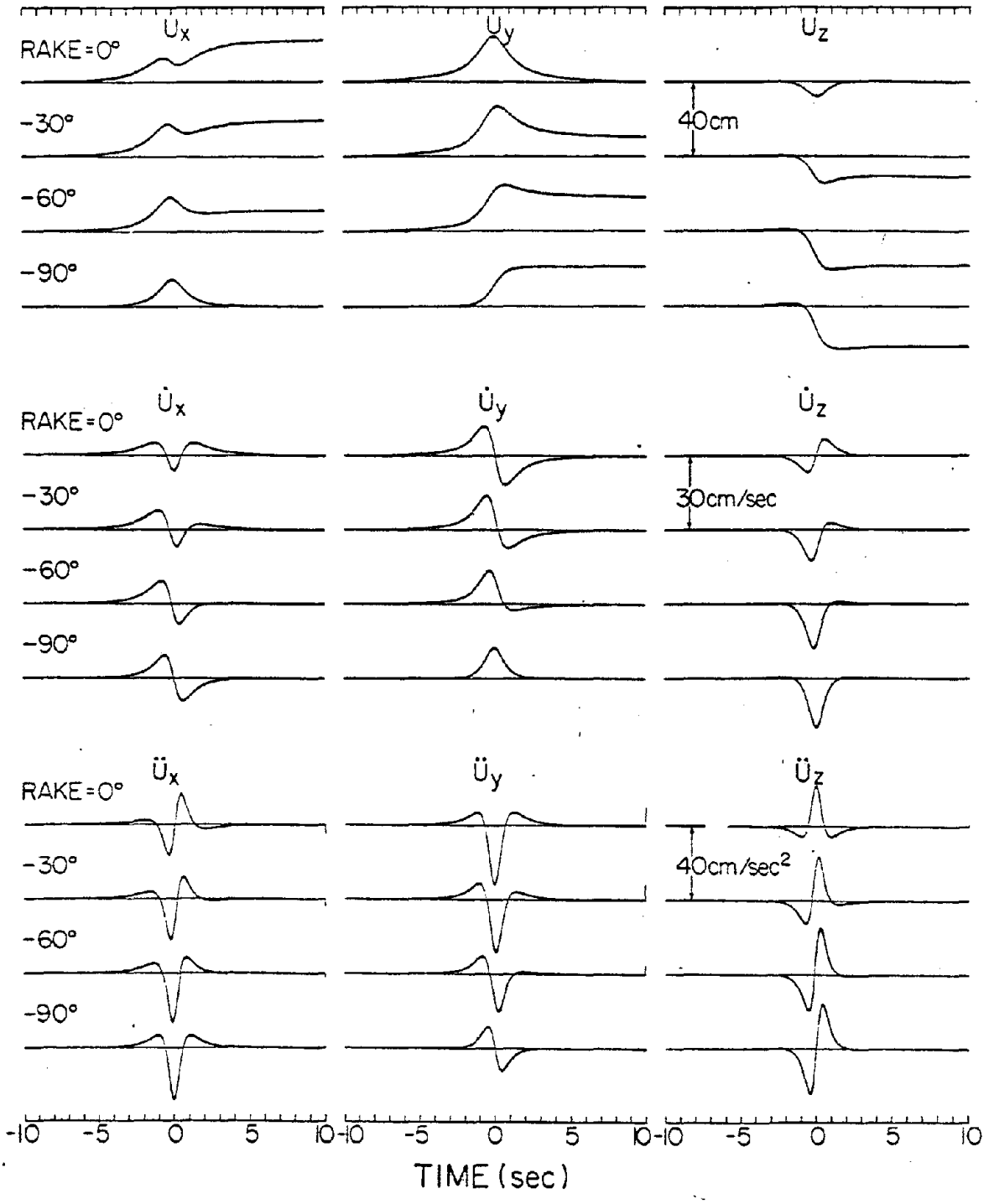

Figure 2. Evolution of synthetic waveforms on a vertical fault as the slip direction (rake) changes from pure strike slip (Rake = 0°) to pure thrust (Rake = −90°). This plot shows synthetic displacement (top), velocity (center) and acceleration (bottom). Other parameters are dip = 90°, $y = 5.0$ km, $y_u = 0.0$ km, $c_1 = 3.0$ km/sec, $c_2 = \infty$, $\Delta_o = 100$ cm, $z_u = 2.0$ km, $z_d = 10.0$ km. Synthetics are calculated at 50 points per second.

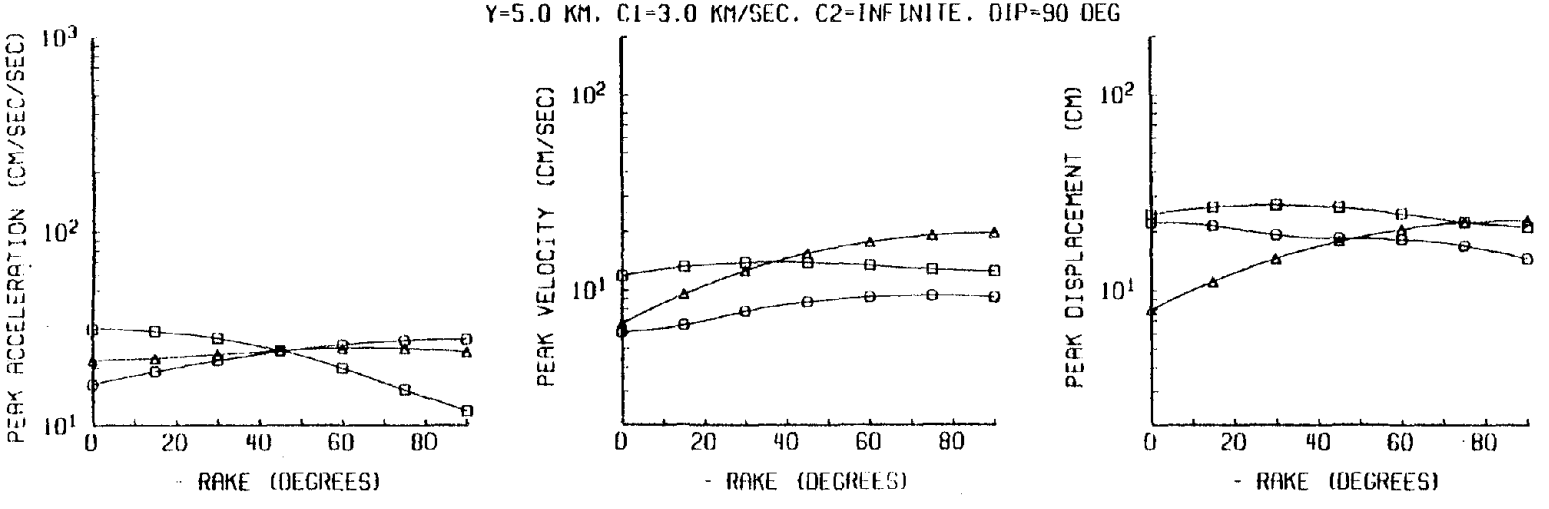

Figure 3. **Peak amplitudes as a function of rake near a vertical fault. Faulting parameters are the same as those for Figure 2. Symbols are: circle $-U_x$, square $-U_y$, triangle $-U_z$. Symbols are plotted at all values of the rake where calculations were carried out; curved lines are cubic spline interpolations.**

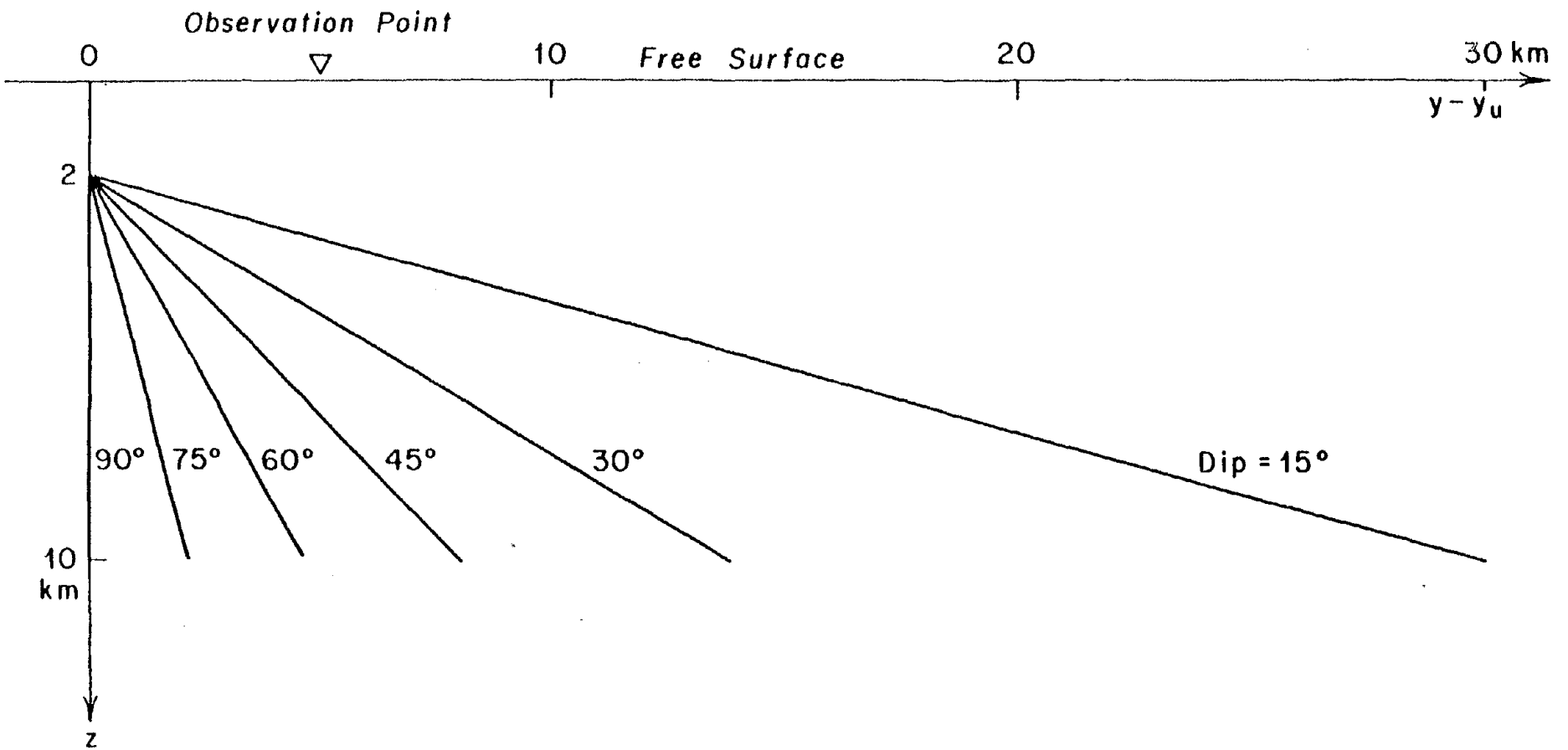

Figure 4. Observer-fault geometry for results shown in Figures 5 and 6.

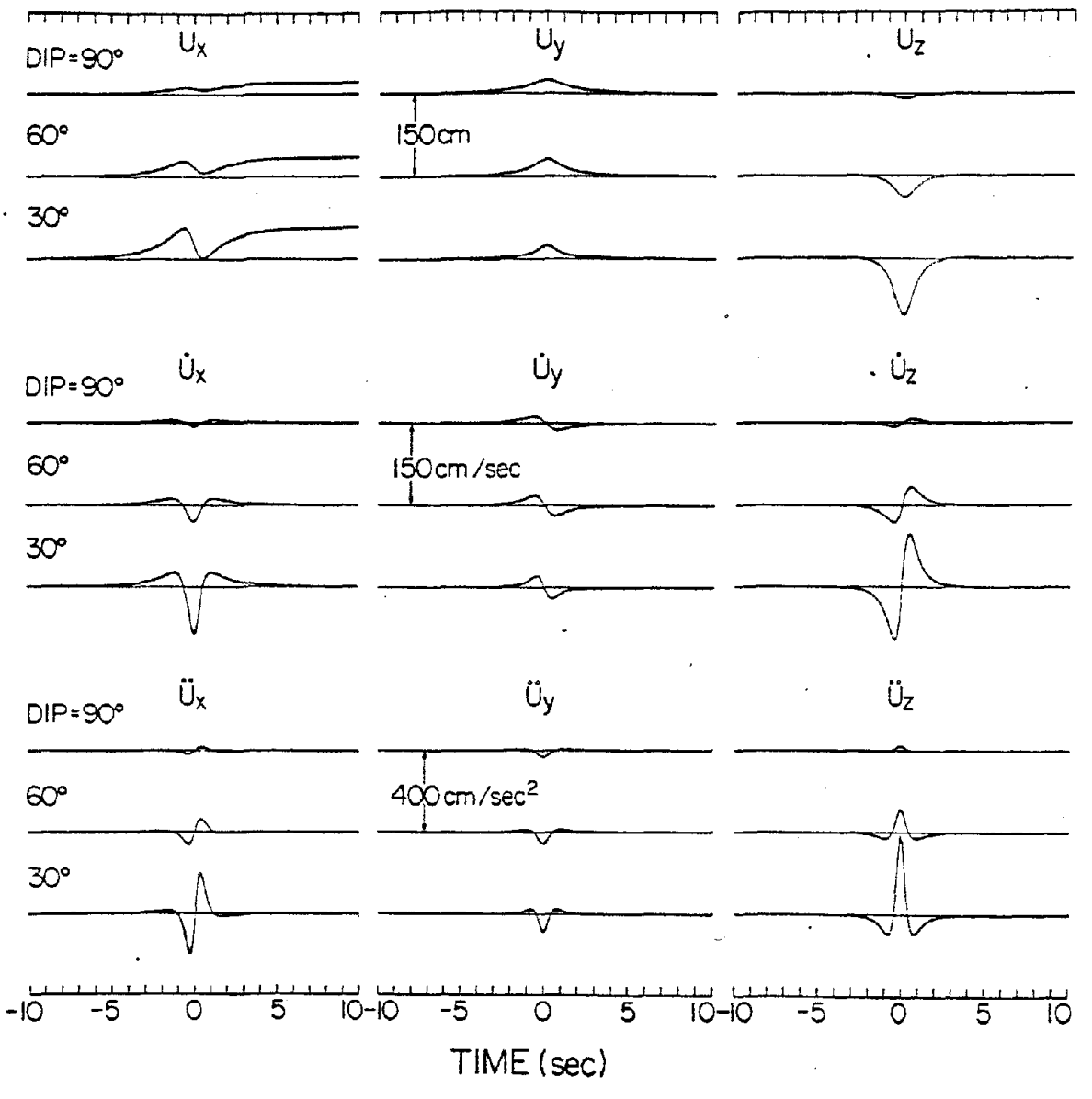

Figure 5. Evolution of synthetic waveforms above a strike slip fault of variable dip. The observation point is on the upper block, 5.0 km from the vertical projection of the top of the fault. Dip of 90° corresponds to a vertical fault. Synthetic displacement is at the top, velocity in the center, and acceleration at the bottom. Parameters are rake $=0°$, $y-y_u=5.0$ km, $c_1=3.0$ km/sec, $c_2=\infty$, $\Delta_o=100$ cm, $z_u=2.0$ km, $z_d=10.0$ km. Synthetics are calculated at 50 pts/sec.

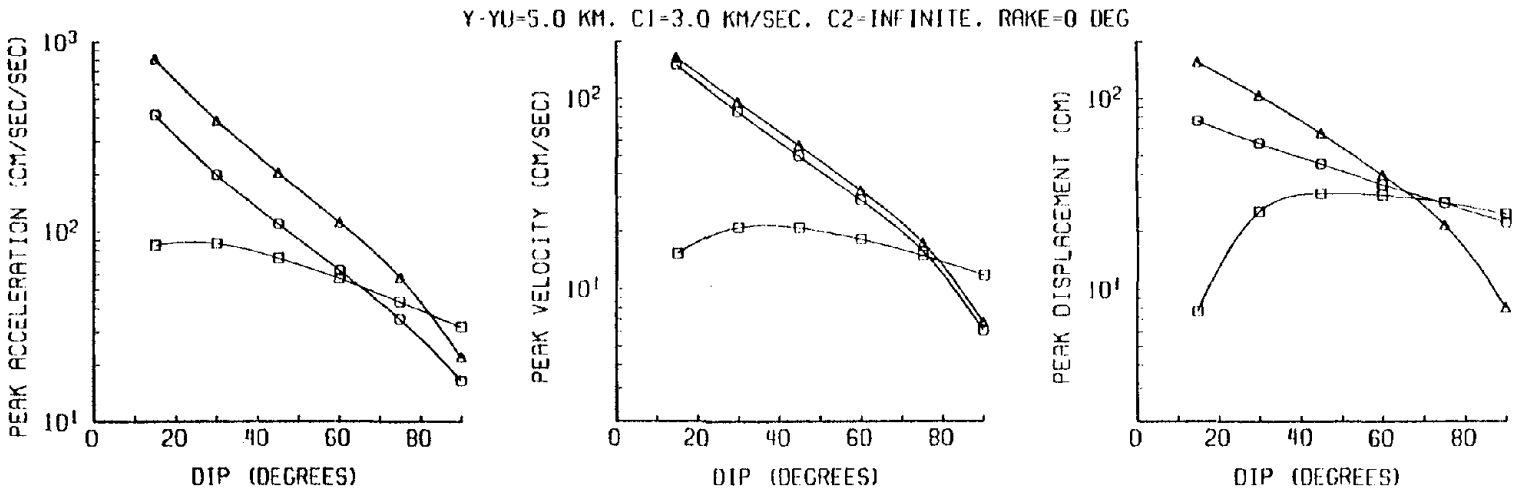

Figure 6. Peak amplitudes above a strike-slip fault of variable dip at a site on the upper fault block, 5.0 km from the vertical projection of the top edge of the fault. Model parameters are the same as in Figure 5. Symbols are circle $-U_x$, square $-U_y$, triangle $-U_z$. Symbols are plotted at each point where calculations are carried out, curves are cubic spline interpolations between these points.

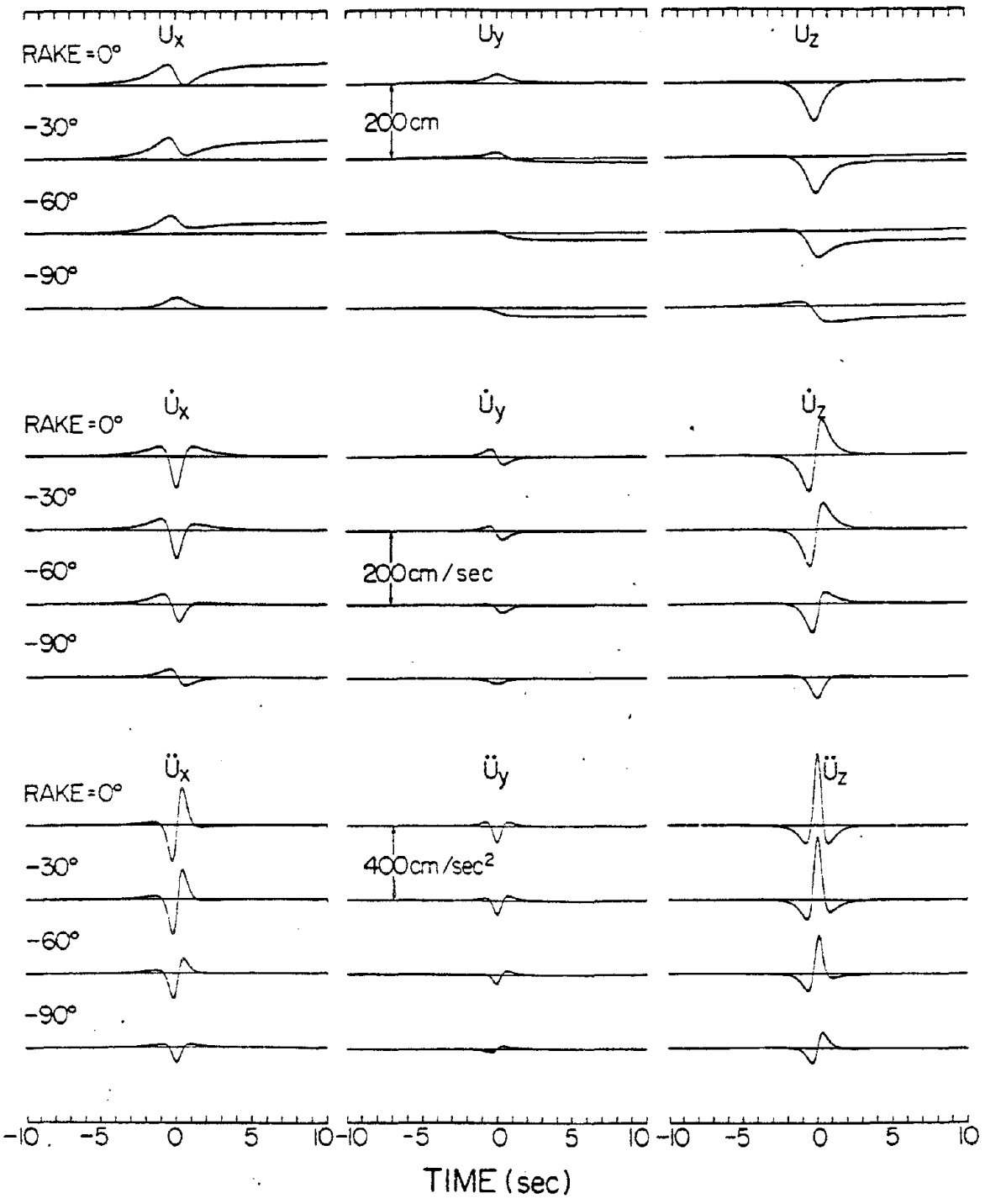

Figure 7. Evolution of synthetic waveforms on a dipping fault (dip =30°) as the slip direction changes from pure strike slip (rake = 0°) to pure thrust (rake = −90°). The observation point ($y - y_u = 5$ km) is above the fault on the upthrust block. Synthetic displacement is at the top, velocity in the center, and acceleration at the bottom. Parameters are dip = 30°, $y - y_u = 5.0$ km, $c_1 = 3.0$ km/sec, $c_2 = \infty$, $\Delta_o = 100$ cm, $z_u = 2$ km, $z_d = 10.0$ km. Synthetics are calculated at 50 points/second.

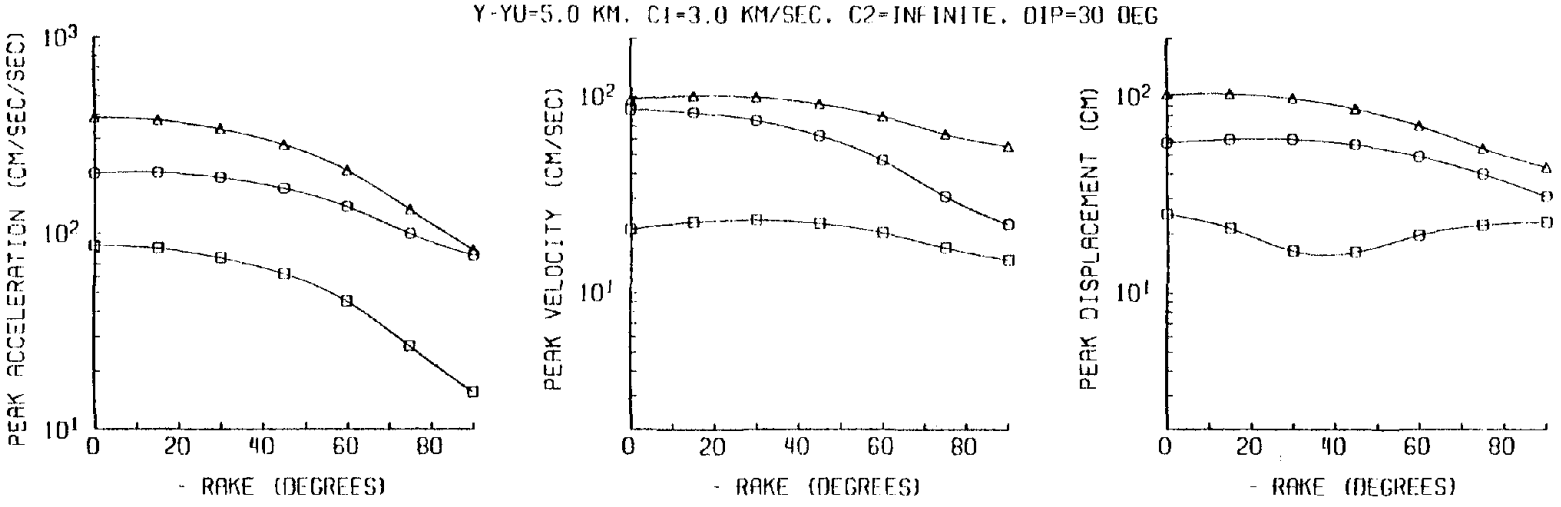

Figure 8. **Peak amplitudes as a function of rake on the upthrust block of a thrust fault. Model parameters are the same as those of Figure 7. Symbols are circle $-U_x$, square $-U_y$, triangle $-U_z$. Symbols are plotted at each value of the rake where calculations were carried out; curved lines are cubic spline interpolations.**

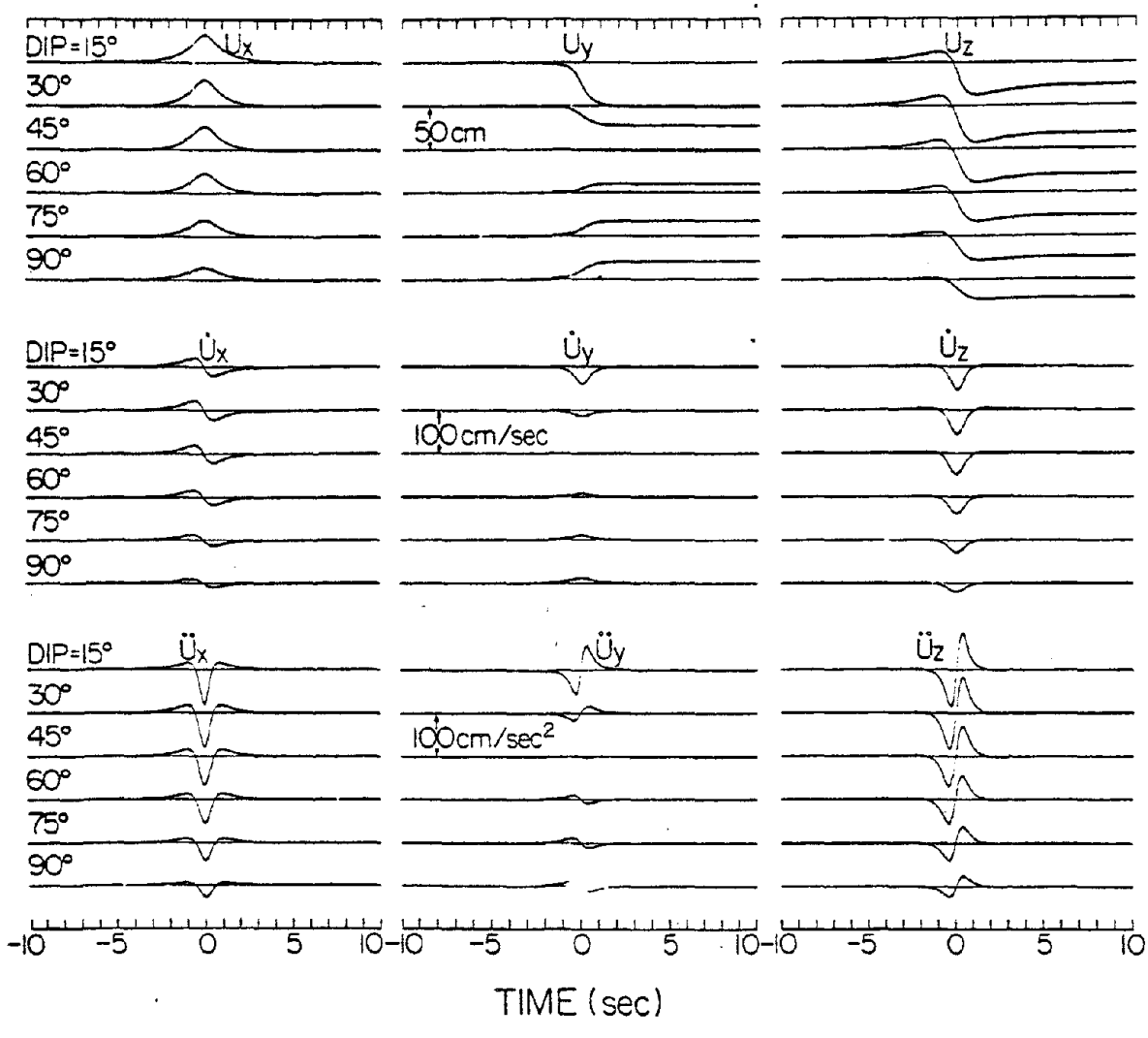

Figure 9. Evolution of synthetic waveforms above a thrust fault of variable dip. The observation point is on the upper block, 5.0 km from the vertical projection of the top of the fault. Dip of 90° corresponds to a vertical fault. Synthetic displacement is at the top, velocity at center, acceleration at the bottom. Parameters are rake $= -90°$, $y - y_u = 5.0$ km, $c_1 = 3.0$ km/sec, $c_2 = \infty$, $\Delta_0 = 100$ cm, $z_u = 2.0$ km, $z_d = 10.0$ km. Synthetics are calculated at 50 points/sec.

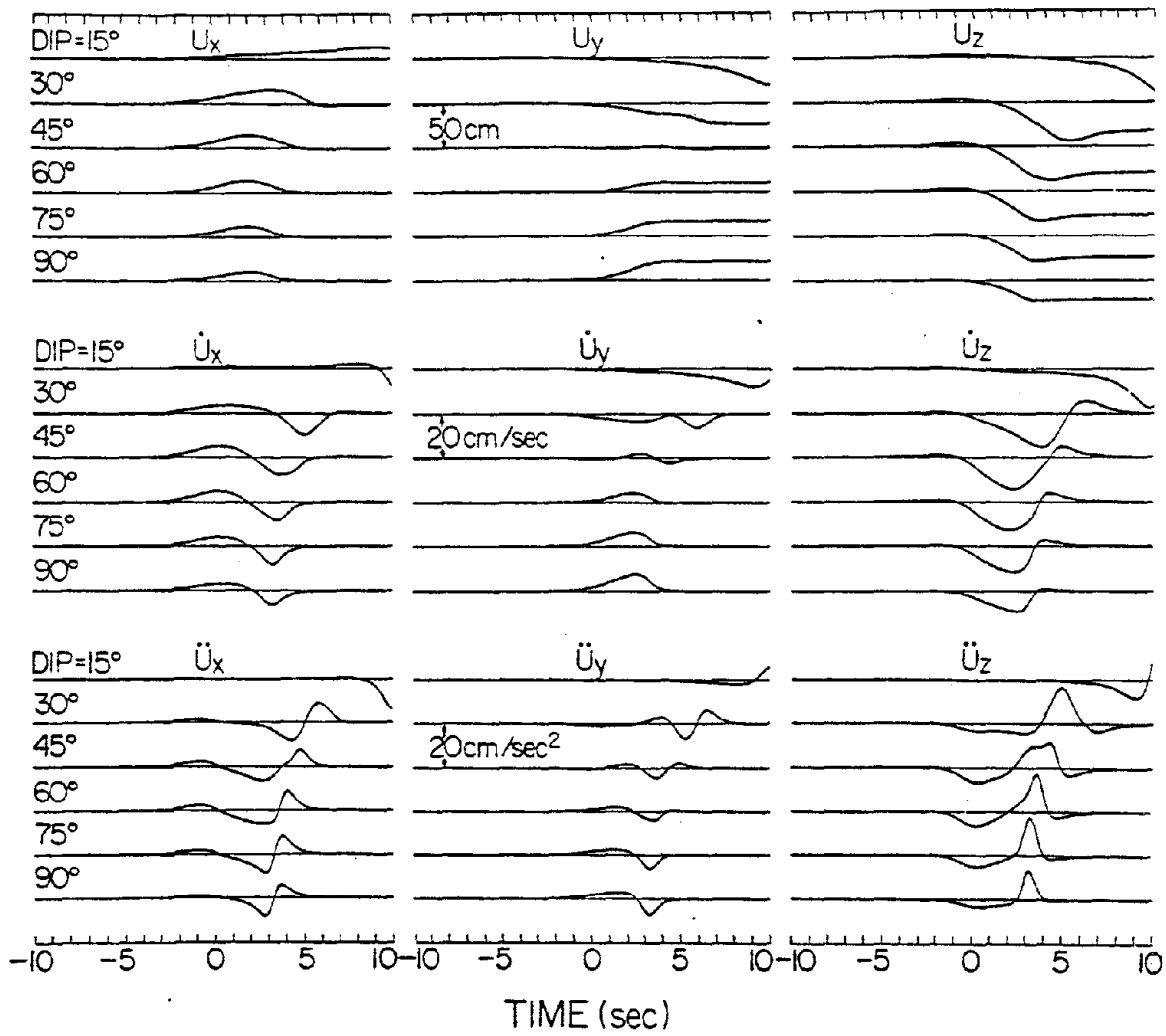

Figure 10. Equivalent of Figure 9, except that $c_2 = -2.5$ km/sec.

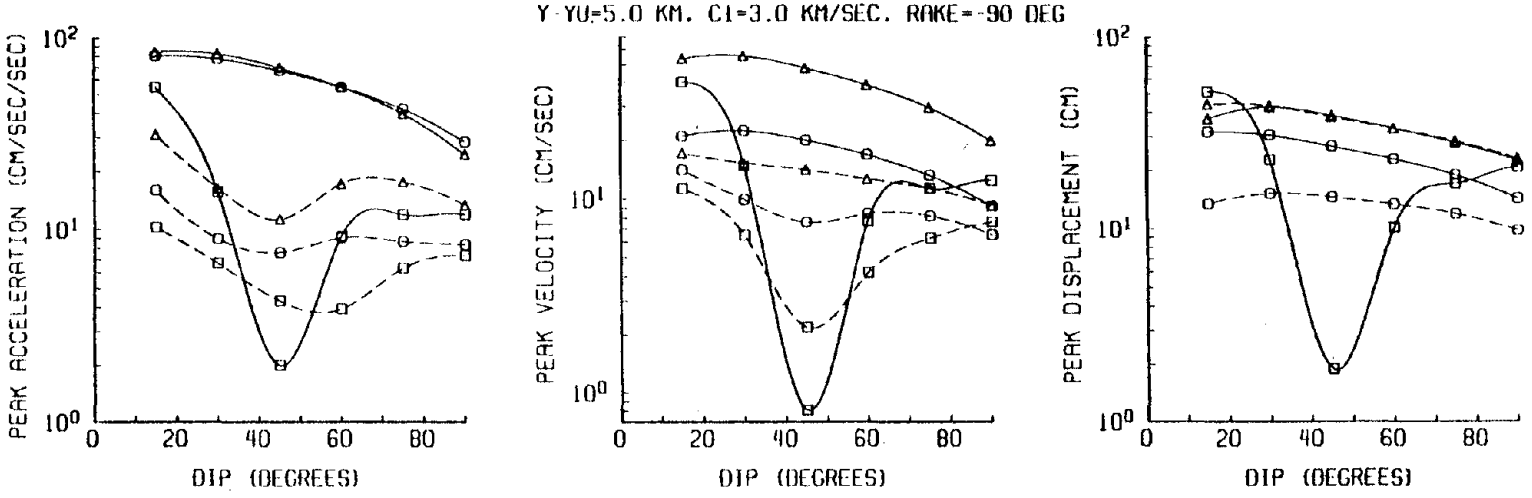

Figure 11. Peak amplitudes above a thrust fault of variable dip at a site on the upper fault block, 5.0 km from the vertical projection of the top edge of the fault. Model parameters are the same as in Fig. 9 and 10. Solid lines correspond to $c_2 = \infty$, dashed lines to $c_2 = 2.5$ km/sec. Symbols are circle $- U_x$, square $- U_y$, triangle $- U_z$. Symbols are plotted at each point where calculations are carried out; curves are cubic spline interpolations between these points.

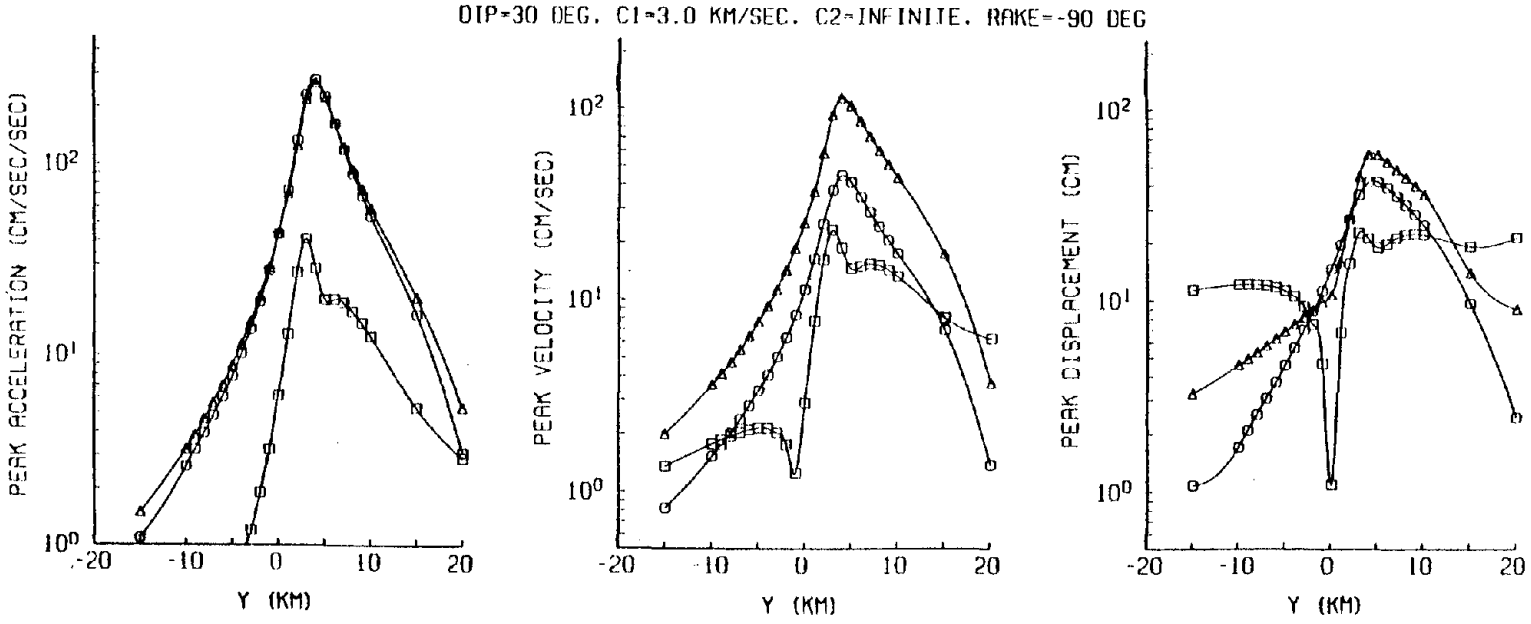

Figure 12. Peaks in acceleration, velocity, and displacement along a profile of sites perpendicular to a thrust fault with dip 30°. The upper edge of the fault occurs at $y_u = 3.464$ km. Model parameters are dip 30°, $c_1 = 3.0$ km/sec, $c_2 = \infty$, $\Delta_o = 100$ cm, $z_u = 2.0$ km, $z_d = 10.0$ km. Symbols are circle $- U_x$, square $- U_y$, triangle $- U_z$. Symbols are plotted at each point where calculations were performed, curves are cubic spline interpolations between these points.

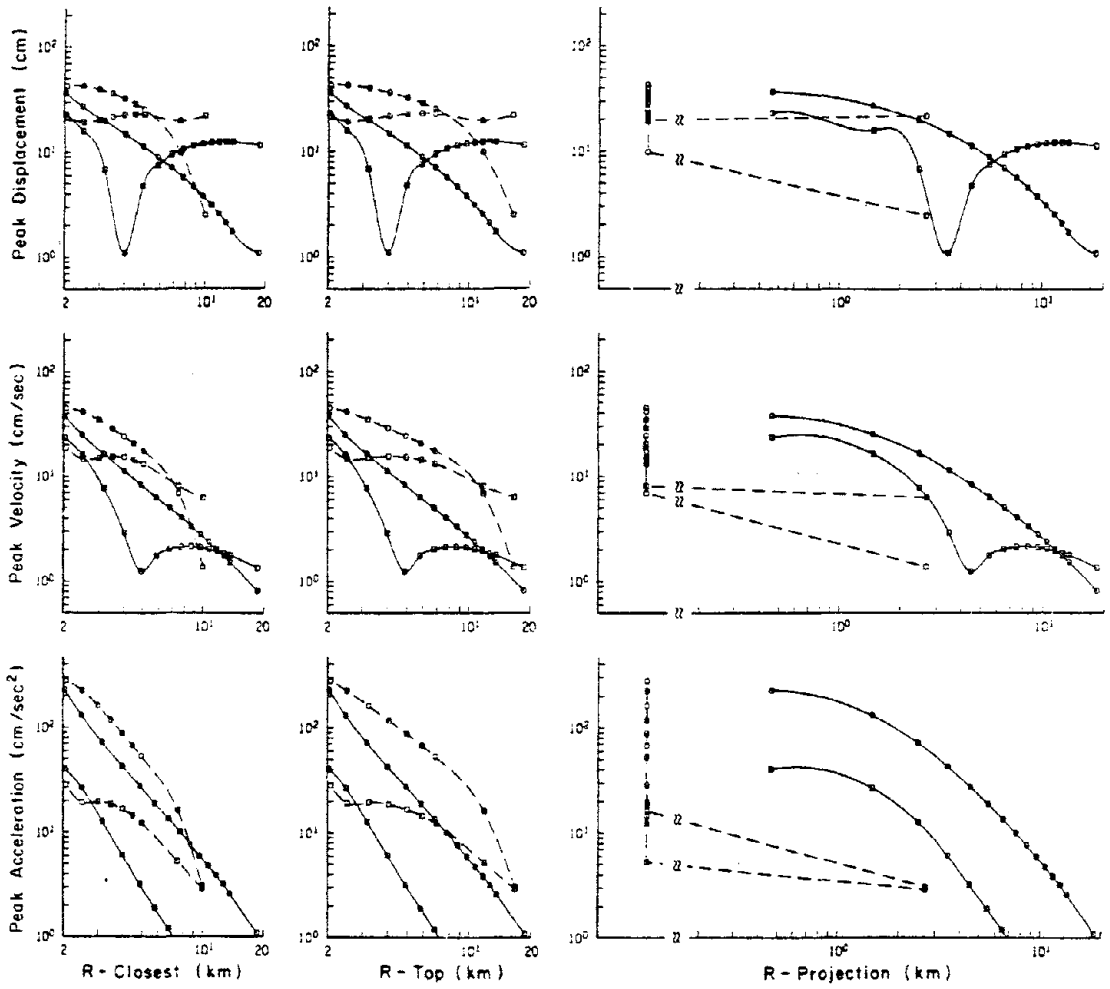

Figure 13. Peak amplitudes from Fig. 12 plotted against three measures of distance to the fault : R-Closest is the distance between the closest point on the fault rupture and the site, R-Top is the distance between the top edge of the fault rupture and the site, and R-Projection is the distance between the site and the nearest surface location of a vertical projection of the fault. Dashed lines connect points with $y - u_y > 0$ (on the upthrust block) and solid lines connect points with $y - y_u < 0$. Circles indicate peak values of the u_x component, and squares indicate peak values of the u_y component; the vertical component is not plotted. The vertical line of points on the attenuation curves plotted against R-Projection are all from sites above the fault plane (R-Projection = 0), and have been plotted to the left of a broken scale.

Finite Faults and Inverse Theory

with Applications to the 1979 Imperial Valley Earthquake*

Allen H. Olson† and Randy J. Apsel††

Abstract

Using a representation theorem from elastodynamics, subsurface slip on a known fault is formulated as the solution to an inverse problem in which recorded surface ground motion is the data. Two methods of solution are presented: the least squares method, which minimizes the squared differences between theory and data, and the constrained least squares method which simultaneously maintains a set of linear inequalities. Instabilities in the solution are effectively eliminated in both methods and the sensitivity of the solution to small changes in the data is quantitatively stated. The inversion methodology is applied to 77 components of near-field ground acceleration recorded during the October 15, 1979 Imperial Valley earthquake. The faulting is constrained to propagate bilaterally away from the epicenter at an average velocity of 90 percent of the shear wave speed on a vertical fault plane extending from the surface to ten kilometers depth. Inequality constraints are used to keep the faulting sequence physically reasonable by maintaining right lateral motion and positive slip velocity. The preferred solution is stable and provides a good fit to the data; it is also realistic and consistent with observed surface offsets and independent estimates of seismic moment.

1. Introduction

Faulting is characterized by the slipping of one side of a fault surface with respect to the other. If the earth is modeled as an elastic solid, then the displacement field due to a point dislocation can be taken as a Green's function for the earthquake faulting problem. The displacement field at all points in the earth due to an arbitrary distribution of slip on a fault is expressed as an integral over the fault surface of the slip distribution convolved with the Green's function. The slip distribution enters linearly into the integrand so that it may be obtained as the solution to a linear inverse problem in which recorded ground motion at the earth's surface is taken as data.

---

*Presented at: *The Dynamics of Earthquake Faulting as Inferred from Recordings of Strong Ground Motion.* Hyatt Lake Tahoe Hotel, Incline Village, Nevada, October 21—23, 1981.

†Institute of Geophysics and Planetary Physics, Scripps Institution of Oceanography, University of California, San Diego, La Jolla, California, 92093.

††Del Mar Technical Associates, P.O. Box 1083, Del Mar, California, 92014.
Present address: Sierra Geophysics, 15446 Bell-Red Rd., suite 400, Redmond, Washington, 98052.

In order for a particular slip distribution to be an acceptable solution to the inverse problem, it must satisfy the following three conditions.

(1) The solution must explain the data.

(2) The solution must be physically reasonable (consistent with independent constraints).

(3) If more than one solution fits the data equally well, additional information must be supplied to uniquely define which solution is being obtained.

Conditions (1) and (2) simply amount to finding a realistic model which fits the data. Often, there may be many solutions which fit the data equally well. When this occurs the solution may be divided into two parts: a stable and an unstable part. The unstable part of the solution is comprised of distributions of slip which have little or no effect on the data. By definition, an arbitrary amount of the unstable part may be added to the stable part of the solution without affecting the fit to the data. In the presence of this effective nonuniqueness, condition (3) requires that additional information be supplied to uniquely define which solution is to be obtained. For example, the added information might lead to: the smallest solution (small in the sense that the integral of the slip over the fault plane is minimized); or, the slip distribution most like a preferred solution. No matter which solution is obtained, only the stable part is demanded by the data; the unstable aspects of the solution are simply not recoverable based upon the data alone.

The following discussion is divided into three major parts contained in Sections 2, 3, and 4. In Section 2, the forward problem of computing the theoretical ground motion due to earthquake faulting is reduced to specifying a set of parameters which correspond to slip across planar sections of fault surface. The slip parameters are linearly related to the ground motion data by a matrix. Two methods of inverting the matrix are presented in Section 3: the least squares method which minimizes the squared differences between theory and data and the constrained least squares method which simultaneously maintains a set of inequality constraints. A stabilizing procedure is also presented which determines the significance of particular details in the solution. In Section 4, the inversion methodology is applied to 77 components of near-field ground acceleration recorded during the October 15, 1979 Imperial Valley earthquake; four solutions are obtained which fit the data. Differences in the four solutions represent either unstable or nonphysical fault motions. The fourth solution is preferred since it: (1) provides a good fit to the data; (2) is physically reasonable; and (3) is related to the to the data in a stable manner.

2. Theoretical Formulation of the Forward Problem

2.1 A Representation Theorem in Elastodynamics

The representation theorem provides an expression for the radiation in an elastic media resulting from the creation of a discontinuity in the displacement and stress fields across a fault surface. The Green's function, G, used in the representation is the response of the medium to a point force in the absence of discontinuities. This Green's function can be used to satisfy any boundary condition on the fault surface; hence, the elastodynamic equations need only be solved once.

A derivation of the representation theorem for general anisotropic elastic media is given by Burridge and Knopoff (1964). Since faulting is defined by the slipping of one side of a fault surface relative to the other, the representation theorem is specialized to the case where the stress field is continuous across the fault surface and only the displacement field is allowed to be discontinuous:

$$U^i(y,t) = \int_{-\infty}^{+\infty} \int_S s(x,\tau)\, n(x) : G^i(x, t-\tau; y)\, dx\, d\tau . \qquad (2\text{-}1)$$

The first integral in Eq. (2-1) is a convolution in time, t; the second is over the fault surface S. In Figure 1, S is illustrated as a plane striking along the x_1 axis at a dip δ from the vertical. The unit normal to the fault surface is given by the vector $\mathbf{n}(x)$ which depends upon position x. The slip vector, $\mathbf{s}(x,\tau)$, is the local discontinuity in displacement across the fault surface at time $t=\tau$ and position x. The quantity $U^i(y,t)$ is the i'th component of displacement at position y and time t resulting from the slip on S. The Green's function, $\mathbf{G}^i(x,t-\tau;\, y)$, is the second order stress tensor in the unfaulted elastic media as a function of position x and time t due to an impulsive point load applied at position y in the i'th coordinate direction at time $t=\tau$. The tensor components of $\mathbf{G}^i(x,t-\tau;\, y)$ can also be interpreted as the i'th component of displacement at position y due to a point dislocation at x. Once the Green's function is known and the slip prescribed, the theoretical ground displacements are obtained by performing the integration in Eq. (2-1). The symbol : is used to denote the inner product of the components of the two second order tensors $\mathbf{s}\,\mathbf{n}$ and $\mathbf{G}$.

2.2 Discretization of the Fault Surface

In this study, the fault surface is divided into a set of cells, each cell being a rectilinear planar zone. Locations within each cell are assumed to undergo the same slip within a specified time shift. Within each cell, the slip is described by a two component vector in the plane of the fault having an unknown time dependence (a three component vector can be just as easily used if the fault surface is allowed to separate). The functional form of the parameterization is given in Eqs. (2-2) through (2-4).

$$\mathbf{s}(x,t) = \sum_{j=1}^{J} X_j(x) \sum_{k=-K}^{K} s_{jk} P_k(x,t) \tag{2-2}$$

$$X_j(x) = \begin{cases} 1 & \text{if } x \text{ in } j\text{'th cell} \\ 0 & \text{otherwise} \end{cases} \tag{2-3}$$

$$P_k(x,t) = F(t - T(x) + k\,\delta t) \tag{2-4}$$

The first sum in Eq. (2-2) is over the J cells representing the fault surface. The second sum defines the slip within the j'th cell: the vector s_{jk} is the slip direction of the j'th cell at the k'th time point and has two components in the plane of the fault; the function $P_k(x,t)$ contains the time dependence of the k'th slip. Each cell is allowed to slip $2K+1$ times at successive increments of δt in time; each slip varies according to the specified time function $F(t)$. The absolute time at which slip takes place within the cell is centered about $T(x)$.

Equation (2-2) simplifies if each cell is allowed to slip only once; in which case, the sum over k goes away and the slip within each cell varies as $F(t)$, progressing through the cell as a rupture front prescribed by $T(x)$. When the cells are allowed to slip more than once, $T(x)$ represents an average rupture time. By only allowing slip to occur within a prescribed time window about a predetermined average rupture time, the number of parameters is kept to a minimum. This also allows for the local rupture velocity to differ from the average rupture velocity.

By substituting Eq. (2-2) for $\mathbf{s}(x,t)$ in Eq. (2-1), the integration over x and convolution in t can be performed since the space and time dependence of the integrand is known completely.

$$U^i(y,t) = \sum_{j=1}^{J} \sum_{k=-K}^{K} s_{jk} \cdot \mathbf{g}^j(y, t + k\,\delta t) \tag{2-5}$$

The vector $\mathbf{g}^j(y,t+k\,\delta t)$ is the Green's function for the j'th cell at position y in i'th component direction. Equation (2-5) is a matrix version of the integral in Eq. (2-1). The columns of the matrix correspond to components of the Green's function vectors $\mathbf{g}^j(y,t+k\,\delta t)$ for fixed values of j and k. Since s_{jk} and $\mathbf{g}^j(y,t+k\,\delta t)$ are two-component vectors, the total number of scalar parameters is $2J(2K+1)$. The number of rows in the matrix equals the number of components (index i) being considered times the number of time points for which each component is sampled.

The Green's function for the cell, $\mathbf{g}^j$, is the integral of the point source Green's function, $\mathbf{G}$, over the cell according to a prescribed rupture velocty. In practice, the integral in Eq. (2-1) is done

numerically by sampling the Green's function, G, at a grid-work of points on the fault plane. The Green's function at a location which does not coincide with a sample point is approximated by the Green's function at the nearest grid-point subject to a time shift; the time shift is determined according to the phase velocity of the dominant body wave (usually the S wave). This approximation is exact for nondispersive waves and is a very good approximation when one particular body wave dominates the Green's function. For a line source of uniform slip, this numerical integration is equivalent to convolving a single Green's function with a box car.

The continuous integral in Eq. (2-1) is known to represent an underdetermined problem for the solution $s(x,t)$ (Backus and Gilbert, 1968). However, the discrete system in Eq. (2-5) appears to be overdetermined since the number of unknown parameters, s_{jk}, may be far less than the number of time points of observed ground motion. This apparent difference between the continuous and discrete problems disappears if the cells on the fault are made sufficiently small so that the matrix for the discrete problem becomes ill-conditioned, thereby allowing many solutions. The ill-conditioning results from redundancies in the matrix which occur for two principal reasons: (1) many columns in the matrix are simply time shifts of each other by an amount $k\,\delta t$; and (2) columns corresponding to cells which are spatially close to each other are very similar.

3. Inverse Theory for the Discrete Problem

Inverse theory for the discrete problem requires solving a system of linear equalities such as those in Eq. (2-5). In general, these equalities may be satisfied exactly or approximately, depending on whether the system is underdetermined or overdetermined. Two methods of solution are presented in this section; they are, the least squares method, which satisfies the equalities by minimizing the sum of the squared differences between calculated and observed data, and the constrained least squares method which simultaneously maintains a set of linear inequalities. Measures of stability for each of these two methods are presented so that the significance of particular details in the solution can be determined with respect to possible nonuniqueness.

3.1 The Generalized Inverse and the Least Squares Solution

The system of linear equality constraints in Eq. (2-5) can be written more compactly as

$$\mathbf{A}\,\mathbf{x} = \mathbf{f}. \qquad (3\text{-}1)$$

The vector $\mathbf{x}$ of length n corresponds to the unknown parameters; the vector $\mathbf{f}$ of length m contains the data; and the matrix $\mathbf{A}$ with m rows and n columns contains the theory relating the parameters to the data. If $m=n$ and $\mathbf{A}$ is nonsingular, then $\mathbf{x}$ is found by calculating the inverse of $\mathbf{A}$. In the presence of inconsistent data and/or a singular matrix, the exact inverse of $\mathbf{A}$ is not defined and an alternate definition of inverse is needed. One such alternative is the generalized inverse (Penrose, 1955) which always exists and includes the exact inverse as a special case.

An overview of the literature on the generalized inverse, *GI*, is presented in Ben-Israel and Charnes (1963). Of the many ways of defining *GI*, the one chosen here is attributed to Penrose (1956). The norm being used is the Euclidean norm defined by

$$|| \mathbf{x} || = (\mathbf{x}'\mathbf{x})^{1/2} = \left(\sum_{i=1}^{n} x_i^2 \right)^{1/2} \qquad (3\text{-}2)$$

in which $\mathbf{x}'$ denotes the transpose of $\mathbf{x}$.

Definition: Among all solutions $\mathbf{x}$ *satisfying*

$$\textit{minimum} \; || \mathbf{A}\mathbf{x} - \mathbf{f} || \,, \tag{3-3}$$

there is a unique solution, $\tilde{\mathbf{x}}$, *which satisfies*

$$\textit{minimum} \; || \mathbf{x} || \,. \tag{3-4}$$

The generalized inverse of $\mathbf{A}$, $\tilde{\mathbf{A}}$, *is the matrix which produces* $\tilde{\mathbf{x}}$ *from the data.*

$$\tilde{\mathbf{x}} = \tilde{\mathbf{A}}\mathbf{f} \,. \tag{3-5}$$

Note that $\tilde{\mathbf{x}}$ is: 1) the least squares solution in the presence of inconsistent data; 2) the smallest solution satisfying the data exactly for the underdetermined case; and 3) the smallest least squares solution in the presence of inconsistent data and a singular matrix. In the remaining discussion, $\tilde{\mathbf{x}}$ refers to the *GI* solution while $\mathbf{x}$ refers to other candidate solutions to Eq. (3-3).

A discussion of the construction of $\tilde{\mathbf{A}}$ is given by Lawson and Hanson (1974) in terms of orthogonal decompositions. A particular decomposition which proves useful in examining the stability of $\tilde{\mathbf{x}}$ is the singular value decomposition, *SVD*, given by

$$\mathbf{A} = \mathbf{U}\Lambda\mathbf{V}' \,. \tag{3-6}$$

$\mathbf{U}$ and $\mathbf{V}$ are orthogonal matrices of dimension m by n, and n by n, respectively. The matrix Λ is an n by n diagonal matrix in which the diagonal elements, λ_{ii}, are arranged in decreasing order down the diagonal. Since $\mathbf{U}$ and $\mathbf{V}$ have orthonormal columns, the inverse of each is is simply its transpose so that the *GI* of $\mathbf{A}$ is

$$\tilde{\mathbf{A}} = \mathbf{V}\Lambda^{-1}\mathbf{U}' \,. \tag{3-7}$$

The components of Λ^{-1} are defined by

$$\left(\Lambda^{-1}\right)_{ii} = \begin{cases} \lambda_{ii}^{-1} \text{ for } \lambda_{ii} > 0 \\ 0 \quad \text{for } \lambda_{ii} = 0 \end{cases} . \tag{3-8}$$

The inclusion of the second criterion in Eq. (3-8) allows for the case where the exact inverse does not exist.

The null space of $\mathbf{A}$ is spanned by the columns of $\mathbf{V}$ associated with the zero singular values. Distributions of $\mathbf{x}$ which lie in the null space vanish when multiplied by $\mathbf{A}$. The exact inverse does not exist since information about the null space can never be recovered. The *GI* does exist because it sets the null space component of $\mathbf{x}$ to zero. In the case of inconsistent data, the *GI* similarly considers only that part of the data which is in the column space of $\mathbf{A}$. In the remaining discussion, the *GI* solution is referred to as simply the least squares solution.

Although the least squares solution is unique in theory, it may be very unstable in practice since small changes in the data can often lead to large changes in the solution. One useful measure of stability is presented in Franklin (1970) where a perturbation in the data, $\delta\mathbf{f}$, is compared with the related perturbation in the solution, $\delta\mathbf{x}$. The relative change in the solution divided by the relative change in the data is

$$S = \left(\frac{|| \delta\mathbf{x} ||}{|| \mathbf{x} ||} \right) \left(\frac{|| \delta\mathbf{f} ||}{|| \mathbf{f} ||} \right)^{-1} . \tag{3-9}$$

For a stable problem, the value of S should not be much greater than one. The maximum value that S can attain is called the condition number of A; Franklin (1970) shows that the condition number is given by the ratio of the largest to smallest singular value in Λ. The example given there is that a 3 percent change in the data could produce a 60 percent change in the solution if the condition number is 20. A condition number of 20 is not an uncommon occurrence.

Another useful measure of stability is obtained through statistics by determining the variance in the solution due to random errors of known variance, σ^2, in the data (Backus and Gilbert, 1970; Jackson, 1972; Wiggins, 1972). The covariance of the solution parameters caused by adding independent

random errors to the data is

$$E|\delta\tilde{\mathbf{x}}\,\delta\tilde{\mathbf{x}}'| = \sigma^2 \mathbf{V}\boldsymbol{\Lambda}^{-2}\mathbf{V}', \tag{3-10}$$

where $E|\ |$ denotes the usual expected value and $\delta\tilde{\mathbf{x}}$ is the change in the solution vector. Small singular values in $\boldsymbol{\Lambda}$ give rise to large covariances in the solution parameters since Eq. (3-10) involves taking the squared inverse of small numbers. Just as in the condition number, instability is indicated by small singular values.

One method of handling ill-conditioning is to filter the solution. Filtering eliminates the ill-conditioned part of the solution and involves a trade off between resolution and variance (Backus and Gilbert, 1970; Gilbert, 1971; Jackson, 1972; Wiggins, 1972) By filtering, linear combinations of the parameters are determined rather than determining any particular parameter uniquely. If the components of $\mathbf{x}$ correspond to values of a sampled continuous function, then the linear combinations of $\mathbf{x}$ mostly involve neighboring parameters so that the filter is performing a local average of the unknowns.

A pseudo low-pass filter, $\mathbf{V}\mathbf{L}\mathbf{V}'$, is defined by a set of filter coefficients in the diagonal matrix $\mathbf{L}$. The matrix $\mathbf{L}$ consists of ones in the first i diagonal entries and zeroes in the last $n-i$ entries. The filtered version of $\mathbf{x}$ is denoted by $\mathbf{y}$ where

$$\mathbf{y} = \mathbf{V}\mathbf{L}\mathbf{V}'\tilde{\mathbf{x}}. \tag{3-11}$$

The filter retains only that part of $\mathbf{x}$ associated with the large singular values. The components of $\mathbf{y}$ represent local averages of the components of $\mathbf{x}$ in as much as the rows of the filter matrix are concentrated about the diagonal. If $\mathbf{L}$ has all ones on the diagonal, $i = n$, then the filter is the identity matrix and no filtering is being done. The filter becomes increasingly spread about the diagonal as the number of zeroes along the diagonal of $\mathbf{L}$ is increased, thus sacrificing resolution.

Using the definition of $\tilde{\mathbf{x}}$ given in Eqs. (3-5) and (3-6), along with Eq. (3-11), the filtered least squares solution becomes

$$\mathbf{y} = \mathbf{V}\mathbf{L}\boldsymbol{\Lambda}^{-1}\mathbf{U}'\mathbf{f}. \tag{3-12}$$

The matrix $\mathbf{L}$ cancels the large values in $\boldsymbol{\Lambda}$ which arise from division by small numbers. The filter can simply be thought of as modifying the GI of Eqs. (3-7) and (3-8) by treating the small singular values as zero and not allowing them to participate in the solution. The covariance matrix for $\mathbf{y}$ is

$$E|\delta\mathbf{y}\,\delta\mathbf{y}'| = \sigma^2 \mathbf{V}\mathbf{L}^2\boldsymbol{\Lambda}^{-2}\mathbf{V}' \tag{3-13}$$

where $\delta\mathbf{y}$ is the change in the filtered solution vector due to random errors of variance σ^2 in the data. The small singular values of $\boldsymbol{\Lambda}$ are canceled by zeroes in $\mathbf{L}$, having the net effect of decreasing the variance. The number of nonzero values in $\mathbf{L}$ is at the discretion of the user and the transition from one to zero along the diagonal can either be abrupt or smooth just as in Fourier filtering. Any number of transitions may yield similar variances.

Another way to achieve stability in the inversion is to append equations to the original matrix $\mathbf{A}$ in such a way that only the unstable part of the solution is affected. To isolate the unstable part of the solution, a pseudo high-pass filter is defined in terms of a diagonal matrix $\mathbf{H}$ containing zeroes in the first i diagonal entries and ones in the last $n-i$ entries. The unstable part of the solution, $\mathbf{e}$, is given by

$$\mathbf{e} = \mathbf{V}\mathbf{H}\mathbf{V}'\tilde{\mathbf{x}}. \tag{3-14}$$

By defining $\mathbf{L}$ and $\mathbf{H}$ in this manner, the solution $\tilde{\mathbf{x}}$ to the least squares problem is viewed as the sum of two parts, a stable and an unstable part.

$$\tilde{\mathbf{x}} = \mathbf{y} + \mathbf{e} \tag{3-15}$$

If a smoother transition is desired in the filter, the only requirement for Eq. (3-15) to hold is that the diagonal elements of $\mathbf{L}$ and $\mathbf{H}$ sum to unity.

$$\mathbf{L} + \mathbf{H} = \mathbf{I}\ \text{(identity)} \tag{3-16}$$

The inversion is stabilized by appending a high-passed set of equalities to the original matrix and data.

$$\begin{bmatrix} \mathbf{A} \\ k_o \mathbf{V}\mathbf{H}\mathbf{V}' \end{bmatrix} \{\mathbf{x}\} = \begin{Bmatrix} \mathbf{f} \\ \mathbf{b} \end{Bmatrix} \tag{3-17}$$

The augmented matrix and data will be denoted by $\mathbf{A}_a$ and $\mathbf{b}_a$ respectively. If k_o is set very large and $\mathbf{b}$ is set equal to zero, the unstable part of $\mathbf{x}$ is effectively eliminated as in the low-pass filter example above. By adjusting k_o, H, and b in Eq. (3-17), the ill-conditioned vector e may be eliminated, made small, or used to make $\mathbf{x}$ resemble some preferred solution. Inversion of the augmented system is stable provided k_o is set large enough to result in a stable condition number.

The *SVD* of the augmented matrix, $\mathbf{A}_a$, is

$$\mathbf{A}_a = \mathbf{U}_a \Lambda_a \mathbf{V}', \tag{3-18}$$

where

$$\left(\Lambda_a\right)_{ii} = \sqrt{\lambda_{ii}^2 + (k_o H_{ii})^2} \tag{3-19}$$

and

$$\mathbf{U}_a = \begin{bmatrix} \mathbf{U}\Lambda_a^{-1}\Lambda \\ k_o \mathbf{V}\Lambda_a^{-1}\mathbf{H} \end{bmatrix}. \tag{3-20}$$

The matrix V is unchanged and the singular values are ordered in the diagonal matrix Λ_a. The *SVD* of $\mathbf{A}_a$ is easily verified: (1) the columns of $\mathbf{U}_a$ and V are orthonormal; (2) the diagonal matrix Λ_a has positive elements; and (3) the equality in Eq. (3-18) is satisfied. Appending equations reduces the condition number since previously small singular values become larger in Eq. (3-19); this is a much more stable situation.

The least squares solution to the augmented system is $\mathbf{y}_a$, where

$$\mathbf{y}_a = \mathbf{V}\Lambda_a^{-2}(\Lambda\mathbf{U}'\mathbf{f} + k_o\mathbf{H}\mathbf{V}'\mathbf{b}). \tag{3-21}$$

If k_o is set very large and $\mathbf{b}$ set to zero, the last $n-i$ singular values in Λ_a become very large; when these terms are inverted in Eq. (3-21), the ill-conditioned part of the solution is effectively eliminated and $\mathbf{y}_a$ takes on the same value as the filtered solution $\mathbf{y}$ in Eq. (3-12).

If $\mathbf{b}$ is set to zero, k_o set to an intermediate value between the largest and smallest singular value, and i set to zero so that the appended matrix is the scaled identity matrix; then, Eq. (3-21) reduces to the damped least squares solution of Levenberg (1944) and Neumann (1981). The damped least squares solution is $\mathbf{y}_d$, where

$$\mathbf{y}_d = \mathbf{V}\Lambda(\Lambda^2 + k_o^2\mathbf{I})^{-1}\mathbf{U}'\mathbf{f}. \tag{3-22}$$

In damped least squares, the ill-conditioned part of the solution is suppressed while the stable part is affected by an amount determined by k_o; usually k_o is taken to be small.

3.2 The Constrained Least Squares Solution

Inequality constraints arise when bounds are placed on some aspect of the solution. These constraints can occur when the solution parameters correspond to physical quantities which may be required to be positive, or not allowed to exceed a certain maximum value. Conventional least squares as presented in Section 3.1 does not incorporate inequality constraints. The following defines an extension of the *GI* for the constrained least squares problem.

Definition: Among all solutions $\mathbf{x}$ *satisfying*

$$\mathbf{G}\mathbf{x} > \mathbf{h}, \tag{3-23}$$

and

$$\textit{minimum} \; ||\,\mathbf{A}\mathbf{x} - \mathbf{f}\,||, \tag{3-24}$$

there is a unique solution $\tilde{\mathbf{x}}_c$ *which satisfies*

$$\textit{minimum} \; || \mathbf{x} || \, . \tag{3-25}$$

The constrained generalized inverse of $\mathbf{A}$, $\tilde{\mathbf{A}}_c$, *is the matrix which produces* $\tilde{\mathbf{x}}_c$ *from the data.*

$$\tilde{\mathbf{x}}_c = \tilde{\mathbf{A}}_c \mathbf{f} \tag{3-26}$$

The only difference between this definition and that of Eqs. (3-3) through (3-5) is the inclusion of the inequality constraints in Eq. (3-23).

A complete description and derivation of the properties of $\tilde{\mathbf{A}}_c$ is given in Lawson and Hanson (1974). The first difficulty which may be encountered is that the inequality constraints in Eq. (3-23) may be incompatible so that no solution exists. Assuming the inequalities can be satisfied, there still may be many solutions which satisfy Eq. (3-24); once again, the inverse is uniquely defined by finding the smallest solution. All of this is similar to the previous discussion except that an explicit formula relating $\tilde{\mathbf{A}}_c$ to $\mathbf{A}$ and $\mathbf{G}$ cannot be found. The method by which the solution $\tilde{\mathbf{x}}_c$ is produced from the data is an iterative one and depends upon the data $\mathbf{f}$ and constraint data $\mathbf{h}$ as well.

Lawson and Hanson (1974) show that $\tilde{\mathbf{x}}_c$ is simply the least squares solution to an unconstrained problem of smaller dimension. The dimension of the problem is reduced by satisfying a subset of the inequalities in Eq. (3-23) exactly as equalities; the particular subset to be satisfied is determined from an iterative procedure. As an example, if $\mathbf{G}$ is the n by n identity matrix and $\mathbf{h}$ is zero, the constrained generalized inverse $\tilde{\mathbf{A}}_c$ is the *GI* of a modified $\mathbf{A}$ in which certain columns of $\mathbf{A}$ have been set to zero. The components of $\tilde{\mathbf{x}}_c$ associated with the zeroed columns are zero.

Due to the iterative method of obtaining $\tilde{\mathbf{x}}_c$, the linear analysis used in section 3.1 is not tractable and a new definition of stability is needed. Stability is defined as the length of the smallest data perturbation required to change a linear combination of the parameters by a prescribed amount. If the linear combination taken involves an isolated parameter, then the measure indicates the smallest change in data needed to change that particular parameter by a prescribed amount. One parameter is said to be more stable than another if a larger data perturbation is required to change it by an equal amount. The stability measure is derived from the solution to the following problem.

Definition: Among all solutions $\mathbf{x}$ *satisfying*

$$\mathbf{G}\mathbf{x} > \mathbf{h} \, , \tag{3-27}$$

$$\mathbf{w}'\mathbf{x} = \mathbf{w}'\tilde{\mathbf{x}}_c + \delta x \, , \tag{3-28}$$

and

$$\textit{minimum} \; || \mathbf{A}(\mathbf{x} - \tilde{\mathbf{x}}_c) || = || \delta \mathbf{f} || = \delta f \, , \tag{3-29}$$

there is a unique solution $\hat{\mathbf{x}}$ *which satisfies*

$$\textit{minimum} \; || \mathbf{x} || \, . \tag{3-30}$$

In this definition, the quantities $\mathbf{G}$, $\mathbf{A}$, $\mathbf{h}$, and $\tilde{\mathbf{x}}_c$ are the elements of the constrained least squares problem given in Eqs. (3-23) through (3-26); the purpose of this definition is to test the stability of the linear combination $\mathbf{w}'\tilde{\mathbf{x}}_c$. After solving Eqs. (3-27) through (3-30), the residual vector $\delta\mathbf{f}$ is the smallest change in the data of Eq. (3-24) sufficient to increase the linear combination $\mathbf{w}'\tilde{\mathbf{x}}_c$ by an amount δx. Large values of δf indicate greater stability of $\mathbf{w}'\tilde{\mathbf{x}}_c$ than small values of δf.

For the least squares problem without inequality constraints, this stability measure can be expressed in closed form. If the linear combination being tested is the j'th parameter (*i.e.* $\mathbf{w}'$ is all zeroes except for a one in the j'th location), the data perturbation necessary to increase the j'th parameter by an amount δx is given by

$$\delta f = \left[\frac{\delta x^2}{(\mathbf{V}\boldsymbol{\Lambda}^{-2}\mathbf{V}')_{jj}} \right]^{1/2} . \tag{3-31}$$

The expression in the denominator is also the variance in the j'th parameter due to independent errors of unit variance in the data as given in Eq. (3-10). If a general linear combination of parameters is to be tested, one can simply make a change of variables so that the j'th parameter has the value of the linear combination and Eq. (3-31) can be applied. Hence, for least squares without inequality constraints, this new definition of stability is equivalent to the more commonly used variance estimates.

A closed form solution for δf is not known when inequality constraints are maintained due to the iterative method of obtaining the solution. When analyzing the stability of the constrained least squares solution, the inverse problem of Eqs. (3-27) through (3-30) must be solved for each combination of parameters being tested. One important feature of this stability measure is that it simply involves solving another constrained least squares problem. By virtue of the fact that the original problem can be solved, the stability analysis can be performed and requires no further expertise.

Two methods of stabilizing the solution were presented in Section 3.1: low-pass filtering (Eq. (3-11)) and augmentation of the original matrix (Eq.(3-17)). Only the augmented matrix method can be used to stabilize the constrained least squares solution since low-pass filtering generally causes the inequality constraints to be violated.

3.3 Computer Implementation of Inversion Methods

Once the matrices and data vectors are formed, the inversion follows a three step procedure designed to eliminate redundant calculations. The following discussion presumes that $m > n$ so that the system appears overdetermined.

(1) The matrix A and data f are reduced from an m by n system to the n by n system

$$\Lambda \mathbf{V}'\mathbf{x} = \mathbf{U}'\mathbf{f}, \tag{3-32}$$

which has the same least squares solution as the original system.

(2) The filter H, constant k_o, and data b of Eq. (3-17), are defined and appended to the reduced matrix from step (1) to stabilize the inversion. This composite system which is now $2n$ by n is once again reduced to the n by n equivalent system

$$\Lambda_a \mathbf{V}'\mathbf{x} = \Lambda_a^{-1} \Lambda \mathbf{U}'\mathbf{f} + k_o \Lambda_a^{-1} \mathbf{H}\mathbf{V}'\mathbf{b}. \tag{3-33}$$

(3) The constrained least squares problem of (3-23) through (3-26) is solved using the reduced system of step (2). If inequality constraints are absent, the least squares solution is obtained by multiplying Eq. (3-33) in step (2) by $\mathbf{V}\Lambda_a^{-1}$ to obtain Eq. (3-21).

The number of arithmetic operations associated with each of steps (1) and (3) is proportional to the number of rows in the matrix times the number of columns squared. Hence, step (1) requires $m\,n^2$ operations and step (3) requires n^3 operations. Step (2) requires a negligible amount of calculation since it is known by an exact algebraic expression. Since $m > n$, the utility of step (1) is recognized when the inverse problem is to be solved many times since only steps (2) and (3) need to be repeated for each subsequent inversion. This three step procedure has the added benefit that the amount of computer storage required to perform the inversion in step (3) is also reduced. For large systems, as are encountered in the present application, the reduction of the matrix in step (1) above can be done sequentially to further minimize computer storage (*e.g.*, Lawson and Hanson, 1974).

The following Fortran computer codes are used to form the inversion algorithm. The program SVDRS (Lawson and Hanson, 1974) is used to compute the *SVD*. The programs SQRDC and SQRSL (Dongarra *et al.*, 1979) are used to perform Gram-Schmidt decomposition of the A matrix. The constrained least squares solution is obtained using program LSI written by A. Olson based upon the text of Lawson and Hanson (1974). Routine LSI performs the appropriate transformations necessary to call programs NNLS and LDP (Lawson and Hanson, 1974).

4. Application to the 1979 Imperial Valley Earthquake

In this section, near-field ground accelerations of the 1979 Imperial Valley earthquake are inverted, resulting in four solutions which fit the data. The first two solutions are obtained from least squares and demonstrate the concept of a solution's stability. The third and fourth solutions are obtained by constrained least squares analysis; the slip velocity is constrained to be positive everywhere on the fault to ensure that the solutions are physically reasonable. It should be noted that these constraints do not allow the slip to have an over-shoot, *i.e.*, reverse direction; this type of faulting is not considered here, although it is easily accommodated in the inversion procedure by constraining only the total offset instead of the slip velocity. Finally, the stability of each of these solutions is made quantitative so that the significance of particular details in the solutions can be assessed.

4.1 Description of Fault Geometry and Station Locations

The October 15, 1979 Imperial Valley earthquake had a local magnitude $M_L = 6.6$ and occurred within the vicinity of several permanent seismic networks operating in the United States and Mexico. The magnitude, epicentral location, and origin time are given by Chavez *et al.* (1981). Figure 2 shows the geometry of the recording stations with respect to the epicenter and known major faults. The observed surface offset is predominantly right-lateral strike-slip with the dip-slip component of offset increasing near the northern end of the Imperial Fault. A maximum offset of 70 cm was observed beginning 10 km northwest of the epicenter on the Imperial Fault and decreasing to zero in a distance of 30 km at the fault's northern end (Sharp *et al.*, 1981). The observed offset on the Brawley Fault averaged approximately 25 cm. The orientation of surface offset with respect to epicenter location indicates that the slip on the fault proceeded to the northwest along the Imperial Fault.

A total of 30 three-component accelerometers recorded this earthquake and are listed in Table 1. Four of these are not used in the inversion study due to their proximity to the perimeter of the valley or other structural irregularities (e.g., Cerro Prieto is located on top of a volcano). The remaining 26 stations are those shown in Figure 2. Stations numbered 1 through 22 are part of a permanent array deployed by the United States Geological Survey (USGS). The station locations, component orientations, and trigger times (when available) for these 22 stations are given in Brady *et al.* (1980). Stations 23 through 29 are located in Mexico and are maintained by the University of California at San Diego (UCSD). The ground motion at these seven sites was recorded digitally and the location, component orientations, and trigger times are given in Brune *et al.* (1981). Station 30 is maintained by the California Division of Mines and Geology (CDMG) as described in McJunkin and Ragsdale (1980). A total of 77 acceleration times series from these 26 stations comprise the recorded data for the inversion study.

The Green's functions of Eq. (2-5) are calculated with the computer program PROSE, which generates the complete response of a layered visco-elastic halfspace by means of a wavenumber integral formulation and Fourier transform (Apsel, 1979). The velocity structure used is given in Table 2 and is based upon the interpretation by McMechan and Mooney (1980) of a recent refraction survey in the Imperial Valley conducted by the USGS (Fuis *et al.*, 1981a and 1981b). The layered velocity model is an approximation to the gradient which varies smoothly along the northwest trending axis of the valley. Since the refraction analysis only pertained to P waves, the S wave structure of Table 2 is conjectured based upon a P to S ratio of 1.73 at depths greater than 5.75 km, and a P to S ratio which is 3.38 at the surface of the halfspace and increases linearly with depth. The density structure in Table 2 is consistent with the interpretation of gravity data given in Fuis *et al.* (1981a). The ground acceleration is low-passed before inversion so that periods shorter than 3 seconds are not considered. At this low frequency and distance range, the effects of attenuation and of layering rather than gradient are negligible.

4.2 *Discretization of the Fault Surface*

Inversion requires a discretization of the fault surface into a set of cells as described in Section 2.2. The parameterization is totally defined by: the cell size; the wavefront, $T(x)$; the slip function, $F(t)$; the number of times each cell may slip, $(2K+1)$; and the time step between each slip, δt.

In this study, the Imperial and Brawley faults are approximated as vertical planes extending from zero to 10 km depth. The Imperial Fault is 50 km in length extending 40 km northwest and 10 km southeast of the epicenter. The Brawley Fault is 10 km in length extending northward from the Imperial Fault as shown in Figure 2. The cells are 5 km by 5 km square. This means that there are two cells vertically on each fault, ten cells horizontally on the Imperial Fault, and two cells horizontally on the Brawley Fault. The data are filtered so that the shortest data wavelength is roughly 10 km corresponding to a three-second period wave in the material below 5 km depth. The smallest discretization wavelength and smallest data wavelength are therefore comparable below 5 km. Above 5 km depth, the data wavelength is less than the cell dimension; however, a cell dimension less than 5 km for this problem is not feasible since the number of parameters would become quite large causing excessive computer storage and time requirements.

The average rupture front, $T(x)$, is chosen to be the arrival time of a geometrical ray wavefront defined by 90 percent of the shear wave speed (see Table 2 for shear wave velocity). $T(x)$ initiates at 10 km depth below the epicenter and proceeds bilaterally along the Imperial Fault. $T(x)$ on the Brawley Fault initiates when the wavefront passes on the Imperial Fault. Since the observed surface offset began abruptly at 10 km northwest of the epicenter on the Imperial Fault, a second rupture is allowed to occur here which propagates to the south and is initiated by the passing of the first rupture. This second rupture is equivalent to allowing the average rupture front $T(x)$ to proceed bilaterally from a point 10 km northwest of the epicenter on the Imperial Fault.

The slip function, $F(t)$, is illustrated in Figure 3. $F(t)$ is basically a smooth step function which begins rapidly, achieving about 75 percent of the final offset in one second and terminates in 2.25 seconds. For the frequency range of the filtered data (periods greater than 3 seconds), the departure of $F(t)$ from a step function in Figure 3 is not significant and the reader may simply regard $F(t)$ as a step function. Each cell is allowed to slip five times at sequential delays of $\delta t = 0.75$ seconds. The increment of 0.75 seconds is chosen in accordance with the 3-second low-pass filtering of the data; increments in slip occurring at higher frequencies are not resolved. Each time a cell slips, the slip at every point within the cell occurs according to $F(t)$ while the slip progresses through the cell according to $T(x)$. The term "dynamic slip" used in the following sections refers to the vector values of the five slip increments experienced by each cell.

The number of parameters equals twice the number of cells multiplied by the number of times each cell can slip. The factor of two arises since each slip vector, s_{jk} in Eq. (2-5), has two components in the plane of the fault. There are 24 cells on the Imperial and Brawley faults combined for the initial bilateral rupture and 8 cells on the Imperial Fault for the second rupture: a total of 32 cells. Each cell is allowed to slip five times. This yields a total of n=320 parameters.

In this study, ground acceleration is used as data rather than ground displacement; as a result, both sides of Eq. (2-5) must be differentiated twice with respect to time. Both sides of Eq. (2-5) are additionally Fourier band-pass filtered to retain only periods longer than 3 seconds and shorter than 10 seconds. Both data and Green's functions are then sampled at 0.25 second increments so that the character of the waveforms is maintained. Only the first 30 seconds of recorded ground motion is considered which results in 120 data points for each of 77 components, a total of m=9240 data points. Absolute timing is maintained between data and Green's functions for the stations at which timing information was available.

For each component of acceleration used in the inversion, the maximum value is found and both data and Green's functions for that component are divided by that value. This has the effect of normalizing the problem so that the inversion is attempting to fit each component to within the same percentage. This particular normalization reflects one idea of "goodness of fit". Other normalization schemes can be employed. For example, one might argue that the greatest importance should be given

to the larger amplitude data near the fault since these are less affected by uncertainties in wave propagation and attenuation. Due to the inability of the inversion to fit the motion at several stations, certain components were weighted small in the inversion; these are marked with a * in Figure 13. The weighting was accomplished by multiplying the rows of the matrix and the data by 0.01 for these components; all other components were not weighted and therefore have an effective weight of 1.

4.3 The Least Squares Solution

The least squares solution is defined in Eqs. (3-3) through (3-5). Figure 4 shows the distribution of slip which results from fitting the data without any attempt to ensure stability in the solution. The area of each triangle is proportional to the slip in a given cell and points in the direction of slip. For example, a triangle pointing to the right indicates right-lateral strike-slip motion; a triangle pointing up indicates dip-slip motion with the west side of the fault surface moving up relative to the east side.

The dynamic slip in Figure 4 (bottom) contains two groups of boxes, each group being five boxes high. The upper group of boxes contains the five slips in the row of cells spanning 0 to 5 km depth on the fault surface; the static offset from 0 to 5 km depth is shown in the upper row of cells above. The lower group of boxes contains the five slips in the row of cells spanning 5 to 10 km depth; the static offset from 5 to 10 km depth is shown in the lower row of cells above. Each dynamic slip vector corresponds to an increment in displacement in the direction of the triangle at 0.75 seconds intervals. In Figure 4, the static offset for a given cell is the vector sum of the five corresponding dynamic slip vectors shown below.

The static offset and dynamic slip are each scaled separately according to their peak values. The peak offset in Figure 4 is 3.96 meters. The peak dynamic slip is 2.05 meters, occurring within a time increment of 0.75 seconds. The seismic moment is 4.04×10^{25} dyne-cm, defined as the scalar length of the vector sum of the offsets in all cells. The offset is very oscillatory with neighboring cells having offsets in opposing directions. Even the dynamic slip within a given cell oscillates, changing direction by as much as 180° in 0.75 seconds. Most of the energy radiating from this fault motion is simply canceling and has a minimal affect upon the fit to the data. This solution is not acceptable due to the erratic spatial and temporal variations and the significant component of left-lateral faulting on known right-lateral faults.

Since the data do not contain long period energy, the static offset cannot be deduced from the data alone. The presence of a nonzero static offset in Figure 4 occurs then for two reasons: (1) additional constraints have been imposed, such as, requiring the slip to occur within a 3.75 second time window centered about 90 percent of the shear wave arrival time; and (2) the solution is unstable and the static component is not needed to fit the data. The erratic character exhibited in Figure 4 is also typical of unstable solutions in which small variations in the data produce large changes in the solution. The stabilizing methodology presented in Section 3.1 is used to suppress the unstable part of the least squares solution, and in so doing, increase the misfit to the data by a small amount. Although the stabilized solution is not the best fit to the data, it is stable in the sense that it is not being controlled by small features in the data.

The condition number of the original matrix is 128 (ratio of the largest to smallest singular value) implying that a one percent change in the data could lead to a 128 percent change in the overall solution. The condition number is reduced in order to stabilize the solution by appending a set of equations to the original matrix as defined in Eq. (3-17). The filter coefficient matrix H is prescribed to be: zero where the singular value ratio is between 1 and 4; unity where the singular value ratio is greater than 20; and linear in between. The vector **b** is set to zero and the constant k_μ is made large enough to reduce the condition number from 128 to 6. Stabilizing the matrix in this manner suppresses the unstable part of the solution associated with small singular values.

Figure 5 shows the stabilized least squares solution obtained using the augmented matrix and data. Both the static offset and dynamic slip are much smoother than the unstabilized solution in Figure 4. The peak offset decreases from 3.96 meters in Figure 4 to 1.31 meters in Figure 5; the peak dynamic slip also decreases from 2.05 meters to 0.75 meters. The seismic moment similarly decreases from

4.04×10^{25} to 3.37×10^{25} dyne-cm. While the offset and slip are smaller by a factor of three, the moment is smaller by only 20 percent. Such a small change in moment is due to the near cancellation of the unstable slip distributions. This cancellation results from the vector sum of slip vectors having opposing orientations. The small change in moment suggests, quite expectedly, that moment is a more stable quantity than offset or slip. The nonzero value resulting in the static offset is due entirely to the 3.75 second time window in the stabilized solution. Increasing the time window results in progressively smaller static offsets since the very long period slip is not recoverable based upon only short period data. In other words, additional information or assumptions must be supplied in order to infer the static offset in this problem.

The geology and tectonics for the Imperial Valley indicate that faulting is predominantly right-lateral strike-slip; the dip-slip component is much smaller with the west side of the Imperial Fault moving up and the west side of the Brawley Fault moving down relative to the east side. The stabilized solution (Figure 5) also exhibits predominantly right-lateral offset. The dip-slip component of offset in Figure 5 has the wrong polarity but is much smaller in amplitude than the strike-slip component.

The dynamic slip for the stabilized solution still shows intermittent left-lateral motion, *i.e.*, reversals. Even the offset shows a few neighboring cells which moved in opposing directions, especially on the Brawley Fault. These reversals, both in static offset and dynamic slip, are no longer due to instabilities in the solution. They are a characteristic of the least squares solution to this particular data set and no further amount of stabilization can make them disappear.

Opposing static offsets along the fault contradict the expected fault motion based upon the tectonic stress field and are therefore unphysical. The interesting question remains as to whether a distribution of slip can be found which: (1) has no reversals; (2) is consistent with tectonic and geologic evidence; and (3) satisfies the recorded ground motion data. Since the ground motion data alone does not require the solution to be nonreversing, additional information must be added to the inversion to ensure this outcome as discussed in the next section.

4.4 The Constrained Least Squares Solution

By solving the constrained least squares problem of Eqs. (3-23) through (3-26), only nonreversing solutions are allowed. The inequalities of Eq. (3-23) take the form of positivity constraints for the parameters representing strike-slip motion. By keeping these parameters positive, each strike-slip parameter remains right-lateral. The dip-slip parameters for the Imperial Fault are constrained to be positive while the dip-slip parameters for the Brawley Fault are constrained negative.

The constrained least squares solution is shown in Figure 6. Only the data and inequality constraints are used in this inversion and no attempt is made to ensure the stability of the solution. The remarkable difference between this solution and the least squares solution (Figure 4) is due entirely to the inclusion of the inequality constraints in the constrained least squares inversion. The static offset is much smoother in Figure 6 with all cells being right-lateral and having the appropriate dip-slip component in accordance with the inequality constraints. The dynamic slip is also quite reasonable in appearance showing the coherent temporal behavior resulting from the inequality constraints.

The peak values of static offset and dynamic slip for the constrained solution (Figure 6) are nearly the same as the corresponding values for the least squares solution (Figure 4). The amount of static offset within any given cell is also nearly the same for these two solutions, although, the polarity of the offset sometimes differs significantly. The constrained solution has a moment of 1.71×10^{26} dyne-cm which is four times larger than the moment of 4.04×10^{25} in the least square solution. As was pointed out earlier, cancellation is responsible for the low value of moment in the least squares solution. The inequality constraints force the slip within each cell to be nearly parallel; hence, the amount of possible cancellation is minimized and the moment increased.

Although the constrained least squares solutions seems reasonable (Figure 6), it does not follow from this judgement alone that it is also stable. Certainly, the addition of the inequality constraints can only increase the stability of the solution when compared with the unconstrained solution; however, the

amount of increase has yet to be determined. The constrained least squares inversion is stabilized exactly as the least squares inversion (Section 4.3, Figure 5). A set of equations are appended to the original matrix and the solution to the augmented system is then found. The filter coefficient matrix **H** and vector **b** are defined exactly as in Section 4.3. The constant k_o is set large enough to change the condition number from 128 to 7.

The stabilized constrained least squares solution is shown in Figure 7. Once again, stabilization produces significant changes in the solution. The moment is 9.13×10^{25} dyne-cm compared with 1.71×10^{26} in the unstabilized solution, nearly a factor of two smaller. The peak static offset and peak dynamic slip are also smaller by nearly a factor of two: 1.65 meters and 0.93 meters in the stabilized solution; 2.6 meters and 1.93 meters in the unstabilized solution. In the stabilized solution (Figure 7), the relative offset in the upper five km on the Imperial Fault is much smaller at the northern end than in the unstabilized solution (Figure 6).

It is interesting to note that, in contrast to the unconstrained least squares solution, the static offset in the constrained solution does not go to zero as the time window is increased. This follows since only the zero solution has a zero static offset when the slip is not allowed to reverse directions. Hence, the positivity constraints act as additional data which allow the long period slip to be inferred from shorter period data, provided of course that the constraints are justified. This coupling of long and short periods is evidence of the nonlinearity associated with inequality constraints.

A noticeable trend can be seen going from the upper middle to the lower right in the dynamic slip at depth on the Imperial Fault (Figure 7). To interpret this trend, consideration must be given to the wavefront $T(x)$ which defines the absolute time for the five point time window. Zero time for the five point time window is defined as the travel time of a wavefront initiating at the earthquake epicenter and traveling at 90 percent of the local shear wave velocity. Trends which go across the boxes from left to right correspond to slip propagating along the fault with a horizontal phase velocity equal to the wavefront $T(x)$. Trends which go from upper left to lower right correspond to slip propagating with a horizontal phase velocity greater than the wavefront $T(x)$. Similarly, trends which go from lower left to upper right correspond to phase velocities less than $T(x)$.

The bottom group of boxes contains the five slips for the single row of cells at five to ten km depth; hence, the trend corresponds to slip propagating in this depth range at a horizontal phase velocity greater than 90 percent of the shear wave speed. The actual phase velocity is between 4.0 and 5.0 km/sec which more nearly equals the compressional wave velocity. Since this is the horizontal phase velocity of slip propagation, the actual velocity may be less. For example, if the slip is propagating vertically as a plane wave the horizontal phase velocity is infinite. With only two cells in the vertical direction on the fault, the vertical phase velocity can not be accurately determined.

Figure 7 (bottom) shows the right-lateral component of offset on the Imperial Fault for the stabilized solution. The dark triangular shaded region is a schematic representation of the observed surface offset (Sharp *et al.*, 1981). The consistency of the solution and observation is remarkable since the inversion is based only on the acceleration recordings. Both inversion and observation show the offset near the surface to be concentrated between 10 and 35 km north of the epicenter decaying to zero at the most northern end. The inversion shows about 70 percent more displacement in the upper five km than reflected in the observed offset at the surface. The offset between 5 km and 10 km is about twice that in the upper five km but the overall shape is very similar. It is interesting to note that no large concentrations of slip are required by the data; this is evidenced by the smooth character of the stabilized solution.

The moment estimated from long period surface waves is 6×10^{25} dyne-cm (Kanamori and Regan, 1981). Laser strain meter measurements taken at Pinon Flat Observatory approximately 140 km away indicate a moment of 9×10^{25} dyne-cm (Wyatt, 1981). The moment for the stabilized solution in Figure 7 is 9.13×10^{25} dyne-cm, consistent with these independent estimates of moment.

The fits to the data by the stabilized solution (Figure 7) are plotted geographically in Figures 8, 9, and 10 for the 230°, 140°, and vertical components of motion respectively. Figures 11 through 13 show the same fits in greater detail. The overall agreement in both amplitude and phase is very good. Figure 13 shows the detailed fit to the stations farthest south in Mexico; although there is agreement in

amplitude, the fit to the phase is not very good due to the more complicated nature of the data in the south. Recordings denoted by a * in Figure 13 were weighted small in the inversion since their complexity was not well modeled by the inversion.

By stabilizing the solution, a certain amount of fit to the data is sacrificed. Figure 14 shows the fit to the 230° component of data by the unstabilized least squares solution. While the fit is nearly perfect, the corresponding solution (Figure 4) contains a very oscillatory slip distribution. Conversely, the distribution of slip in the stabilized constrained least squares solution (Figure 7) is smoothly varying while the fit to the 230° component of data (Figure 8) is less perfect. Although in this study the nonreversing slip constraint did not cause the fit to the data to deteriorate, the presence of substantial deterioration in other applications would cause the validity of such a constraint to be questioned. The amount of misfit in Figure 8 is not much considering the improvement in the slip distribution. Of the four slip distributions (Figures 4 through 7), the stabilized least squares solution (Figure 7) is preferred due to its stability, coherence, and compatibility with geologic, tectonic, and other independent observations.

4.5 Stability Analysis of Inversion Results

The condition number provides an estimate of the overall stability of the solution. In order to test the significance of particular details in the solution, stability is defined in terms of the smallest change in the data required to change the offset in a given cell by one meter (see Eqs. (3-27) through (3-30)). A cell which requires a small change in the data is less stably determined than a cell which requires a large change in data.

Figure 15 shows the stability results for the two least squares solutions shown in Figures 4 and 5. The most stable cell in the least squares solution is the third from the upper right corner on the Imperial Fault (Figure 15, top). An 8.5 percent change in the data is required to change the dip-slip component of offset in this cell by one meter, while a 3.4 percent change is required to produce an equal change in the strike-slip component. Other cells (Figure 15, top) contain lower values for stability, sometimes only a fraction of a percent as in the northern upper corner of the Imperial Fault. These low values correspond to the least stably determined offsets in the least squares solution.

The stability of the stabilized least squares solution is shown in Figure 15 (bottom). It is clear that the effect of the stabilizing procedure is to make the stability of the strike-slip and dip-slip components more nearly equal and the same in each cell. An 18 percent change in the data is required to produce a one meter change in the offset of the stabilized solution. Using this measure, the stability is improved by roughly a factor of 2 to 20 depending upon the cell. Again, improved stability is caused by suppressing the unstable slip distributions.

The stability of the two constrained least squares solutions are shown in Figure 16. Comparing Figure 16 (top) with Figure 15 (top), the constrained least squares solution is seen to be everywhere more stable than the least squares solution. This confirms the earlier statement that adding information to the inversion has the effect of stabilizing the solution. A 9.6 percent change in the data is required to change the dip-slip component of offset in third cell from the upper corner on the Imperial Fault (Figure 16, top). The cell with the most stably determined strike-slip component of offset is now near the southern upper corner of the Imperial Fault (Figure 16, top) requiring a 6.6 percent change in the data to produce a one meter change. Just as in least squares (Figure 15, top), stability varies from cell to cell.

The stability of the stabilized constrained least squares solution (Figure 16, bottom) is much greater than the unstabilized solution (top). The stability of the dip-slip component is nearly a constant 14.2 percent everywhere, while the strike-slip stability is almost uniformly 12.8 percent. It should be noted that more than a 14.2 percent change in the data is likely to be required to change the dip-slip component of offset in two cells simultaneously; this amount has not been determined here. The same holds for simultaneously changing the strike-slip and dip-slip components of offset in one cell.

To put the stability analysis in perspective, note that multiplying the data by two will change the solution by exactly a factor of two since the problem in linear in this regard. Since the offsets in the

stabilized solutions (Figures 5 and 7) are roughly one meter, a 100 percent change in the data can therefore change the offset in every cell by roughly one meter. To change a component of offset in only one cell by one meter will require less than a 100 percent change in the data. Hence, the 14.2 percent change in the data shown in Figure 16 (bottom) indicates a stable solution.

5. Conclusions

Due to the linear relation between the displacement discontinuity on a fault surface and the resulting seismic radiation, it was shown that linear inverse theory could be used to infer subsurface slip distributions on a known fault from recordings of ground motion at the Earth's surface. In order to obtain physically reasonable slip distributions, inequality constraints were satisfied in addition to the recorded data. Not only did inverse theory allow a reasonable solution to be systematically found, it provided a framework wherein the solution was decomposed into a stable and an unstable component. When many distributions of slip fit the data, differences in the solutions were found to correspond to the unstable component which is not determined by data.

Inverse theory was applied to 77 components of low frequency acceleration recorded in the near-field of the October 15, 1979 Imperial Valley earthquake. A solution was obtained in Section 4.4 which satisfies the data, is physically reasonable, and only contains the stable component of slip distribution. The seismic moment of 9.13×10^{25} dyne-cm obtained for this solution is consistent with independent estimates of moment from long period surface waves and static strain measurements. The corresponding peak offset is 1.65 meters occurring between 5 km and 10 km depth and 15 to 20 km north of the epicenter on the Imperial Fault; the offset in the upper five kilometers conforms in both amplitude and shape to observations of surface offset and has a peak value of one meter. The offset obtained was predominantly right-lateral and smoothly varying requiring no localized zones of high offset; offset on the Brawley Fault is much less than that on the Imperial Fault. The time behavior of slip was constrained to propagate at an average velocity of 90 percent of the local shear wave speed; however, over a distance of 20 to 30 km on the Imperial Fault, the horizontal propagation of slip was found to occur at a velocity approaching that of the compressional wave.

6. Acknowledgments

The authors wish to express their appreciation for discussions with James Brune, Gerald Frazier, Freeman Gilbert, and Jeff Fried. Mr. Fried additionally provided valuable computational expertise in optimally adapting the Fortran inversion programs to the virtual processing of the PRIME 400 computer. Many of the suggestions by David Boore and Paul Spudich were helpful in clarifying parts of this paper. The computational facilities of Del Mar Technical Associates, DELTA, are also greatly appreciated. This work was supported in part by the National Science Foundation Grant PFR79-26539.

7. References

Apsel, R. J. (1979). *Dynamic Green's Functions for Layered Media and Applications to Boundary Value Problems*, Ph.D. Thesis, University of California, San Diego, Ca.

Backus, G. and F. Gilbert (1968). The resolving power of gross earth data, *Geophys. J. R. astr. Soc.*, **16**, 169—205.

Backus, G. and F. Gilbert (1970). Uniqueness in the inversion of inaccurate gross earth data, *Phil. Trans. R. Soc. Lond.*, **266A**, 123—192.

Ben-Israel, A. and A. Charnes (1963). Contributions to the theory of generalized inverses, *J. Soc. Indust. Appl. Math.*, **11**, 667—699.

Brady, A. G., V. Perez, and P. N. Mork (1980). The Imperial Valley earthquake, October 15, 1979, digitization and processing of accelerograph records, *U.S. Geol. Survey open-file report*, 80-703, Menlo Park, Ca.

Brune, J. N., J. Prince, F. Vernon III, E. Mena, and R. Simons, (1981). Strong motion data recorded in Mexico for the 10/15/79 Imperial Valley earthquake, *U.S. Geol. Survey professional paper*, Menlo Park, Ca.

Burridge, R. and L. Knopoff (1964). Body force equivalents for seismic dislocations, *Bull. Seism. Soc. Am.*, **54**, 1875—1888.

Chavez, D., J. Gonzales, J. N. Brune, F. Vernon III, R. Simons, K. L. Hutton, P. T. German, and C. E. Johnson (1981). Mainshock location and Magnitude determination using combined U.S. and Mexican Data, *U.S. Geol. Survey professional paper*, Menlo Park, Ca.

Dongarra, J. J., J. R. Bunch, C. B. Moler, and G. W. Stewart (1979). *Linpack Users' Guide*, S.I.A.M., Philadelphia, Penn.

Franklin, J. N. (1970). Well posed stochastic extensions of ill-posed linear problems, *J. Math. Anal. Appl.*, **31**, 682—716.

Fuis, G. S., W. D. Mooney, J. H. Healey, G. H. McMechan, and W. J. Lutter (1981a). Seismic refraction studies of the Imperial Valley region, California - Profile models, a traveltime contour map, and a gravity model, *U.S. Geol. Survey open file report*, **81-270**, Menlo Park, Ca.

Fuis, G. S., W. D. Mooney, J. H. Healey, G. H. McMechan, and W. J. Lutter (1981b). Crustal structure of the Imperial Valley region, *U.S. Geol. Survey professional paper*, **1254**, Menlo Park, Ca.

Gilbert, F. (1971). Ranking and winnowing gross earth data for inversion and resolution, *Geophys. J. R. astr. Soc.*, **23**, 125—128.

Jackson, D. D. (1972). Interpretation of inaccurate, insufficient, and inconsistent data, *Geophys. J. R. astr. Soc.*, **28**, 97—109.

Kanamori, H. and J. Regan (1981). Long-period surface waves generated by the Imperial Valley earthquake of 1979, *U.S. Geol. Survey professional paper*, Menlo Park, Ca.

Lawson, Charles L. and Richard J. Hanson (1974). *Solving Least Squares Problems*, Prentice-Hall, Inc., Englewood Cliffs, New Jersey.

Levenberg, K. (1944). A method for the solution of certain non-linear problems in least squares, *Quarterly of Applied Mathematics*, **2**, 163—168.

McJunkin, R. D. and J. T. Ragsdale (1980). Compilation of strong-motion records and preliminary data from the Imperial Valley earthquake of 15 October, 1979, *California Division of Mines and Geology preliminary report 26*, Sacramento, Ca.

McMechan, G. A. and W. D. Mooney (1980). Asymptotic ray theory and synthetic seismograms for laterally varying structures: theory and application to the Imperial Valley, California, *Bull. Seism. Soc. Am.*, **70**, 2021—2035.

Neumann, G. (1981). Determination of lateral inhomogeneities in reflection seismics by inversion of traveltime residuals, *Geophysical Prospecting*, **29**, 161—177.

Penrose, R. (1955). A generalized inverse for matrices, *Proc. Camb. Phil. Soc.*, **51**, 406—413.

Penrose, R. (1956). On best approximate solution of linear matrix equations, *Proc. Camb. Phil. Soc.*, **52**, 17—19.

Sharp, R. V., *et al.* (1981). Surface faulting in central Imperial Valley, *U.S. Geol. Survey open-file report*, Menlo Park, Ca.

Wiggins, R. (1972). The general linear inverse problem: implications of surface waves and free oscillations on earth structure, *Rev. Geophys. Space Phys.*, **10**, 251—285.

Wyatt, F. (1981). Distant deformation from the Imperial Valley, California earthquake 1979, submitted to *Bull. Seism. Soc. Am.*.

Figures

Figure 1: Geometry of fault surface S in an elastic halfspace. In this figure, a planar fault surface at a dip of δ from the vertical is divided into two-dimensional rectilinear cells. Each cell requires a two component vector to described the relative slip across the surface.

Figure 2: Map showing fault geometry and station locations for the October 15, 1979 Imperial Valley earthquake. The 26 stations shown are used in the inversion for the distribution of slip on the Imperial and Brawley faults.

Figure 3: The time function $F(t)$ (bottom) and its derivative (top) used in the discretization of the inverse problem. Each point on the fault is allowed to slip a prescribed number of times, slipping as $F(t)$ each time.

Figure 4: Slip on the Imperial and Brawley faults obtained by least squares inversion without stabilization. Triangles have an area proportional to the displacement, and point in the direction of slip; the peaks define the scales for static and dynamic displacements. The static offset (top) is shown for the two horizontal rows of 5 km square cells which make up the fault surface. The two groups of boxes (bottom) contain the dynamic slip for the two rows of cells (top). Each triangle in the dynamic slip corresponds to one of the s_{jk} vectors in Eq. (2-5). The vector sum of the five sequential slips plotted vertically (bottom) equals the static offset in the corresponding cell above. Zero time for the dynamic slip is the time required by a wavefront moving at 90 percent of the shear wave velocity to travel from the hypocenter to the cell.

Figure 5: Slip on the Imperial and Brawley faults obtained by least squares inversion with stabilization (analogous to Figure 4 for the unstabilized solution). Stabilization provides a much smoother offset (top) and dynamic slip (bottom) than the unstabilized result in Figure 4; this is evidenced by the more uniform direction and amplitude of adjacent triangles.

Figure 6: Slip on the Imperial and Brawley faults obtained by constrained least squares inversion without stabilization (analogous to the unconstrained solution shown in Figure 4). In this solution, the slip is constrained to be: right-lateral; west side up on the Imperial Fault; and west side down on the Brawley Fault. As a result of the constraints, the dynamic slip (bottom) does not reverse direction and the static offsets (top) in adjacent cells are not in opposing directions (compare with Figures 4 and 5).

Figure 7: Slip on the Imperial and Brawley faults obtained by constrained least squares inversion with stabilization (analogous to the unstabilized solution in Figure 6). The seismic moment is much smaller than in Figure 6. Also, a noticeable trend with a horizontal phase velocity between 4.0 and 5.0 km/sec has emerged in the dynamic slip of the bottom row of cells on the Imperial Fault. The strike-slip component of offset on the Imperial Fault is shown in the lower left superimposed upon a shaded schematic of the observed surface offset.

Figure 8: Comparison of the data (heavy line) with the fit to the data (light line) for the stabilized constrained least squares solution shown in Figure 7. The seismograms are plotted geographically beginning at the station location marked with an X. The 230° component (perpendicular to the Imperial Fault) is shown. The accelerograms for stations EC5 and EC7 are shown in the lower left for clarity along with EC4, EC6, and EC8.

Figure 9: Comparison of the data (heavy line) with the fit to the data (light line) for the stabilized constrained least squares solution shown in Figure 7 (analogous to Figure 8). The 140° component (parallel to the Imperial Fault) is shown.

Figure 10: Comparison of the data (heavy line) with the fit to the data (light line) for the stabilized constrained least squares solution shown in Figure 7 (analogous to Figures 8 and 9). The vertical component is shown with orientation given in Table 1.

Figure 11: Comparison of data (solid line) with theory (dashed line) by the stabilized constrained least squares solution of Figure 7. Nine of the stations compared in Figures 8 through 10 are shown in greater detail. Component orientations are listed in Table 1 with the left-most horizontal orientation in Table 1 corresponding to the left-most horizontal component plotted above. The numbers at the side of each component are the maximum filtered horizontal acceleration in cm/sec^2. The absolute time scale and acceleration scale pertain to both data and inversion.

Figure 12: Comparison of data (solid line) with theory (dashed line) by the stabilized constrained least squares solution of Figure 7 (analogous to Figure 11 for nine additional stations).

Figure 13: Comparison of data (solid line) with theory (dashed line) by the stabilized constrained least squares solution of Figure 7 (analogous to Figures 11 and 12 for eight additional stations). Components marked with a * are weighted very small in the inversion and have a negligible effect upon the final solution; they are shown for comparison purposes only.

Figure 14: Comparison of the data (heavy line) with the fit to the data (light line) for the unstabilized least squares solution shown in Figure 4. The 230° component (perpendicular to the Imperial Fault) is shown. The fit is almost exact. Compare with Figure 8 for the stabilized constrained least squares fit to the data.

Figure 15: Stability analysis results for the least squares solution (Figure 4) and the stabilized least squares solution (Figure 5). The height of each box is proportional to the smallest percentage change in the data required to change a component of offset in the corresponding cell by one meter. The peak value for each component of offset is given since each of the four results shown is scaled separately. Large values depict cells with most stably determined offset. The stabilized solution (bottom) is more stable everywhere than the unstabilized solution (top), and all cells (bottom) are equally stable.

Figure 16: Stability analysis results for the constrained least squares solution (Figure 6) and the stabilized constrained least squares solution (Figure 7) (analogous to Figure 15 for the stability of unconstrained least squares). The constrained least squares solution (top) is everywhere more stable than the unconstrained least squares solution (Figure 15, top). Also, the stabilized solution (bottom) is more stable everywhere than the unstabilized solution (top).

Tables

Table 1: List of component orientations for near-field stations recording the October 15, 1979 Imperial Valley earthquake.
* Horizontal direction measured in degrees clockwise from North.
** Stations not considered in the inversion studies.

Table 2: Crustal structure consisting of homogeneous plane layers used in the calculation of theoretical Green's functions for the Imperial Valley, California.

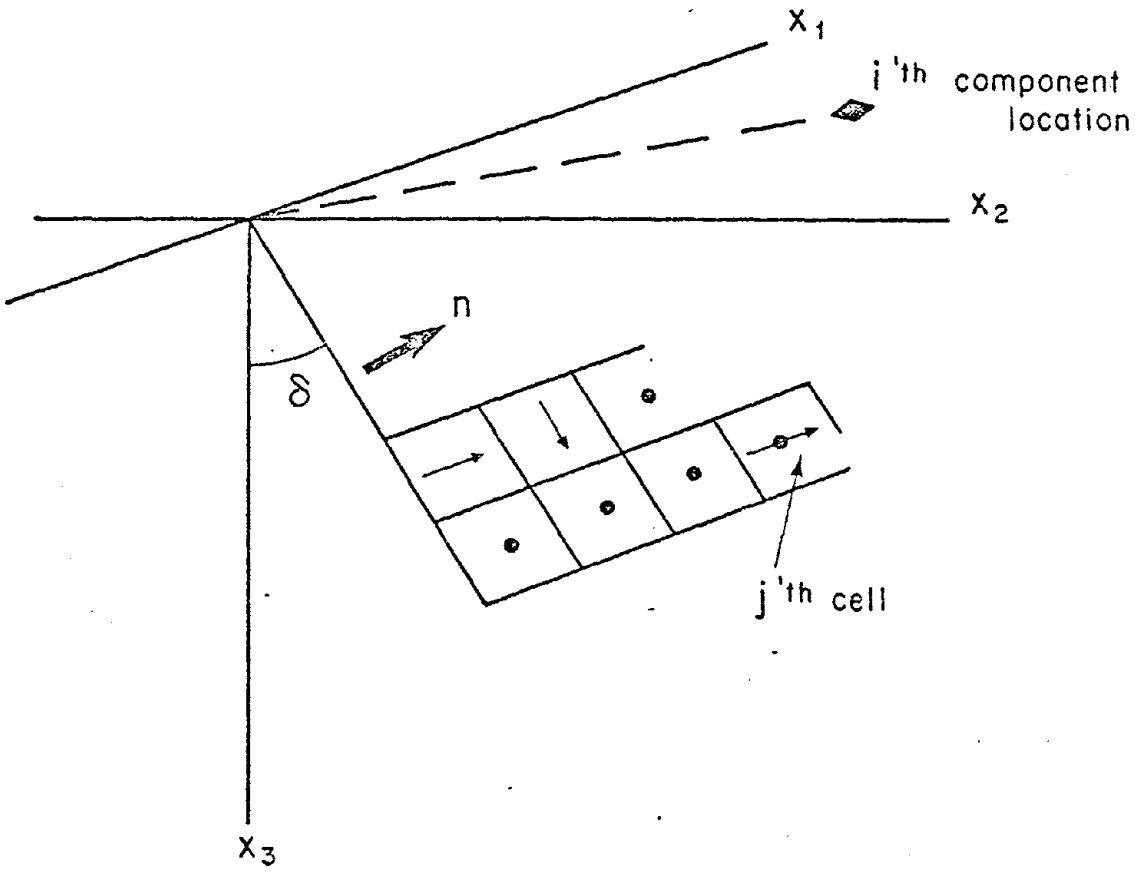

Figure 1: Geometry of fault surface S in an elastic halfspace. In this figure, a planar fault surface at a dip of δ from the vertical is divided into two-dimensional rectilinear cells. Each cell requires a two component vector to described the relative slip across the surface.

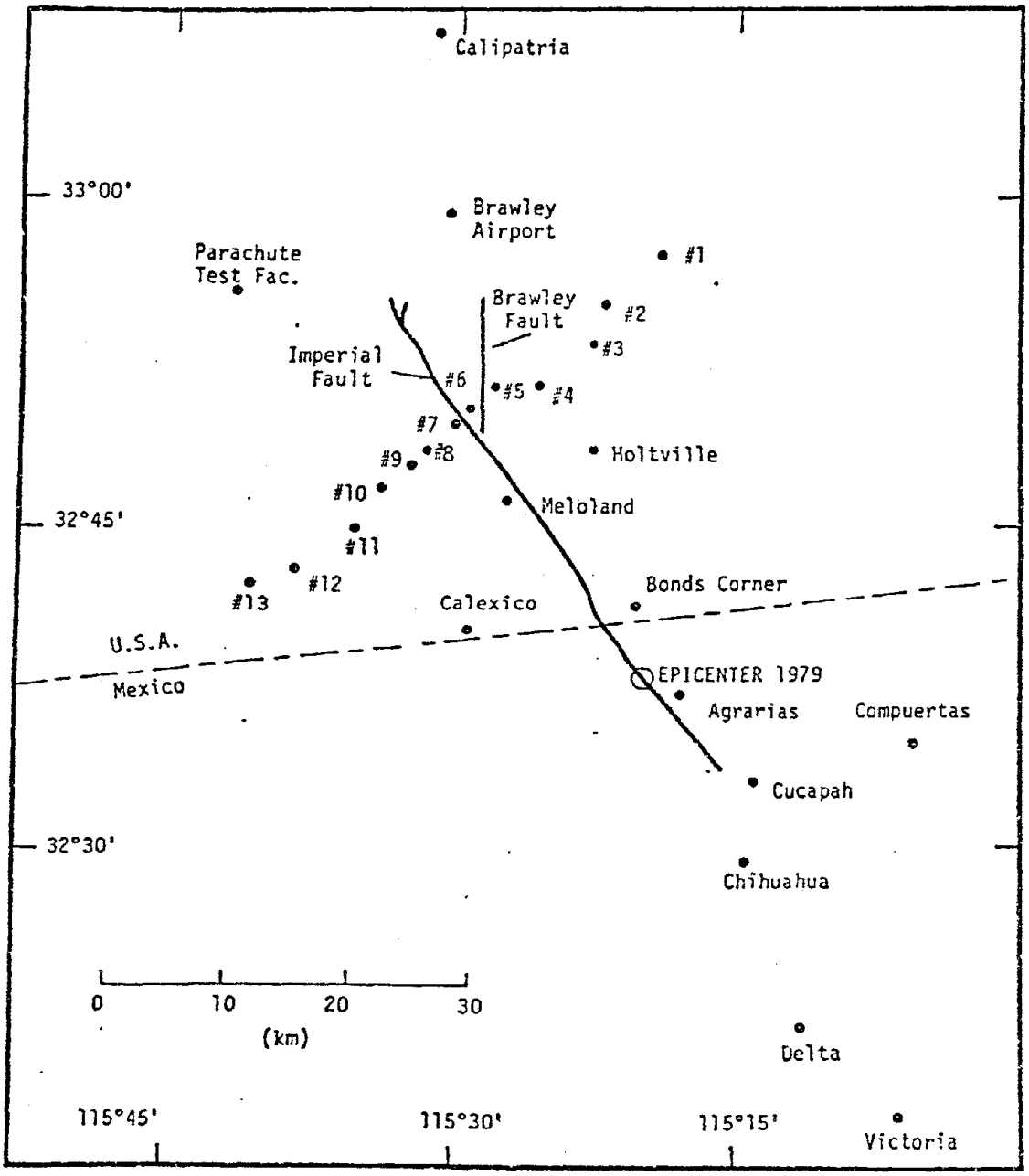

Figure 2: Map showing fault geometry and station locations for the October 15, 1979 Imperial Valley earthquake. The 26 stations shown are used in the inversion for the distribution of slip on the Imperial and Brawley faults.

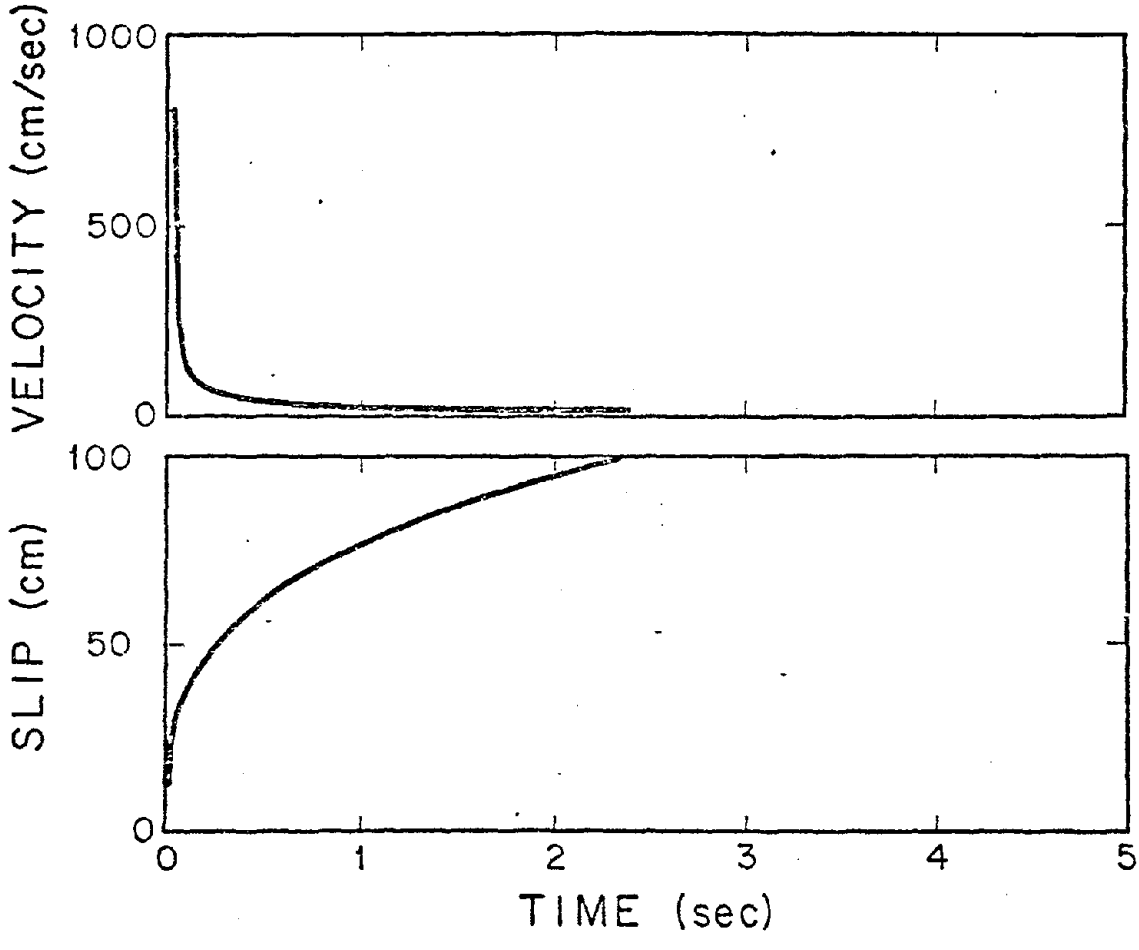

Figure 3: The time function $F(t)$ (bottom) and its derivative (top) used in the discretization of the inverse problem. Each point on the fault is allowed to slip a prescribed number of times, slipping as $F(t)$ each time.

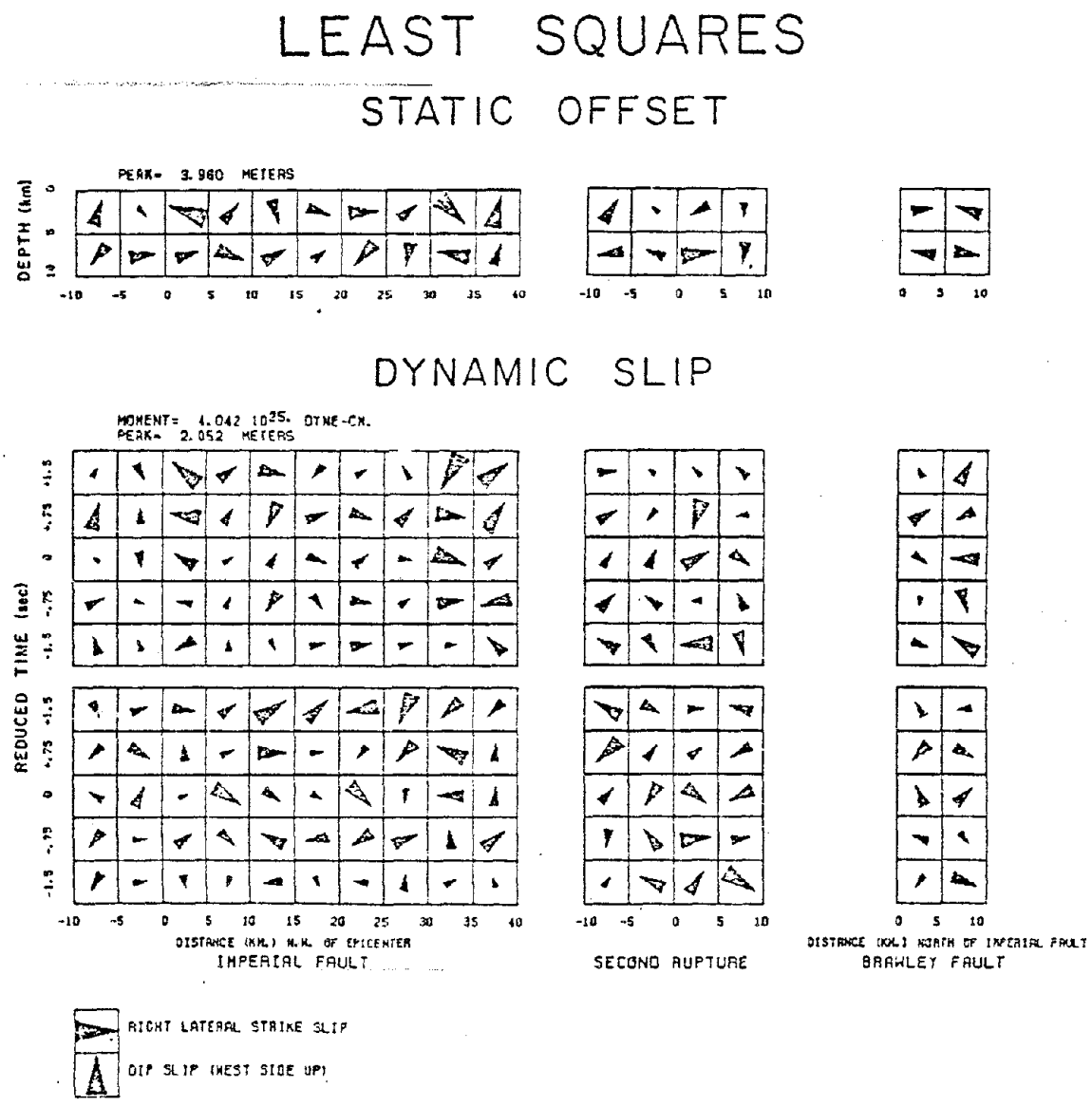

Figure 4: Slip on the Imperial and Brawley faults obtained by least squares inversion without stabilization. Triangles have an area proportional to the displacement, and point in the direction of slip; the peaks define the scales for static and dynamic displacements. The static offset (top) is shown for the two horizontal rows of 5 km square cells which make up the fault surface. The two groups of boxes (bottom) contain the dynamic slip for the two rows of cells (top). Each triangle in the dynamic slip corresponds to one of the s_{ik} vectors in Eq. (2-5). The vector sum of the five sequential slips plotted vertically (bottom) equals the static offset in the corresponding cell above. Zero time for the dynamic slip is the time required by a wavefront moving at 90 percent of the shear wave velocity to travel from the hypocenter to the cell.

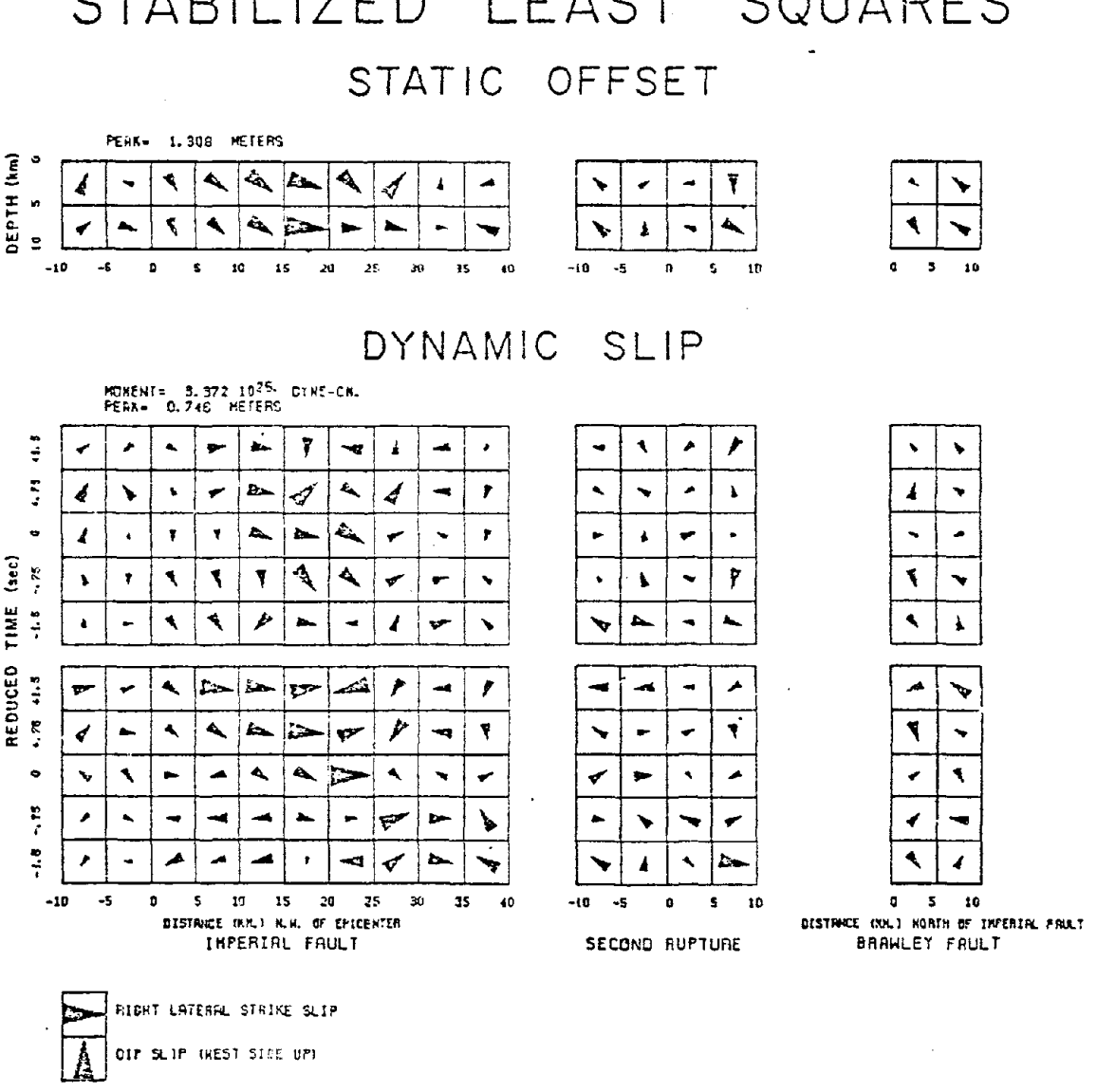

Figure 5: Slip on the Imperial and Brawley faults obtained by least squares inversion with stabilization (analogous to Figure 4 for the unstabilized solution). Stabilization provides a much smoother offset (top) and dynamic slip (bottom) than the unstabilized result in Figure 4; this is evidenced by the more uniform direction and amplitude of adjacent triangles.

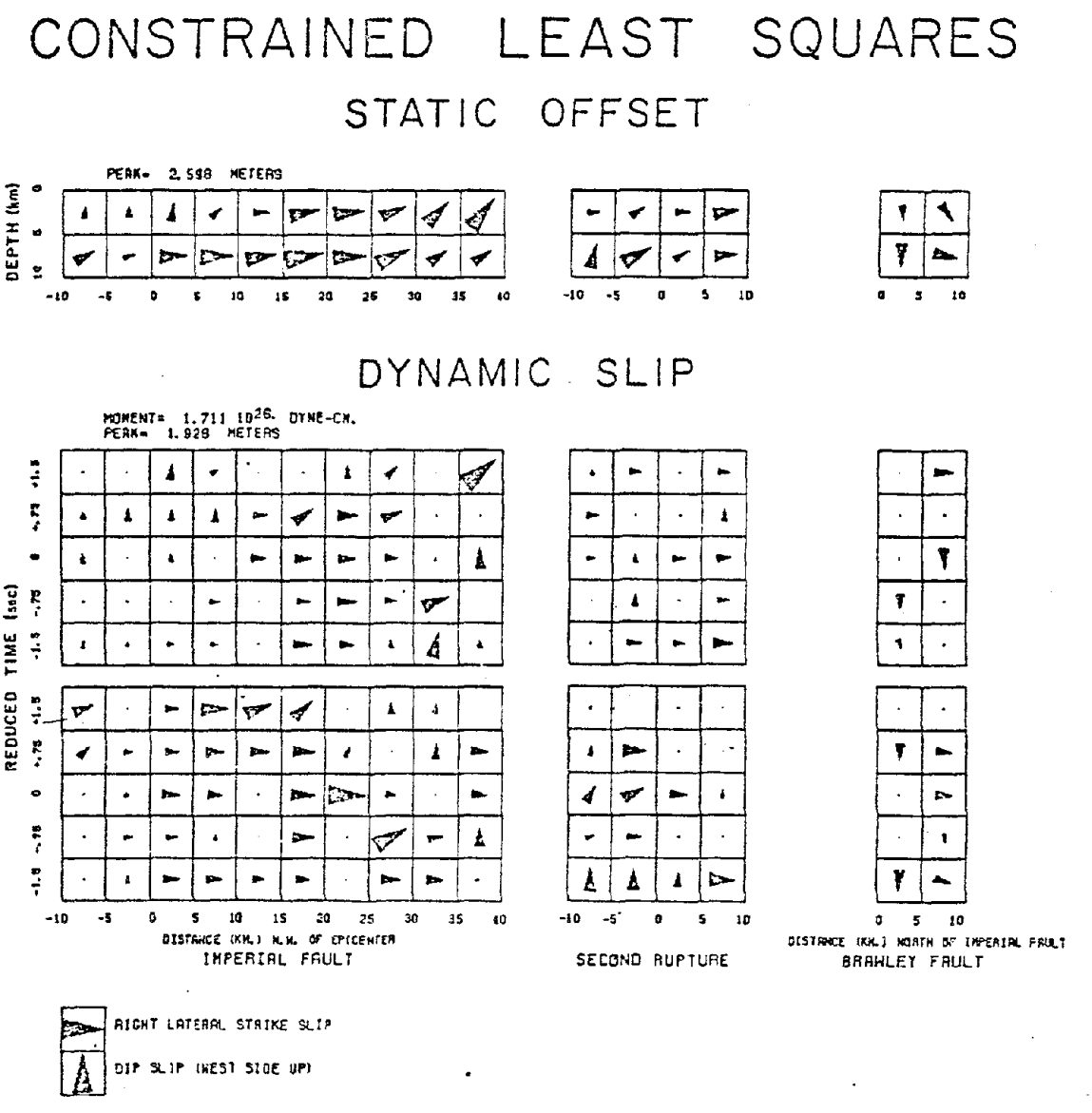

Figure 6: Slip on the Imperial and Brawley faults obtained by constrained least squares inversion without stabilization (analogous to the unconstrained solution shown in Figure 4). In this solution, the slip is constrained to be: right-lateral; west side up on the Imperial Fault; and west side down on the Brawley Fault. As a result of the constraints, the dynamic slip (bottom) does not reverse direction and the static offsets (top) in adjacent cells are not in opposing directions (compare with Figures 4 and 5).

STABILIZED CONSTRAINED LEAST SQUARES

STATIC OFFSET

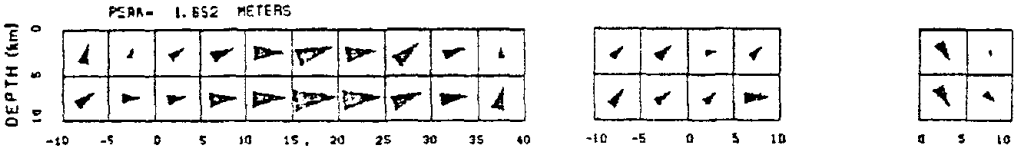

DYNAMIC SLIP

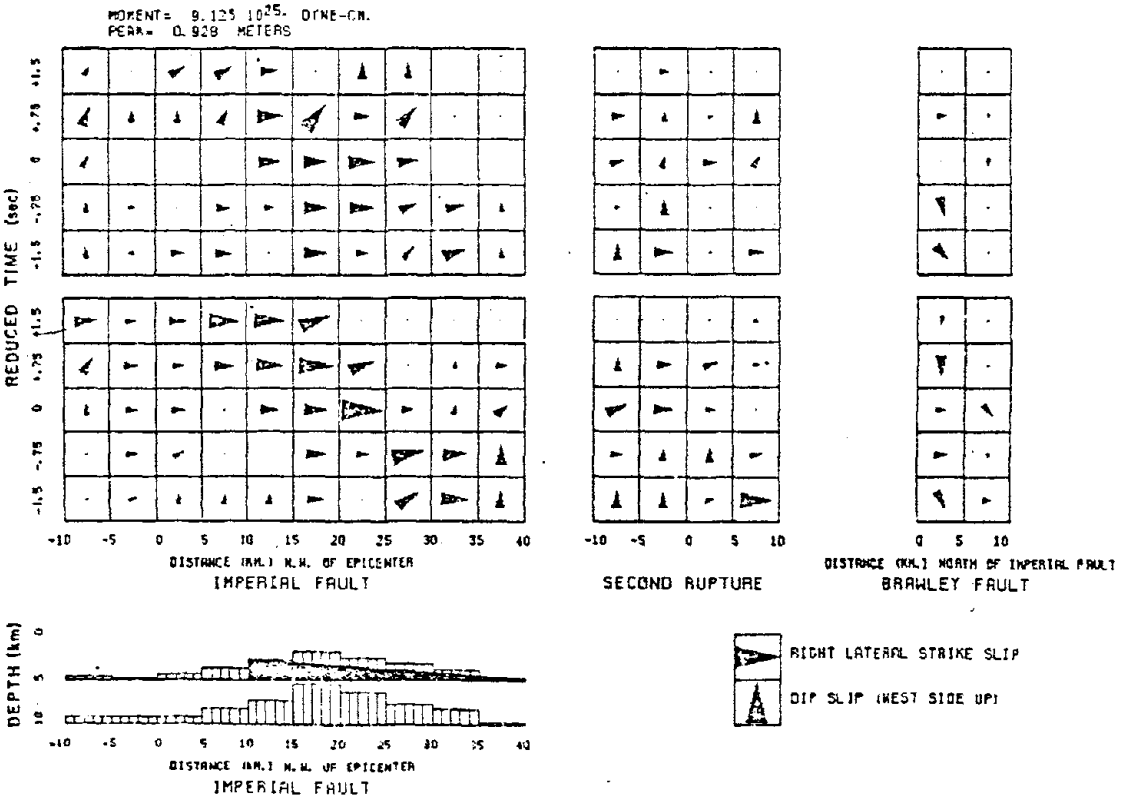

Figure 7: Slip on the Imperial and Brawley faults obtained by constrained least squares inversion with stabilization (analogous to the unstabilized solution in Figure 6). The seismic moment is much smaller than in Figure 6. Also, a noticeable trend with a horizontal phase velocity between 4.0 and 5.0 km/sec has emerged in the dynamic slip of the bottom row of cells on the Imperial Fault. The strike-slip component of offset on the Imperial Fault is shown in the lower left superimposed upon a shaded schematic of the observed surface offset.

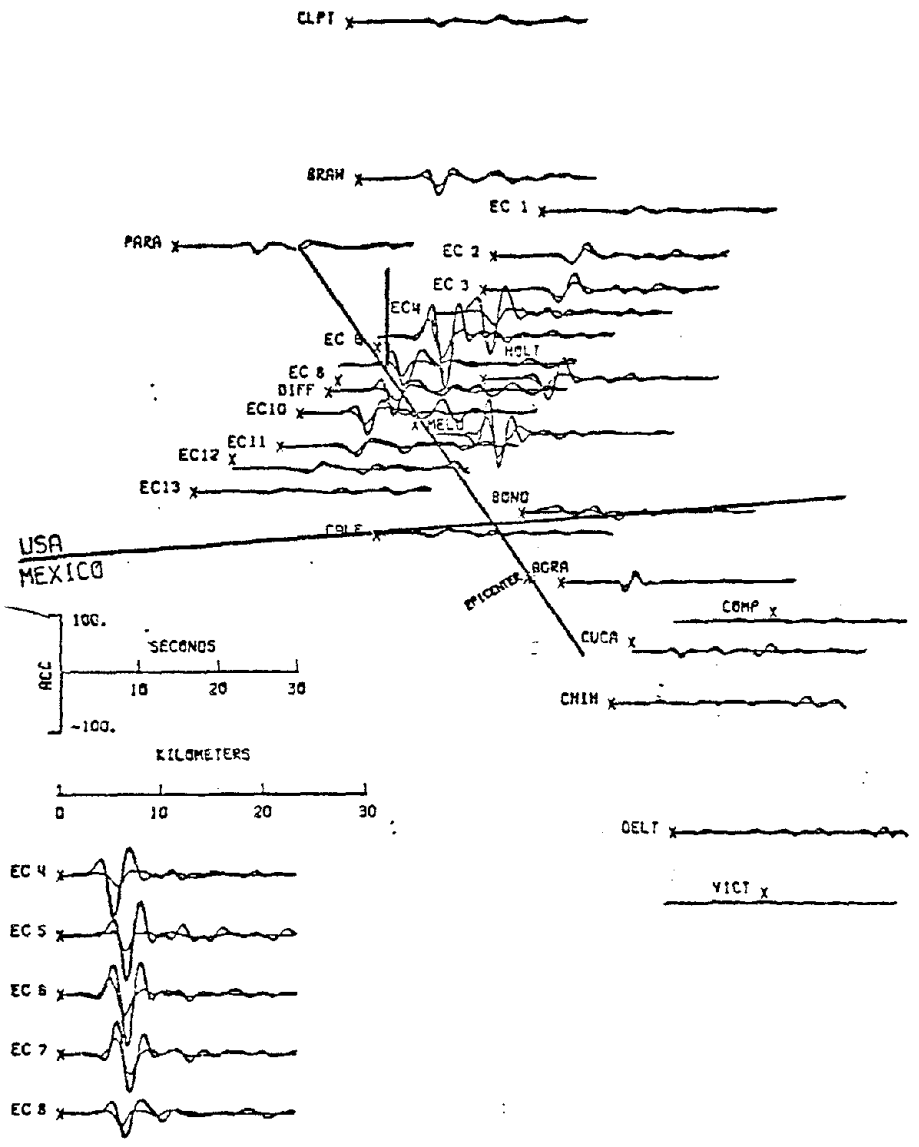

Figure 8: Comparison of the data (heavy line) with the fit to the data (light line) for the stabilized constrained least squares solution shown in Figure 7. The seismograms are plotted geographically beginning at the station location marked with an X. The 230° component (perpendicular to the Imperial Fault) is shown. The accelerograms for stations EC5 and EC7 are shown in the lower left for clarity along with EC4, EC6, and EC8.

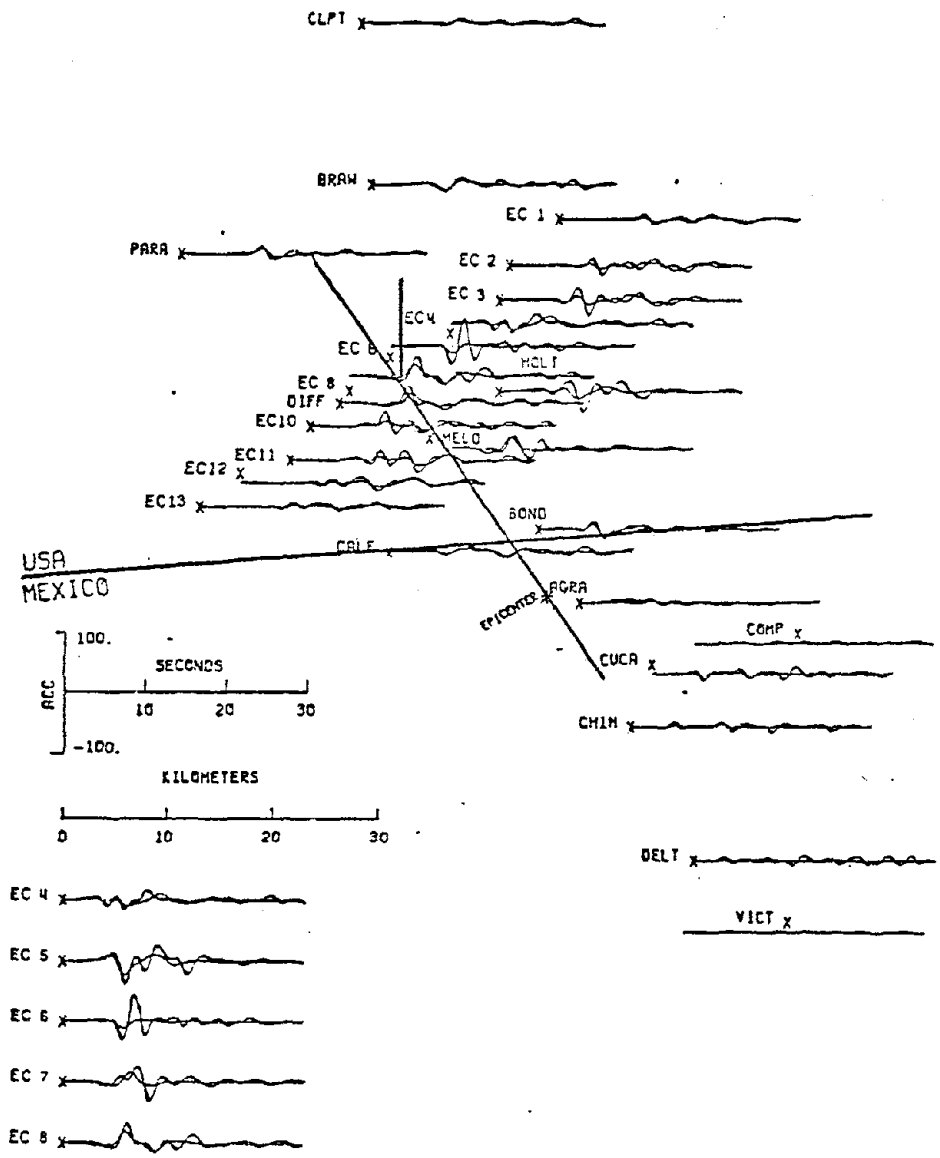

Figure 9: Comparison of the data (heavy line) with the fit to the data (light line) for the stabilized constrained least squares solution shown in Figure 7 (analogous to Figure 8). The 140° component (parallel to the Imperial Fault) is shown.

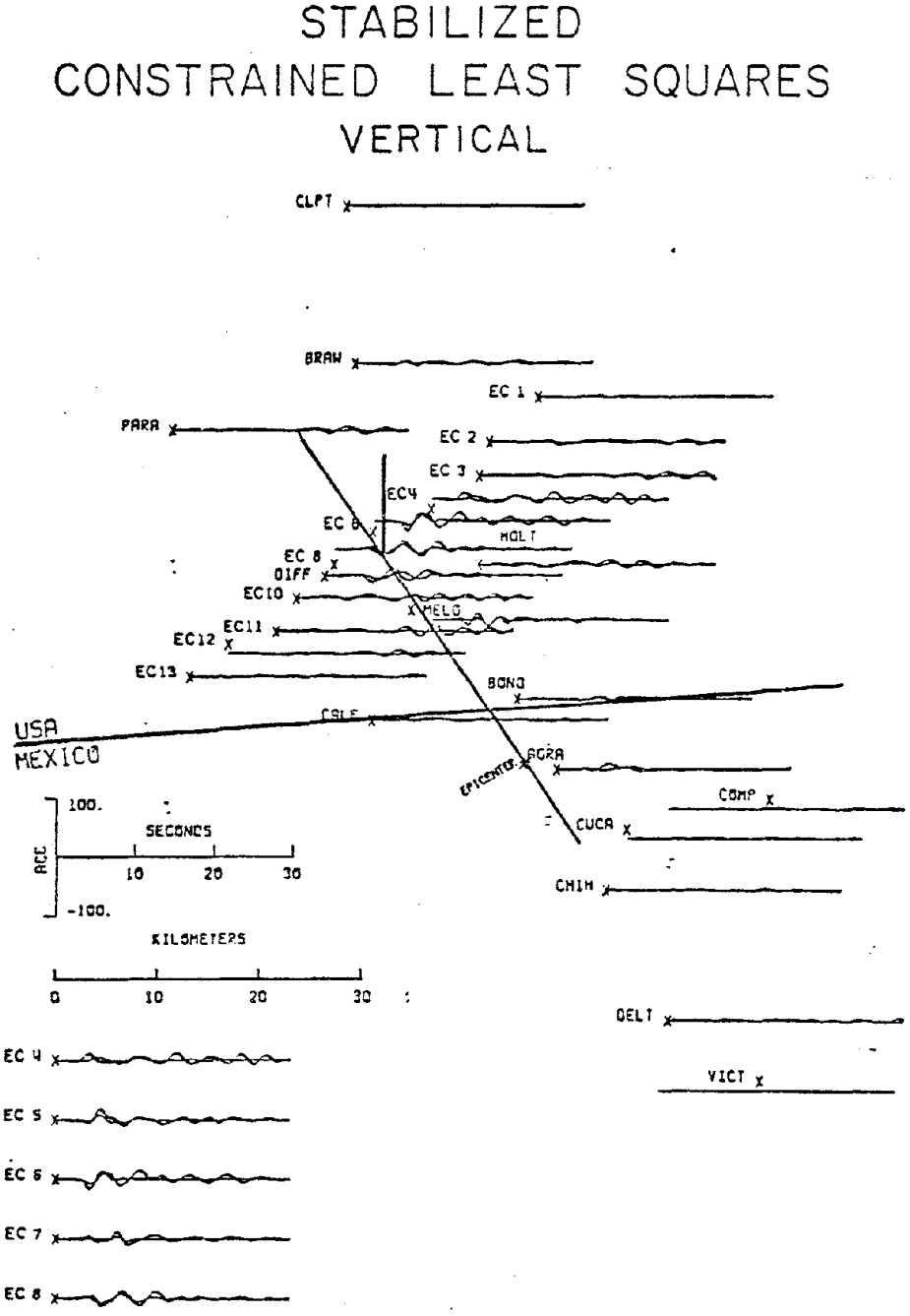

Figure 10: Comparison of the data (heavy line) with the fit to the data (light line) for the stabilized constrained least squares solution shown in Figure 7 (analogous to Figures 8 and 9). The vertical component is shown with orientation given in Table 1.

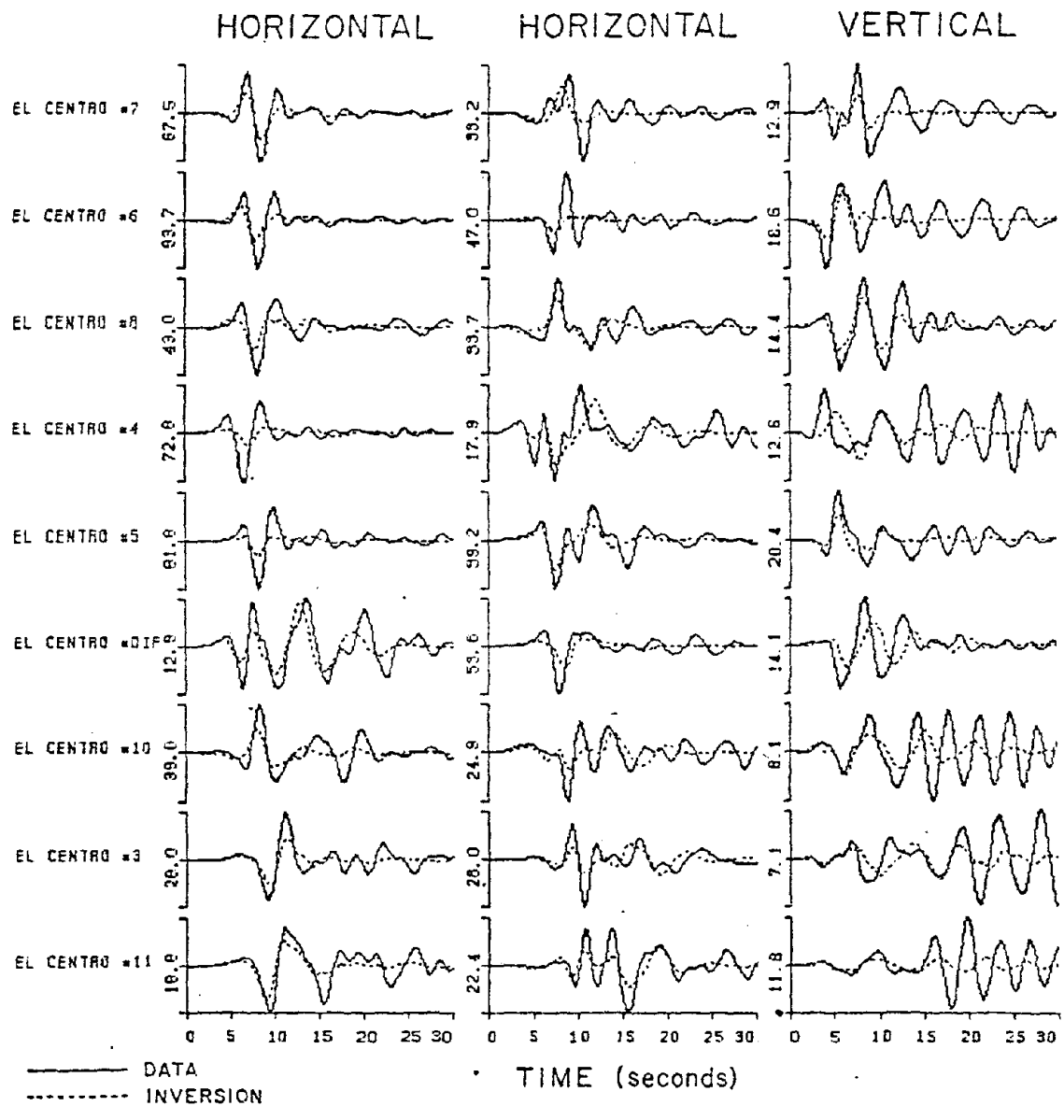

Figure 11: Comparison of data (solid line) with theory (dashed line) by the stabilized constrained least squares solution of Figure 7. Nine of the stations compared in Figures 8 through 10 are shown in greater detail. Component orientations are listed in Table 1 with the left-most horizontal orientation in Table 1 corresponding to the left-most horizontal component plotted above. The numbers at the side of each component are the maximum filtered horizontal acceleration in cm/sec^2. The absolute time scale and acceleration scale pertain to both data and inversion.

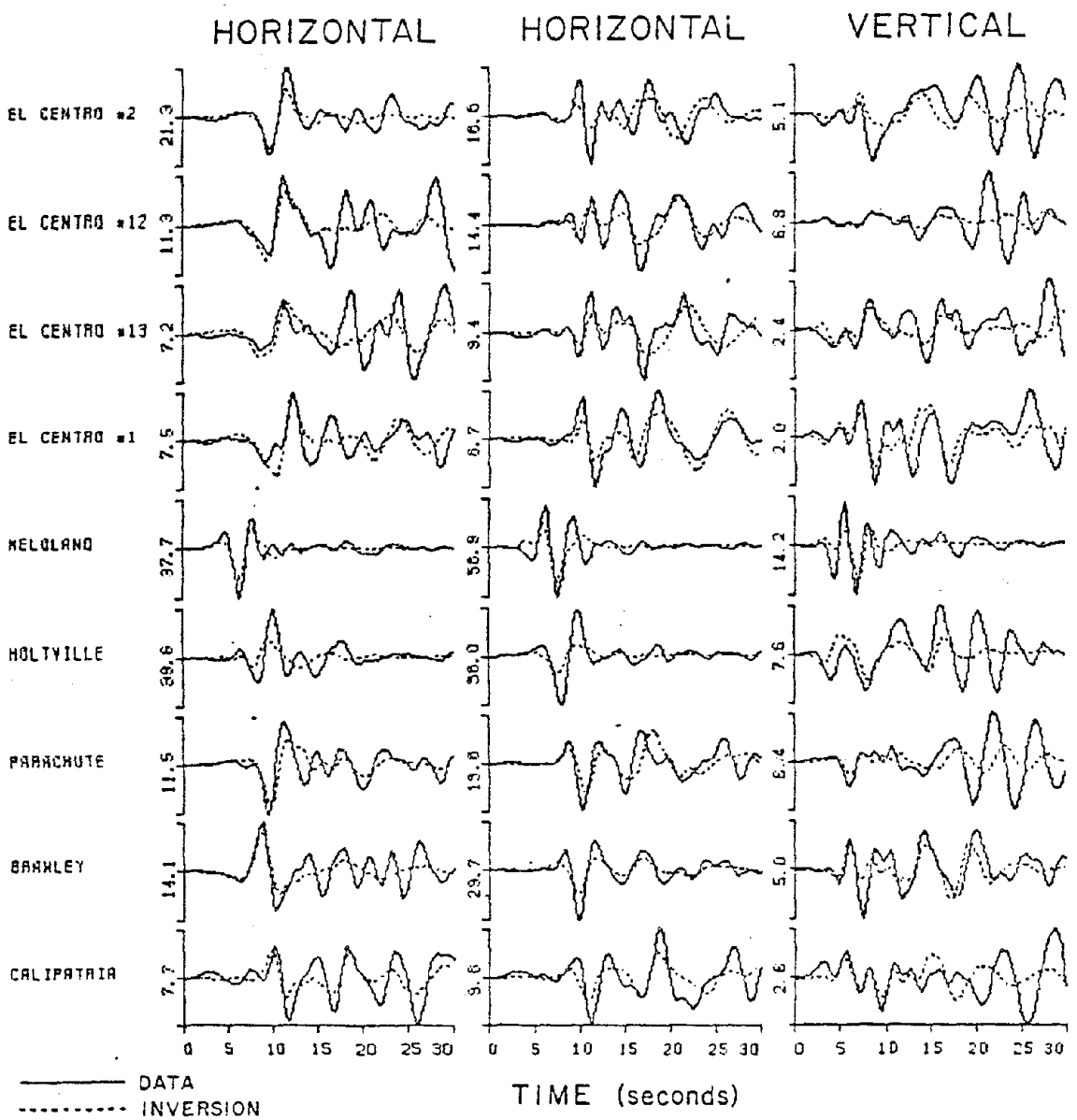

Figure 12: Comparison of data (solid line) with theory (dashed line) by the stabilized constrained least squares solution of Figure 7 (analogous to Figure 11 for nine additional stations).

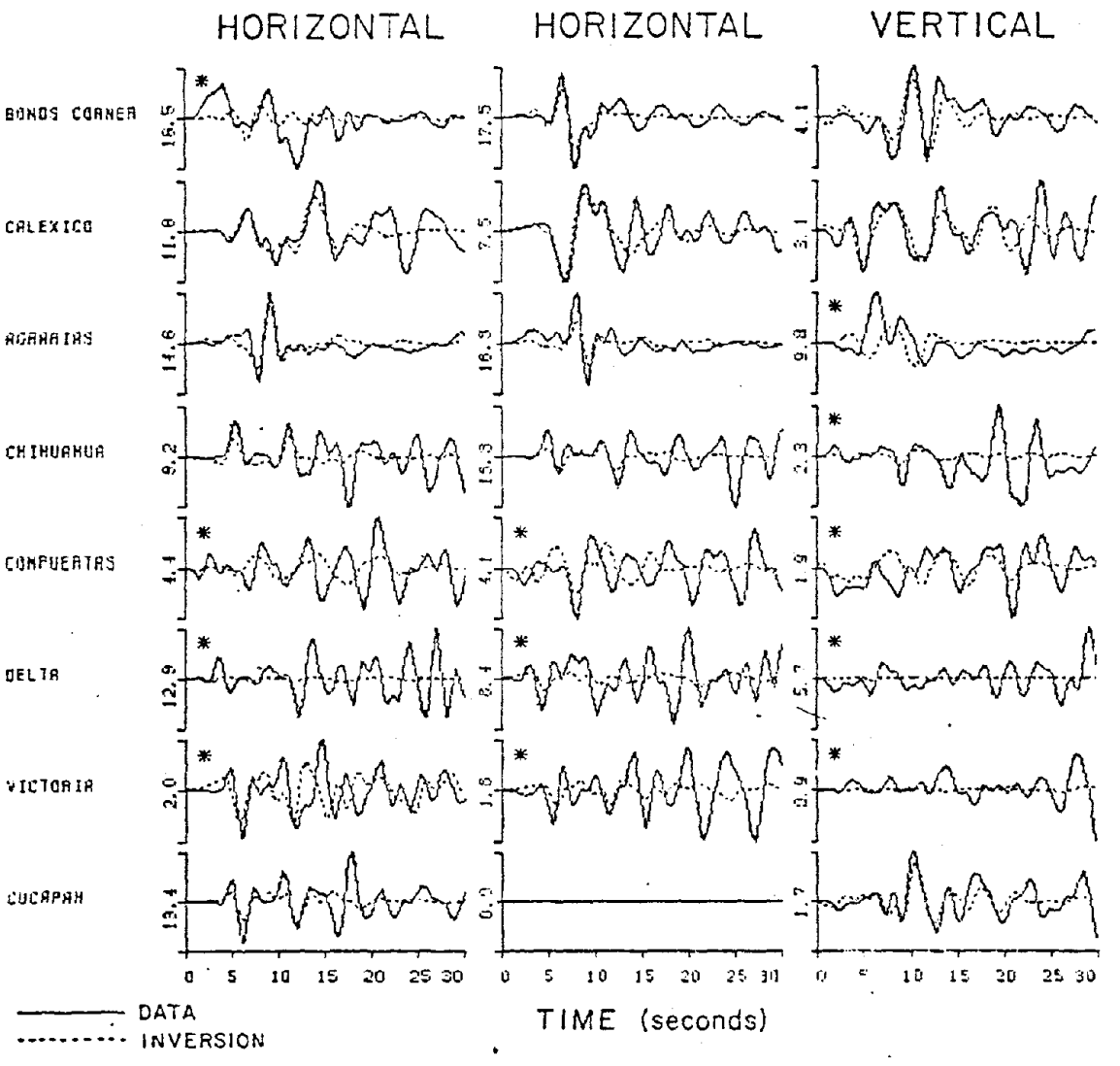

Figure 13: Comparison of data (solid line) with theory (dashed line) by the stabilized constrained least squares solution of Figure 7 (analogous to Figures 11 and 12 for eight additional stations). Components marked with a * are weighted very small in the inversion and have a negligible effect upon the final solution; they are shown for comparison purposes only.

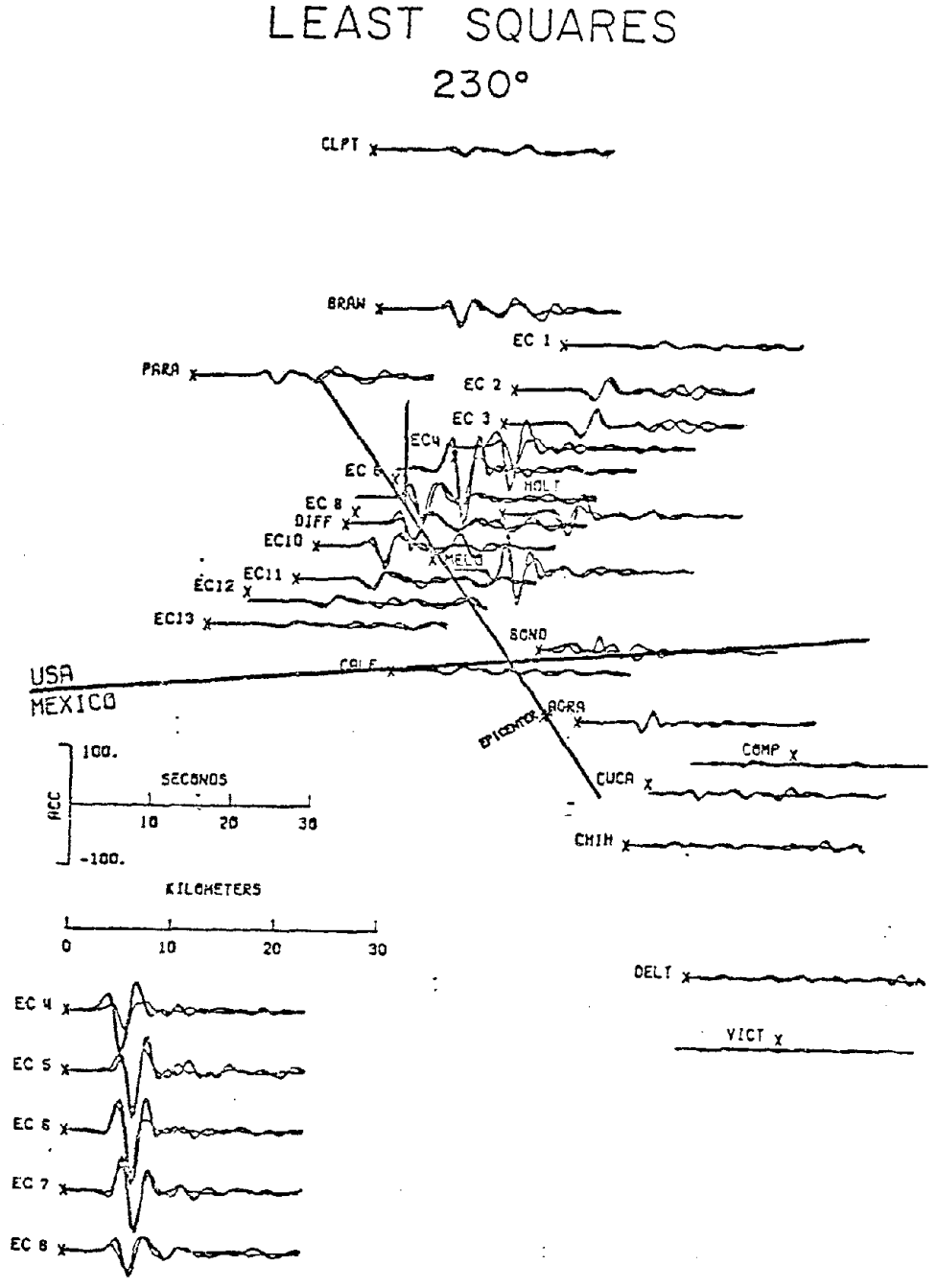

Figure 14: Comparison of the data (heavy line) with the fit to the data (light line) for the unstabilized least squares solution shown in Figure 4. The 230° component (perpendicular to the Imperial Fault) is shown. The fit is almost exact. Compare with Figure 8 for the stabilized constrained least squares fit to the data.

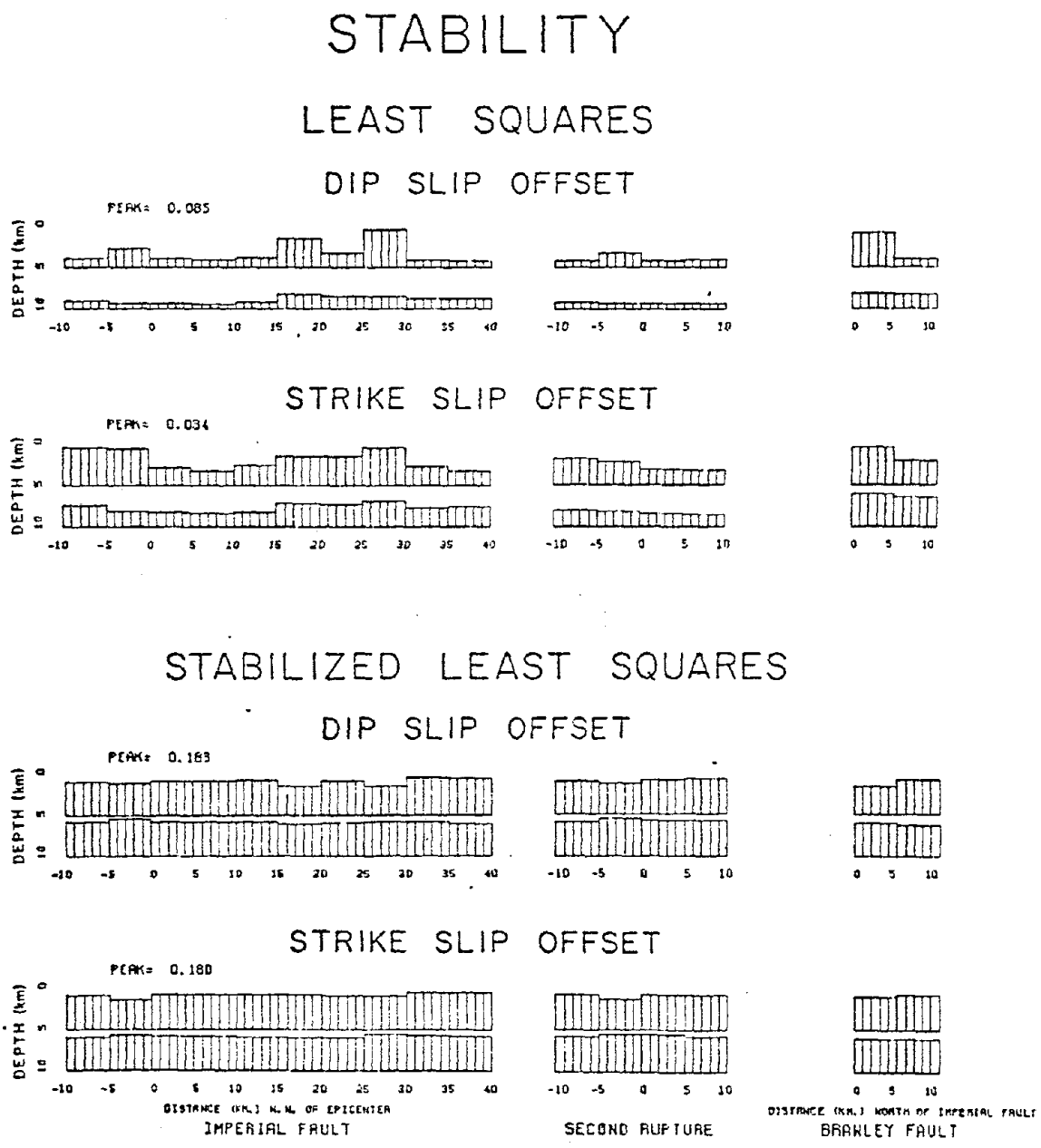

Figure 15: Stability analysis results for the least squares solution (Figure 4) and the stabilized least squares solution (Figure 5). The height of each box is proportional to the smallest percentage change in the data required to change a component of offset in the corresponding cell by one meter. The peak value for each component of offset is given since each of the four results shown is scaled separately. Large values depict cells with most stably determined offset. The stabilized solution (bottom) is more stable everywhere than the unstabilized solution (top), and all cells (bottom) are equally stable.

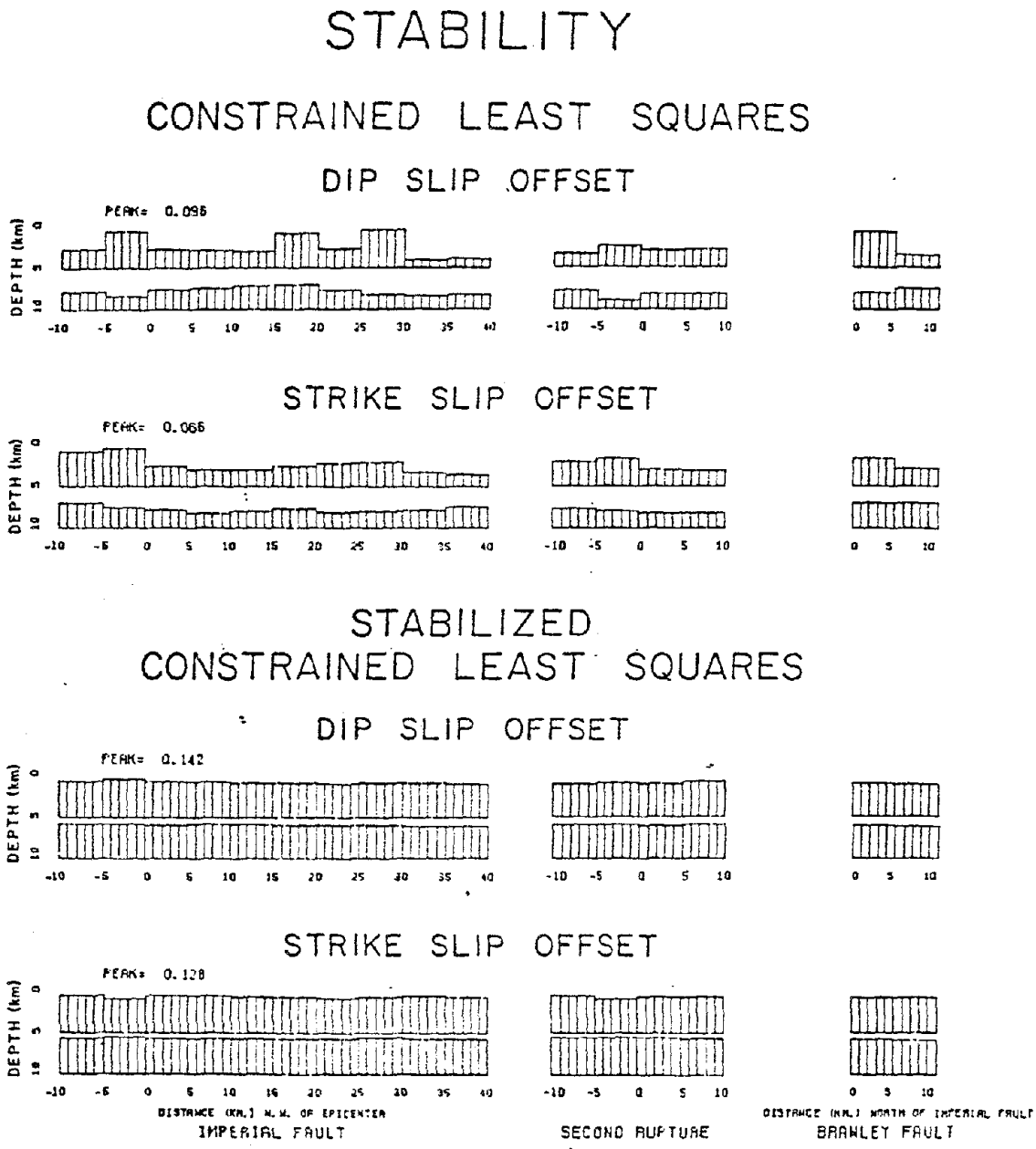

Figure 16: Stability analysis results for the constrained least squares solution (Figure 6) and the stabilized constrained least squares solution (Figure 7) (analogous to Figure 15 for the stability of unconstrained least squares). The constrained least squares solution (top) is everywhere more stable than the unconstrained least squares solution (Figure 15, top). Also, the stabilized solution (bottom) is more stable everywhere than the unstabilized solution (top).

Station Number	Station Name	Component Orientations*
1	El Centro #7	230°, up, 140°
2	El Centro #6	230°, up, 140°
3	Bonds Corner	230°, up, 140°
4	El Centro #8	230°, up, 140°
5	El Centro #5	230°, up, 140°
6	El Centro Diff.	360°, up, 270°
7	El Centro #4	230°, up, 140°
8	Brawley Airport	315°, up, 225°
9	Holtville Post Office	315°, up, 225°
10	El Centro #10	50°, up, 320°
11	Calexico	315°, up, 225°
12	El Centro #11	230°, up, 140°
13	El Centro #3	230°, up, 140°
14	Parachute Test Fac.	315°, up, 225°
15	El Centro #2	230°, up, 140°
16	El Centro #12	230°, up, 140°
17	Calipatria	315°, up, 225°
18	El Centro #13	230°, up, 140°
19	El Centro #1	230°, up, 140°
20	Superstition Mt.**	135°, up, 45°
21	Plaster City**	135°, up, 45°
22	Coachella Canal #4**	135°, up, 45°
23	Agrarias	183°, down, 93°
24	Cerro Prieto**	57°, down, 327°
25	Chihuahua	192°, down, 102°
26	Compuertas	195°, down, 105°
27	Delta	172°, down, 82°
28	Cucapah	85°, up, 355°
29	Victoria	75°, up, 345°
30	Meloland	0°, up, 270°

Table 1: List of component orientations for near-field stations recording the October 15, 1979 Imperial Valley earthquake.

* Horizontal direction measured in degrees clockwise from North.

** Stations not considered in the inversion studies.

Layer	Thickness/ Depth (km)		P-Wave Velocity, km/sec	S-Wave Velocity, km/sec	Density gm/cm^3
1	0.10	0.0	1.690	0.500	2.04
2	0.15	0.10	1.790	0.818	2.06
3	0.50	0.25	2.167	1.010	2.13
4	0.50	0.75	2.533	1.200	2.21
5	0.50	1.25	2.900	1.410	2.28
6	0.50	1.75	3.267	1.620	2.35
7	0.50	2.25	3.633	1.850	2.43
8	0.50	2.75	4.000	2.080	2.50
9	0.50	3.25	4.367	2.330	2.57
10	0.50	3.75	4.733	2.590	2.65
11	0.50	4.25	5.100	2.870	2.72
12	0.50	4.75	5.375	3.060	2.77
13	0.50	5.25	5.650	3.260	2.83
14	5.25	5.75	5.750	3.320	2.85
15	0.30	11.0	6.700	3.870	3.04
16	0.30	11.3	6.900	3.980	3.08
17	0.30	11.6	7.100	4.100	3.12
18	13.1	11.9	7.300	4.210	3.16
19	25.0	25.0	7.800	4.500	3.26
20	--	50.0	8.100	4.670	3.32

Table 2: Crustal structure consisting of homogeneous plane layers used in the calculation of theoretical Green's functions for the Imperial Valley, California.